Inaugural-Dissertation zur Erlangung des Doktorgrades der Naturwissenschaftlichen Fakultät der Justus-Liebig-Universität Giessen

Investigation of ground and isomeric states of exotic nuclei using advances in multiple-reflection time-of-flight mass spectrometry: Unraveling riddles surrounding the proton-emitting isomer(s) in ^{94}Ag

vorgelegt von

Gabriella Kripkó-Koncz

aus Debrecen, Ungarn

Fachbereich 07 - Mathematik und Informatik, Physik, Geographie

II. Physikalisches Institut Justus-Liebig-Universität Gießen

Gießen, September 15, 2025

Zusammenfassung

Die Masse eines Atomkerns, bzw. seine Bindungsenergie, spiegelt dessen Kernstruktur, Stabilität und Form wider. Hochpräzise Massenmessungen exotischer Kerne mit extremen Proton-Neutron-Verhältnissen ermöglichen die Untersuchung der Entwicklung von Schalenabschlüsse des Kernes, des Beginns von Deformationen, des Vorhandenseins metastabiler (isomerer) Zustände, der Synthese schwerer Elemente im Universum und vieler weiterer bemerkenswerter Phänomene. Ein besonders auffälliges Beispiel für einen isomeren Zustand in der Nähe von ^{100}Sn ist ein Spinfallen-Isomer in ^{94}Ag mit einer Spin/Parität von (21^+), welches Eigenschaften besitzt, die in der gesamten Nuklidkarte einzigartig sind. Dieses Isomer weist verschiedene Zerfallskanäle auf, wie z.B. β-Zerfall, β-verzögerte Protonenemission, direkten Ein-Protonen-Zerfall (1p) und überraschenderweise sogar direkten Zwei-Protonen-Zerfall (2p), wobei die beiden letztgenannten Beobachtungen die Kernphysik-Gemeinschaft seit 20 Jahren vor Rätsel stellen. Die leistungsstarke Technik der Multireflexions-Flugzeit-Massenspektrometrie (MR-TOF-MS), die hochpräzise Massenmessungen von Kernen mit Halbwertszeiten von mindestens einer Millisekunde ermöglicht, wurde in dieser Arbeit verwendet, um verschiedene Grund- und Isomeriezustände in mittelschweren exotischen Kernen zu untersuchen und letztendlich die Rätsel um die 1p/2p-Zerfallszweige von ^{94}Ag weiter zu lösen.

Die in dieser Arbeit implementierten Entwicklungen zur Datenerfassung und -analyse ermöglichten es, die Möglichkeiten der verwendeten MR-TOF-MS-Aufbauten voll auszuschöpfen. Zu diesen Entwicklungen gehören beispielsweise die Validierung und Feinabstimmung eines Softwarepakets zur Simulation der erwarteten TOF-Spektren, die Durchführung systematischer Studien zur Massenunsicherheit mittels Breitband-Massenmessungen mit relativen Masse-Ladungs-Fenstern von mehr als 10% und die Gewährleistung eines schnellen und reproduzierbaren Wechsels des Betriebsmodus eines MR-TOF-MS von längeren Flugzeiten, die ein höheres Massenauflösungsvermögen ermöglichen, zu kürzeren Zykluslängen, die den Zugang zu Kernen mit kurzen Halbwertszeiten von wenigen Millisekunden ermöglichen.

Mit dem MR-TOF-MS dem TITAN-Experiment (TRIUMF's Ion Trap for Atomic and Nuclear Science) am TRIUMF in Vancouver, Kanada, wurde die Masse neutronenreicher Indiumisotope über den Schalenabschluss $N = 82$ gemessen. Dies beinhaltet die erste Massenmessung der Nuklide ^{133,134}In und die erste direkte Massenmessung des Nuklids ^{132}In. Darüber hinaus besitzen die gemessenen Indiumisotope mehrere isomere Zustände mit unterschiedlichen Anregungsenergien und Halbwertszeiten. Viele dieser Zustände wurden in dieser Arbeit beobachtet, darunter beispielsweise die erstmalige Messung der Anregungsenergie des $(1/2^-)$-Isomers von ^{133}In, die signifikante Verringerung der Unsicherheit der Anregungsenergien zweier hochliegender Isomere, $^{127\mathrm{n}}$In und $^{131\mathrm{n}}$In, sowie die Beobachtung eines kurzlebigen Isomers in ^{125}In mit einer Halbwertszeit von nur 5 ms. Insgesamt unterstreichen diese Messungen die Leistungsfähigkeit der eingesetzten Massenmessungs- und Datenanalysetechniken, wobei die letztgenannten Techniken in dieser Arbeit speziell für die präzise Verarbeitung der spezifischen Datensätze mit mehreren überlappenden Verteilungen entwickelt wurden.

Mit dem Messaufbau des FRS-IC-Experiment (FRS Ion Cacher) am GSI Helmholtzzentrum für Schwerionenforschung in Darmstadt, Deutschland wurde die erste direkte Massenmessung von ^{93}Pd, dem 1p-Zerfallstochteratom des (21^+)-Isomers in ^{94}Ag, durchgeführt. Die Messung ergab einen Massenüberschuss von $-59127(35)$ keV, wodurch die Massenunsicherheit um eine Größenordnung reduziert wurde. Infolgedessen wurde eine entscheidende Inkompatibilität im zuvor berichteten Zerfallsschema der 1p- und 2p-Zweige festgestellt: Die Messung zeigt erstmals zweifelsfrei, dass die Anregungsenergien der vermuteten Mutterzustände der 1p- und 2p-Zerfallszweige in ^{94}Ag voneinander abweichen, was die bisherige Interpretation dieser Zerfallszweige in Frage stellt. Drei Szenarien, die diesen scheinbaren Widerspruch auflösen könnten, werden diskutiert und durch modernste Schalenmodell- und Mean-Field-Theorie-Berechnungen er-

läutert. Die letztgenannten Berechnungen stützen die Existenz zweier strukturell unterschiedlicher High-Spin-Zustände in ^{94}Ag, die die 1p- und 2p-Zerfallszweige speisen, was mögliche Erklärungen für fast alle historischen Rätsel rund um diese exotischen Zerfallsmodi liefern würde.

Abstract

The mass of an atomic nucleus, i.e. its nuclear binding energy, reflects its nuclear structure, stability and shape. High-precision mass measurements of exotic nuclei with extreme proton-to-neutron ratios allow to study the evolution of nuclear shell closures, the onsets of deformation, the presence of metastable (isomeric) states, the synthesis of heavy elements in the universe and many more striking phenomena. There exists a particularly striking example of an isomeric state in the vicinity of ^{100}Sn, a spin-trap isomer in ^{94}Ag with spin-parity of (21^+), which is known to possess properties that are unique in the entire Chart of Nuclei. This isomer has been reported to have multiple decay channels, such as β decay, β-delayed proton emission, direct one-proton (1p) decay and, surprisingly, even direct two-proton (2p) decay, out of which the latter two observations have puzzled the nuclear physics community for the last 20 years. The powerful technique of multiple-reflection time-of-flight mass spectrometry (MR-TOF-MS), which enables to perform accurate mass measurements of nuclei with half-lives down to a millisecond, was used in this work to study different ground and isomeric states in medium-heavy exotic nuclei and, ultimately, to further unravel the riddles surrounding the 1p/2p-decay branches of ^{94}Ag.

The data acquisition and analysis developments, implemented in this work, allowed to fully exploit the capabilities of the used MR-TOF-MS setups. These developments include, e.g., the validation and fine-adjustments of a software package, which allows for the simulation of the expected TOF spectra, the completion of systematic studies of the mass uncertainty using broadband mass measurements with relative mass-to-charge windows of more than 10% and the assurance of a quick and reproducible change of the operation mode of an MR-TOF-MS from longer flight times, enabling higher mass resolving powers, to shorter cycle lengths, allowing access to nuclei with small half-lives of a few milliseconds.

The MR-TOF-MS of TRIUMF's Ion Trap for Atomic and Nuclear Science in Vancouver, Canada was used to measure the mass of neutron-rich indium isotopes across the $N = 82$ shell closure. This includes the first mass measurement of the nuclides ^{133,134}In and the first direct mass measurement of the nuclide ^{132}In. Furthermore, the measured indium isotopes possess multiple isomeric states with varying excitation energies and half-lives, many of which were observed in this work including, e.g., the first-time measurement of the excitation energy of the $(1/2^-)$ isomer in ^{133}In, the significant uncertainty reduction of the excitation energies of two high-lying isomers, $^{127\mathrm{n}}$In and $^{131\mathrm{n}}$In, and the observation of a short-lived isomer in ^{125}In with half-life of only 5 ms. Overall, these measurements highlight the capabilities of the employed mass measurement and data analysis techniques, the latter of which was tailored in this work to accurately treat the specific data sets containing multiple overlapping peaks.

The measurement setup of the FRS Ion Catcher at GSI in Darmstadt, Germany was used to perform the first direct mass measurement of ^{93}Pd, the 1p-decay daughter of the (21^+) isomer in ^{94}Ag, which resulted in a mass excess value of $-59127(35)$ keV reducing the mass uncertainty by an order of magnitude. As a consequence, a crucial incompatibility in the previously reported decay scheme of the 1p and 2p branches is found: the measurement shows for the first time beyond doubt that the excitation energies of the presumed parent states of the 1p and 2p decay branches in ^{94}Ag disagree, which calls into question the present interpretation of these decay branches. Three scenarios are discussed, which could resolve this apparent contradiction, and elucidated by performing state-of-the-art shell-model and mean-field calculations. The latter calculations confirm that, based on the reported decay information, the 2p emission cannot be fed from the same (21^+) isomer as the 1p emission, but indicate that it could originate from a second, structurally different, high-spin state. This would give possible explanations to almost all historical riddles surrounding these exotic decay modes.

Contents

Motivation **1**

1 From the production to the mass measurement of exotic nuclei **2**
1.1 Motivation for mass measurements . . . 3
1.2 Production and separation techniques . . . 5
1.2.1 Isotope Separation On-Line techniques, e.g. at TRIUMF: ISAC . . . 6
1.2.2 In-flight separation techniques, e.g. at GSI: FRS . . . 7
1.2.3 Hybrid techniques, e.g. at GSI: FRS Ion Catcher . . . 9
1.3 Mass measurement techniques . . . 10

2 Improvements of the FRS Ion Catcher experiment **19**
2.1 Flexible and reliable preparation of the measurement settings . . . 19
2.2 Fast and reproducible experimental tuning of the MR-TOF-MS . . . 22
2.3 Removal of reference clock effects on the mass accuracy . . . 24

3 MR-TOF-MS data analysis procedure and its improvements **27**
3.1 The data analysis procedure . . . 28
3.2 Enhanced speed and flexibility of the data analysis framework . . . 31
3.3 Uncertainty contributions . . . 33
3.4 Final mass values from individual measurements . . . 51
3.5 Special cases of overlapping peaks . . . 52
3.6 Consistency checks . . . 54

4 Mass measurements of neutron-rich indium isotopes at TITAN, TRIUMF **62**
4.1 Description of the experiment . . . 62
4.2 Overview of measured masses and comparison to literature . . . 64
4.3 Desired improvements . . . 74

5 Mass measurements of neutron-deficient nuclides close to the $N = Z$ line below ^{100}Sn at FRS Ion Catcher, GSI **76**
5.1 Verification of identification: yields observed in FRS vs. FRS Ion Catcher . . . 78
5.2 Overview of measured masses and comparison to literature . . . 87
5.3 Implications to the 1p/2p decay branches of the (21^+) spin-trap isomer of ^{94}Ag . . . 95
5.3.1 Estimating the ground-state mass of ^{94}Ag . . . 99
5.3.2 Scenarios to resolve the discrepancy between the 1p/2p decay branches . . . 112
5.3.3 Theoretical interpretation and possible explanations to the puzzles . . . 114

6 Summary and outlook **120**

Acknowledgements **123**

List of Figures **126**

List of Tables **127**

References **156**

Motivation

"They Do It with Mirrors"
— Agatha Christie

Nowadays, experimental studies of exotic nuclei far from the valley of β stability, complemented by theoretical investigations, are at the forefront of nuclear physics research. The mass of a nucleus reflects its nuclear binding energy. Therefore, precisely measuring the mass of exotic nuclei may provide key information for understanding the synthesis of heavy elements in the universe and it allows to study nuclear structure phenomena including, e.g., the evolution of nuclear shell closures, the onsets of deformation or the presence of metastable (isomeric) states. The powerful technique of multiple-reflection time-of-flight mass spectrometry (MR-TOF-MS) enables high-precision direct mass measurements of short-lived nuclides with half-lives down to a millisecond. It is compatible with all methods for the production and separation of exotic nuclei, and, due to its sensitivity, high mass resolving power and broadband and non-scanning measurement characteristics, it is well suited for the studies of isomeric states.

In this work, advances were made to two instances of MR-TOF-MSs, one of them belonging to the TRIUMF's Ion Trap for Atomic and Nuclear Science (TITAN) experiment at TRIUMF in Vancouver, Canada and another one belonging to the FRS Ion Catcher (FRS-IC) experiment at GSI Helmholtz Centre for Heavy Ion Research in Darmstadt, Germany. Then, these measurement setups were used to study different ground and isomeric states in medium-heavy exotic nuclei.

Firstly, mass measurements of neutron-rich indium isotopes were performed using TITAN's MR-TOF-MS crossing the $N = 82$ shell closure. These isotopes possess a large multiplicity and variety of isomeric states, with excitation energies ranging from a few tens of keV to a few MeV, half-lives ranging from a few milliseconds to a few seconds and covering a large dynamic range, which represents an ultimate test for the mass measurement and data analysis techniques.

Secondly, mass measurements of neutron-deficient nuclei in the vicinity of ^{100}Sn were performed at FRS-IC, including the first direct mass measurement of ^{93}Pd, reducing its mass uncertainty by an order of magnitude. This allows to study a spin-trap isomer in ^{94}Ag with spin-parity of (21^+), which is known to possess properties that are unique in the entire Chart of Nuclei. This isomer has been reported to have various decay channels, such as β decay, β-delayed proton emission, direct one-proton (1p) decay and, surprisingly, even direct two-proton (2p) decay, out of which the latter two observations have puzzled the nuclear physics community for the last 20 years. Combining the results of the mass measurements reported here with state-of-the-art shell-model and mean-field calculations allows to further unravel the historical riddles surrounding the 1p/2p-decay branches.

Chapter 1

From the production to the mass measurement of exotic nuclei

Most of our current knowledge about the structure of atomic nuclei has been obtained from experiments conducted with nuclei that are located in the Chart of Nuclides in and around the valley of β stability and naturally occur on Earth. Through studying the natural abundance of the different isotopes, it has been noticed that the isotopes containing 2, 8, 20, 28, 50, 82 etc. neutrons and/or protons occur more frequently in nature than other isotopes. Such nuclei, like the noble gases, have a particularly stable structure, spherical shape and a larger proton/neutron-separation energy, and are difficult to excite [Groeppert Mayer, 1948]. These observations could not be interpreted with the liquid drop model of atomic nuclei widely used at the time [Bethe & Bacher, 1936, Weizsäcker, 1935], hence the above-mentioned special numbers have been called magic numbers. The discovery of these magic numbers played a crucial role in shaping our understanding of the structure of atomic nuclei and have lead to the development of the nuclear shell model, where the origin of the magic numbers could be explained as results of nuclear shell closures [Groeppert Mayer, 1948, Groeppert Mayer, 1949]. The constancy of magic numbers had been a fundamental principle in nuclear structure physics for several decades.

Moving away from the valley of β stability, reaching the so-called exotic nuclei with extreme ratios between the number of protons and neutrons, a number of new striking phenomena emerge. The magic numbers can change or disappear driven by the evolution of nuclear shell closures [Sorlin & Porquet, 2008], e.g., in some of the exotic nuclei near closed shells, states with deformed shapes start to appear even at low excitation energies [Thibault et al., 1975, Détraz et al., 1979]. Additionally, the density distribution of some of the exotic nuclei shows surprising properties, e.g., they can be surrounded by a neutron or proton halo, making their overall size significantly larger [Anne et al., 1990, Riisager, 1994], or, in some cases, even a bubble-like proton distribution may develop [Mutschler et al., 2017]. Furthermore, these nuclei can have different exotic decay channels, such as β-delayed or direct one- or two-proton/neutron emission [Pfützner et al., 2023, Spyrou et al., 2012] and, even, β-delayed fission [Andreyev et al., 2013]. Finally, studies of these nuclei can also provide crucial information for the nucleosynthesis of heavy elements above iron-nickel, i.e. with mass number $A \gtrsim 60$, because the paths of most of the nucleosynthesis processes are located far away from the valley of β stability [Burbidge et al., 1957]. These processes include, e.g., the astrophysical rapid neutron-capture process (r-process) [Kajino et al., 2019], the path of which proceeds through many neutron-rich nuclei, the neutrino-induced nucleosynthesis process (νp-process) [Fröhlich et al., 2006, Pruet et al., 2006] and the astrophysical rapid proton-capture process (rp-process) [Schatz et al., 2001, Cyburt et al., 2016], the paths of which proceed through neutron-deficient nuclei.

The experimental study of exotic nuclei has been made possible by the technical development of particle accelerators in the last few decades. Nowadays, in leading laboratories worldwide,

experiments are being carried out with radioactive ion beams (RIB) to investigate the structure of these nuclei. In this chapter, an introduction is given to the main experimental techniques used for the study of exotic nuclei with emphasis on their mass measurements.

1.1 Motivation for mass measurements

The binding energy of the nucleons in an atomic nucleus reflects its nuclear structure, stability and shape, etc., and it is related to the mass of the nucleus ($M_{\mathrm{nucl}}(N,Z)$) via

$$M_{\mathrm{nucl}}(N,Z) = Z \cdot m_p + N \cdot m_n - \mathrm{BE}(N,Z)/c^2 \ . \tag{1.1}$$

Here and further on, Z and N are the atomic and neutron numbers of the nucleus, c is the speed of light, m_p and m_n are the masses of the proton and neutron, and $\mathrm{BE}(N,Z)$ is the nuclear binding energy. Therefore, precisely measuring the masses of exotic nuclei allow to study, e.g., the limits of existence, the evolution of nuclear shell closures, the onsets of deformation etc. [Yamaguchi et al., 2021]. Furthermore, the masses of exotic nuclei influence the paths of different nucleosynthesis processes. This is shown in Ref. [Mumpower et al., 2016] for the case of the astrophysical rapid neutron-capture process, where the nuclei are identified, the masses of which have a large impact on final r-process abundances in multiple astrophysical conditions.

In this work, the emphasis is given to nuclear structure studies guided by mass measurements of exotic nuclei, a few basic concepts of which are described below.

Nuclear structure studies guided by systematic trends of BE derivatives

Different combinations of binding energy differences can be defined to isolate different nuclear properties, such as the one- or two-nucleon separation energies, the empirical shell gaps [Manea et al., 2023], the empirical pairing gaps [Changizi et al., 2015], the empirical and the residual proton-neutron interaction strengths [Bender & Heenen, 2011, Wu et al., 2016], and the Wigner energy [Satula et al., 1997]... Examining the systematic trends of these binding energy (BE) differences, also called as BE derivatives or BE filters, allows to study the evolution of different nuclear properties, e.g., the limits of existence, the evolution of nuclear shell closures, the onsets of deformation along the isotonic or isotopic chains [Yamaguchi et al., 2021]. A few of these BE filters are used in Section 5.3.1 of this work and are described below in a bit more details.

The one-proton and two-proton separation energies, $S_{\mathrm{p}}(N,Z)$ and $S_{2\mathrm{p}}(N,Z)$, represent the energy needed to remove one or two protons from the nucleus and are defined as

$$S_{\mathrm{p}}(N,Z) = \mathrm{BE}(N,Z) - \mathrm{BE}(N,Z-1) \text{ and } S_{2\mathrm{p}}(N,Z) = \mathrm{BE}(N,Z) - \mathrm{BE}(N,Z-2) \ . \tag{1.2}$$

In general, these one- and two-proton separation energies are expected to steadily decrease along an isotopic chain with a decreasing number of neutrons (N) towards the one- and two-proton driplines, which are defined as the first isotopes along the isotopic chain, for which the corresponding one- and two-proton separation energies change their signs to negative. In case of the one-proton separation energy, on top of this steady decrease, there is also an odd-even staggering due to contributions from the proton-proton pairing interactions. In addition, the signature of shell closures is represented by a rapid decrease of the corresponding one- and/or two-proton separation energies at magic proton and neuron numbers.

For odd-odd nuclei, i.e. for nuclei containing odd number of protons and neutrons, the BE filter called as $\delta V_{\mathrm{np}}^{\mathrm{oo}}(N,Z)$ is defined as the following double-difference of the binding energies of four neighboring nuclei:

$$\begin{aligned} \delta V_{\mathrm{np}}^{\mathrm{oo}}(N,Z) &= S_{\mathrm{p}}(N,Z) - S_{\mathrm{p}}(N-1,Z) = \\ &= [\mathrm{BE}(N,Z) - \mathrm{BE}(N,Z-1)] - [\mathrm{BE}(N-1,Z) - \mathrm{BE}(N-1,Z-1)] \ . \end{aligned} \tag{1.3}$$

Assuming that the nuclear core is not changed significantly for the four neighboring nuclei in Eq. (1.3), e.g. they all have the same nuclear shape, this $\delta V_{\rm np}^{\rm oo}$ quantity isolates the empirical interaction strength between the "last" (valence) neutron and proton [Zhang et al., 1989, Cakirli et al., 2005], which has two terms in a typical case, i.e. when $N \not\approx Z$. Its first term (bulk) probes the symmetry energy of the macroscopic mass formula [Stoitsov et al., 2007, Reinhard et al., 2006] and its second term gives the residual interaction strength between the last unpaired neutron and proton, which is only relevant for odd-odd nuclei [Wu et al., 2016].

In case of $N = Z$ nuclei, theory predicts that the value of $\delta V_{\rm np}^{\rm oo}$ is expected to be five times larger compared to $N \neq Z$ nuclei, which is qualitatively consistent with the measured nuclear masses [Van Isacker et al., 1995]. These results are further supported by the fact that the $\delta V_{\rm np}^{\rm oo}$ quantity has been related to the spatial overlap between the wave functions of the valence proton and neutron [Brenner et al., 1990, Brenner et al., 2006], which is expected to be the highest for $N = Z$ nuclei, where the protons and neutrons occupy the same orbitals. In general, the value of $\delta V_{\rm np}^{\rm oo}$ is expected to decrease smoothly with increasing A and/or Z, both along the $N = Z$ line and for $N \neq Z$ nuclei. This is because of three main reasons [Mardor et al., 2021]: (i) Firstly, with increasing A, the nuclear radii increase, thus the average distance between last neutron and proton increases even when they are occupying the same orbital [Brenner et al., 1990]. (ii) Secondly, with increasing Z, the Coulomb-interaction between the protons increases, thus differentiating the proton and neutron wave functions even when they are occupying the same orbital [Brenner et al., 2006]. (iii) Finally, with increasing A, the spin-orbit interaction increases, thus gradually breaking the spin part of Wigner's spin-isospin SU(4) symmetry proposed in Ref. [Wigner, 1937], which reflects the empirical proton-neutron interaction strength according to Ref. [Van Isacker et al., 1995]. Any variation from the smooth decreasing trend of $\delta V_{\rm np}^{\rm oo}$ can be a result of distinct nuclear structure effects, such as a partial symmetry restoration [Mardor et al., 2021] or effects due to nuclear shell closures [Chen et al., 2009, Hamaker et al., 2021].

Nuclear structure in the vicinity of ^{100}Sn

The nucleus ^{100}Sn, containing 50 protons and 50 neutrons, is the heaviest doubly-magic self-conjugate nucleus that is stable with respect to particle emission. In general, $N \approx Z$ nuclei containing the same or similar number of protons and neutrons are highly interesting to study, because they exhibit various phenomena and symmetries, most of which are unique to these nuclei, and their studies provide important benchmarks for theoretical models. Despite the general interest among the nuclear physics community to study theses nuclei, the presently available data concerning the nuclear structure and properties of heavy $N \approx Z$ nuclei are very scarce due to the fact that producing and measuring these nuclides close to the proton-dripline is very challenging. The small production yields and short half-lives of these nuclei hinder the experimental efforts. For an overview of experimental and theoretical efforts in the vicinity of the doubly-magic nucleus ^{100}Sn, see Ref. [Faestermann et al., 2013].

A few examples of the striking phenomena, appearing in heavy $N \approx Z$ nuclei, include, e.g., the formation of high-spin metastable (isomeric) states [Plettner et al., 2004, Nara Singh et al., 2011], the particularly large strength of neutron-proton pairing correlations [Frauendorf & Macchiavelli, 2014], the presence of isobaric analog states and their properties and other effects related to the isospin symmetry and its breaking [Bentley, 2022], the direct and/or β-delayed (two-)proton emission from ground or excited states [Mukha et al., 2006], and the strong resonances in Gamow-Teller transitions close to the proton dripline [Juodagalvis & Dean, 2005]. Experiments with these nuclei also represent stringent tests for theoretical models, e.g., aiming to predict the location of the proton-dripline, i.e. the so-called limits of existence [Herndl & Brown, 1997], or to answer the question if and when the emergence of prolate deformation and shape coexistence starts to become relevant with removing nucleons from the doubly-magic system, ^{100}Sn [Yaneva et al., 2024]. Additionally, these nuclei also allow to test fundamental physics

principles, such as the conserved vector current hypothesis [Hardy & Towner, 2020]. Moreover, the heavy $N \approx Z$ nuclei also have a high impact in modelling nuclear astrophysics processes (rp-process, νp-process), see e.g. [Cyburt et al., 2016, Fröhlich et al., 2006].

In this work, a few of the above-listed striking phenomena are discussed and elucidated guided by mass measurements and guiding mass predictions of neutron-deficient nuclei in the vicinity of ^{100}Sn (see Chapter 5).

Isomeric states and their studies

"Metastable" excited states with half-lives ranging from nanoseconds to years are collectively called as nuclear isomers [Walker & Podolyák, 2020]. Experimental studies of these metastable excited states, complemented by theoretical calculations, can shed light to understanding the underlying reasons for their longer half-lives. Depending on these underlying reasons, i.e. physical mechanisms of hindrance in their respective decays, nuclear isomers are classified into different categories, such as spin-trap isomers, K-isomers, seniority isomers, shape and fission isomers [Jain et al., 2021]. Additionally, measuring the isomer-to-ground state ratio of a certain isomer state may provide important information on the employed production mechanism, see e.g. Refs. [Gao et al., 2023, Häfner et al., 2019]. Furthermore, it is also interesting to study whether certain isomeric states may have a so-called astromeric nature, i.e. may provide crucial information for the synthesis of heavy elements in the universe [Misch et al., 2021, Misch & Mumpower, 2024].

Depending on their half-life and excitation energy, different methods are available for their detection and measurement ranging from decay spectroscopy to different mass measurement techniques [Dickel & Mollaebrahimi, 2024]. To this end, resolving and measuring the mass of ground and isomeric states covering a large dynamic range, which have small excitation energies of a few tens of keV and very short half-lives of a few milliseconds can serve as ultimate tests for the capabilities of the employed mass measurement and data analysis techniques, see e.g. [Xing et al., 2023] and Chapter 4.

In the vicinity of ^{100}Sn, the formation of high-spin isomers is discussed extensively in literature, see e.g. [Plettner et al., 2004, Nara Singh et al., 2011]. As one particularly striking example, Ref. [Plettner et al., 2004] reported the observation of a spin-trap isomer in ^{94}Ag with a very high excitation energy of more than 6 MeV and with the highest spin observed so far for β-decaying nuclei, (21^+). This isomer possesses properties that are unique in the entire Chart of the Nuclides; it is has been reported to undergo multiple decay modes, see e.g. [Plettner et al., 2004, Mukha et al., 2004, Mukha et al., 2005, Cerny et al., 2009, Mukha et al., 2006]. Out of these observations, the historical riddles surrounding the direct one- and two-proton decay of this high-spin isomer are further investigated in this work (see Chapter 5).

1.2 Production and separation techniques

Experimental studies of exotic nuclei far from the valley of β stability require fast and efficient production and separation techniques, recent reviews of which can be found in [Blumenfeld et al., 2013, Geissel & Morrissey, 2023]. Since most of these nuclei are short-lived and, therefore, are not readily available on Earth, they need to be produced through specific nuclear or atomic reactions or through radioactive decays. These reactions or decay modes include, e.g., spontaneous or particle-induced fission, spallation, fragmentation, fusion, deeply inelastic or (multi-)nucleon transfer reactions [Geissel et al., 1995]. Due to the nature of these processes, usually, a large number of different reaction products are created and among them the exotic nuclei of interest are usually produced with the smallest production yields. This necessitates the usage of fast and efficient separation techniques to separate the isotopes of interest from the other, typically more abundantly produced species, which are commonly referred to as "contaminants".

Nowadays, two main complementary production and separation techniques are employed at different accelerator facilities worldwide to study the properties of exotic nuclei, namely, the isotope separation online (ISOL) and the in-flight separation techniques. Presently existing ISOL facilities include, e.g., ISOLDE at CERN, Genf, Switzerland [Kugler, 2000] and ISAC at TRIUMF, Vancouver, Canada [Ball et al., 2016]. Presently existing and future in-flight facilities include, e.g., ARIS at FRIB, East Lansing, USA [Hausmann et al., 2013], FRS at GSI and, in the future, Super-FRS at FAIR, Darmstadt, Germany [Geissel et al., 1992] and BigRIPS at RIKEN, Wako, Japan [Kubo, 2003]. In this subchapter, the basic principles, advantages and disadvantages of the ISOL and in-flight techniques are discussed. Two example for existing facilities, where these production and separation techniques are employed, are discussed in a bit more details, because they are relevant for this work.

Notably, besides the ISOL and the in-flight separation techniques, there are more techniques available for the production and separation of exotic nuclei, e.g., the so-called ion guide isotope separator online method (IGISOL), the so-called in-gas laser ionization and spectroscopy method (IGLIS) or the production of exotic nuclei via neutron capture in nuclear reactors. These methods, however, are omitted from the present discussion as they are not relevant for this work.

1.2.1 Isotope separation online techniques, e.g. at TRIUMF: ISAC

At ISOL facilities, typically two kinds of nuclear reactions are responsible for the production of exotic nuclei: (i) the proton-induced fragmentation of a heavy target, known as spallation, and (ii) nuclear fission, i.e. the disintegration of heavy nuclei into two large fragments [Geissel et al., 1995]. A target, which is usually composed of heavy elements, such as uranium or tantalum, with typical areal densities of a few tens and up to a few hundreds of g/cm^2, is bombarded with a proton or a light-ion beam at energies of 100-1500 MeV/nucleon and with beam intensities of 1-100 μA in a typical ISOL facility [Blumenfeld et al., 2013]. The reaction products are stopped in the target, which is kept at a high temperature causing the reaction products to diffuse through and effuse out of the target. The products extracted from the target are then transported towards the ion source, where they are ionized by different means, e.g., by electron impact, laser and/or surface ionization.

The very high intensities of the proton or light-ion beams provided by the accelerators of ISOL facilities allow to reach exceptionally high production yields for some of the exotic nuclei of interest. On the other hand, both the efficiency and the time of the diffusion and effusion processes in the target and the efficiency of the ionization of the reaction products depend on the geometry and temperature of the target and strongly depend on the chemical properties of the target elements and reaction products [U. Köster, 2002]. Overall, this can lead to relatively long diffusion and effusion times, typically longer than a few tens of milliseconds and up to a few seconds, which limits the half-life of the nuclei accessible by this method. Furthermore, the chemistry-dependence of the efficiency of this method results that there is a list of refractory elements that have not yet been produced successfully at ISOL facilities. This remains a major challenge and requires a continuous development of this production and separation technique (for example Ref. [Jajčišinová et al., 2024] presents a recent study of the production of different actinide elements, which are challenging to produce employing the ISOL technique).

In the next step, the singly-charged reaction products are re-accelerated to a few tens of keV and are separated by electromagnetic separators, e.g., most commonly, by large double-stage magnetic separators [Wollnik & Becker, 1985]. Although the resolving power of such magnetic separators usually allows to separate the ions according to their mass-to-charge ratio, but it is typically not sufficient to separate isobaric species from each other. This results that the radioactive beams produced by the ISOL method are typically governed by a large amount of isobaric contaminant species, especially the ones with low ionization potential, which are surface ionized easily. This may hinder the measurement or the identification of the less abundant

exotic nuclides of interest, the rates of which have to be enhanced by other means, e.g., by resonant laser ionization techniques [Marsh, 2014]. If there is a need to further suppress the isobaric background, the usage of resonant laser ionization techniques can be combined with, e.g., the application of multiple-reflection time-of-flight mass-spectrometers (MR-TOF-MSs) as high-resolution isobar separators [Wolf et al., 2013, Hirsh et al., 2016, Dickel et al., 2017a], see Section 1.3 below for more details.

After their separation according to their mass-to-charge ratios, the reaction products can be either (i) directly delivered to experimental setups that require beams with low energy to study different properties of the exotic nuclei of interest, e.g., for high-precision mass measurements using different ion trapping techniques, decay and/or laser spectroscopy studies, or (ii) post-accelerated up to beam energies of a few tens of MeV/nucleon available at present ISOL facilities and sent to a secondary target, e.g. for in-flight spectroscopy studies of exotic nuclei, or delivered to other experimental setups, which require higher energy beams.

The results presented in this work include measurements performed at the Tri University Meson Factory (TRIUMF) in Vancouver, Canada employing the ISOL technique for the production and separation of exotic nuclei, see Chapter 4. There, TRIUMF's main cyclotron is used to accelerate H^- ions to an energy of 480 MeV. The electrons are then removed with stripper foils leading to a proton beam. At the Isotope Separator and Accelerator (ISAC) [Ball et al., 2016], the generated proton beam with an intensity of up to 100 μA hits a target composed of heavy elements and the extracted and ionized ions undergo a subsequent re-acceleration and separation. The latter is achieved using the ISAC mass separator, which has a mass separation power of up to 2000 [Bricault et al., 2002]. Overall, the ISAC facility at TRIUMF is an ISOL facility, which can handle the highest beam power on the target among the existing ISOL facilities worldwide with a beam energy of about 500 MeV and an intensity of up to 100 μA corresponding to a power of up to 50 kW [U. Köster, 2002]. Ultimately, this can lead to considerably high production yields even for the most exotic ion species, many of which are, therefore, accessible at ISAC, TRIUMF.

1.2.2 In-flight separation techniques, e.g. at GSI: FRS

While the chemistry dependence of the production yields of the ISOL technique hinders the production of certain elements at ISOL facilities, a complementary technique of in-flight separation provides an element-independent production of exotic nuclei. At in-flight facilities, depending on the beam energy, typically three kinds of nuclear reactions are responsible for the production of exotic nuclei: (i) at low primary beam energies near the Coulomb barrier, exotic nuclei are produced through fusion reactions often followed by a sequential evaporation of nucleons (usually neutrons) or sequential fission, which has been used to produce a large range of neutron-deficient nuclei across the nuclear chart and to synthesize the heaviest elements, and (ii) at much higher primary beam energies, projectile fragmentation of a heavy-ion beam impinging on a light target and Coulomb-fission and abrasion-fission of the projectile are used for the production of exotic nuclei [Geissel & Morrissey, 2023]. A target, which is usually composed of lighter elements, such as beryllium, with typical areal densities ranging from a few tens of μg/cm^2 up to a few tens of g/cm^2, is bombarded with a heavy-ion beam at energies ranging from low energies near the Coulomb barrier up to a few GeV/nucleon.

The reaction products emerge from the target ionized and mainly in the forward direction and, notably, they are subject to having characteristic charge-state distributions [Scheidenberger et al., 1998]. Therefore, the accessible half-lives of exotic nuclei produced and separated in flight are mainly defined by the flight time of the reaction products through the electromagnetic separators, which are used separate the ions of interest from the unreacted primary beam and other uninteresting reaction products. The flight time of the ions through the separators is typically on the order of a microsecond and below, thus giving an element-independent access to very short-lived exotic nuclei employing the in-flight separation techniques. On the other hand,

the available primary beam intensities for heavy-ion beams are smaller than those for the ISOL techniques, limiting the production yields that can be reached using the in-flight methods.

While for an efficient separation and collection of the products of fusion reactions, gas-filled separators (see e.g. [Semchenkov et al., 2008]) or in-vacuum velocity filters (see e.g. [Münzenberg et al., 1979]) are used, the products of fission and projectile fragmentation are separated by so-called in-vacuum fragment separators (see e.g. [Geissel et al., 1992]). In the latter case, the usage of higher primary beam energies and larger target thicknesses ensures that the reaction products emerge from the target in a fully stripped charge state ($q = Z$) or with only a few electrons attached to them allowing to maximize the their transmission efficiency through the in-flight fragment separators. In contrast to the low-energy magnetic separators employed by the ISOL technique, the in-flight fragment separators can provide highly clean, essentially contamination-free beams of projectile fragments down to a single isotope [Geissel et al., 1992]. Additionally, using an event-by-event particle identification, cocktail beams of fragments can also be treated allowing a simultaneous measurement of multiple isotopes.

After their in-flight separation in electromagnetic separators, the projectile fragments possess relativistic velocities, therefore they can be sent to a secondary target, e.g. for studies of nuclear reactions or for in-flight spectroscopy studies, or directly delivered to experimental setups, which require high energy beams, e.g. for high-precision direct mass measurements using storage rings. On the other hand, for performing low-energy experiments, e.g. high-precision direct mass measurements using ion trapping techniques, they first need to be slowed down and cooled. This is achieved, for example, by the hybrid techniques as described in Section 1.2.3 below.

The results presented in this work include measurements performed at the GSI Helmholtz Centre for Heavy Ion Research in Darmstadt, Germany employing the in-flight separation technique for the production and separation of exotic nuclei, see Chapter 5. There, the universal linear accelerator UNILAC [Angert & Schmelzer, 1969] combined with the heavy-ion synchrotron SIS18 [Blasche et al., 1993] can deliver a bunched, relativistic beam of stable ions up to uranium with a magnetic rigidity up to 18 Tm corresponding to energies up to 1 GeV/nucleon for $^{238}U^{73+}$ and relativistic ion velocities up to ∼90% of the speed of light. The relativistic beam is then delivered to the fragment separator FRS [Geissel et al., 1992], where the exotic nuclei of interest are produced in projectile fragmentation and fission reactions at the production target and the fragments emerging from the target in the forward direction are separated in flight. Notably, the fact that the SIS18 can deliver high energy beams at GSI facilitates the usage of thick production targets with areal densities of several g/cm^2 at FRS, where secondary (multi-step) reactions are expected to start to play a significant role in the overall production of the fragments [Dickel et al., 2024]. This approach was used in the experiment reported here to enhance the production yields of the ions (see Chapter 5).

Fig. 1.1 shows a schematic view of the FRS, which has two symmetric separation stages, each of which consists of two dipole magnets for probing the magnetic rigidity of the ions, and a set of quadrupole and hexapole magnets for the focusing of the ions. Slits can be used at each focal planes of the measurement setup to control the variety of isotopes included in the cocktail beam of fragments. A wedge-shaped degrader is located between the two symmetric separation stages, i.e. at the central focal plane of the FRS. The separation of isotopes at the final focal plane of the FRS is based on the $B\rho - \Delta E - B\rho$ method, where the magnetic rigidity of the ions ($B\rho$) is proportional to their mass-to-charge ratio and their energy loss in the degrader at the central focal plane (ΔE) is proportional to the square of their proton number. The FRS particle identification (PID) detectors allow to determine the ions' mass-to-charge ratio and proton number event-by-event based on the $B\rho - \Delta E* - \mathrm{TOF_{FRS}}$ method, which refers to a simultaneous measurement of the ions' velocity between the central and final focal planes of the FRS using plastic scintillators ($\mathrm{TOF_{FRS}}$), their energy deposition in a multiple sampling ionization chamber (MUSIC) detector ($\Delta E*$) and their position and angle at the FRS focal planes using time-projection chambers

(TPC) reflecting their magnetic rigidity ($B\rho$).

Changing the angle of the wedge-shaped degrader enables to select between the two main operation modes of the FRS: achromatic mode or monoenergetic mode [Geissel & Scheidenberger, 1998]. An achromatic FRS optics allows to achieve an optimal spatial separation of the isotopes at the final focal plane of the FRS [Geissel et al., 1992]. On the other hand, this operation mode leads to a large range straggling at the final focal plane of FRS, which in turn decreases the ions' stopping efficiencies relevant for high-precision experiments with trapped exotic nuclei. To treat these cases, the monoenergetic FRS optics has been developed to minimize the range straggling of the separated ions and enable higher stopping efficiencies for the isotopes of interest [Scheidenberger et al., 2003]. In this operation mode the isotopes are separated in stopping range. On the other hand, optimizing the primary beam energy with the SIS18 might allow to stop more than one isotopes simultaneously with similarly high stopping efficiencies, which has been described conceptually in Ref. [Dickel et al., 2024] and tested experimentally for the first time within the context of this work (see Chapter 5).

Currently, with the ongoing construction of the new underground heavy-ion ring accelerator SIS100, relativistic ion velocities up to ∼99% of the speed of light will be available in the future at the Facility for Antiproton and Ion Research (FAIR) near Darmstadt, Germany. The new superconducting fragment separator (Super-FRS) is a central instrument of the research program of early science days at FAIR, which will enable a higher acceptance than the existing FRS and allow studies of nuclear structure, astrophysics and reactions.

1.2.3 Hybrid techniques, e.g. at GSI: FRS Ion Catcher

Hybrid techniques allow to perform low-energy experiments with exotic nuclei that were produced and separated in flight employing a gas-filled stopping cell to stop and thermalize the ions. In the process of thermalization, the mean kinetic energy of the ions becomes the same as that of the buffer gas atoms, i.e. in the order of few tens of meV. Afterwards, the thermalized ions are extracted from the stopping cell with typical extraction times of 10–100 ms, which limits the half-lives of the exotic nuclei accessible by the hybrid methods. Except for this limitation for the accessible half-lives, the hybrid techniques typically inherit most of the properties of the in-flight separation techniques, such as an element-independent production of exotic nuclei or the ability to provide highly clean beams of projectile fragments.

The technical developments and part of the results presented in this work (see Chapters 2 and 5) were obtained with the FRS Ion Catcher (FRS-IC) measurement setup [Plaß et al., 2013a], which is a test bench for the hybrid techniques at FRS, GSI. Fig. 1.1 shows a schematic view of the FRS in combination with the FRS-IC, the latter of which has three main components: a gas-filled cryogenic stopping cell (CSC) [Ranjan et al., 2011, Purushothaman et al., 2013, Ranjan et al., 2015], a radiofrequency quadrupole (RFQ) beamline [Greiner et al., 2020, Haettner et al., 2018, Yu et al., 2024a] and a multiple-reflection time-of-flight mass spectrometer (MR-TOF-MS) [Plaß et al., 2008, Dickel et al., 2015b]. Before the fragment beam hits the CSC, the largest part of the beam energy is removed by the degrader setup of the FRS, the thickness of which is optimized using a variable degrader setup and a MUSIC detector located in front of the CSC. Afterwards, the gas-filled CSC is used to fully slow down and thermalize the ions by collisions with the helium buffer gas atoms, guide them to the exit side of the CSC by electric fields along the stopping cell provided by the so-called DC cage, radially focus them onto an extraction nozzle using an RF Carpet [Reiter, 2015] and extract them with the gas flow. The CSC was designed to thermalize ions produced at unprecedented energies of 1000 MeV/u. Using the so-called long DC cage [Miskun, 2019], the performance characteristics of the CSC at its current stage include e.g. an areal density of up to 9 mg/cm^2, an extraction efficiency of ∼60%, a mean extraction time of about 25 ms, and a rate capability of ∼10^4 ions/s incident beam intensities [Plaß et al., 2019, Reiter et al., 2016]. In comparison, using the so-called short DC cage the CSC demonstrates

practically no loss of the extraction efficiency at incident beam intensities up to 2×10^5 ions/s [Amanbayev, 2023]. After their extraction from the CSC, the ions of interest are transported towards the MR-TOF-MS using the RFQ beamline, which allows to perform low-energy beam diagnostics and to identify and select the desired ions of interest employing a pair of RFQ-based mass filters, a set of silicon surface barrier and channeltron detectors and a set of ion sources including, e.g., the newly-commissioned laser ablation carbon cluster ion source (LACCI) [Yu et al., 2024a]. Furthermore, using the so-called isolation-dissociation-isolation technique, i.e. combining the pair of mass filters with a collision-induced dissociation step in between, the RFQ beamline allows to suppress the molecular contaminants by more than 4 orders of magnitude [Greiner et al., 2020]. At the MR-TOF-MS, high-precision direct mass measurements of the ions of interest are performed (for more details, see Section 1.3 below).

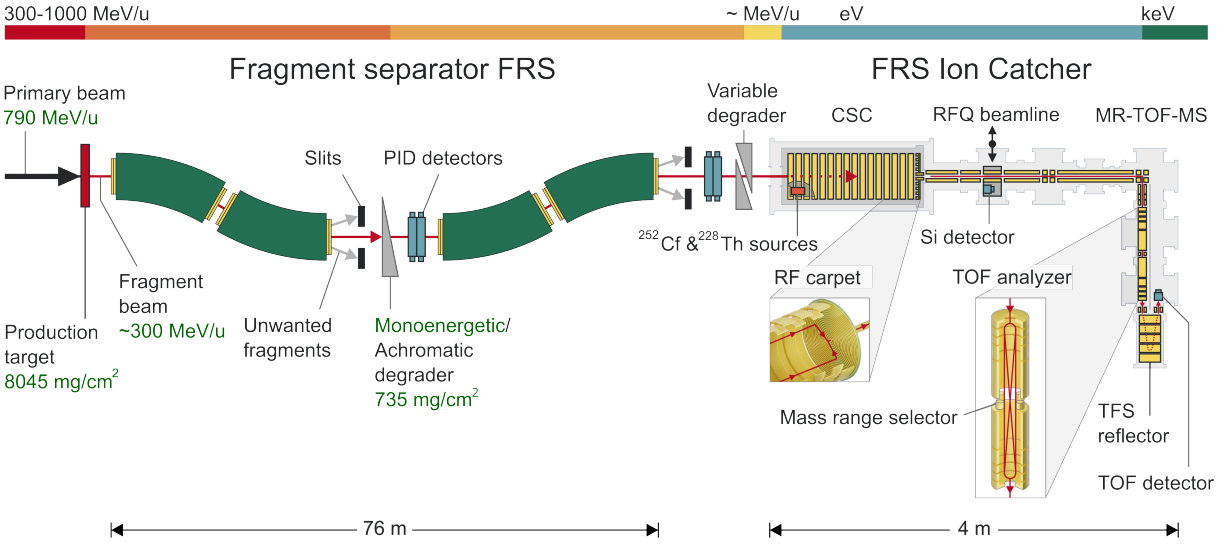

Figure 1.1: Schematic figure of the experimental setup, including the FRS [Geissel et al., 1992] and the FRS-IC [Plaß et al., 2013a]. Detailed descriptions are given in the corresponding subsections, see Sections 1.2.2 and 1.2.3. The dark green colour marks experimental-settings-related information that are specific to the measurements close to the $N = Z$ line reported in Chapter 5. Adopted and modified from [Amanbayev, 2023].

1.3 Mass measurement techniques

Since the mass of a nucleus provides key information for studying nuclear structure and astrophysics, different techniques for high precision mass measurements of exotic nuclei have been developed, a recent review of which can be found in [Yamaguchi et al., 2021].

The mass of a nucleus can be either measured directly or determined via indirect measurement methods. While the direct mass measurement techniques are based on the charged particles' interaction with external electromagnetic fields, the indirect techniques rely on deducing the mass of a nucleus through nuclear reactions using the known masses and the measured kinetic energies of all other reaction products and applying the rules of energy conservation. In case of radioactive decay, measuring the kinetic energies (or in case of β decay the kinetic energy spectrum) of the emitted particles allows to deduce the decay energy of the given decay channel, the so-called decay Q value, which can then be used to derive the mass of the mother nucleus assuming that the mass of the daughter nucleus is known or vica versa. In case of heavy proton-rich nuclides in the vicinity of ^{100}Sn, which are studied in this work, the predominant β decay mode is positron emission or, in other words, β^+ decay. This is due to the fact that for these

nuclides the available decay energy is much larger than the difference between the decay energy windows corresponding to positron emission and electron capture (EC), which is given by the difference between two times the electron mass, $2m_e$, and the binding energy of the electron in the atomic shell, which is to be captured by the electron capture process [Park, 2017]. Therefore, the mass excess (ME) difference between the parent and daughter nuclides, ${}^{A}_{Z}X$ and ${}^{A}_{Z-1}X$, in case of these heavy $N \approx Z$ nuclides is given by

$$\mathrm{ME}\left({}^{A}_{Z}X\right) - \mathrm{ME}\left({}^{A}_{Z-1}X\right) = Q_{\mathrm{EC}} = Q^{x}_{\beta} + E_x + 2m_e, \tag{1.4}$$

where Q_{EC} is the ground-state–to–ground-state energy difference and Q^{x}_{β} is the β decay end-point energy for a particular final state x in the daughter nucleus with an excitation energy E_x.

One of the main strengths of the indirect methods is that they provide access to very short-lived nuclei including species, which are formed in resonance reactions. Another advantage is that the knowledge of a single mass value allows to determine all masses in the complete decay chain, because this single mass provides an anchor point for the entire chain. Consequently, these indirect methods are well suited for exploring the limits of existence of proton-rich nuclides, see e.g. [Lykiardopoulou et al., 2023]. On the other hand, one important drawback of the indirect methods is related to the fact that they often require spectroscopic information, which can be rather scarce, especially for exotic nuclei. This is especially relevant for the cases when the mass values are derived based on β decay end-point energy measurements. There, for determining β-decay branching ratios in complex β-decay schemes, a connected problem arises, the so-called pandemonium problem, which creates a bias in favor of the dominant transitions [Hardy et al., 1977]. Ultimately, this may result in significant systematic deviations of the mass values that are derived based on indirect methods from the "true mass values", see e.g. [Haettner et al., 2011, Xing et al., 2018, Van Schelt et al., 2012, Van Schelt et al., 2013]. To overcome this disadvantage, direct mass measurements are needed, which are in the focus of this work.

Nowadays, high-precision direct mass measurements of exotic nuclei are performed mainly using one or by combining the usage of two of the following three measurement devices: Penning traps, storage rings or multiple reflection time-of-flight mass spectrometers (MR-TOF-MSs). These measurement methods vary in terms of their achievable mass accuracy, resolution and sensitivity. Additionally, the half-lives of the nuclides, the mass of which can be measured directly with high accuracy, and the maximum dynamic range and mass-to-charge window that can be covered in a single measurement is also different depending on the employed measurement technique. As a consequence, these measurement methods are complementary to each other and can be used to tackle different experimental goals and challenges, such as the short half-lives and the small production cross sections of the ions of interest, the large isobaric contamination of the radioactive beams delivered by ISOL facilities or the population of low-lying isomeric states, which need to be separated from the ground state of the same nucleus.

In this subchapter, the basic principles and associated performance characteristics of the most frequently employed direct mass measurement techniques are discussed.

Direct mass measurements with Penning traps

The highest mass accuracies and mass resolving powers for mass measurements of stable and exotic nuclei are reached with Penning traps (see Fig. 1.3), recent reviews of which can be found in e.g. [Dilling et al., 2018, Eronen et al., 2016]. There are two main Penning trap mass measurement techniques for exotic nuclei, namely the conventional time-of-flight ion-cyclotron-resonance (TOF–ICR) technique, reviewed in e.g. [Blaum, 2006], and the more recently developed phase-imaging ion-cyclotron-resonance (PI–ICR) technique [Eliseev et al., 2013], both of which are based on measuring the ions' cyclotron frequency, ν_c, as briefly described below.

In Penning traps, the ions are radially trapped by a static strong homogeneous magnetic field of strength B and they are axially confined by a static weak quadrupolar electric potential.

The ions' motion in such a trap can be described by the superposition of three independent trap eigenmotions. Two characteristic eigenfrequencies describe the ions' radial motion, the so-called trap-modified cyclotron frequency (ν_+) and the so-called magnetron frequency (ν_-). The ions' axial motion along the magnetic field lines is described by the frequency ν_z. As described in Ref. [Gabrielse, 2009], the cyclotron frequency, ν_c, which is related to the ions' mass-to-charge ratio, m/q, can be calculated by the sum of the ions' radial motion's eigenfrequencies, ν_+ and ν_-, as given by

$$\nu_c = \nu_+ + \nu_- = \frac{1}{2\pi} \cdot \frac{qB}{m}, \tag{1.5}$$

which implies that the sum of the modified cyclotron and the magnetron frequencies is constant, therefore these two eigenmotions can be converted into each other.

The technique of TOF-ICR is based on resonantly converting the ions' magnetron motion in the trap into a modified cyclotron motion by applying an RF quadrupolar excitation of the electric fields for a fixed duration and, afterwards, measuring the ions' time-of-flight (TOF) from their ejection in axial direction from the trap and transport by a magnetic field gradient until they hit the TOF detector. There, the frequency of the RF quadrupolar excitation is varied until a complete resonant conversion between the ions' radial motions is achieved corresponding to the shortest measured TOF, which provides the ions' cyclotron frequency. The method allows to achieve mass resolving powers of a million and beyond and relative mass uncertainties, $\delta m/m$, of a few 10^{-8} with about 3000 measured events and within a measurement time of about 1 second as has been demonstrated in Ref. [Kellerbauer et al., 2003]. On the other hand, due to the scanning nature of this method, it requires $\sim$100 ions to perform a mass measurement, therefore the TOF-ICR measurements can take long, when the production yields are small. Additionally, this method can only cover a narrow mass-to-charge range as defined by the scanned range of frequencies, which limits its usability for the search for high-lying isomeric states and, in some cases, it may even lead to an ambiguous identification of the measured nuclides, see e.g. [Porter et al., 2022]. Finally, the TOF-ICR technique does not allow to simultaneously achieve the highest possible mass accuracy and mass resolving power using the same RF quadrupolar excitation pattern [Eliseev et al., 2014]. The recently developed PI-ICR technique relaxes most of these disadvantages.

The technique of PI-ICR is based on independently measuring the phases of the ions' magnetron and modified cyclotron motions, which is accumulated after a certain number of revolutions in the trap, by projecting the ions' radial motion onto a position-sensitive detector located in axial direction from the trap outside of the strong magnetic field. This method allows to achieve an up to 40 times larger expected mass resolving power and an about 5 times higher expected mass accuracy as compared to the TOF-ICR technique under similar measurement conditions [Eliseev et al., 2013]. As an exemplary result, for mass measurements of stable light ions, superlative mass accuracies of $\delta m/m < 10^{-11}$ have been reached using PI-ICR [Myers, 2024]. On the other hand, for mass measurements of short-lived nuclides with half-lives below 1 second, the typically achieved mass accuracies are $\delta m/m \sim 10^{-8} - 10^{-7}$, which is mostly determined by the available statistics (see Fig. 1.3 and the corresponding discussions). Due to the non-scanning nature of this technique, $\sim$10 ions are sufficient to perform a mass measurement. As a secondary consequence of its non-scanning nature, this method allows to more efficiently study isomeric states of exotic nuclei as compared to the method of TOF-ICR. The PI-ICR technique has been successfully used, e.g., to discover new isomeric states [Stryjczyk et al., 2025] or to measure the mass of both low- and high-lying isomers with excitation energies ranging from less than 100 keV to more than 1 MeV allowing to understand their spin-parity assignments and level ordering [Vilén et al., 2019, Jaries et al., 2024]. On the other hand, to perform PI-ICR measurements with high accuracy the ions first need to be cooled, which increases the measurement cycle and limits the accessibility of short-lived exotic nuclides using this method. Furthermore, the mass-

to-charge window, where all ions can be unambiguously identified as they undergo the same number of revolutions inside the trap, is extremely narrow for the PI-ICR technique, making it inefficient for a large-scale mapping of the nuclear mass surface.

Direct mass measurements with TOF-$B\rho$-MSs and storage rings

At facilities employing projectile fragmentation and in-flight separation techniques, the simultaneous measurement of the time-of-flight (TOF) and magnetic rigidity ($B\rho$) allows to measure the mass of the most exotic and short-lived species (see Fig. 1.3 and the corresponding discussions). Past and present examples of such TOF-$B\rho$ mass spectrometers (TOF-$B\rho$-MSs) worldwide include, e.g., the SPEG spectrometer at GANIL, Caen, France [Savajols, 2001], the S800 spectrometer at NSCL, East Lansing, USA [Matos et al., 2012] and the SHARAQ spectrometer at RIKEN, Wako, Japan [Michimasa et al., 2018]. On the other hand, due to the small overall flight time, masses measured with this method have large uncertainties often dominated by systematic effects; uncertainties above 100 keV up to almost 1 MeV are common ($\delta m/m \sim 10^{-6} - 10^{-5}$), see e.g. [Jurado et al., 2007, Michimasa et al., 2018]. Increasing the overall flight time, e.g. using storage rings, allows to improve the achievable mass accuracy.

The usage of heavy-ion storage rings for mass measurements was pioneered at the Experimental Storage Ring ESR at GSI [Franzke, 1987], where two complementary methods, Schottky mass spectrometry (SMS) [Schlitt et al., 1997, Litvinov et al., 2005] and isochronous mass spectrometry (IMS) [Wollnik, 1987, Hausmann et al., 2000] were established. Besides ESR, nowadays, mass measurements are being performed at two additional storage-ring facilities, namely, at the Cooler Storage Ring for experiments (CSRe) at IMP, Lanzhou, China [Xia et al., 2002] and at the Rare-RI Ring (R3) at RIKEN, Wako, Japan [Yamaguchi et al., 2013]. A recent review of heavy-ion storage rings can be found in [Steck & Litvinov, 2020].

Storage-ring mass spectrometry is based on measuring the revolution time or frequency of the ions in the ring and obtaining their mass-to-charge ratio. While in Schottky mass spectrometry the momentum spread of the ions needs to be minimized using stochastic and/or electron cooling [Nolden et al., 2004, Steck et al., 2004], in isochronous mass spectrometry the mean revolution time of the ions in the ring is independent from their momentum spread, when the isochronous condition is precisely fulfilled. In case of the SMS technique, the revolution frequency of the stored and cooled ions is measured by Schottky noise detection [Borer et al., 1975], and in case of the IMS technique, the revolution time is determined using a time-of-flight (TOF) detector.

Advantages of the SMS technique include the ability to perform very broadband mass measurements, i.e. covering a very large mass-to-charge range and allowing the simultaneous measurement of hundreds of nuclides [Litvinov et al., 2005]. Additionally, due to the non-destructive nature of the Schottky noise detection, a single ion is sufficient for a mass measurement [Chen et al., 2009]. Notably, the SMS technique has also been successfully used to search for long-lived isomeric states with half-lives of several seconds or longer [Reed et al., 2010, Franzke et al., 2008]. On the other hand, when the SMS technique is used, a few seconds are required for the cooling process, therefore the half-lives of the nuclei that can be measured with this method are limited.

For species with half-lives less than seconds, the IMS technique is used, where a mass measurement can be performed within 10-100 μs. However, in conventional IMS techniques, a good isochronicity is realized only for a narrow mass-to-charge range, significantly limiting the achievable mass resolving power and accuracy for the ion species outside of this small range. In Refs. [Geissel et al., 2006, Zhang et al., 2023] possible developments to the IMS technique are reported and tested experimentally, which can relax this limitation. The latter technique of $B\rho$-defined IMS [Zhang et al., 2023] is routinely used at the CSRe storage ring nowadays, where the velocity of the ions is determined without efficiency losses by two TOF detectors installed at the storage ring. This enables to reach mass accuracies of $\delta m/m \sim 10^{-7}$ on a wider mass-to-charge

range at CSRe using the IMS technique (see Fig. 1.3 and the corresponding discussions). Notably, the IMS technique can also be applied for the mass measurements of close-lying isomeric states (with excitation energies of 200-300 keV), however, it may require advanced data analysis methods due to its limited mass resolving power and revolution-time-dependent peak shapes, see e.g. [Xing et al., 2023].

Direct mass measurements with MR-TOF-MSs

In the last two decades, as an alternative method for high precision direct mass measurements of short-lived exotic nuclei, the technique of the multiple reflection time-of-flight mass spectrometry (MR-TOF-MS) has been extensively developed in multiple accelerator facilities worldwide [Yamaguchi et al., 2021].

In MR-TOF-MS devices, firstly, the ions are bunched and cooled in a buffer gas-filled radio-frequency (RF) trap and, then, they are extracted from the trap with a homogeneous extraction field strength. Then, the measurement of the ions' mass-to-charge ratio is performed though measuring their time-of-flight (TOF) in a field-free drift tube with a given path length. The ions' flight path length is extended by reflecting them between two symmetric electrostatic mirrors, thus allowing to achieve high mass resolving powers on the order of a few times 100,000 [Wollnik & Przewloka, 1990]. These reflections are done in an isochronous manner, i.e. minimizing the TOF differences due to the variation of the initial energies, positions and angles of the ions injected to the TOF analyzer, such that the ions' TOF primarily only depends on the ions' mass-to-charge ratio.

Among its advantages, the MR-TOF-MS is a sensitive and non-scanning technique (less than 10 ions per nuclide are sufficient for an accurate mass measurement), therefore small production yields are in reach of this technique. Furthermore, an accurate mass measurement with $\delta m/m \sim 10^{-7}$ can be performed within a measurement time on the order of 10 ms, thus allowing access to short-lived nuclei with half-lives of a few milliseconds without significantly deteriorating the achievable mass accuracy (see Fig. 1.3 and the corresponding discussions). Notably, as opposed to storage-ring mass spectrometry, both Penning traps and MR-TOF-MSs are compatible with all methods for the production and separation of exotic nuclei, each of which can produce different spin states with different yields. For example, the (21^+) isomer of ^{94}Ag have only been observed, so far, in low-energy fusion evaporation reactions [Plettner et al., 2004, Cerny et al., 2009] and could not yet be sufficiently produced by in-flight separation techniques [Park, 2017]. Overall, these above features ensure that this technique is well suited for the studies of isomeric states [Dickel & Mollaebrahimi, 2024]. Furthermore, this technique allows to cover a medium-to-broad mass-to-charge window, therefore it is well suited to a larger-scale mapping of the nuclear mass surface of short-lived exotic nuclei.

Notably, the applications of MR-TOF-MSs are not restricted to high-precision mass measurements, but these measurement setups can also be used for, e.g., verification and calibration of the particle identification at in-flight facilities [Hornung et al., 2023], beam diagnostics, optimization and yield measurements guiding the development of rare isotope beams (RIB) at accelerator facilities [Reiter et al., 2020, Wolf et al., 2013] and nuclear reaction studies including, e.g., studies of multi-nucleon transfer reactions [Mollaebrahimi et al., 2025], studies of spontaneous fission [Mardor et al., 2020] and decay half-life and branching-ratio measurements [Miskun et al., 2019, Mukul et al., 2020, Ayet San Andrés et al., 2020]. Additionally, MR-TOF-MSs can also be used for beam purification, isobar or isomer separation, which can significantly suppress the isobaric contaminants from the radioactive beams or even provide isomerically clean ion samples [Wolf et al., 2013, Dickel et al., 2015a, Hirsh et al., 2016, Dickel et al., 2017a]. With these purified beams further experiments or investigations can be perform using measurement setups located downsteam after the MR-TOF-MS, such as for laser and/or decay spectroscopy studies, or for further mass measurements with ultimate mass accuracy using Penning traps. To

a large extent, many of these applications listed above can benefit from the broadband measurement capabilities of MR-TOF-MS devices. For example, the measurement of independent isotopic fission yields performed at FRS-IC using a ^{252}Cf spontaneous fission source mounted inside the cryogenic stopping cell would not have been possible without covering a larger region of the nuclear chart within a single measurement settings [Waschitz et al., 2023].

FRS-IC's MR-TOF-MS at GSI and TITAN's MR-TOF-MS at TRIUMF

In this work, two instances of MR-TOF-MS setups were used to study different ground and isomeric states in medium-heavy exotic nuclei, one of them belonging to the TRIUMF's Ion Trap for Atomic and Nuclear Science (TITAN) experiment [Dilling et al., 2006] at TRIUMF and another one belonging to the FRS Ion Catcher (FRS-IC) experiment [Plaß et al., 2013a] at GSI. This subchapter briefly introduces and compares these two MR-TOF-MS setups.

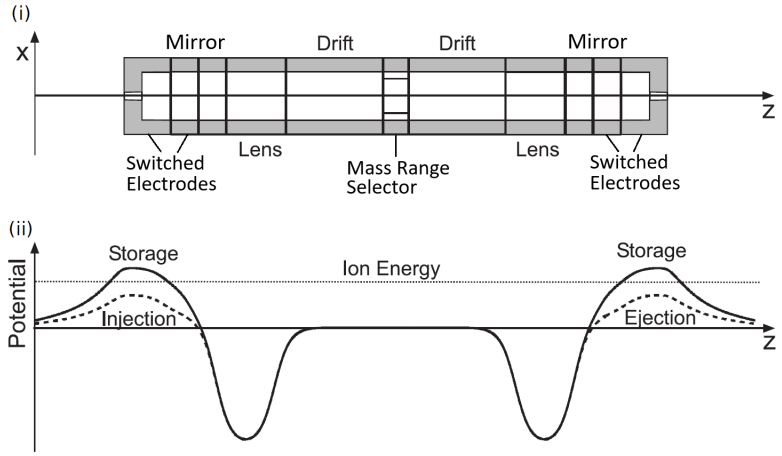

Figure 1.2: Schematic drawings of (i) the TOF analyzer of the MR-TOF-MS setups used in this work and (ii) electrostatic potentials along the optical axis that the ions experience during their injection into, storage inside, and ejection from the TOF analyzer. Adopted and modified from [Dickel et al., 2015b].

Both the MR-TOF-MS setups of TITAN and FRS-IC were designed and built at JLU Gießen in Gießen, Germany, and they are both based on the same ion-optical design of their TOF analyzer, only differently scaled in size [Dickel, 2010, Yavor et al., 2015, Jesch, 2016]. Other differences of the two setups include, e.g., the usage of a different RFQ beam line and trap system for the bunching and cooling of the ions and for injecting them into the TOF analyzer. Concerning the similarities of their design, firstly, in addition to the switchable mirror electrodes in their TOF analyzer, both MR-TOF-MSs use electrostatic lenses to achieve a higher order energy focusing of the ions and, thus, a better isochronicity and resolving power [Yavor et al., 2015]. Secondly, in both MR-TOF-MS setups, the injection of the ions into and their ejection from the TOF analyzer is performed by switching the voltages of the electrostatic mirror electrodes as illustrated in Fig. 1.2, thus allowing to achieve a larger unambiguous mass-to-charge window as opposed to, e.g., using a switchable drift tube [Plaß et al., 2013b]. Thirdly, a switchable electrostatic deflector, the so-called mass range selector (MRS), is located in the center of the TOF analyzer of both setups and helps with the peak identification in a folded TOF spectrum [Plaß et al., 2013b, Dickel et al., 2015b]. Finally, for both MR-TOF-MSs, an isochronous motion of the ions can be achieved on a broad mass-to-charge range, independently from the ions' number of reflections and, thus, path length inside the TOF analyzer. In case of the MR-TOF-MS of FRS-IC, this is facilitated by a so-called time-focus-shift reflector, which is located downstream after the TOF analyzer and allows to shift the time focus of the ions from their focus inside

the analyzer to the detector. In comparison, to achieve the same task, TITAN's MR-TOF-MS uses the concept of the dynamical time-focus shift with performing one time-focus shift turn first before letting the ions to undergo a given number of isochronous turns as described in Ref. [Dickel et al., 2017b]. Note, however, that the application of this latter concept slightly increases the systematic uncertainties of the mass values obtained using TITAN's MR-TOF-MS as compared to FRS-IC's MR-TOF-MS, because, in this latter case, all voltages of the TOF analyzer are switched during the time the ions are inside the TOF analyzer performing their first reflections.

While the measurement setup of TITAN employs the ISOL technique for the production and separation of exotic nuclei, the measurement setup of FRS-IC uses in-flight separation techniques (see Section 1.2 for more details). The goal of treating the typical challenges of these two production and separation techniques guided the development of the two MR-TOF-MS setups. Concerning TITAN's MR-TOF-MS, it enables superior background handling capabilities employing the technique of mass-selective re-tapping [Dickel et al., 2017a, Beck, 2023], which makes it well suited to handle the large isobaric contamination typical for ISOL techniques. Concerning the MR-TOF-MS of FRS-IC, to cope with the small production yields, it can be often advantageous to simultaneously measure multiple ions of interest on a broad mass-to-charge range. As discussed above, this is facilitated by the design features of both MR-TOF-MSs used in this work. With the developments of the data acquisition and analysis techniques presented in this work, these broadband capabilities can be fully exploited for the MR-TOF-MS of FRS-IC (see Section 2.1 and Chapter 3).

Concerning their additional performance characteristics, nowadays, TITAN's MR-TOF-MS allows to reach high mass resolving powers of $R_m > 600,000$, routinely, see e.g. [Porter et al., 2022], and small relative mass uncertainties of $\delta m/m \sim 1 \times 10^{-7}$, see e.g. [Lykiardopoulou et al., 2025]. In comparison, with the MR-TOF-MS of FRS-IC even higher mass resolving powers of 1,000,000 and beyond [Beck, 2023] and smaller relative mass uncertainties of a few times 10^{-8} [Mardor et al., 2021] are in reach.

Comparison of mass measurement methods: mass accuracy wrt. half-life

Performing high-precision direct mass measurements using very short-lived ions is considered as one of the biggest experimental challenges among the nuclear physics community of present days. In the past decade, steady progress in the mass measurement and production techniques of exotic nuclei has been made; direct mass measurements of nuclides with short half-lives of a few milliseconds and with corresponding mass accuracies of $\delta m/m \sim 10^{-7} - 10^{-6}$ have been achieved using the present techniques (see Fig. 1.3). Plots of the relative mass uncertainty achieved using different direct mass measurement techniques as a function of the half-life of the measured isotopes can be found in Refs. [Lunney, 2008, Lunney, 2015, Lunney, 2019], which were compiled out of the mass measurements carried out until the date of the given plot. In comparison, Fig. 1.3 shows an updated version of those plots, containing data points corresponding to direct mass measurements that were included in the most recent atomic mass evaluation (AME2020) [Huang et al., 2021, Wang et al., 2021]. Looking at the figures one after the other in the order of their appearance, the steady progress throughout the past years becomes apparent, which is mainly due to a combination of the usage of Penning traps, MR-TOF-MSs and storage rings offering exquisite mass accuracies and sensitivities.

The achievable mass accuracy is mostly determined by the available statistics for the isotopes of interest, therefore the most exotic species with small production yields are typically measured with limited mass accuracies [Lunney, 2019]. As a secondary effect, the shorter half-lives can also result in limiting the achievable mass accuracy, e.g., in case of mass measurements performed using Penning traps, the shorter storage times result in larger mass uncertainties. Notably, comparing the red data points corresponding to the mass measurement technique of IMS using storage rings in Fig. 1.3 to the data points of the same kind shown in the earlier plots reported

in Refs. [Lunney, 2008, Lunney, 2015, Lunney, 2019], a significant improvement of the mass accuracy typically achieved in measurements performed nowadays using the CSRe storage ring [Xia et al., 2002] becomes apparent. This is, to a large extent, due to recent developments of the isochronous mass spectrometry technique at CSRe reported in Ref. [Zhang et al., 2023].

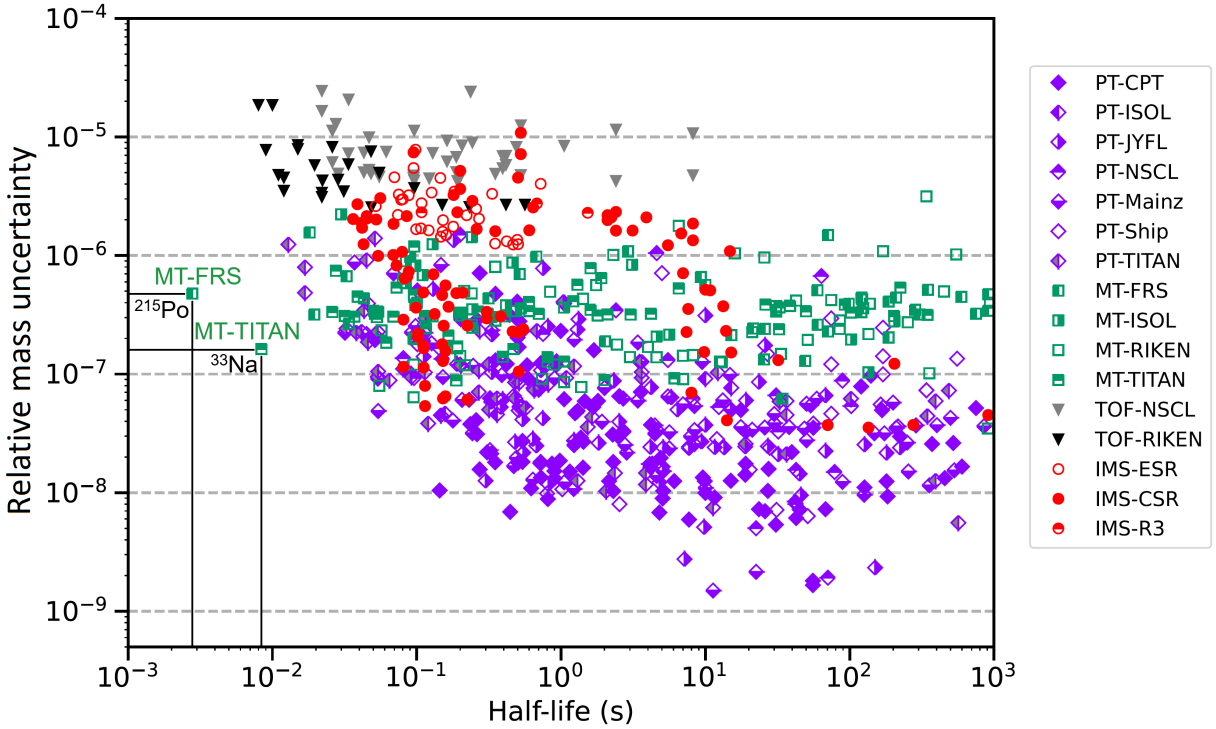

Figure 1.3: Plot of relative mass uncertainty using different direct mass measurement techniques with respect to the half-life of the measured isotopes. PT-xxxxx, MT-xxxxx, TOF-xxxxx and IMS-xxxxx refer to Penning trap, MR-TOF-MS, TOF-$B\rho$-MS and IMS mass measurement techniques at the RIB facility or experiment xxxxx, respectively, recent reviews of which can be found in [Lunney, 2019, Yamaguchi et al., 2021]. The plot mostly contains data points corresponding to direct mass measurements that were included in the AME2020 [Huang et al., 2021, Wang et al., 2021]. The original plot was prepared by X. Xing from the Institute of Modern Physics, Lanzhou, China [Xing & Wang, 2023] (priv. comm.). It was then modified to include (i) the first direct mass measurement of the nuclide ^{215}Po with half-life of 1.781(3) ms performed at FRS-IC, GSI [Rink, 2017] and (ii) the high-precision, direct mass measurement of the nuclide ^{33}Na with half-life of 8.2(2) ms performed at TITAN, TRIUMF [Lykiardopoulou et al., 2025].
Courtesy Xu Xing and Meng Wang.

Although the shortest half-lives tend to be reached employing projectile fragmentation reactions for the production of exotic nuclei and the TOF-$B\rho$-MS techniques for their mass measurement, which is at the expense of the achievable mass accuracy [Lunney, 2019], some of the nuclides measured using TITAN's Penning trap and TITAN's, FRS-IC's and ISOLTRAP's MR-TOF-MSs are also of quite short half-lives. To further demonstrate this, two particularly striking examples are shown in Fig. 1.3: (i) the first one corresponds to the shortest-lived nuclide, ^{215}Po with $T_{1/2}$ = 1.781(3) ms, the mass of which could be measured so far at FRS-IC[1] with an

[1]Note that the first direct mass measurement of ^{215}Po has been performed offline, using a ^{223}Ra source mounted inside the cryogenic stopping cell of the FRS-IC [Rink, 2017]. Nevertheless, this measurement demonstrates the potential of the FRS-IC measurement setup to enable mass measurements of short-lived nuclides with half-lives of a few milliseconds, which has been already utilized in online experiments performed with the setup, see e.g. [Ayet San Andrés et al., 2019, Tortorelli, 2024].

achieved mass accuracy of $\delta m/m = 3.8 \times 10^{-7}$ [Rink, 2017] and (ii) the second one corresponds to the shortest-lived nuclide, ^{33}Na with $T_{1/2} = 8.2(2)$ ms, the mass of which could be measured so far using TITAN's MR-TOF-MS with an achieved mass accuracy of $\delta m/m = 1.4 \times 10^{-7}$ [Lykiardopoulou et al., 2025][2]. These two striking examples further confirm an essentially constant pattern of the dark green data points shown in Fig. 1.3, which highlights the strength of MR-TOF-MS setups to perform mass measurements, where the order of magnitude of the achieved mass accuracies is primarily independent from the half-lives of the measured nuclides.

Overall, multiple-reflection time-of-flight mass spectrometry is a powerful technique both for the high-precision mass measurement of very short-lived nuclides and for the studies of close- and high-lying isomeric states, therefore this method was selected for the mass measurements of ground and isomeric states of exotic nuclei reported in this work (see Chapters 4 and 5).

[2]Notably, in the same reference of [Lykiardopoulou et al., 2025], the mass of two other short-lived isotopes were also measured using TITAN's MR-TOF-MS (these were omitted from Fig. 1.3 in order to preserve its readability): the mass of ^{32}Na with $T_{1/2} = 13.2(3)$ ms was measured with a mass accuracy of $\delta m/m = 1.8 \times 10^{-7}$ and the mass of ^{35}Mg with $T_{1/2} = 11.3(6)$ ms was measured with a mass accuracy of $\delta m/m = 2.2 \times 10^{-7}$. In comparison, the previous mass measurement of the nuclide ^{32}Na performed using TITAN's Penning trap achieved a mass accuracy of $\delta m/m = 1.2 \times 10^{-6}$ [Gallant et al., 2017], which is about an order of magnitude lower compared to the accuracy of the measurement performed with the MR-TOF-MS.

Chapter 2

Improvements of the FRS Ion Catcher experiment

With recent developments of the FRS Ion Catcher measurement setup described in Section 1.2.3, it enables very good performance characteristics, see e.g. [Beck, 2023, Amanbayev, 2023, Ayet San Andrés, 2018, Miskun, 2019]. In connection with the MR-TOF-MS of the FRS-IC, these good performance characteristics include, but are not limited to the following features; high mass resolving powers of 1,000,000 and beyond [Beck, 2023], high mass accuracies of $\delta m/m \sim 10^{-8}$ [Mardor et al., 2021], access to short-lived nuclides with half-lives of a few milliseconds [Rink, 2017, Tortorelli, 2024] and the ability to perform mass measurements covering a broad relative mass-to-charge range of more than 10%, thus enabling the simultaneous measurement of several nuclides within a single settings of the MR-TOF-MS, see e.g. [Amanbayev, 2023, Spătaru et al., 2025, Fowler-Davis, 2025].

This chapter presents technical developments to the MR-TOF-MS, which enable to maintain these above-listed performance characteristics long term and, in addition, they ensure a flexible, user-friendly and reproducible operation of the measurement setup.

2.1 Flexible and reliable preparation of the measurement settings

With the development of the mean range bunching mode of the FRS [Dickel et al., 2023] and the mounting of a ^{252}Cf spontaneous fission source inside the CSC of the FRS-IC, broadband mass measurements covering a complete part of the nuclear chart are done more and more frequently, see e.g. [Amanbayev, 2023, Spătaru et al., 2025, Fowler-Davis, 2025]. The measurement-settings preparation and data analysis of such broadband measurements, however, require a special care. In this subchapter, the emphasis is given to the dedicated measurement-preparation and data-recording methods developed in a collaborative effort [Bergmann et al., 2020] (priv. comm.) and commissioned at the FRS Ion Catcher as part of this work, which enable to prepare, optimize and perform mass measurements with the MR-TOF-MS of the FRS-IC.

The TTL signals used to control the timings of the measurement setup are generated by an FPGA-based device called "trigger system" [Jesch, 2016]. These TTL signals are used to define, e.g., the timings of switching the voltages of the analyzer mirror electrodes for the injection and extraction of the ions from the analyzer or the timings of switching the voltages of the mass-range selector (MRS) [Dickel et al., 2015b] in the center of the TOF analyzer. The in-house-developed and custom-tailored TOFControl software [Bergmann, 2024], which is responsible for the communication with the trigger system, enables a low-level-expertise operation of the system by only modifying a few parameters, such as the mass-to-charge ratio used for defining the timings of switching the analyzer electrodes and its corresponding number of isochronous turns, the goal mass-to-charge range transmitted by the MRS or the mass-to-charge ratio used for defining the

timings of the mass-selective transport through the trap system. Once these parameters are defined by the user, the software can automatically calculate the necessary timings. For this, these timings are first determined from offline, preparatory measurements with reference ions (typically with ^{133}Cs ions produced by the thermal ion source of the MR-TOF-MS), which are performed prior to the experiment itself. The measured timings corresponding to the reference ions are then scaled to the goal mass-to-charge ratios of the given measurements as defined by the user. This new operation mode of the trigger system was commissioned at the FRS Ion Catcher in 2018-2020 and, afterwards, in 2021, it was further extended by implementing the possibility to select two separate mass-to-charge windows in the analyzer using the mass-range selector and transmit both of them to the TOF detector. This operation mode can be used to, e.g., include calibrant ions in the TOF spectrum, which have slightly different mass-to-charge ratios as compared to the ions of interest, or to measure the mass of the ions of interest, which may pick up adducts in the CSC or in the RFQ beam line and therefore they may arrive in at least two different molecular forms at the TOF detector.

Besides enabling a user-friendly operation of the measurement setup, including a flexible selection of the desired mass-to-charge range, the newly-commissioned operation modes of the trigger system also ensure that a given settings used to measure a given TOF spectrum can be easily reproduced even years after performing the original measurement. This is true, independently from the nature the originally performed measurement, which can be also broadband, i.e., covering a larger mass-to-charge window. This is illustrated in Fig. 2.1, where two TOF spectra of ^{252}Cf fission products are compared; the bottom spectrum was measured 3 years after the measurement of the top spectrum, both spectra were acquired for the same time ($\sim$14 hours) and the same parameters were used to define the relevant timings for controlling the measurement setup, when obtaining both spectra (more details about the measurement conditions are given in footnote[1]). Although the voltages of the analyzer electrodes and, thus, the time it takes for the ions to perform an isochronous turn (IT) inside the analyzer were different for the two measurements, the newly-commissioned operation mode of the trigger system allowed to set up both measurements such that they cover the same mass-to-charge range of $m/q \sim (71-84)$ u/e and the number of ITs performed by the different ion species are also the same, ranging from 323 to 350 IT. This allows a direct comparison between the layout and dominating peaks inside the TOF spectra and, ultimately, it allows to directly compare various properties of the measurement setup between the measurements performed in the past and in the present including, e.g., a direct comparison between the magnitude of the chemical and charge-exchange reactions that the ions undergo in the FRS-IC, which is primarily defined by the cleanliness of the buffer gas used for stopping and cooling the ions inside the measurement setup.

To perform mass measurements with high mass accuracy, the above-described parameters used to define the relevant timings for controlling the measurement setup need to be selected carefully, taking into account multiple different considerations, the most important ones being the following: (i) A TOF spectrum measured with the MR-TOF-MS has two degrees of freedom, namely, the mass of an ion flying inside the analyzer and its number of isochronous turns. When selecting the goal mass-to-charge range transmitted by the MRS and the number of isochronous turns performed by the different ion species within the full mass range, the probability that the

[1]Both TOF spectra shown in Fig. 2.1 were measured offline, using a ^{252}Cf source mounted inside the CSC. The top spectrum was measured in 2020 using the long DC Cage [Miskun, 2019] of the CSC, which was filled with He buffer gas with an areal density of 3.6 mg/cm^2 (see more details about experiment conditions in Refs. [Spătaru et al., 2025, Waschitz et al., 2023]). The bottom spectrum was measured in 2023 using the short DC Cage [Amanbayev, 2023] of the CSC with an areal density of 2.1 mg/cm^2, the data analysis of which is ongoing [Narang, 2024] (priv. comm.). The efficiency factors throughout the FRS-IC setup (see e.g. Ref. [Waschitz et al., 2023]) were different for obtaining both TOF spectra, which resulted that the detected count rates of the observed fission products were reduced by 1-to-2 orders of magnitude for the measurements performed in 2023 (bottom spectrum) as compared to 2020 (top spectrum).

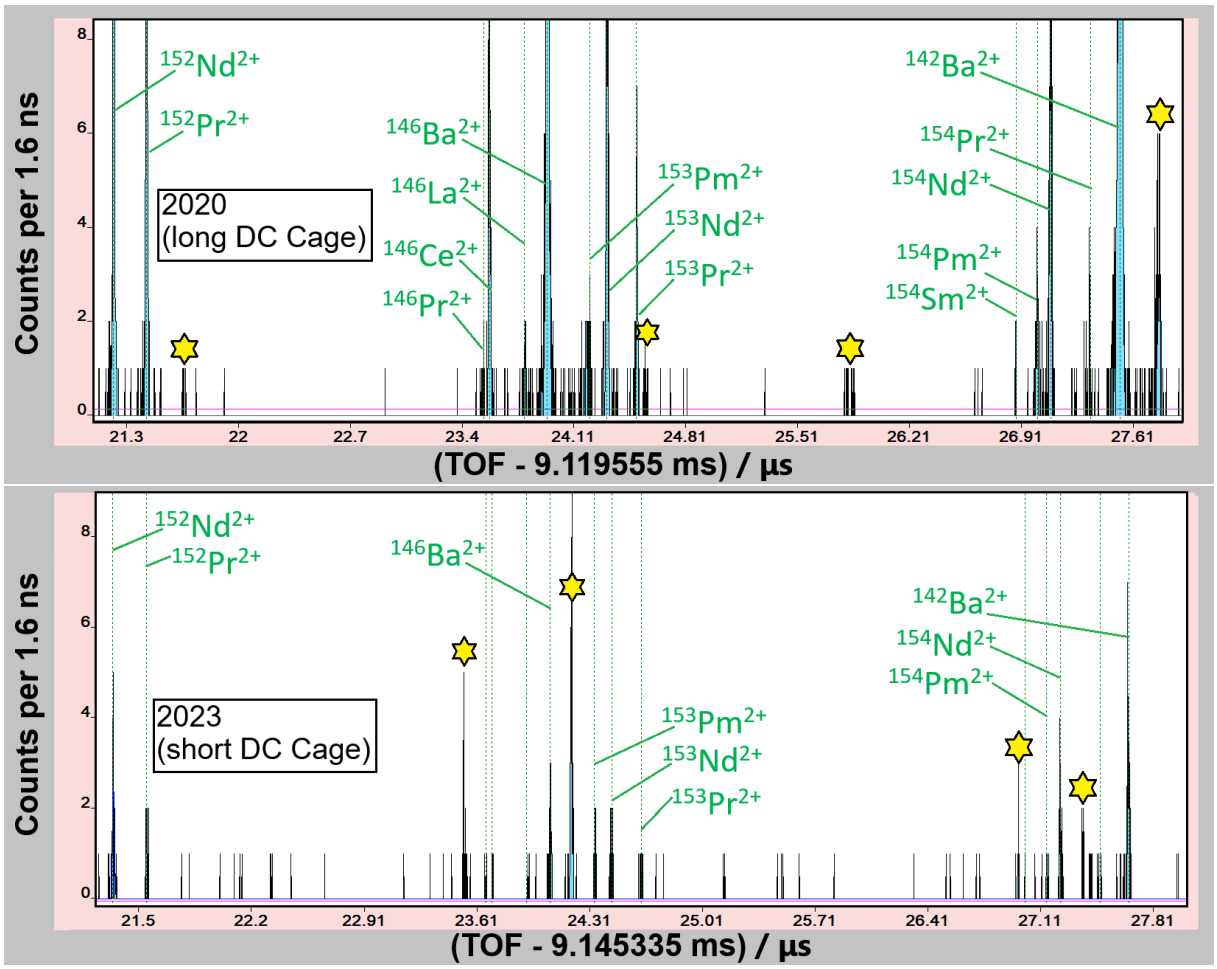

Figure 2.1: Comparison between two TOF spectra of neutron-rich nuclei produced in spontaneous fission of ^{252}Cf measured at the FRS-IC in 2020 using the long DC Cage of the CSC (top) and in 2023 using the short DC Cage of the CSC (bottom). The ordinate and the abscissa of both TOF spectra are zoomed to show a similar range for an easier comparison between the two spectra and for a better display of low-intensity peaks. The green labels at the individual peaks indicate the identified peaks of ^{252}Cf fission products (the data analysis of the bottom spectrum is still ongoing and, in that case, the labels indicate a preliminary identification [Narang, 2024] (priv. comm.)). All identified ions in this region of the TOF spectra are doubly charged. The yellow stars mark the peaks that has not yet been identified. The dashed green lines are to guide the eye.

resulting TOF peaks of the different ion species overlap or coincide with each other in the TOF spectrum needs to be minimized. (ii) In addition to this, the timings related to opening or closing the analyzer mirror electrodes also define whether certain ion species feel switched electrical fields or experience an electrical ringing from the mirror electrodes during their injection to or extraction from the analyzer. Since this would cause that the kinetic energy and hence the flight time of these ions are slightly shifted, this results in a decreased mass accuracy (see more details in Section 3.3). Furthermore, the trajectory of the ion species, which experience the switched fields directly, changes significantly and these species can not be transmitted to the TOF detector. Therefore, when preparing the measurement settings, it needs to be ensured that the ions of interest and calibrant ions don't feel these switched electrical fields or electrical ringing. For the task of the optimization of the parameters that define the relevant timings for controlling the measurement setup, a software package has been developed [Bergmann, 2024], which allows for

the simulation of the expected TOF spectra. The results of these simulations have been validated by performing systematic preparatory measurements at the FRS Ion Catcher, and this software package has been used to prepare and optimize the settings of the trigger system in multiple offline and online experiments including, e.g., the mass measurements of neutron-deficient nuclides in the vicinity of ^{100}Sn reported here (see Chapter 5).

2.2 Fast and reproducible experimental tuning of the MR-TOF-MS

The repetition frequency of the MR-TOF-MS, which defines the maximum cooling times of the ions in the trap system of the MR-TOF-MS and the maximum flight times of the ions inside the TOF analyzer, can be adjusted to fit the goals of the given experiment and its corresponding experimental conditions and challenges. Operating the MR-TOF-MS at small repetition frequencies of <50 Hz corresponding to cycle lengths of >20 ms allows longer flight times and flight paths in the TOF analyzer and, therefore, it allows to achieve higher mass resolving powers providing a better separation of close-lying TOF peaks and it also allows to achieve a higher mass accuracy in measurements, where the statistics of the ions of interest is limited, e.g. due to low production cross-sections. For example, the results of Refs. [Beck, 2023, Mardor et al., 2021] demonstrating mass resolving powers of 1,000,000 and beyond were achieved with operating the MR-TOF-MS at repetition rates of 25 Hz. On the other hand, operating the MR-TOF-MS at higher repetition frequencies and, thus, shorter cycle lengths allows to measure the mass of very short-lived nuclides with half-lives of a few milliseconds. This has been demonstrated in offline measurements operating the MR-TOF-MS at a repetition rate of 400 Hz corresponding to a cycle length of 2.5 ms, which enabled the first direct mass measurement of the nuclide ^{215}Po, which has a half-life of only 1.781(3) ms [Rink, 2017]. Furthermore, the higher repetition frequency allows measurements with higher incoming rates, while reducing effects due to ion-ion interactions in the traps and inside the analyzer, which have an influence on the mass resolving power of the measurement setup and on the mass accuracy of the measurements. This concept was also used in online measurements, where the MR-TOF-MS was operated using a repetition frequency of 200 Hz to enable a measurement of short-lived nuclides and, in addition, to enable higher incoming rates without the emergence of space charge effects [Tortorelli, 2024]. Finally, the usage of higher repetition rates also has a technical advantage, namely, it decreases the dead time of the time-to-digital converter used for the data taking. In this subchapter, a new addition to the electronics devices at the FRS-IC is presented, which helps in the long-term maintenance of the high mass resolving power and, when required, it eases up the change of the MR-TOF-MS repetition frequency.

In order to ensure that drifts of the ions' time-of-flight are minimized due to voltage and thermal drifts, the voltages of the electrodes of the TOF analyzer are supplied by highly stable analog low-noise power supplies mounted in a temperature stabilized cabinet and, additionally, stabilized with 4th order low-pass filters [Ayet San Andrés, 2018, Beck, 2023]. When tuning the MR-TOF-MS for high mass resolving power, the voltages of the electrodes of the TOF analyzer need to be measured very precisely, because a small deviation of $\mathcal{O}(\pm 0.1\ \mathrm{V})$ from the fully isochronous set of voltages results in small shifts of the time focus in each individual isochronous turn, which effect is magnified, when the ions undergo multiple isochronous turns in the TOF analyzer. Since the electrodes of the TOF analyzer are supplied with high voltages above 1000 V, their accurate measurement is challenging and can be achieved, e.g., using high-precision 1:1000 voltage divider devices. For the task, a temperature-stabilized, 8-fold resistive divider has been developed in collaboration with M. Vencelj [Vencelj et al., 2020] (priv. comm.) and commissioned at the FRS-IC in 2020 as part of this work. The device allows a continuous, temperature-independent and accurate readout of the voltages of the electrodes of the TOF analyzer. The

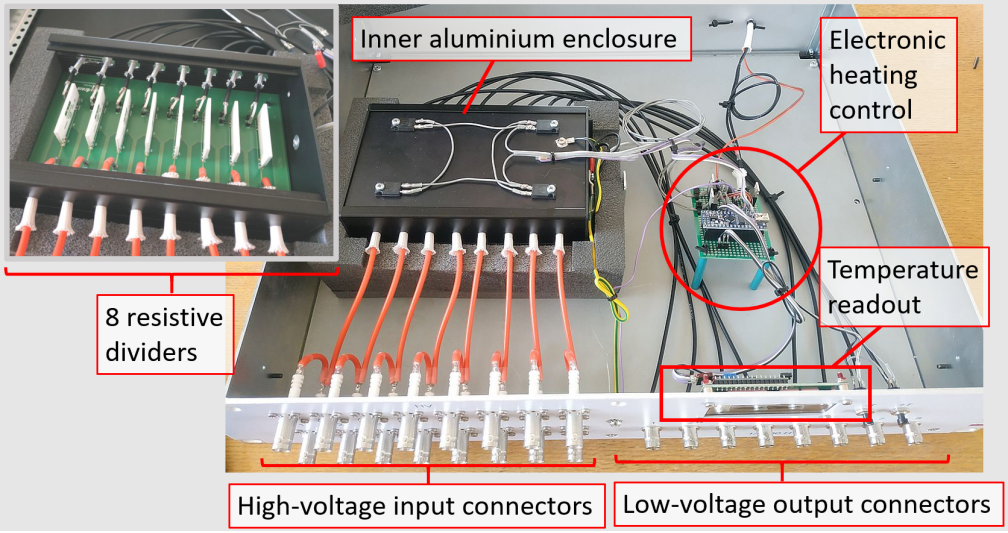

(a)

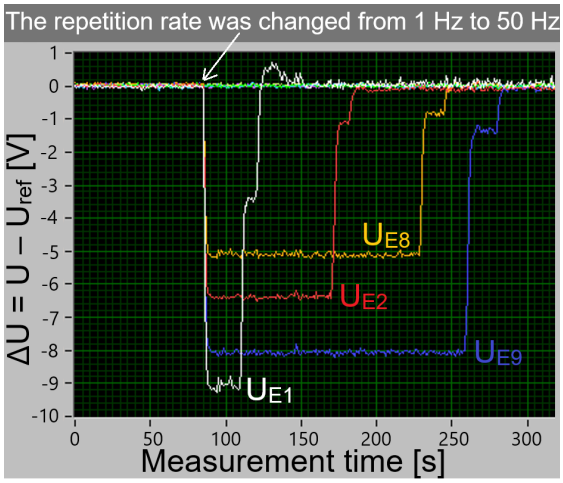

(b)

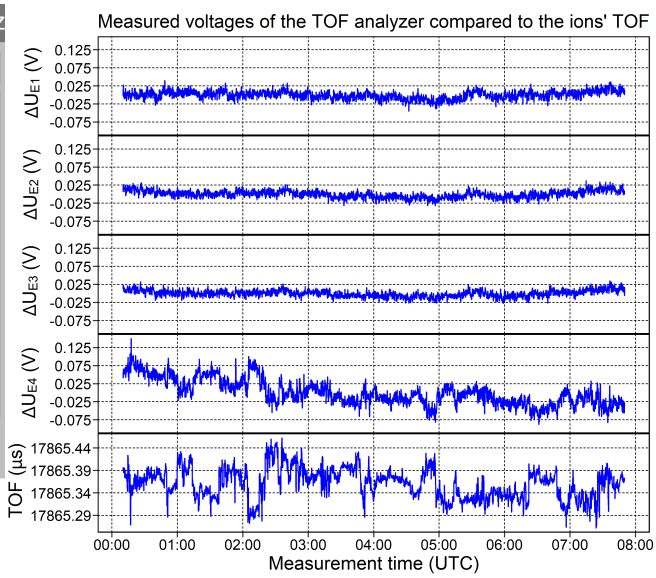

(c)

Figure 2.2: Photograph of the newly-commissioned 8-fold resistive divider device (a) and two examples of its most frequent applications at the FRS Ion Catcher (b and c). The inset of the figure (a) on the left side shows the printed circuit board with 8 resistive dividers, which is mounted in a thermally insulated heated inner aluminum enclosure held at a constant temperature by electronic control as shown by the photograph on the right side of the figure. On the plot (b), the procedure to change of the MR-TOF-MS repetition frequency is illustrated, which allows to maintain the same asymptotic mass resolving power. On the plot (c), the influence of voltage fluctuations of $\mathcal{O}(0.1\ \mathrm{V})$ on the output mirror electrode of the analyzer (E9) on the ions' TOF is depicted. These latter two plots (b and c) show the deviations between the voltages of the analyzer electrodes from a set of reference voltages ($\Delta U = U - U_{\mathrm{ref}}$) as a function of the measurement time. In case of the plot (c), the evolution of the measured TOF of the ^{133}Cs ions after undergoing 500 isochronous turns inside the TOF analyzer is also shown, in comparison, as a function of the measurement time.

device includes a printed circuit board with 8 resistive dividers, each of which is a CADDOCK HVD5-A50M-050-05 Ultra-Precision Voltage Divider [Manufacturers & Products, 2025]. This

PCB is mounted in a thermally insulated heated inner aluminum enclosure, which is held at a constant temperature (within a ±0.5 °C interval) by electronic control. A photograph of the device is shown on Fig. 2.2a. For the example presented here, the continuous readout of the resulting voltages on the low-voltage output connectors has been achieved using a LabJack T7-Pro analog-to-digital converter [Manufacturers & Products, 2025].

During its commissioning at the FRS Ion Catcher, the individual channels of the 8-fold resistive divider device were calibrated and the device was connected to the measurement setup. Since then, the device has been used for various purposes, out of which its two most frequent applications are highlighted below.

Firstly, when changing the repetition rate of the MR-TOF-MS, the voltage drop over the electronics changes in case of the four outermost electrodes, i.e. the electrostatic mirror electrodes of the TOF analyzer (called as E1, E2, E8 and E9 in Fig. 2.2), because these electrodes are switched with the same frequency as the repetition frequency of the MR-TOF-MS allowing to inject or eject the ions from the TOF analyzer. With the 8-fold resistive divider connected to the measurement setup, the change of the voltages of all analyzer electrodes can be now monitored real time and these voltages can be adjusted such that they are identical to values used prior to the change of the repetition frequency. As illustrated in Fig. 2.2b, this procedure allows to change the repetition rate of the MR-TOF-MS within a few minutes, while maintaining the same ion optical tuning of the measurement setup and, thus, the same asymptotic mass resolving power. Therefore, this procedure is well suited to experiments with varying goals and challenges, which may require a quick change of the repetition frequency of the MR-TOF-MS.

Secondly, when one of the electronics components, such as the low-noise power supplies or the 4th order low-pass filters, connected to a given electrode of the TOF analyzer, has a malfunction, this may result in an increased fluctuation of the voltage of the given electrode. As a result, the measured time-of-flight of the ions may fluctuate, thus limiting the mass resolving power of the MR-TOF-MS and the accuracy of the mass measurements performed with it. The newly-commissioned 8-fold resistive divider allows an easier diagnostics of potential issues connected to the voltages applied to the electrodes of the TOF analyzer and, thus, it helps in the long-term maintenance of the high mass resolving power of the MR-TOF-MS. In case of the example shown in Fig. 2.2c, voltage fluctuations of $\mathcal{O}(0.1\ \mathrm{V})$ were observed on the output mirror electrode of the analyzer (E9), which resulted in correlated TOF fluctuations of $\mathcal{O}(100\ \mathrm{ns})$ after undergoing 500 isochronous turns inside the TOF analyzer corresponding to a flight time of 17.9 ms. These fluctuations were caused by a damaged electronics component in the 4th order low-pass filter of the output mirror electrode of the analyzer (E9). The damaged component could be found within a few days with the help of the newly commissioned 8-fold divider and the issue could be resolved prior to the experiments performed in 2020 aiming at mass measurements of proton-rich nuclides in the vicinity of ^{100}Sn and ^{70}Br. This allowed to reach high mass resolving powers of about 700,000 and beyond both for (i) the results reported in this work (Chapter 5) and (ii) the results reported in Ref. [Mardor et al., 2021], where the 8-fold divider played a crucial role.

Finally, it is worth to mention that with the newly developed feedback control loop feature in the TOFControl software [Bergmann, 2024], the usage possibilities of the 8-fold resistive divider can be extended in the future to also allow a software-based stabilization of the voltages of the TOF analyzer electrodes directly based on the voltages measured using this device.

2.3 Removal of reference clock effects on the mass accuracy

With the achieved high mass resolving powers, see e.g. Ref. [Beck, 2023], small relative mass uncertainties of $\delta m/m \sim 10^{-8}$ are in reach for the mass measurements performed at the FRS Ion Catcher [Mardor et al., 2021]. Achieving this, however, requires an accurate quantification of all systematic uncertainty sources connected to the measurement setup (see more details in

Section 3.3). One of the systematic uncertainty sources has been found, quantified and its magnitude has been reduced significantly by upgrading the measurement setup in 2020-2021 in the context of [Ayet San Andres et al., 2021] (priv. comm.), as described below.

The timing delay between the ejection of the ions from the injection trap and the opening of the output mirror electrodes for the extraction of the ions from the TOF analyzer is defined by the trigger system [Jesch, 2016]. The measured time-of-flight of the ions is given by the sum of (i) this timing delay defined by the trigger system and (ii) the flight time of the ions starting from the opening of the output mirror electrodes until they reach the TOF detector, the signal of which is first amplified and then digitized by a time-to-digital converter (TDC), in the present work, the model of which was an MCS6A provided by the manufacturer FAST ComTec [Manufacturers & Products, 2025]. Therefore, an inaccuracy of any of these two devices, the trigger system and the TDC, can lead to a subsequent inaccuracy of the measured time-of-flight of the ions.

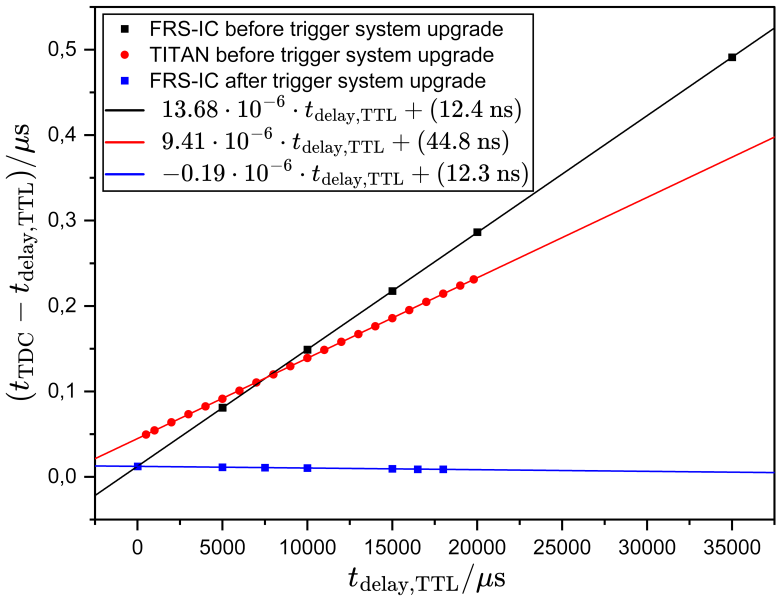

Figure 2.3: Measurement of the difference between timing delay set by the trigger system ($t_{\mathrm{delay,TTL}}$) and measured using the TDC (t_{TDC}) as a function of $t_{\mathrm{delay,TTL}}$ performed at FRS-IC before (black) and after (blue) upgrading the trigger system and at TITAN before upgrading the trigger system (red). Here, the timing delay represents the time between the ejection of the ions from the injection trap and the opening of the output mirror electrodes of the TOF analyzer. The curves represent linear fits to the data points, the corresponding equations of which are shown in the legend of the figure. After upgrading the trigger system at FRS-IC, the slope of the linear correlation decreased by almost two orders of magnitude.

In order to quantify the possible inaccuracies associated with the data acquisition setup, in the first step, the TDC was set up such that it receives its acquisition start signal from the timing signal corresponding to the ejection of the ions from the injection trap and it gets its stop signal from the timing signal corresponding to the opening of the output mirror electrodes of the TOF analyzer. Afterwards, the timing delay between the ejection of the ions from the injection trap and the opening of the output mirror electrodes set by the trigger system ($t_{\mathrm{delay,TTL}}$) was modified between 0 ms and 35 ms and its value was measured using the TDC (t_{TDC}). This investigation showed a linear correlation between the $t_{\mathrm{delay,TTL}}$ set by the trigger system and the deviation of the measured timing delay from its set value, which had a slope of 13.7×10^{-6}, in case of the FRS-IC setup (black data points in Fig. 2.3), and 9.4×10^{-6}, in case of the TITAN

setup (red data points in Fig. 2.3). Besides the observed slopes, the measurements also showed an offset of 12.4(1) ns at FRS-IC and 44.8(1) ns at TITAN. The reason for this constant offset could not yet be understood. On the other hand, it does not contribute to the systematic uncertainty sources of the measurement setup, since the offset is the same for all ion species inside the TOF spectrum, thus it is included inside the calibration parameters, when performing the calibration of the TOF spectrum (see more details in Chapter 3).

In the next step, the inaccuracy of the trigger system and the TDC were both measured, independently, in order to figure out which of these two devices' inaccuracies dominates:

(A) **Inaccuracy of the TDC:** The time-to-digital converter MCS6A has a 10 MHz reference clock. To quantify the inaccuracy of the TDC, a frequency counter TF930 [Manufacturers & Products, 2025] was used in this work to measure the frequency of this reference clock. This measurement yielded a frequency of 9.99999633 MHz, which corresponds to a relative difference between the measured and set frequency of the reference clock of the TDC of only $-0.37(20)$ ppm. This relative difference is comparable to the ± 0.2 ppm uncertainty of the frequency counter device used for the measurement suggesting that the inaccuracy of the TDC is negligible.

(B) **Inaccuracy of the trigger system:** To generate the timing signals of the measurement setup, the trigger system "counts" the amount of cycles of a 200 MHz clock corresponding to a period of 5 ns. As described in Ref. [Jesch, 2016], the 200 MHz clock is derived from a reference clock with nominal frequency of 10 MHz, which is an oven-controlled crystal oscillator (OCXO), the model of which used to be an AOCJY1A-10.000MHZ [Manufacturers & Products, 2025]. According to its specifications, this clock is stable against changes in time on the level of ± 50 ppb, but its frequency could be slightly inaccurate at production. To quantify the inaccuracy of the trigger system, the set frequency of one of the trigger system channels was modified between 1 MHz and 1 Hz and it was measured using a frequency counter TF930. The results of this measurement performed at FRS-IC showed a linear correlation with a slope of $14.2(2) \times 10^{-6}$ and an offset of 7.5(15) ns between the time period set by the trigger system and the deviation between the time period measured with the counter and set by the trigger system. The measured slope of this correlation is in good agreement with the slope of the linear correlation shown in Fig. 2.3, which was obtained earlier using the TDC as a measurement device.

Since it was found that the inaccuracy of the trigger system gives the dominating factor, in the final step, the 10 MHz OCXO clock installed in the trigger system has been exchanged to model AOC2012VAJC-10.0000C [Manufacturers & Products, 2025]. Besides providing stable frequencies on the level of ± 10 ppb, this latter clock also provides a frequency accuracy of ± 0.5 ppm at the time of its production according to its specifications. As a result of this upgrade of the trigger system at FRS-IC, the slope of the correlation between the set and measured timing delays has been decreased by almost two orders of magnitude (blue data points in Fig. 2.3), which ensures that any inaccuracy due to the data acquisition setup is well below other systematic uncertainty sources of FRS-IC's MR-TOF-MS (see more details in Section 3.3). In case of TITAN's MR-TOF-MS, this effect is negligible compared to the uncertainty contribution used to estimate an upper limit of the systematic uncertainties of the setup (see more details in Chapter 4). Nevertheless, the OCXO clock of the trigger system can be also exchanged at TITAN in the future, once an accurate quantification of all systematic uncertainty sources is achieved and the effect due to the inaccuracy of the trigger system becomes non-negligible.

Chapter 3

MR-TOF-MS data analysis procedure and its improvements

The analysis of the MR-TOF-MS data collected during the experiments presented in Chapters 4 and 5 is based on a procedure and a corresponding data analysis infrastructure developed and extensively described in multiple PhD theses and publications, see e.g. [Ebert, 2016, Ayet San Andrés, 2018, Hornung, 2018, Ayet San Andrés et al., 2019, Bergmann, 2024]. The procedure has been proven to yield accurate mass values even for very challenging conditions, such as for few events per ion species only [Mardor et al., 2021, Mollaebrahimi et al., 2023b] or for overlapping mass lines [Ayet San Andrés et al., 2019, Hornung et al., 2020]. This work presents further developments to the procedure and the corresponding data analysis framework.

At the FRS-IC setup, there are two typical challenges, which are frequently met and need to be correctly tackled when analyzing MR-TOF-MS data. Firstly, the most exotic ions of interest are often measured with very low statistics of only 3-10 detected events within a peak, see e.g. [Mardor et al., 2021, Mollaebrahimi et al., 2023b]. Secondly, with the recent development and application of the mean range bunching mode of the FRS [Dickel et al., 2023] and the mounting of a ^{252}Cf source inside the CSC, broadband mass measurements covering a larger part of the nuclear chart are done more and more frequently, see e.g. [Amanbayev, 2023, Spătaru et al., 2025, Fowler-Davis, 2025]. At the TITAN setup, a typical MR-TOF-MS spectrum contains multiple (more than two) overlapping TOF peaks due to the isobaric contamination typical for ISOL facilities and many ions of interest are often measured with relatively large statistics, see e.g. [Izzo et al., 2021, Beck, 2023].

For the analysis of low-statistics data a reliable quantification of the expected background level and contamination peak density are desired in order to achieve a realistic estimate of the experimental uncertainties (see Section 3.3). For the analysis of broadband mass measurements, increasing the flexibility of the data analysis framework (see Section 3.2) and developing standardized procedures to check the consistency of the deduced mass values (see Section 3.6) are needed. Overall, with the help of the broadband mass measurements systematic checks on the experimental mass uncertainty were done and the resulting modifications to the uncertainty determination are reported here (see Section 3.3). Moreover, for the analysis of high statistics data and/or for fitting many peaks in a broadband mass spectrum a speed enhancement of the data analysis framework is essential (see Section 3.2). For the analysis of multiple overlapping TOF peaks, several advances of the data analysis technique are needed. The first attempts to cope with this latter challenge are reported here (see Sections 3.3 and 3.5), although an ultimate solution is still a task for the future.

3.1 The data analysis procedure

The main steps of the data analysis procedure are illustrated by the block diagram shown in Fig. 3.1. The two main software used during the data analysis are the TOFControl software [Bergmann, 2024] and the MSmarple[1] data analysis framework [Ebert, 2016, Ayet San Andrés, 2018]. The here-presented improvements of the data analysis procedure (highlighted in light red color on the figure) concentrate on the determination of the final mass values and uncertainties and the corresponding development of the MSmarple data analysis framework, which was developed in R programming language [R Core Team, 2021]. These improvements are the result of the work of multiple people, where S. Ayet San Andrés and S. Beck took an active role also in the code development and testing [Ayet San Andrés et al., 2024] (priv. comm.).

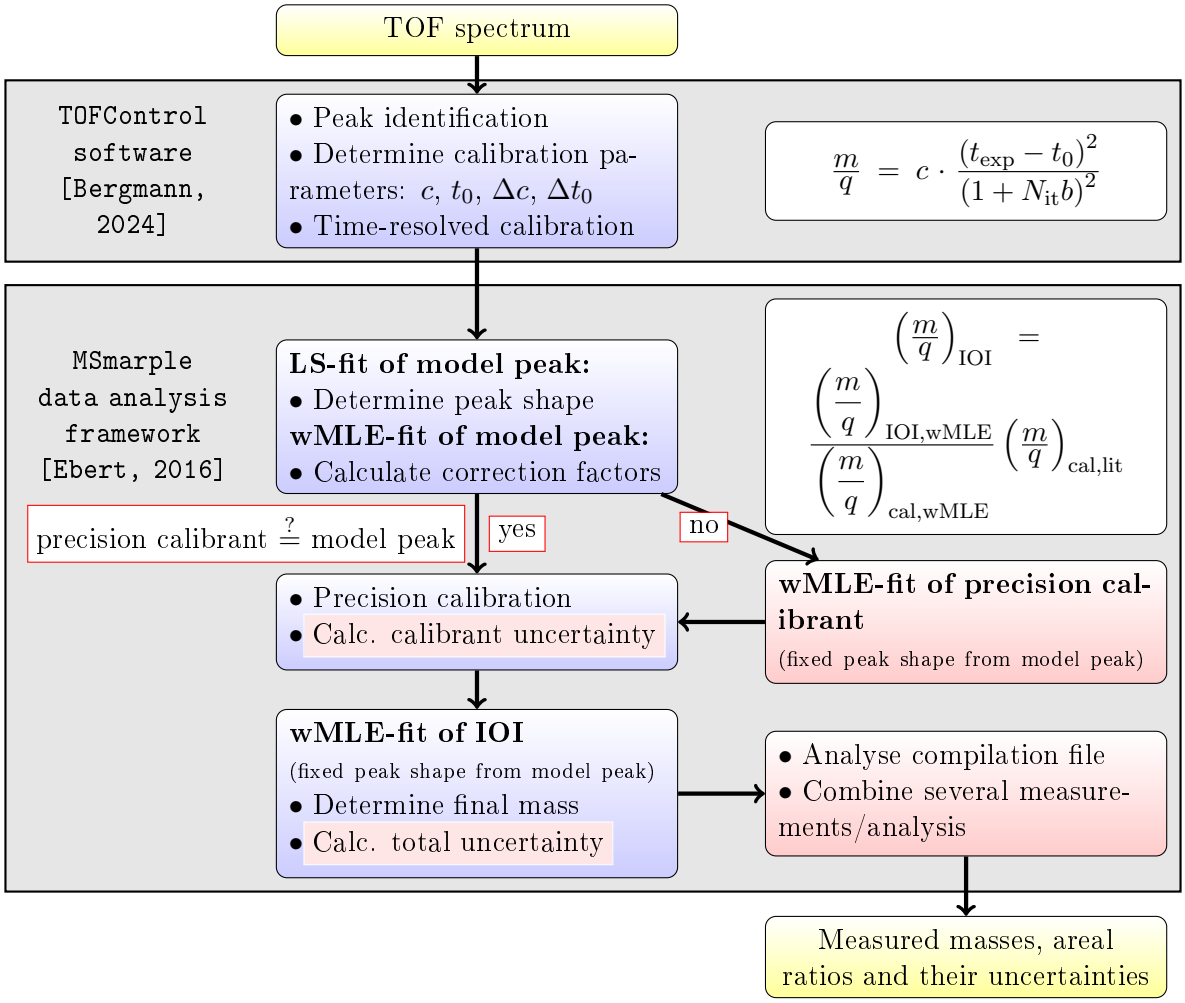

Figure 3.1: Schematic overview of the main steps and software used during data analysis. The steps that are marked with light red were implemented in the data analysis framework within this work in order to enhance the flexibility of the data analysis procedure. Besides making the data analysis scripts more convenient to use, the calculation of multiple uncertainty components were also modified with the goals to give a more precise estimate of their value and/or adapt their calculation to the increased flexibility of the data analysis procedure. See more explanations in the text.

The data analysis starts with a time-of-flight (TOF) spectrum recorded by the MR-TOF-

[1]Long name for MSmarple: Mass SpectruM Analysis R Package weighted Likelihood Estimate

MS data acquisition system. The data acquisition and the first steps of the data analysis are performed using the TOFControl software [Bergmann, 2024]. The relationship between time-of-flight (TOF) and the mass-to-charge ratio is defined by the following equation:

$$\frac{m}{q} = c \cdot \frac{(t_{\mathrm{exp}} - t_0)^2}{(1 + N_{\mathrm{it}} b)^2} \ , \tag{3.1}$$

where t_{exp} is the measured time span for which ions are flying in the MR-TOF-MS, and N_{it} is the number of turns the ions undergo inside the time-of-flight analyzer. The calibration parameter b describes the ratio of the path length for one turn in the analyzer and the path length from the injection trap to the detector, the parameter c is proportional to the effective voltage felt by the charged particles in the MR-TOF-MS and is inversely proportional to the square of the path length from the injection trap to the detector, and the parameter t_0 describes the time delay between the start signal and the real start of the ions (for more details see [Ayet San Andrés et al., 2019]). As long as the length of the cables used in the electronics components responsible for data acquisition are not changed between two consecutive measurement runs, the value of the t_0 parameter stays the same, i.e. it is independent of the effective voltage felt by the ions and thus the number of isochronous turns they undergo in the analyzer. Therefore, the value of the parameter t_0 and its uncertainty (Δt_0) is determined prior to the experiments in an offline measurement using at least 2 calibrant ions spanning a large mass-to-charge range and undergoing zero isochronous turns.

For every data set measured with the MR-TOF-MS of FRS-IC/TITAN, where the ions of interest undergo multiple isochronous turns, the calibration parameters c and b are determined via the following steps (see Fig. 3.1):

1. Firstly, the peaks in the measured MR-TOF-MS spectra need to be identified and one needs to select the peak candidates for calibrants and ions of interest. The peak identification can be supplemented by additional information besides the expected mass-to-charge ratios of the peaks; such as expected yields from known reaction cross-sections, data measured by the FRS PID detectors, another MR-TOF-MS data set acquired with the same ions undergoing different number of isochronous turns or, at TITAN, measurements performed with switching the LASERs off.

2. Secondly, using the TOFControl software, a time-resolved calibration (TRC) to correct drifts of the time-of-flight due to voltage and thermal drifts and a multi-turn (MT) calibration covering the full mass-to-charge range are performed. For the TRC, the usage of a single, preferably high statistics peak is sufficient, whose mass does not need to be well known[2]. For the MT calibration using Eq. (3.1), at least 2, but preferably even more, calibrant ions with a well-known literature mass are required[3]. After this step, the value of the parameter c and its uncertainty (Δc) are fixed and the multi-turn-calibrated and drift-corrected mass-to-charge spectrum is exported from TOFControl in list mode.

[2] In order to perform the TRC, the total length of the measured data set is divided into individual calibration blocks, which were acquired for a few seconds typically. The value of the parameter b is determined for each calibration block, separately, and a linear interpolation is applied between the values of the parameter b in each calibration blocks. The optimum choice concerning the length of the calibration blocks is a compromise between how accurately the parameter b can be determined in each block and the resulting time resolution of the TRC.

[3] When the measured spectrum contains only isobaric ions, i.e. the calibrants and ions of interest undergo the same number of turns, the relationship given in Eq. (3.1) is simplified to

$$\frac{m}{q} = a \cdot (t_{\mathrm{exp}} - t_0)^2 \tag{3.2}$$

In this case, the step of the MT calibration is not needed and a single peak with a well-known literature mass is sufficient to calibrate the entire spectrum, i.e. determine the value of the parameter a.

3. The next steps of the data analysis procedure are done with the MSmarple data analysis framework. Here, the peak shape is determined using a single, high statistics model peak, preferably measured simultaneously with the ions of interest. For this, the data is binned according to the Freedman-Diaconis rule [Freedman & Diaconis, 1981] and fitted with a hyper-exponentially modified Gaussian (hyper-EMG) function [Purushothaman et al., 2017], which incorporates exponential tails from ion-optical aberrations in a phenomenological way, using a least squares (LS) method. For validating the goodness of the fit a reduced χ^2 test and a Kolmogorov–Smirnov (KS) statistical test [Massey, 1951] are used. Once the parameters of the hyper-EMG peak shape are determined, the unbinned data of the model peak are fitted using a weighted maximum likelihood estimation (wMLE) method[4], where the only free parameter is the peak centroid. This is done to calculate the correction factors required later on for the peak shape uncertainty determination [Ayet San Andrés et al., 2019].

4. In the following, the so-called precision calibration is done, which comprises from calculating the ratio $(m/q)_{\mathrm{cal,lit}} \big/ (m/q)_{\mathrm{cal,wMLE,corrected}}$ (see Eq. (3.3)) and the corresponding uncertainty components of the precision calibrant peak. For this, the $(m/q)_{\mathrm{cal,wMLE}}$ value is determined via fitting the unbinned data of the precision calibrant peak[5] using the wMLE method with a fixed and, if needed, scaled peak shape obtained from the model peak. This is done in order to unify the fitting methods used in the treatment of the precision calibrant ion and ion of interest (IOI) data. Prior to the data analysis developments presented here, it was hard-coded in the data analysis framework that the same peak, which is used to determine peak shape, had to be also used for precision calibration. Within the context of this work, this has been made more flexible, i.e. the model peak used to determine the peak shape and the peak used to obtain the precision calibration can now be selected independently (for more details see Section 3.2).

5. Inside the TOF analyzer of the MR-TOF-MS, all ions are subject to the same ion-optical aberrations. Therefore, all ions with the same charge state appearing in the same TOF spectrum have the same peak shape. Therefore, the peak shape parameters obtained from the model peak in the third step explained above can be scaled to the ions of interest (for more details on the peak-shape scaling, see Section 3.3), the unbinned data of which can be fitted using the wMLE method yielding the $(m/q)_{\mathrm{IOI,wMLE}}$ value.

6. In order to re-establish the mass-to-charge scale after the wMLE fitting, which also recalculates the value of the b calibration parameter (see Eq. (3.1)), and to determine the final mass-to-charge values of the ions of interest, the following equation is used:

$$\left(\frac{m}{q}\right)_{\mathrm{IOI}} = \frac{\left(\frac{m}{q}\right)_{\mathrm{IOI,wMLE,corrected}}}{\left(\frac{m}{q}\right)_{\mathrm{cal,wMLE,corrected}}} \left(\frac{m}{q}\right)_{\mathrm{cal,lit}} \tag{3.3}$$

Here, the quantities $(m/q)_{\mathrm{cal/IOI,wMLE,corrected}}$ are obtained from the $(m/q)_{\mathrm{cal/IOI,wMLE}}$ values after applying corrections due to relativistic effects and, if non-zero, due to the

[4] Compared to the LS method, the wMLE is more robust, when treating low-statistics data. Furthermore, it enables to fit unbinned data, and thus avoids uncertainties associated with data binning. As a weighting function, the truncated natural logarithm of the hyper-EMG function itself ($f(x_i)$) is used to increase the robustness of the fit by minimizing the influence of outliers on the determination of the peak centroid [Ebert, 2016]. Here, the truncation means that events outside of the mass-to-charge range defined by $ln(f(x_i)) > 0$ are weighted by zero for the fit.

[5] For precision calibration a single peak corresponding to an ion with a well-known literature mass, $(m/q)_{\mathrm{cal,lit}}$, is sufficient.

operation of the MRS. In case of fitting overlapping peaks, a so-called bias correction has to be applied in addition [Ayet San Andrés et al., 2019]. In case the mass-to-charge ranges for the wMLE fits need to be restricted due to multiple overlapping peaks, such that the weighting of the fit is above zero ($ln(f(x_i)) > 0$) an additional correction, the so-called cut-bias correction, needs to be applied, which was developed within the context of this work (see Section 3.3).

7. Finally, the total uncertainties of the mass-to-charge ratio of ions of interest are calculated by adding in quadrature individual components, see Section 3.3 for more details, and the final atomic mass values of the ions of interest (m_{IOI}) and their uncertainties (σ_{IOI}) are deduced using the following equations:

$$m_{\mathrm{IOI}} = \left(\frac{m}{q}\right)_{\mathrm{IOI}} \cdot q_{\mathrm{IOI}} + m_e \cdot q_{\mathrm{IOI}}/e \text{ and } \sigma_{\mathrm{IOI}} = \sigma_{\mathrm{IOI,ionic}} \cdot q_{\mathrm{IOI}} \tag{3.4}$$

where $(m/q)_{\mathrm{IOI}}$ and $\sigma_{\mathrm{IOI,ionic}}$ are the mass-to-charge ratio and uncertainty values obtained in the data analysis procedure explained above, m_e is the electron mass, e is the elementary charge and q_{IOI}/e is the charge state of the IOI. Since the mass measurements usually include only singly- or doubly-charged ions, the electrons' binding energy in the neutral atom (few eV) can be neglected.

After the mass values and uncertainties of the nuclides of interest are determined in the individual data sets, the results are averaged with the weighted mean for the nuclides, which are measured in multiple data sets, see Section 3.4 for more details.

3.2 Enhanced speed and flexibility of the data analysis framework

With the increased variety of data sets obtained with the MR-TOF-MSs at FRS Ion Catcher and TITAN, ranging from very broadband data sets covering a mass-to-charge range larger than 10 u/e and including more than 50 nuclides within a single TOF spectrum (see e.g. [Spătaru et al., 2025, Fowler-Davis, 2025]) to data sets including multiple overlapping TOF distributions with high statistics (see e.g. Chapter 4), there is a need to increase both the flexibility and speed of the data analysis framework written in R language.

The two most important examples for the flexibility enhancements implemented within the context of this work are the following:

- Firstly, the model peak used to determine the peak shape and the peak used to obtain the precision calibration can now be selected independently. Often, the largest statistics peak in the spectrum, which is perfect for determining the peak shape, can not be used for an accurate precision calibration, because its time-of-flight is a bit shifted, e.g., due to experiencing an electrical ringing from the mirror electrodes during their extraction from the TOF analyzer. Moreover, in case of broadband mass measurements it is often advantageous to select a precision calibrant, which is isobaric to the ions of interest, because it removes systematic uncertainties associated with calibrating the ions of interest using non-isobaric species (see e.g. the Δm_c and the NPI uncertainty components defined in Section 3.3). An isobaric precision calibration can now be done independently from the choice of the model peak, which will be further exploited in future mass measurements, where the newly-commissioned LACCI ion source of the FRS-IC is used, which can provide isobaric calibrants for mostly all mass unit [Yu et al., 2024a].

- Secondly, the developments of this work also enabled to start the fits of the individual IOIs and the corresponding calculations of the mass uncertainty automatically, one after

another, i.e. to start the fits in the so-called batch mode. Once the mass value and different uncertainty components of all IOIs are determined, the results are collected together in an excel output file, the so-called compilation file, which enables a fast comparison of the mass and uncertainty values determined for different IOIs. This increases the user friendliness and avoids potential user mistakes through performing an automatic and standardized calculation and comparison of all mass values and uncertainties, see more details in Section 3.6. This latter feature is essential for the treatment of broadband mass measurements, where a large amount of ions of interest (often more than 50) can be included in a single TOF spectrum, and a quick comparison of the results of the fits for all IOIs is desired.

The most computing-power- and time-consuming tasks of the data analysis framework are the calculation of the peak-shape uncertainty and the Monte Carlo simulations for the calculation of the statistical and contamination uncertainties, and in case the peaks' tails need to be restricted, the Monte Carlo simulations for the newly-implemented cut-bias correction and, in case of overlapping peaks, for the bias correction (see Section 3.3). For data with high statistics (∼100,000 events) overlapping peaks, determining the mass values and corresponding uncertainty components can take up to a 1-2 days, when a single CPU core is used to perform the calculations. Similarly, determining the mass values and uncertainties of several IOI measured in a broadband mass spectrum is also very time-consuming. It is, therefore, necessary to parallelize the uncertainty calculations, i.e. spread the task to multiple CPU cores. The script running-time tests shown in Fig. 3.2 illustrate the enhanced speed of the MSmarple data analysis framework due to parallel coding.

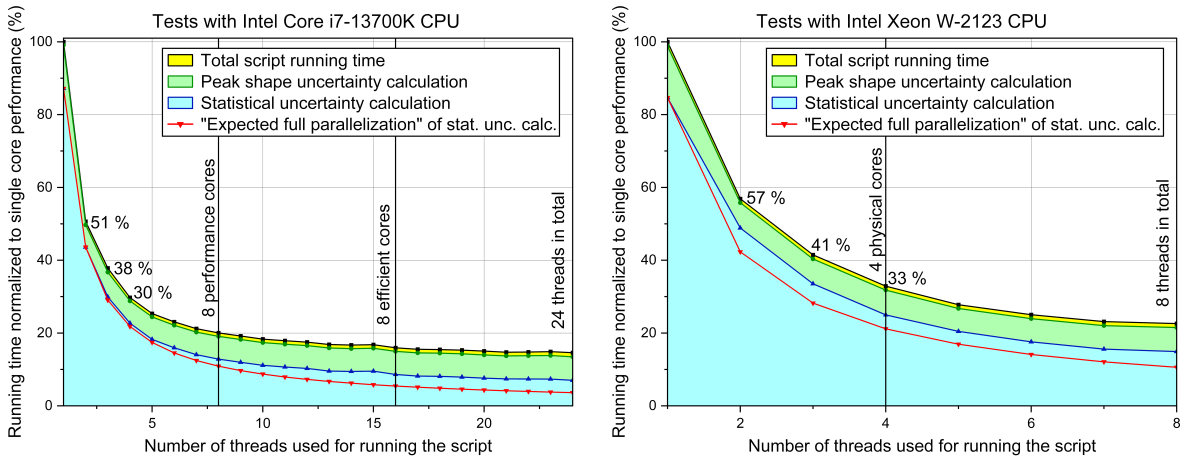

Figure 3.2: Figure to illustrate the enhanced speed of the data analysis framework due to parallel coding. The points measured using different number of CPU threads are connected with lines only to guide the eyes. Here, the total script running time (black curve) is dominated by the peak-shape (greed area) and statistical (blue curve) uncertainty calculations. For the performance of these running time tests, only the Monte Carlo simulations for the statistical uncertainty calculations were used, while any other numerical simulations were switched off. The running-time tests were performed using two different CPUs; for the plot on the left side an Intel Core i7-13700K CPU[6] was used and for the plot on the right side an Intel Xeon W-2123 CPU[7] was used.

[6] An Intel Core i7-13700K CPU has 8 performance cores, considered as the most powerful cores for parallel coding, 8 efficient cores and in total 24 threads [Manufacturers & Products, 2025].

[7] An Intel Xeon W-2123 CPU has 4 physical cores and in total 8 threads [Manufacturers & Products, 2025].

For the performed running-time tests, the total script running time was dominated by the peak-shape- and statistical-uncertainty calculations (Fig. 3.2). The measured running times corresponding to the Monte Carlo simulations of the statistical-uncertainty calculations (blue curves) follow closely their expected full parallelization (red curves) calculated by dividing the single-core performance by the number of the used CPU threads. On the other hand, the present implementation of the peak-shape uncertainty calculations (illustrated by the green areas on the figures) is non-parallelizable except for the factor of 2 improvement shown on the figure, when spreading the task across 2 CPU cores instead of 1. A future refactoring of the code will solve this problem, i.e. speed up the peak-shape uncertainty calculations further. Overall, the figures show a significant improvement in the total script running time with the increased number of CPU cores.

3.3 Uncertainty contributions

The total uncertainty of the mass-to-charge ratio is calculated by adding in quadrature individual components. Refs. [Ayet San Andrés, 2018, Ayet San Andrés et al., 2019] include a comprehensive list of the individual uncertainty components, their definitions and quantification relevant for mass measurements performed before 2019 at the FRS Ion Catcher. Within this work, a few uncertainty components relevant to analyze the data partially reported in this work (see Chapters 4 and 5) and, additionally, in Ref. [Amanbayev, 2023, Spătaru et al., 2025, Mollaebrahimi et al., 2023b], were re-measured or the formalism to calculate them was modified yielding more accurate uncertainty estimates. The re-fined uncertainty calculation will be also used in future works concerning the analysis of data obtained with the MR-TOF-MS of the FRS Ion Catcher setup.

Fig. 3.3 summarizes the composition of the different uncertainty components. For the definitions of the uncertainty components marked with a white background on the figure, the reader is referred to [Ayet San Andrés et al., 2019], because the present work reports no significant modifications concerning their formalism and, in the data presented here, these effects can be neglected. The uncertainty components marked with a grey background are relevant for the data presented here (see Chapters 4 and 5), but their definitions and calculation remains unchanged as compared to Refs. [Ayet San Andrés, 2018, Ayet San Andrés et al., 2019]. These uncertainties will be summarized in a few sentences below:

- Peak-shape uncertainty: The quadratic sum of the relative differences in the peak centroids resulted by the wMLE fit for the IOI and the model peak due to changing each parameters of the Hyper-EMG function by its corresponding uncertainty, while keeping the others constant.

- Bias correction and corresponding uncertainty: In case of fitting overlapping peaks the so-called bias correction is performed in order to correct for the smaller distance between the deduced peak centroids of overlapping peaks caused by the weighting of the wMLE fits. This is an iterative correction performed using Monte Carlo simulations, which is explained and tested in the works of [Ebert, 2016, Ayet San Andrés, 2018, Ayet San Andrés et al., 2019]. The uncertainty from the correction is estimated to be 25% of the difference between the mass-to-charge ratio obtained with and without the correction.

- Uncertainty due to known unresolved peaks: When there are reasons to expect multiple ions or nuclear states, which have a known chemical formula, arriving at the same spot in the time-of-flight spectrum and cannot be resolved by the spectrometer, an uncertainty component is required to account for this effect. In particular, when the peaks have a known distance, but their abundance ratio is unknown, e.g., an unresolved isomer, isobar,

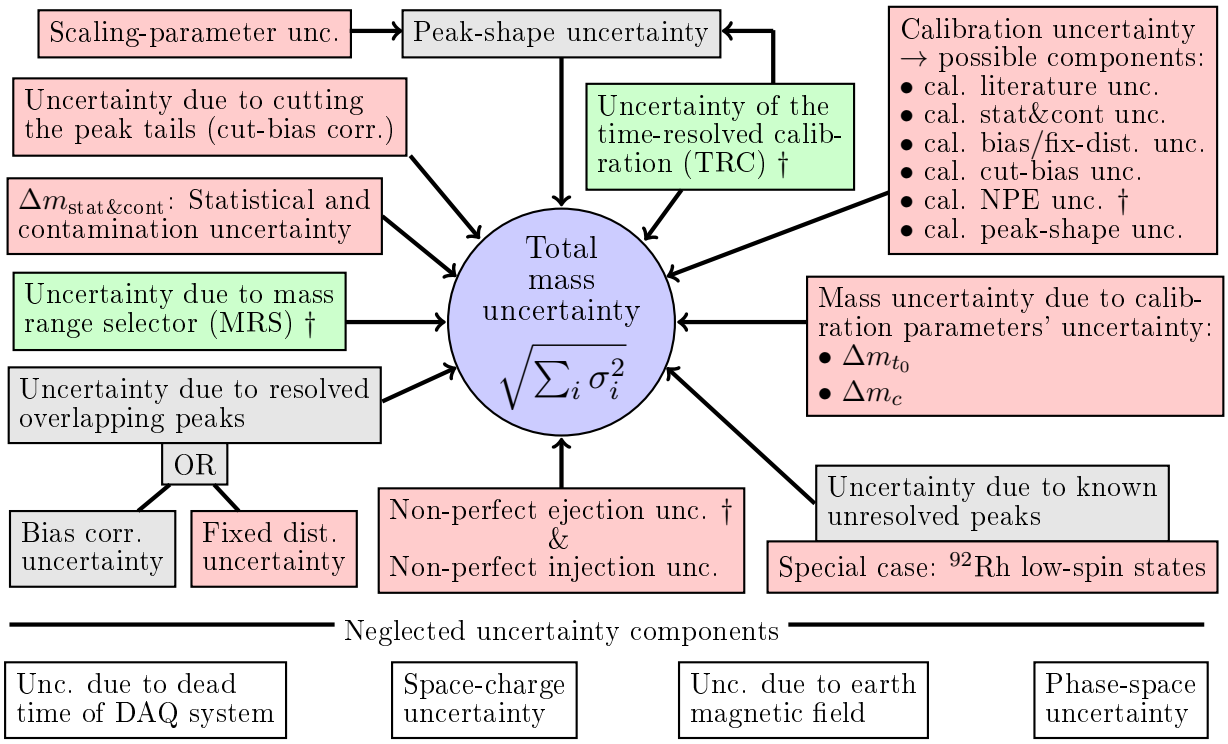

Figure 3.3: A schematic overview of the relationship of uncertainty contributions to the total mass uncertainty. In case of the analysis of the data collected at TITAN, the uncertainty contributions that are marked with a dagger (†) were all covered by a single uncertainty component, which will be referred to as "TITAN's systematic uncertainty" (see Chapter 4). The light green colour marks the uncertainty components that were mathematically zero in all measurements reported here. The uncertainty contributions that are marked with light red were further investigated or newly determined or measured after Refs. [Ayet San Andrés, 2018, Ayet San Andrés et al., 2019]. See more explanations in the text.

or an expected contamination, an uncertainty component and mass value correction are applied following recommendations from AME2020 Appendix B.1 [Huang et al., 2021]. Note that in the case of the unresolved ^{92}Rh low-spin states, the expected abundance ratio is known, therefore, in this case, special considerations were taken and reported here, see Section 5.2.

The uncertainty components marked with a light red background in Fig. 3.3 were further investigated or newly determined/measured in this work. The results of some of these investigations will be detailed in the upcoming subchapters.

Statistical and contamination uncertainty ($\Delta m_{\text{stat\&cont}}$)

For the wMLE fits of the precision calibrant and ions of interest with a Hyper-EMG function, the parameters of which were determined from the model peak, an empirical approach has been taken to determine the statistical and contamination uncertainties. These uncertainty components are determined based on Monte Carlo simulations, i.e random numbers are drawn according to the same distribution function as the fit functions of the calibrant and IOI and they are fitted with the wMLE method. Here, the total number of events as measured for the calibrant or ions of interest (together with the background events or the events of the unknown, unresolved contaminant peak) are shared between the main peak and the background for the statistical uncertainty simulations and shared between the main peak, background and contaminant peak for

the contamination uncertainty simulations. This process of generating and fitting the simulated data with the wMLE method is repeated many times (typically 100-to-1000 times depending on the total number of measured and simulated events of the peak) and the standard deviation of the mass-to-charge values obtained from this process gives the value of Δm_{stat} (in case of the statistical uncertainty simulations) and Δm_{cont} (in case of the contamination uncertainty simulations). These two values are then combined linearly using the contamination probability (p_{cont}) resulting in the statistical and contamination uncertainty component ($\Delta m_{\mathrm{stat\&cont}}$) of the calibrant and the IOI:

$$\Delta m_{\mathrm{stat\&cont}} = (1 - p_{\mathrm{cont}}) \cdot \Delta m_{\mathrm{stat}} + p_{\mathrm{cont}} \cdot \Delta m_{\mathrm{cont}} \tag{3.5}$$

For handling data with very low statistics, down to only a few events per peak, see e.g. Chapter 5 or [Mardor et al., 2021, Mollaebrahimi et al., 2023b], an accurate determination of the expected level of background and possible contamination under the peaks is essential.

In a typical MR-TOF-MS spectrum a constant background is expected from two sources: (i) dark counts on the TOF detector corresponding to events from the residual gas generating secondary electrons resulting in single hits, which are not correlated to the window of ejection from the analyzer, and (ii) scattered ions with a completely different phase space compared to the typically measured ions in the spectrum, which also result in single hits, however, in this case, those hits are correlated to the window of ejection from the analyzer. While the influence of the constant background and outliers on the fitting procedure was systematically studied in [Ebert, 2016], here the emphasis is given to the estimation of the level of the constant background in a given time-of-flight spectrum. The constant background often has very low statistics, i.e., the measurement method is practically background-free as illustrated by a typical TOF spectrum obtained at the FRS Ion Catcher in Fig. 5.5. Consequently, the deduced background level depends on the choice of the "peak-free" region of the spectrum, which is used for its determination. In order to minimize the user-choice dependence, a standalone R script has been written to deduce the level of the constant background within a given TOF spectrum. Here, the complete range of the time-of-flight spectrum (corresponding to the complete window of ejection from the analyzer) is binned in units of a few FWHM, which is determined from the peaks in the spectrum, and the resulting bin-height distribution is deduced. Fig. 3.4a shows an example bin-height distribution deduced from the TOF spectrum corresponding to the measurement of ^{93}Pd presented in Fig. 5.5 using a binwidth of 4 FWHM. Here, the zeroth and the first bins correspond to the so-called "peak-free" regions of the TOF spectrum, where either no hits or only single hits are found within a binwidth of 4 FWHM, and the rest of the bins correspond to the contaminant, calibrant or ion of interest peaks in the spectrum. The zeroth and the first bins are then used to estimate the level of the constant background within the spectrum, by "fitting" a Poisson distribution with a given area (A_{Pois}) and expectation value (λ) to this two bins and then dividing the resulting λ by the given binwidth used to bin the TOF spectrum, which gives the background density. The "fit" of the Poisson distribution, which is illustrated by the red curve in Fig. 3.4a, is performed by numerically solving the following system of non-linear equations:

$$\begin{aligned} A_{\mathrm{Pois}} \cdot \frac{\lambda^0 \cdot e^{-\lambda}}{0!} &= \text{number of events in the zeroth bin} \\ A_{\mathrm{Pois}} \cdot \frac{\lambda^1 \cdot e^{-\lambda}}{1!} &= \text{number of events in the first bin} \end{aligned} \tag{3.6}$$

To reduce the dependence of the determined background level on the choice of the binwidth and on the scatter of the single events, the above procedure is repeated for multiple binwidths between 2 and 4 FWHM units and the deduced background densities are then averaged, see Fig. 3.4b. After the expectation value of the background density is determined, it is used to generate the number of background counts under the calibrant and ion of interest peaks with a truncated

Poisson distribution for the Monte Carlo simulations to deduce statistical and contamination uncertainties. The truncation limits the number of the background events to be maximum 50% of the total number of measured and simulated events below the given peak.

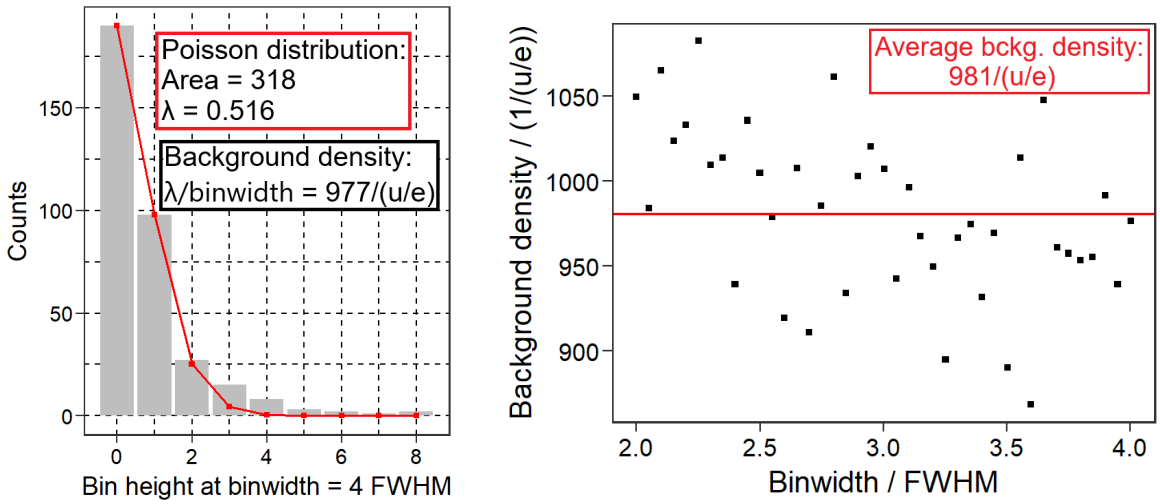

(a) (b)

Figure 3.4: Calculation of the background density in the time-of-flight spectrum corresponding to the measurement of ^{93}Pd (data set I, see more details in Chapter 5). (a) The histogram on the left side shows the bin-height distribution deduced after binning the TOF spectrum in units of 4 FWHM. The zeroth and the first bins in this histogram are fitted with a Poisson distribution shown by the red data points. The Poisson distribution is a discrete distribution, so the red lines connecting the points are only drawn to guide the eyes. (b) The plot on the right side shows the deduced background densities for multiple binwidths between 2 and 4 FWHM units and their average (shown by the horizontal red line).

Besides the constant background, there may be hidden unexpected peaks (contaminant ions) under the peaks of the ions of interest and calibrant ions, which may shift the measured mass of the calibrant or IOI and lead to a corresponding uncertainty contribution (the contamination uncertainty). Although this happens with a larger probability in case of measurements with a lower resolving power and covering a larger mass-to-charge and dynamic range, in principle, each measurements are prone to this effect. An unexpected peak (contaminant) can correspond to a peak, which could not be identified in the spectrum or to an identified peak, the origin of which cannot be explained in the given measurement and therefore can not be used as a potential calibrant in the spectrum. Before 2020, the abundance ratio between the IOI and the contaminant ions has been estimated by the largest statistics unexpected peak appearing in the TOF spectrum and the information from the contamination peak density in the given TOF spectrum was not considered in the uncertainty calculations, see e.g. [Ayet San Andrés et al., 2019]. In some cases, this previous procedure resulted in an overestimation of the contamination uncertainty contribution, which motivated the development of a new procedure to estimate the contamination uncertainty corresponding to the measured mass of ions of interest and calibrant ions. The main steps of this newly developed procedure are:

1. Firstly, the contamination peak density (ρ_{cont}) is estimated via counting the number of the unexpected peaks observed in the measured spectrum and dividing it by the complete mass-to-charge range of the spectrum. The value of ρ_{cont} can reflect many features of the given measurement, such as, whether the achieved resolving power is low or high or whether the covered mass-to-charge and dynamic range is small or large. Therefore, this value

directly reflects the magnitude of the contamination uncertainty necessary to describe a given measurement. For example, in the case of the TOF spectrum shown in Fig. 5.5, there are only a few unidentified or unexpected peaks in the spectrum, thus the measurement of ^{93}Pd is not strongly prone to a possible underlying contaminant below the peak.

2. Secondly, the contamination probability (p_{cont}), which reflects the probability of an unexpected unresolved peak (contaminant) hidden beneath the peak of the calibrant or IOI, can be estimated by

$$p_{\mathrm{cont}} = 2 \cdot \rho_{\mathrm{cont}} \cdot \left(\left(\frac{m}{q} \right)_{\mathrm{max}} - \left(\frac{m}{q} \right)_{\mathrm{min}} \right) \tag{3.7}$$

Here, normally, the $((m/q)_{\mathrm{max}} - (m/q)_{\mathrm{min}})$ difference represents the mass-to-charge range of the calibrant or IOI peak, where the weighting of the wMLE fit is above zero. The only exception is the case, when the mass-to-charge range for the wMLE fit needs to be restricted, e.g. due to multiple overlapping peaks. In this case, the $((m/q)_{\mathrm{max}} - (m/q)_{\mathrm{min}})$ difference is defined by this restricted mass-to-charge range. Note that, typically, the contaminant peaks are not perfectly uniformly distributed within the complete spectrum measured with the MR-TOF-MS, because the analyzer transmission is often tuned otherwise. Therefore, in Eq. (3.7), a multiplication factor of 2 (fudge factor) is applied in order to prevent an underestimation of the p_{cont} probability and the corresponding the $\Delta m_{\mathrm{stat\&cont}}$ mass uncertainty component calculated by Eq. (3.5).

3. The next step is to determine the average number of contaminant events ($\overline{N_{\mathrm{cont}}}$) via calculating the average area of the observed unexpected peaks in the measured spectrum[8].

4. The determined value of $\overline{N_{\mathrm{cont}}}$ is then used as an input data for the Monte Carlo simulations of the contamination uncertainty calculations. As the first step of the latter simulations, the total number of the measured and simulated events (N_{total}) corresponding to the given peak of the calibrant or IOI are shared between the main peak, the constant background and the contaminant events. For the generation of the number of contaminant and background events, the following conditions apply:

   - The number of the contaminant events (N_{cont}) are generated with a phenomenological probability distribution that has been tailored to empirically describe the observed distribution of the events of unexpected peaks in various offline and online measurements with the FRS-IC, i.e., to describe the typical pattern of molecular contaminants from the CSC and MR-TOF-MS. This phenomenological probability distribution first follows a uniform distribution between $0 \leq k \leq \overline{N_{\mathrm{cont}}}$ and then it follows a Poisson decay with $\lambda = 1$ for $\overline{N_{\mathrm{cont}}} \leq k \leq \infty$. Since the resulting distribution has a larger mean value than $\overline{N_{\mathrm{cont}}}$, in the next step, the distribution is scaled such that it's expectation value matches with $\overline{N_{\mathrm{cont}}}$. This is achieved by dividing the distribution by

[8] Note that besides the density and the average area of the unexpected peaks observed in the spectrum, there can be also other more direct evidences hinting on the magnitude of the possible contamination below the peaks. For example, in case of mass measurements obtained at TITAN, data is collected with switching the LASERs off for the resonant ionization of the IOI species. A comparison of the LASER on/off data provides direct evidence on the maximum number of the possible contaminant events hidden below the IOI peaks, which can be used to estimate the contamination uncertainty in the measurements obtained at TITAN, for more details see Section 4.2. Similarly, in case of mass measurements obtained at FRS-IC, the degrader settings and with this the stopping range of the ions can be changed, such that the IOI are not stopped, while keeping the same amount of ionization in the CSC, which results that the same amount of molecules are formed. Performing a measurement with a changed degrader settings would provide direct evidence on the expected amount of contamination below the IOI peaks at FRS-IC. On the other hand, such a measurement is very time consuming in case of the most exotic species measured with very low count rate, therefore is typically not done and the contamination uncertainty needs to be estimated from the observed unexpected peaks in the spectrum as explained in the text.

a scaling factor of 1.315. After this, the distribution is truncated, such that the generated number of contaminant events are larger than 2 (single events are considered as background counts) and smaller than 50% of the total number of measured and simulated events below the given peak.

- The number of the background events (N_{bckg}) are generated following a truncated Poisson distribution, as explained earlier, and the remaining events of $N_{\mathrm{cal/IOI}} = N_{\mathrm{total}} - N_{\mathrm{cont}} - N_{\mathrm{bckg}}$ are then used to generate the main peak of the calibrant or IOI.
- As a boundary condition; the sum of the number of the contaminant and background events are limited to maximum 50% of the total number of measured and simulated events below the given peak. This is done, because as soon as the number of contaminant and background events exceeds 50% of the total number of measured events of the peak then the peak is considered misidentified rather than "contaminated", see more details in footnote[9].

5. In the next step of the Monte Carlo simulations, the centroid of the contaminant peak is generated with a uniform distribution between $(m/q)_{\mathrm{min}}$ and $(m/q)_{\mathrm{max}}$ and for the peak shape of the contaminant peak the same peak shape is assumed as the one used for the wMLE fit of the calibrant ion or ion of interest. Then the simulated data of the constant background plus the contaminant peak plus the main peak are fitted as a single peak using the wMLE method. In the next step, a Kolgomorov-Smirnov statistical test [Massey, 1951] is performed to validate the goodness of the fit. The resulting p value of the KS test should be larger than a threshold value (typically $p_{\mathrm{threshold}} = 0.05$) in order to ensure that the simulated peaks (the contaminant peak and the main peak) are not separated or resolved from each other, i.e. the simulated data remain indistinguishable from the fit function applied to fit the simulated data as a single peak. The generation of the centroid of the contaminant peak is repeated as long as this condition for the KS does not apply.

6. Finally, the Δm_{cont} from Eq. (3.5) is calculated as the standard deviation of the mass-to-charge values obtained by the wMLE fits of the Monte Carlo simulations for the contamination uncertainty calculations.

The validity of the newly developed procedure to estimate the contamination uncertainty was first tested with the help of synthetic data, then the new procedure was applied to mass measurements performed at FRS-IC. As an example, the results of the Monte Carlo simulations for the statistical and contamination uncertainty calculations of the ^{91}Tc peak ($N_{\mathrm{total}} = 23$ events, see more details in Chapter 5) are shown in Fig. 3.5. In this data set, the expectation value for the number of background counts within the mass-to-charge range of the fit of ^{91}Tc is $\overline{N_{\mathrm{back}}} = 2$ events and the average area for unexpected peaks observed in the spectrum is $\overline{N_{\mathrm{cont}}} = 9$ events. The probability that a contaminant peak is hidden beneath the peak of ^{91}Tc is $p_{\mathrm{cont}} = 12\%$. Fig. 3.5a illustrates the influence of the choice of the KS test $p_{\mathrm{threshold}}$ value for the distribution of the difference between the simulated centroid of the contaminant peak and the centroid of the main (IOI) peak. In case of the simulations with $p_{\mathrm{threshold}} = 0.0001$ the KS test condition is essentially switched off, which leads that the simulated contaminant peak is uniformly distributed across the entire mass-to-charge range between $(m/q)_{\mathrm{min}}$ and $(m/q)_{\mathrm{max}}$. Consequently, in some cases, the simulated contaminant peak can be easily separated by eyes from the simulated main

[9] The presently-described procedure also enables to estimate the probability that a low statistics peak is misidentified (the so-called "misidentification probability") using the determined peak density and average area of the unexpected peaks observed in the spectrum. This latter probability is estimated as the combination of two probabilities; the probability that there is a contaminant peak in a mass-to-charge window given by the experimental mass uncertainties and the probability that this contaminant peak has more events than 50% of the total number of measured events of the peak. For example for the first direct mass measurement of ^{93}Pd from only 9 detected events (see Chapter 5) the probability of misidentification calculates to 4%.

peak of the ion of interest (with a measured FWHM of about 120 keV for the peak of ^{91}Tc, see Fig. 5.5 for the typical peak shape of the peaks in the spectrum). Increasing the threshold value for the performed KS tests to the typically used value of $p_{\text{threshold}} = 0.05$ ensures that the centroid of the contaminant peak is within 1-2 FWHM distance from the centroid of the main peak, thus ensuring that the two simulated peaks are not resolved from each other in agreement with the experimental observations (only one peak was detected for ^{91}Tc showing no clear signature of an underlying contaminant beneath the peak). Fig. 3.5b illustates the final distribution of the mass-to-charge values obtained from fitting the simulated data with the wMLE method during the statistical and contamination uncertainty calculations. The determined standard deviations for the 23 detected events of ^{91}Tc were $\Delta m_{\text{stat}} = 16.8$ keV and $\Delta m_{\text{cont}} = 23.8$ keV for the two simulations, respectively. After combining the two values using Eq. (3.5), this results in a statistical and contamination mass uncertainty component of $\Delta m_{\text{stat\&cont}} = 17.7$ keV for ^{91}Tc.

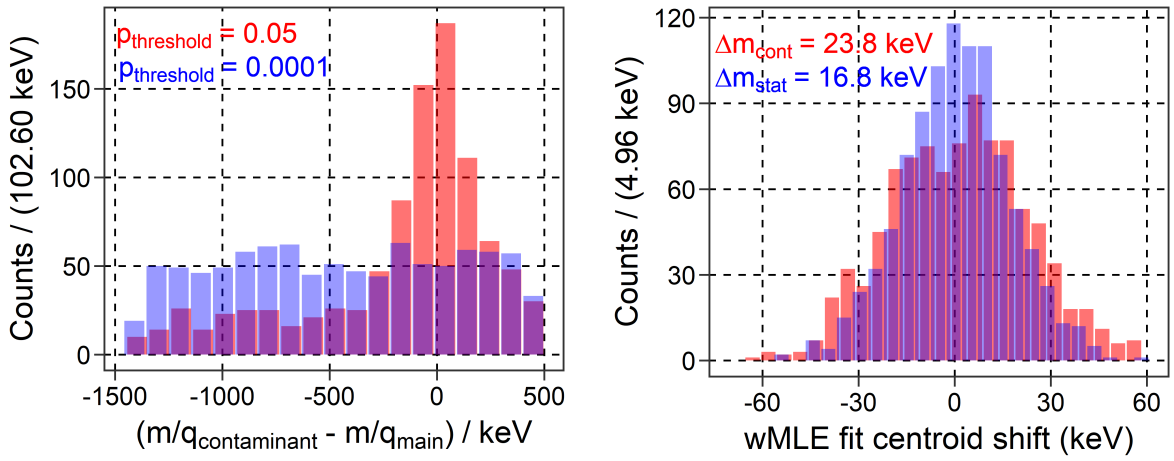

(a) (b)

Figure 3.5: Results of simulations for the statistical and contamination uncertainty calculations of the ^{91}Tc peak measured during the S474 experiment at FRS-IC, see more details in Chapter 5. (a) Concerning the contamination uncertainty calculations, the histogram on the left side shows a comparison of the distribution of the simulated distance between the centroids of the contaminant and main peaks using two different $p_{\text{threshold}}$ values for performing the KS tests on the simulated data. (b) The plot on the right side shows a comparison of the final distribution of the mass-to-charge values obtained from fitting the simulated data with the wMLE method corresponding to either the statistical or the contamination uncertainty calculations (with $p_{\text{threshold}} = 0.05$).

Mass uncertainty due to calibration parameters' uncertainty (Δm_c and Δm_{t_0})

The uncertainties Δt_0 and Δc of the calibration parameters, t_0 and c, are determined during the conversion of the time-of-flight spectrum into a mass-to-charge ratio spectrum using the TOFControl software [Bergmann, 2024]. In case there is the same amount of calibrant ions as unfixed parameters during the zero-turn (0T) or multi-turn (MT) calibration of the given spectrum, then the values of Δt_0 or Δc are calculated by uncertainty propagation. In case the number of calibrant ions is larger than the unfixed parameters during the 0T or MT calibration, then the observed TOF corresponding to the peak centroids of the individual calibrant ions are shifted separately by plus or minus their uncertainty and the calibration parameters are recalculated. The absolute values of the resulting maximum changes of the calibration parameters t_0 and c due to the shifted TOF of the individual calibrant ions with index of $i = 1, 2, \ldots, n$ are referred to as individual $\Delta t_{0,i=1,2,\ldots,n}$ and $\Delta c_{i=1,2,\ldots,n}$ components in the following discussion,

which are combined to deduce the final values of Δt_0 and Δc, respectively.

Recently, a systematic study with the help of broadband mass measurements at the FRS-IC, such as the ones reported in [Amanbayev, 2023, Spătaru et al., 2025, Fowler-Davis, 2025], showed that this latter combination of the individual $\Delta t_{0,i=1,2,...,n}$ and $\Delta c_{i=1,2,...,n}$ components needs to be done in a linear rather than in a quadratic manner, because these individual components are not fully independent from each other. Most of this study was performed in the context of the mass measurements of ^{252}Cf fission products with the FRS-IC reported in [Spătaru et al., 2025]. There, the broadband measurements with a relative mass-to-charge range of more than 10% resulting in a measurement of more than 50 ions within a single settings of the MR-TOF-MS enabled to systematically study the influence of the individual calibrant species on the results of the multi-turn calibration of the measured spectra [Spataru et al., 2024] (priv. comm.). In the present work, only the most important consequences of this systematic study to the data analysis procedure and, in particular, to the determination of the values of Δt_0 and Δc are reported.

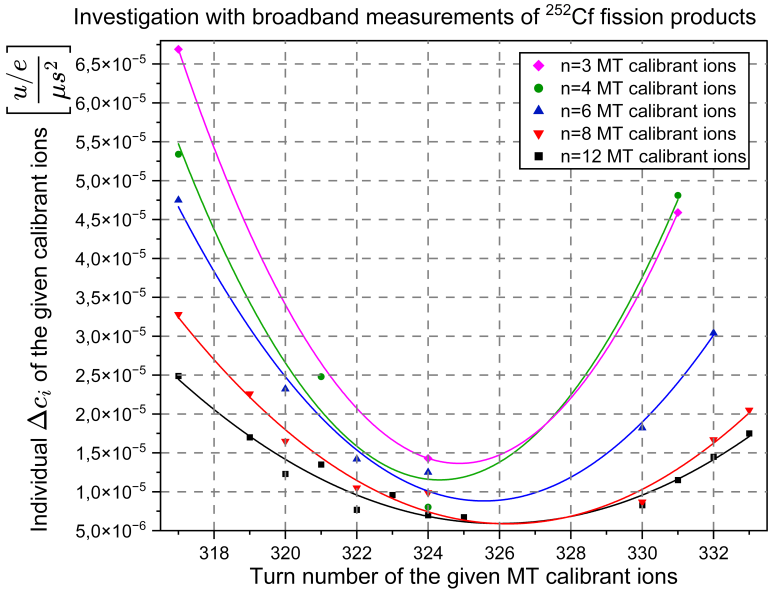

Figure 3.6: Individual $\Delta c_{i=1,2,...,n}$ components, shown by the data points, as a function of the turn number of the individual calibrant ions. Here, the individual $\Delta c_{i=1,2,...,n}$ components were obtained in the MT calibration of a broadband mass measurement of ^{252}Cf fission products (for more details, see [Spătaru et al., 2025]). The different colors of the data points indicate the different sets of calibrant ions used to perform the MT calibration. The data points corresponding to the different sets of calibrant ions are fitted with second order polynomial functions shown by the colorful curves.

One of the highlights of the studies performed with the broadband mass spectra, acquired using the ^{252}Cf fission source, is presented in Fig. 3.6. Here, the number of calibrant ions is varied from $n = 3$ up to $n = 12$ to perform the MT calibration of the ^{252}Cf spectrum, while making sure that the selected calibrant ions are always spread across the entire mass-to-charge range covered by the spectrum (see also in Section 3.6). Then the dependence of the individual $\Delta c_{i=1,2,...,n}$ components on the number of isochronous turns performed by the individual calibrant ions in the TOF analyzer is checked. This is done with the previously selected different sets of MT calibrant ions ($n = 3$, $n = 4$, $n = 6$, $n = 8$ and $n = 12$). As shown in Fig. 3.6, second order polynomial functions (parabolas) explain the measured data points sufficiently well. Besides the fact that the TOF uncertainty of the high statistics calibration peaks is dominated by the systematic uncertainty contributions, which are similar for all high statistics calibration

peaks, this latter results also indicate that the obtained individual $\Delta c_{i=1,2,...,n}$ components are not fully independent from each other. The calibrant ions with a mass-to-charge ratio (and turn number) close to the edges of the mass-to-charge (and turn number) range, covered by the selected calibration peaks, have the highest impact on the results of the MT calibration. Increasing the number of calibrants from $n = 3$ up to $n = 12$ minimizes the influence of the individual calibrants on the results of the MT calibration of the spectrum, i.e. the parabola of the individual $\Delta c_{i=1,2,...,n}$ components becomes more shallow.

As discussed above, in the next step, the individual $\Delta t_{0,i=1,2,...,n}$ or $\Delta c_{i=1,2,...,n}$ components, deduced in the 0T or MT calibration of the given spectrum, are combined linearly to calculate the values of Δt_0 and Δc. Then, in the final step, the mass-to-charge uncertainties due to the uncertainty in the calibration parameters are calculated by Eqs. (3.8) and (3.9), see [Rink, 2017, Hornung, 2018] for more details:

$$\Delta m_{t_0} = \left| 2\sqrt{c} \left(\frac{m}{q}\right)_{\mathrm{IOI}} \cdot \left(\frac{1}{(1 + bN_{\mathrm{it,cal}}) \sqrt{\left(\frac{m}{q}\right)_{\mathrm{cal}}}} - \frac{1}{(1 + bN_{\mathrm{it,IOI}}) \sqrt{\left(\frac{m}{q}\right)_{\mathrm{IOI}}}} \right) \Delta t_0 \right| \tag{3.8}$$

$$\Delta m_c = \left| \frac{c\,(t_{\mathrm{IOI}} - t_0)^2}{\left(1 + \frac{N_{\mathrm{it,IOI}}}{N_{\mathrm{it,cal}}} \left(\sqrt{\frac{c\,(t_{\mathrm{cal}} - t_0)^2}{\left(\frac{m}{q}\right)_{\mathrm{cal}}}} - 1 \right)\right)^2} - \frac{(c \pm \Delta c)\,(t_{\mathrm{IOI}} - t_0)^2}{\left(1 + \frac{N_{\mathrm{it,IOI}}}{N_{\mathrm{it,cal}}} \left(\sqrt{\frac{(c \pm \Delta c)\,(t_{\mathrm{cal}} - t_0)^2}{\left(\frac{m}{q}\right)_{\mathrm{cal}}}} - 1 \right)\right)^2} \right| \tag{3.9}$$

Here, $N_{\mathrm{it,cal/IOI}}$ is the number of isochronous turns that the precision calibrant or the IOI perform in the TOF analyzer, c, t_0 and b are the calibration parameters from Eq. (3.1) and $t_{\mathrm{cal/IOI}}$ is the total time-of-flight of the precision calibrant ion or the IOI, respectively.

Peak-shape scaling and corresponding scaling-parameter uncertainty

Some of the peak-shape parameters of the Hyper-EMG function [Purushothaman et al., 2017] determined in the LS-fit of the model peak have to be scaled to the IOI. The scaling factor takes into account the change of the peak width with the change of the mass-to-charge ratio, as well as well as the different contributions from the mass-resolving power. Here, the peak-shape parameters σ and τ_j, which describe the standard deviation of the Gaussian part and the peak tails of the Hyper-EMG function, respectively, are scaled from the model peak to the IOI using the following equation:

$$\sigma_{\mathrm{IOI}} = \sqrt{(S_\sigma \cdot \sigma_{\mathrm{cal}})^2 + \left(\sigma_{\mathrm{TRC}}^{\mathrm{RMS}} \cdot \left(\frac{m}{q}\right)_{\mathrm{IOI}}\right)^2 + \left(\sigma_{\mathrm{TRC}}^{\mathrm{stat}}\right)^2} \text{ and } \tau_{\mathrm{j,IOI}} = S_\tau \cdot \tau_{\mathrm{j,cal}} \tag{3.10}$$

Here, the parameters $\tau_{\mathrm{j,cal}}$, σ_{cal} are deduced from the LS-fit of the model peak and the scaling factors S_σ, S_τ are given by Eq. (3.11)[10]. For a description of $\sigma_{\mathrm{TRC}}^{\mathrm{RMS}}$ and $\sigma_{\mathrm{TRC}}^{\mathrm{stat}}$, see text below. The remaining parameters of the Hyper-EMG function (θ and η_i) are not scaled.

If the model peak used for determining the peak shape and the peak used for the time-resolved calibration (TRC) of the spectrum are the same, an additional peak broadening due to TRC is added in quadrature to the peak width (see Eq. (3.10)). In this case, one can distinguish between two different scenarios:

1. In case the TRC calibrant ions and the IOI do not experience the same electric fields, i.e. the TRC do not fully corrects the drifts, the relative peak broadening due to TRC is given by the parameter $\sigma_{\mathrm{TRC}}^{\mathrm{RMS}}$. This case is the so-called "external TRC", which has been thoroughly studied in the past, see e.g. [Ayet San Andrés, 2018]. This case is not relevant for the data presented here (see Chapters 4 and 5).

[10] See next page footnote.

2. If the calibrant ions and the IOI experience the same electric fields, the TRC fully corrects the electrical drifts. This case is the so-called "internal TRC", which is relevant for the data presented here. To further study the effect of an internal TRC, an automatic peak broadening is implemented in the data analysis framework. In this case, the peak shapes of the IOI and the TRC calibrant peaks differ purely due to the statistics inside the TRC blocks, which can be explained by the following thought experiment:

   One can picture a measurement, where in every measurement cycle exactly two ions are detected, e.g. one count of ^{85}Rb ion and one count of ^{87}Rb ion. In this case, both ions experience the same electric fields. Without applying TRC, both peaks have a standard deviation of σ_{initial}. Applying a TRC on one peak with corrections in every measurement cycles, the TRC peak will turn into a Dirac-delta distribution, and the other peak will have a standard deviation of $\sqrt{2} \cdot \sigma_{\text{initial}}$. This example illustrates that the effect of TRC broadening appears even for an internal TRC calibration and is purely mathematical. On the other hand, the mass accuracy in this case is not directly affected, since the TOF difference between the two distributions can both before and after TRC be associated with a $\sqrt{2}\cdot\sigma_{\text{initial}}$ accuracy; without TRC: $\sqrt{\sigma^2_{\text{initial}} + \sigma^2_{\text{initial}}}$ and with TRC: $\sqrt{\left(\sqrt{2} \cdot \sigma_{\text{initial}}\right)^2 + 0^2}$.

   In a more general case, the peak broadening caused by the statistics inside the TRC blocks ($\sigma^{\text{stat}}_{\text{TRC}}$) is given by

$$\sigma^{\text{stat}}_{\text{TRC}} = A_{\text{stat}} \frac{\text{FWHM}_{\text{TRC,cal}}}{\sqrt{N_{\text{counts/block}}}} \tag{3.13}$$

   Here, A_{stat} represents the increase of the statistical uncertainty due to Hyper-EMG peak shape compared to the Gaussian peak shape (see definition in Ref. [Ayet San Andrés et al., 2019]), $\text{FWHM}_{\text{TRC,cal}}$ describes the FWHM of TRC calibrant peak and $N_{\text{counts/block}}$ represents the average number of events of the TRC calibrant peak inside one calibration block. Here, an $A_{\text{stat}} = 0.5 \pm 0.1$ is used to estimate $\sigma^{\text{stat}}_{\text{TRC}}$, because this value is typical for the mass measurements reported in Ref. [Ayet San Andrés et al., 2019].

[10]The scaling factors of the peak-shape parameter describing the standard deviation of the Gaussian part of the Hyper-EMG function (σ) and the parameters describing the peak tails of the Hyper-EMG function (τ_i) are given by

$$S_\sigma = \frac{\left(\frac{m}{q}\right)_{\text{IOI}} \left[\frac{(m/q)}{\Delta\,(m/q)}\right]_{\text{cal}}}{\left(\frac{m}{q}\right)_{\text{cal}} \left[\frac{(m/q)}{\Delta\,(m/q)}\right]_{\text{IOI}}} \text{ and } S_\tau = \frac{\left(\frac{m}{q}\right)_{\text{IOI}} \left[\frac{(m/q)}{\Delta\,(m/q)}\right]_{\text{cal},\Delta t_{\text{ta,ref}}=0}}{\left(\frac{m}{q}\right)_{\text{cal}} \left[\frac{(m/q)}{\Delta\,(m/q)}\right]_{\text{IOI},\Delta t_{\text{ta,ref}}=0}} \tag{3.11}$$

Here, $(m/q)_{\text{IOI}}$ and $(m/q)_{\text{cal}}$ are the mass-to-charge ratio of the IOI and the calibrant, respectively, and $((m/q)\,/\Delta\,(m/q))_{\text{IOI}}$ and $((m/q)\,/\Delta\,(m/q))_{\text{cal}}$ are the resolving power for the IOI and the calibrant ion, respectively, as given by Eq. (3.12). For the scaling of the parameters describing the peak tails (τ_i), the peak broadening caused by the turn-around time is set to zero ($\Delta t_{\text{ta,ref}} = 0$). This is done, because the peak tails are due to ion optical aberrations, which do not depend on the turn-around time.

The mass resolving power for all ions that are measured under identical ion-optical conditions as a function of their charge state (q) and their number of isochronous turns (N_{it}) can be calculated by

$$\left[\frac{(m/q)}{\Delta\,(m/q)}\right](q, N_{\text{it}}) = \frac{\frac{t_{\text{tfs,ref}}}{t_{\text{it,ref}}} + N_{\text{it}}}{2\sqrt{\frac{q_{\text{ref}}}{q}\left(\frac{\Delta t_{\text{ta,ref}}}{t_{\text{it,ref}}}\right)^2 + \left(\frac{\Delta t_{\text{tfs,ref}}}{t_{\text{it,ref}}}\right)^2 + \left(\frac{N_{\text{it}}}{2 \cdot R_\infty}\right)^2}}\,. \tag{3.12}$$

Here, the following parameters are determined from offline measurements with reference ions with q_{ref} charge state prior to the experiment itself; $\Delta t_{\text{ta,ref}}$ is the peak broadening (FWHM) caused by the turn-around time (see definition in [Dickel, 2010]), $\Delta t_{\text{tfs,ref}}$ denotes the spread in time-of-flight due to ion-optical aberrations from the injection trap to the detector without reflections in the analyzer, $t_{\text{it,ref}}$ is the time it takes for the reference ions to undergo one isochronous turn and $t_{\text{tfs,ref}}$ is the time-of-flight from the injection trap to the detector without reflections in the analyzer. R_∞ denotes the asymptotic mass resolving power for infinite number of isochronous turns. For more details and the derivation of Eq. (3.12), see [Ayet San Andrés et al., 2019].

When the peak shape parameters are scaled from the model peak to the IOI, their uncertainty is increased following uncertainty propagation (see Eq. (3.14)) and the increased uncertainties of the parameters σ and τ_j are then used for the peak-shape uncertainty determination.

$$\Delta\sigma_{\mathrm{IOI}} = \sqrt{\left(\frac{S_\sigma^2 \cdot \sigma_{\mathrm{cal}} \Delta\sigma_{\mathrm{cal}}}{\sigma_{\mathrm{IOI}}}\right)^2 + \left(\frac{\sigma_{\mathrm{cal}}^2 \cdot S_\sigma \Delta S_\sigma}{\sigma_{\mathrm{IOI}}}\right)^2 + \left(\frac{(m/q)_{\mathrm{IOI}}^2 \cdot \sigma_{\mathrm{TRC}}^{\mathrm{RMS}} \Delta\sigma_{\mathrm{TRC}}^{\mathrm{RMS}}}{\sigma_{\mathrm{IOI}}}\right)^2 + \left(\frac{\sigma_{\mathrm{TRC}}^{\mathrm{stat}} \Delta\sigma_{\mathrm{TRC}}^{\mathrm{stat}}}{\sigma_{\mathrm{IOI}}}\right)^2}$$

$$\Delta\tau_{\mathrm{j,IOI}} = \sqrt{\left(S_\tau \cdot \Delta\tau_{\mathrm{j,cal}}\right)^2 + \left(\tau_{\mathrm{j,cal}} \cdot \Delta S_\tau\right)^2} \tag{3.14}$$

Here, $\Delta\sigma_{\mathrm{cal}}$ and $\Delta\tau_{\mathrm{j,cal}}$ are the uncertainties of the parameters σ and τ_j as determined from the LS-fit of the model peak and ΔS_σ and ΔS_τ are estimated as the difference between the scaling factors using the same and different resolving powers for the model peak and IOI [Ayet San Andrés et al., 2019]. In case of an external TRC, $\Delta\sigma_{\mathrm{TRC}}^{\mathrm{RMS}}$ is the uncertainty of the relative peak broadening, which is estimated as 20% of the $\sigma_{\mathrm{TRC}}^{\mathrm{RMS}}$ value applied when the model and the TRC peaks are the same, for more details see e.g. [Ayet San Andrés, 2018]. In case of an internal TRC, $\Delta\sigma_{\mathrm{TRC}}^{\mathrm{stat}}$ is the uncertainty of the purely mathematical peak broadening due to statistics inside the TRC blocks, when the model and the TRC peaks are the same. This latter uncertainty is estimated in this work via uncertainty propagation from Eq. (3.13) and given by:

$$\Delta\sigma_{\mathrm{TRC}}^{\mathrm{stat}} = \sqrt{\left(0.2 \cdot \sigma_{\mathrm{TRC}}^{\mathrm{stat}}\right)^2 + \left(\frac{\sigma_{\mathrm{TRC}}^{\mathrm{stat}}}{2\sqrt{N_{\mathrm{counts/block}}}}\right)^2} \tag{3.15}$$

Here, the first term is due to the uncertainty of the factor A_{stat}, which is estimated as 20% of the value itself, the second term is due to the statistical uncertainty of the number of events inside one TRC block and the uncertainty of the FWHM of the TRC calibrant peak is neglected.

In order to test the peak broadening due to statistics inside the TRC blocks ($\sigma_{\mathrm{TRC}}^{\mathrm{stat}}$) a dedicated long-term offline measurement was performed. This measurement includes two peaks from the thermal ion source of MR-TOF-MS [Yu et al., 2024b], ^{85}Rb and ^{87}Rb, both with about 80,000 events in total and both ions undergoing only two isochronous turns in the time-of-flight analyzer. At this low turn number, both peaks have a close to Gaussian peak shape and they effectively do not feel any voltage drifts, i.e. their time of flight stays stable throughout the entire measurement. In this data set, the peak of ^{85}Rb was used to perform an internal or continuous TRC while increasing the TRC block size, i.e. increasing the number of events inside the TRC blocks, and the evolution of the σ of the Gaussian-fits of the peaks was checked. As shown in Fig. 3.7, the effect of peak broadening due to statistics inside the TRC blocks is practically negligible, when the average number of ^{85}Rb events inside the TRC blocks is larger than 50, see more details in footnote[11]. On the other hand, with less than 20 events of ^{85}Rb inside the TRC blocks on average, the effect from $\sigma_{\mathrm{TRC}}^{\mathrm{stat}}$ starts to dominate. In the latter case, the width of the IOI peak (shown by the green curve on Fig. 3.7) is increased by more than 5% as compared to width of the TRC calibrant peak after scaling it only by the mass-to-charge ratio to the IOI (shown by the blue curve). With the newly implemented peak broadening due to statistics inside the TRC blocks (shown by the red curve) the value and uncertainty of σ_{IOI} can be more realistically

[11] Looking at Fig. 3.7, one can also notice that there is roughly a 1.5% mismatch in the asymptotic ($\lim_{N_{\mathrm{counts/block}} \to \infty}$) behavior between the green and the red curves. This mismatch is, however, negligible in typical measurement conditions at multiple isochronous turns, where the uncertainty of the FWHM of the peaks is dominated by the uncertainty from the peak tails of the Hyper-EMG peak shape. Notably, the uncertainty bands of the width of the peaks shown on Fig. 3.7 only include the typical uncertainties as calculated by the MSmarple scripts and neglect the uncertainties due to the effect from the binning of the time-of-flight histogram. This latter effect is known and has been investigated, see e.g. Ref. [Valentine & Rana, 1996]. Although this effect is typically negligible for the mass measurements with the MR-TOF-MS obtained at higher number of isochronous turns, in the present offline measurement of ^{85}Rb and ^{87}Rb ions, however, this effect gives a non-negligible uncertainty contribution. Including this latter contribution would already solve the 1.5% mismatch in the asymptotic behavior of the curves in Fig. 3.7.

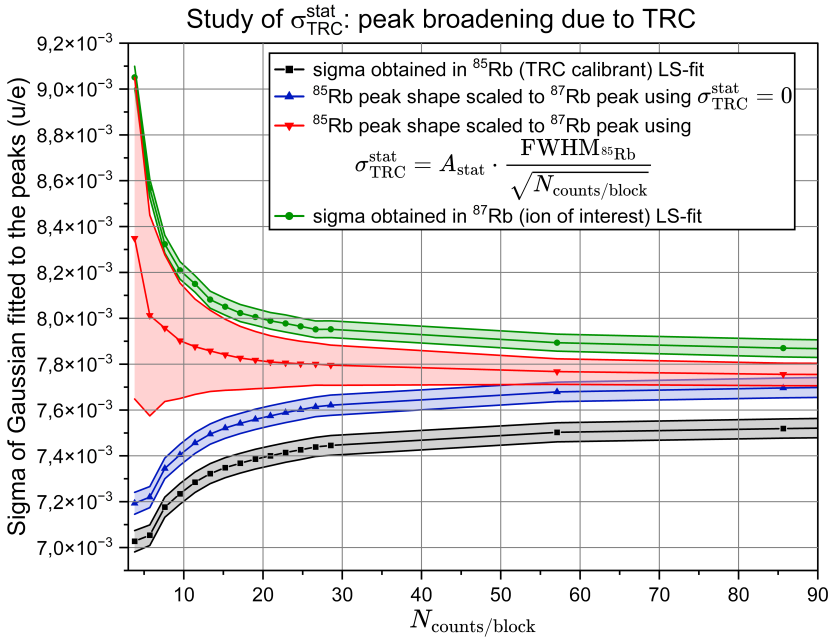

Figure 3.7: Measurement of peak broadening due to the statistics inside the TRC blocks. The measured standard deviation obtained in the LS-fit with a simple Gaussian peak shape, i.e. without including any peak tails, corresponding to the TRC calibrant ions (^{85}Rb) and the ions of interest (^{87}Rb) are represented by the black and the green data points, respectively. The blue and red data points represent the peak width scaled from the TRC calibrant to the IOI using Eq. (3.10) with assuming $\sigma^{stat}_{TRC} = 0$ or deducing it with Eq. (3.13), respectively. Here, the data points and their corresponding uncertainty bands are obtained with step-by-step increasing the TRC block size, i.e. increasing the number of events inside the TRC blocks, and they are connected with lines to better guide the eyes.

estimated, even in case of a small number of events inside the TRC blocks, and used for the fit of the ions of interest with the wMLE method.

Non-perfect ejection and non-perfect injection uncertainties

During one measurement cycle, the voltages of the TOF analyzer mirror electrodes are switched twice in a way that the ions could also feel it; (i) after the injection of the ions into the analyzer, the input mirror electrodes are switched while the ions are performing their first turn in the analyzer and (ii) before their extraction from the analyzer, while the ions are performing their last turn in the analyzer, the output mirror electrodes are switched. After switching, the voltages of the analyzer electrodes need time, a few tenths of μs, to reach their final value. Therefore, the ions with different mass-to-charge ratios, which are spatially separated, might experience different electric fields either during their first turn or during their ejection from the analyzer. These two effects are described by the so-called non-perfect injection (NPI) and non-perfect ejection (NPE) uncertainty components, respectively. While the NPE uncertainty has been measured and discussed already in earlier works, see e.g. [Ayet San Andrés et al., 2019][12], the first studies of the influence of the non-perfect injection on the mass accuracy are reported here.

With the latest upgrades to the high-voltage switches and power supplies of the analyzer electrodes, such as the ones reported in Refs. [Ayet San Andrés, 2018, Beck, 2023], the magnitude

[12] In previous works this uncertainty component has been called as non-ideal ejection or NIE uncertainty. Here, it is renamed in order to avoid its confusion with the non-perfect injection (NPI) uncertainty component.

of the NPE uncertainty component may be a bit different. Therefore, it needs to be measured before or after each experimental runs via a dedicated offline measurement. Here, the time-of-flight of a given reference ion is measured as a function of the opening time of the output mirror and the determined Δt_{NPE} uncertainty component describes the increased standard deviation of the ions' TOF compared to the expected standard deviation of the data from the average TOF uncertainty. The determined TOF uncertainty component, Δt_{NPE}, is then used to calculate the so-called non-perfect ejection (NPE) uncertainty component of the mass-to-charge ratio using Eq. (3.16).

For the mass measurements performed in 2020 at the FRS-IC (see e.g. Chapter 5), the value of $\Delta t_{\mathrm{NPE}} = 0.093$ ns and $\Delta t_{\mathrm{NPE,ringing}} = 0.65$ ns has been determined using a reference ion of $^{12}\mathrm{C}_1{}^{19}\mathrm{F}_3$ (see Fig. 3.8). Here, the $\Delta t_{\mathrm{NPE,ringing}}$ corresponds to the region with small values of TDC TOF (from ~21 μs to ~25 μs), where the standard deviation of the measured TOF of the ions is further increased. This region is the so-called "ringing region", where the ions traveling toward the detector are very close to the output mirror, while it is being opened, hence the ions experience an electrical ringing from the output mirror electrodes. This is reflected in an oscillation in the measured TOF of the ions. In Fig. 3.8, the TDC TOF values of <21 μs and >41.25 μs correspond to ions feeling the switched electrical fields directly and, as a consequence, experiencing a shift in their kinetic energy, which results in a change of their flight time to the detector.

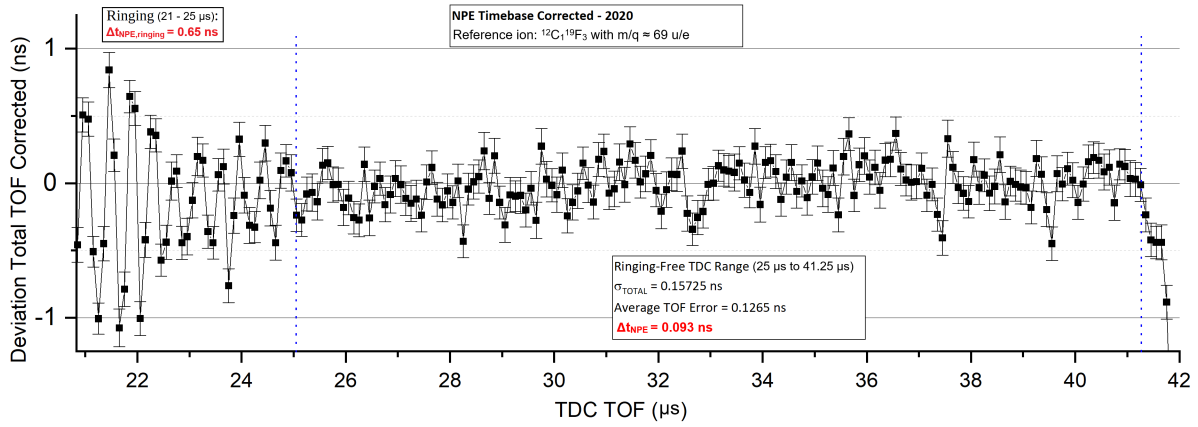

Figure 3.8: Measurement of the non-perfect ejection uncertainty (Δt_{NPE}) relevant for the mass measurements performed in 2020 at the FRS-IC. The measurement was performed with $^{12}\mathrm{C}_1{}^{19}\mathrm{F}_3$ ions after four isochronous turns in the analyzer. Here, the difference between the measured TOF of the ions and the average TOF (calculated between the two blue dashed lines) is first corrected for the inaccuracy due to the trigger system (see Section 2.3) and, afterwards, its dependence is investigated on the opening time of the output mirror electrodes of the analyzer. The value of the TDC TOF, plotted on the abscissa, is obtained by subtracting the opening time of the output mirror from the measured average TOF. As a result of this measurement, a $\Delta t_{\mathrm{NPE,ringing}} = 0.65$ ns and a $\Delta t_{\mathrm{NPE}} = 0.093$ ns are determined for the TDC TOF ranges from 21 μs to 25 μs and from 25 μs to 41.25 μs, respectively.

In order to study the possible influence of the non-perfect injection (NPI) on the mass accuracy, similar dedicated offline measurements were performed after the experimental runs in 2020. Here, the time-of-flight of a given reference ion is measured as a function of the closing time of the input mirror electrodes of the analyzer (see Fig. 3.9). Surprisingly, the measurements showed a continuous growth starting from a deviation of the average TOF of the ions of about -1 ns increasing up to 2 ns with changing the closing time of the input mirror. Since the slope of this increase is independent on the number of turns (see Fig. 3.9a), it indicates that this effect occurs

during the first turn of the ions. The reason for this slow, incremental increase in the ions' TOF could so far not be understood, neither could it be reproduced in ion optical simulations. Nevertheless, one can investigate the influence of this phenomenon on the mass accuracy. Note that the effect due to non-perfect injection is negligible for isobars, because they are not yet spatially separated during their first turn in the analyzer. On the other hand, with performing broadband mass measurements more and more frequently, the relative mass-to-charge ratio difference between the precision calibrant and the ions of interest ($|(m/q)_{\mathrm{cal}} - (m/q)_{\mathrm{IOI}}| / \min((m/q)_{\mathrm{cal/IOI}})$) may increase up to about 40%, which is only limited due to the mass-selective transport through the trap system of the MR-TOF-MS. It is, therefore, interesting to study how the uncertainty due to the non-perfect injection changes with an increasing difference between the mass-to-charge ratio of the calibrants and IOI.

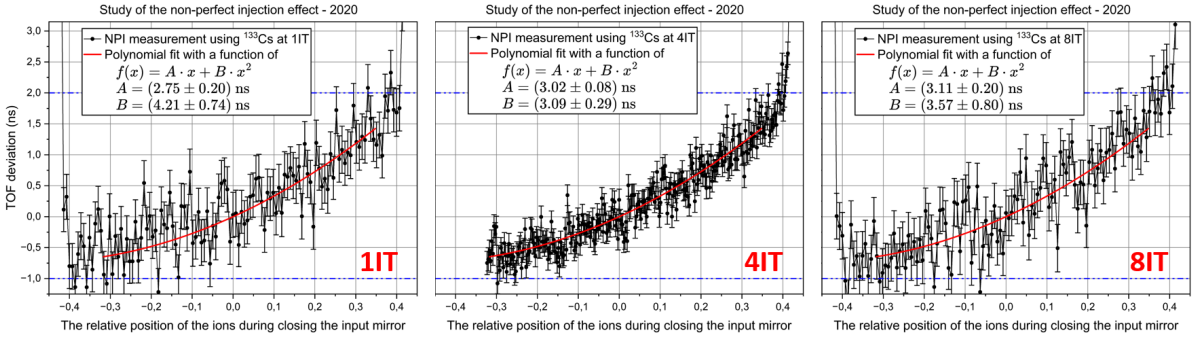

(a)

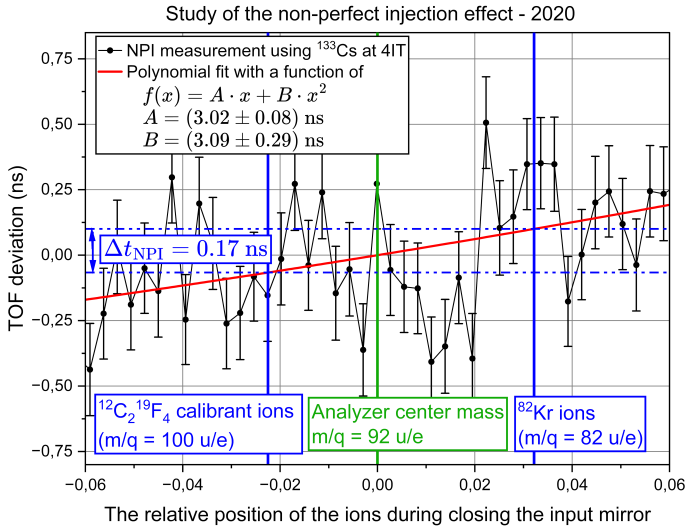

(b)

Figure 3.9: Measurement of the non-perfect injection uncertainty (Δt_{NPI}) relevant for the mass measurements performed in 2020 at the FRS-IC. The measurement was performed with ^{133}Cs ions alternating between the changed and the fixed opening times of the output mirror. Then the difference between the measured TOF of the ions, when using the changed or the fixed opening times, is investigated as a function of the changed opening time of the output mirror electrodes of the analyzer. The opening time of the output mirror is then converted into values of the IP@IS parameter, which is plotted on the x axis of the figures (see text for more details). (a) The top figures show a comparison of the NPI measurement results for one, four and eight isochronous turns in the analyzer. (b) The bottom figure illustrates the procedure of determining the value of Δt_{NPI} in an example of a broadband mass measurement, where the precision calibration was performed from $^{12}C_2{}^{19}F_4$ ions and applied to ^{82}Kr ions as ions of interest for a proof of principle.

In order to quantify the spatial separation of the calibrants and ions of interest with different mass-to-charge ratios during their first turn, it is helpful to define a parameter called as ion position at injection switching, or, in short, IP@IS. This IP@IS parameter can take values between -0.5 and $+0.5$ and reflects the fraction of the ions' path in the TOF analyzer relative to the output mirror, where the ions are situated spatially in the TOF analyzer during closing the input mirror. Since the definition and usage of the IP@IS parameter is very similar to the IP@ES parameter defined in Section 3.6, therefore more details are omitted from here.

The measurement of the NPI effect performed at four isochronous turns (IT) was measured with similarly good statistics (more than 1000 events per data point) and the same step size for the incremental change of the closing time of the input mirror (0.1 μs) as the NPE measurement from Fig. 3.8. Therefore, this measurement at 4IT is used for the further analysis to estimate the magnitude of the uncertainty due to the non-perfect injection. In the first step, the data was fitted with a second order polynomial function with a fixed intercept of zero, i.e. a fixed TOF deviation of 0 ns at IP@IS = 0 (Fig. 3.9). Subtracting the fit function from the data and investigating the remaining scatter of the data, the increased standard deviation of the ions' corrected TOF compared to the expected standard deviation from the average TOF uncertainty is consistent with the value of Δt_{NPE} deduced above. Consequently, it is enough to investigate the influence from the slope of the fit function of the NPI measurement on the mass accuracy and the scatter of the data can be neglected from this investigation. In a typical measurement, when the center mass of the analyzer is within the MRS window, the IP@IS parameter takes small values scattered around zero for the different ions measured in the spectrum. This is illustrated in Fig. 3.9b for the example of data set III measured during the S474 experiment at the FRS-IC (see Section 5.2). From the figure one can see that if the precision calibration is performed using $^{12}C_2{}^{19}F_4$ ions and the mass-to-charge ratio of the ions of interest is about 18 u/e different, just like for ^{82}Kr, the resulting value of Δt_{NPI} obtained from the polynomial fit is only 0.17 ns. This procedure to estimate the value of Δt_{NPI} can be generalized for mass measurements performed with any measurement settings and any mass-to-charge differences between calibrant ions and ions of interest. The determined TOF uncertainty component, Δt_{NPI}, is then used to calculate the so-called non-perfect injection (NPI) uncertainty component of the mass-to-charge ratio using the following equation:

$$\Delta m_{\mathrm{NPE/NPI}} = \frac{2\Delta t_{\mathrm{NPE/NPI}}}{t_{\mathrm{total,IOI}}} \cdot \sqrt{\frac{\left(\frac{m}{q}\right)_{\mathrm{IOI}}}{\left(\frac{m}{q}\right)_{\mathrm{ref}}} \cdot \left(\frac{m}{q}\right)_{\mathrm{IOI}}} \,. \tag{3.16}$$

In the final step, it was investigated that at which conditions the determined values of $\Delta m_{\mathrm{NPE/NPI}}$ become significant compared to the statistical uncertainty obtained from the mass measurements[13]. This study showed that for all mass measurements performed with the FRS Ion Catcher in 2020 within FAIR Phase-0, both the NPE and NPI uncertainties are negligible compared to the statistical uncertainty as long as the measured ions are not in the ringing region of the analyzer during ejection.

[13]For this study, the best ion optical tuning with an asymptotic limit for the resolving power of $R_\infty = 1,450,000$ achieved so far at the FRS-IC was assumed from Ref. [Beck, 2023] and three parameters were varied; the time-of-flight of the ions in the MR-TOF-MS was varied between 1 ms and 30 ms, the mass-to-charge ratio of the ions was varied between 50 u/e and 250 u/e and the relative mass-to-charge ratio difference between the calibrant ions and the ions of interest was varied between 0% and 40%. This study showed that with more than about 700, 1600 or 4700 events measured for the ions of interest and a 40%, 20% or 0% relative difference between the mass-to-charge ratio of the calibrant ions and the IOI, respectively, the quadratic sum of the uncertainties from the NPI and NPE effects becomes similar to the statistical uncertainty. In the first order, the number of events necessary to fulfill this condition is independent from the absolute values of the mass-to-charge ratio and the TOF of the ions. It is, however, not typical to reach so large statistics for the ions of interest measured at the FRS-IC.

Uncertainty due to mass range selector (MRS)

The shift of the ions' time-of-flight and the corresponding mass uncertainty component due the operation of the mass range selector (MRS) was carefully studied and quantified in previous works, see e.g. [Ayet San Andrés et al., 2019]. Since then, however, the electronics responsible for switching the voltages of the MRS electrodes were upgraded to allow steering the beam in the center of the analyzer and achieving high mass resolving powers of about 1 million at the FRS-IC [Beck, 2023]. Therefore, the shift of the ions' TOF and the corresponding uncertainty due to the operation of the MRS has to be re-measured.

For mass measurements within FAIR Phase-0 (after 2020), the TOF shift and the corresponding uncertainty has been measured repeatedly using ^{133}Cs ions under conditions, where the magnitude of the shift due to MRS operation was maximized. It has been found to be consistent with zero within experimental uncertainties for all measurements performed so far within FAIR Phase-0 with the FRS-IC, as long as the MRS is switched on and off on the longer time scale than minutes. During the S530 experiment, however, the MRS was switched on and off on the time scale of seconds, where a non-zero TOF shift due to MRS operation was observed due to instabilities of the power supplies responsible for supplying the voltage of the MRS electrodes [Tortorelli, 2024]. Ultimately, a change between the measurement of the calibrant ions and the ions of interest on the time scale of below a second is desired at the FRS Ion Catcher. Therefore, the TOF shift due to MRS operation needs to be re-checked also in the future before or after each experimental run.

Cut-bias correction and corresponding uncertainty

The cases, when multiple (more than two) overlapping peaks are present in the measurement are analyzed following the procedure explained in Section 3.5. The first step of this procedure is to restrict the mass-to-charge range used to perform the wMLE fits; i.e. in the first step only fit a single or a double peak instead of directly fitting the multiple overlapping peaks. In this process, the measured data corresponding to the peaks needs to be restricted at a point, where the weighting of the wMLE fit is still above zero ($ln(f(x_i)) > 0$), while the shape of the Hyper-EMG function used for the fit remains unchanged, i.e. the relevant mass-to-charge range of the fit function is not restricted to avoid directly biasing the results from the fit with the applied cuts to the data. On the other hand, in this case, the structure of the fit function and the to-be-fitted data, which was restricted on a given mass-to-charge range, are not exactly the same. As a consequence, the peak centroid deduced from the wMLE fit slightly moves towards the other side of the peak, where the data is not restricted. The magnitude of this movement reflects the stringency of the cuts applied to the data. In order to cope with this effect, an empirical correction was developed and applied to the mass-to-charge values obtained from fits, where the peak tails are restricted. This is the so-called cut-bias correction.

This correction is based on the same Monte Carlo simulations as the ones used to determine the statistical uncertainty, for more details, see Section 3.3. The synthetic data generated by the simulations are restricted to the same mass-to-charge range as used for restricting the measured data. This restricted simulated data are then fitted with the wMLE method applying the same peak shape as used for fitting the measured data. Therefore, just like in case of the measured data, also for the simulated data, the peak centroid determined from the fit slightly moves away from the correct mass-to-charge ratio value. In the next step, the difference between the average of the mass-to-charge ratio values obtained from the fits of the many (typically 100-to-1000) simulations and the centroids of the simulated peaks is determined. This difference is then used to correct the slight movement of the mass-to-charge ratio value determined in the wMLE fit of the measured data due to cutting the peak tails. The uncertainty from this correction is estimated to be 25% of the difference between the mass-to-charge ratio obtained with and

without correction.

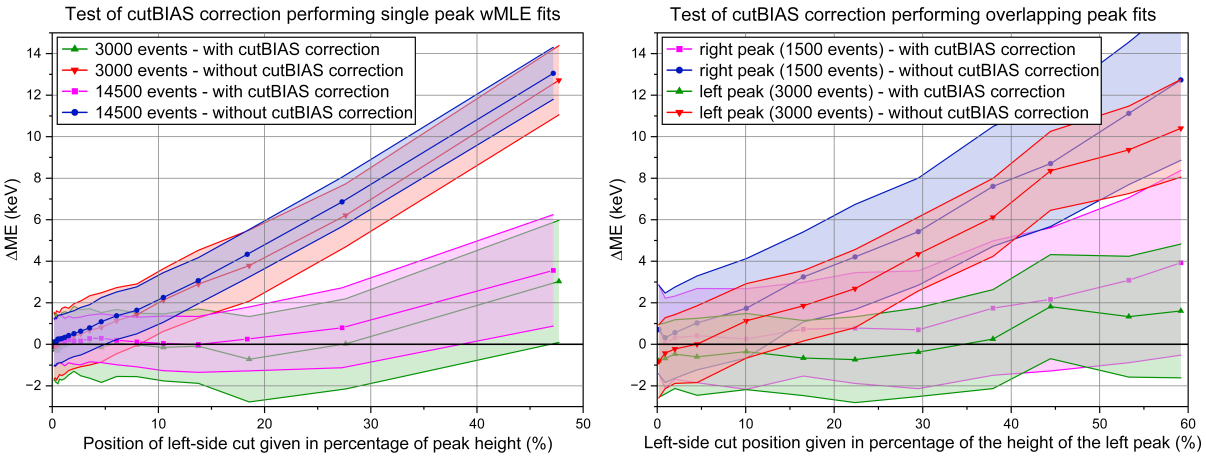

(a) (b)

Figure 3.10: Results of simulations for the cut-bias correction tested with synthetic data containing (a) a fully isolated peak with either 3000 or 14500 events or (b) two well-separated, but slightly overlapping peaks with 3000 and 1500 events for the peaks on the left and right side, respectively, and with a distance between the two peaks of 326 keV (a clear minimum exists between the two peaks at about 20% of the height of the smaller peak). The data corresponding to each peaks was generated with the same Hyper-EMG peak shape incorporating one exponential tail on each sides and with a FWHM of 116 keV. The figures show the dependence of the value of ΔME determined with or without correction on the stringency of the cut applied on the left-side tail of the given peak. (In case of the two slightly overlapping peaks, only the mass-to-charge range of the peak on the left side was restricted.). Here, ΔME marks the difference between the mass excess value, which is determined by the fits performed either with or without cut-bias correction, and the "expected centroid" of the fitted peak.

The validity of the newly developed correction was tested first using synthetic data, then it was applied to the neutron-rich indium mass measurements performed at TITAN, see more details in Chapter 4. Fig. 3.10 shows a few exemplary results of the tests performed with synthetic data of various number of events, but identical peak shapes with a FWHM of 116 keV. The magnitude of the necessary correction depends on the stringency of the cuts applied to the data; in case of the examples shown in the figures, even at very stringent cuts placed at about 50% of the peak height, the peak centroid is only shifted by about 10% of the FWHM. Nevertheless, for the IOI or calibrant ions measured with a higher statistics and, thus, a smaller statistical uncertainty, this may yield a non-negligible shift of the mass-to-charge value, which is tackled by the developed cut-bias correction. As shown by the figures, after performing this correction, the dependence of the deduced peak centroid on the stringency of the applied cuts is significantly reduced. The plot on the right side (Fig. 3.10b) presents the results from the cut-bias correction for the synthetic data of two well-separated, but slightly overlapping peaks (a clear minimum exists between the two peaks). Here, one can make a secondary observation besides the notice that the developed correction is also valid in this case. At the first glance, it may be surprising that although only the mass-to-charge range of the left-side peak was restricted, the centroids deduced from the fits of both well-separated peaks are shifted in a similar way, when no cut-bias correction is applied to the data. This is due to the fact that in case of fitting overlapping peaks, the distance between the two peaks is corrected earlier in an additional set of Monte Carlo simulations[14].

[14]See next page footnote.

Uncertainty components of the precision calibrant peak

Based on uncertainty propagation from Eq. (3.3) and using the approximation that $(m/q)_{\mathrm{cal,wMLE,corrected}} \Big/ (m/q)_{\mathrm{cal,lit}} \simeq 1$, the uncertainty due to the precision calibrant can be written as

$$\Delta m_{\mathrm{cal}} = \left(\frac{m}{q}\right)_{\mathrm{IOI}} \cdot \sqrt{\left(\frac{\Delta\left(\frac{m}{q}\right)_{\mathrm{cal,lit}}}{\left(\frac{m}{q}\right)_{\mathrm{cal,lit}}}\right)^2 + \left(\frac{\Delta\left(\frac{m}{q}\right)_{\mathrm{cal,wMLE,corrected}}}{\left(\frac{m}{q}\right)_{\mathrm{cal,wMLE,corrected}}}\right)^2} \tag{3.17}$$

where $\Delta(m/q)_{\mathrm{cal,lit}}$ is the literature uncertainty for the mass-to-charge ratio of the calibrant and $\Delta(m/q)_{\mathrm{cal,wMLE,corrected}}$ is calculated as the quadratic sum of the following uncertainty components determined in the wMLE fit of the precision calibrant:

- $\Delta m_{\mathrm{cal,stat\&cont}}$: the statistical and contamination uncertainty.
- $\Delta m_{\mathrm{cal,NPE}}$: the non-perfect ejection uncertainty.
- $\Delta m_{\mathrm{cal,peakshape}}$: In case a separate peak is used to determine the peak shape and to perform the precision calibration, the peak-shape uncertainty of the precision calibrant peak is mathematically non-zero, needs to be considered and is added.
- $\Delta m_{\mathrm{cal,cut-bias}}$: In case the mass-to-charge range for the wMLE fit of the precision calibrant is restricted, the corresponding uncertainty component due to the cut-bias correction is added.
- $\Delta m_{\mathrm{cal,bias/fix-dist.}}$: In case the precision calibration is performed from a free- or fixed-distance fit of overlapping peaks (see Section 3.5), the corresponding uncertainty component is added.

Uncertainty components for the excitation energy of isomeric states

The uncertainty of mass-to-charge differences of close-lying peaks, e.g., excitation energy of isomers, partially cancel [Ayet San Andrés et al., 2019]. In this case, the remaining uncertainties are the statistical and contamination uncertainty and, if applicable, the uncertainty due to known unresolved peaks, the peak-shape uncertainty, the uncertainty due to resolved overlapping peaks, the uncertainty due to restricting the peak tails and the uncertainties due to the space charge effects and the dead time of the data acquisition system[15]. The latter two uncertainty components were negligible for all mass measurements reported here.

[14] In case of fitting overlapping peaks with a free distance, where the mass-to-charge range of the fits needs to be restricted, the Monte Carlo simulations are performed in two steps. In the first step, an iterative bias correction is performed [Ebert, 2016, Ayet San Andrés, 2018], which already removes the dependence of the distance between the two peaks on the stringency of the cuts applied to the data. Afterwards, using the value of the determined peak distance from the previous step, a second set of simulations are performed to determine the necessary cut-bias correction for the peak centroids, where the distance between the two peaks is used as a fixed parameter for the wMLE fits.

[15] For the uncertainty of the excitation energy (E_x) of higher-lying isomers, a reduced non-perfect ejection (NPE) uncertainty contribution can also be considered. In case of the mass measurements of neutron-rich indium isotopes performed at TITAN (see Chapter 4), the highest-lying isomer state observed in the measurements, the $(21/2^+)$ state of ^{131}In, was separated by about 0.13 μs of TOF from the ground state of ^{131}In. In order to estimate a reduced contribution from the NPE uncertainty for the observed high-lying isomers in this measurement campaign, a dedicated offline measurement with ^{133}Cs reference ions, similar to the one shown in Fig. 3.8, was performed prior to the experiment at TITAN. In this measurement, the opening time of the output mirror was varied in 0.1 μs steps, which roughly corresponds to the maximum TOF difference between the observed indium ground states and isomers, and the TOF difference between the adjacent points was checked. The increased standard deviation of this TOF difference compared to its expected standard deviation resulted in the value of $\Delta t_{\mathrm{NPE},E_x} = 0.18$ ns. This yielded a ∼5-6 keV NPE uncertainty component for the excitation energy of the high-lying isomeric states of indium isotopes observed in this experiment.

3.4 Final mass values from individual measurements

The final mass values and uncertainties are determined via averaging with the weighted mean for the nuclides, which are measured in multiple data sets. In this process, the mass uncertainties deduced from the individual measurements are divided into two components: an independent one, calculated via the variance of the weighted mean, and a dependent one, calculated via the weighted mean [Ayet San Andrés et al., 2019]. The concept of averaging excitation energies and uncertainties of isomeric states, which are measured in multiple data sets, is the same as the concept of averaging mass values and uncertainties.

In case of averaging N different measurements, the weighted mean for the final mass value ($\overline{m}$) and the corresponding mass uncertainty ($\sigma_{\mathrm{total},\overline{\mathrm{m}}}$) are given by:

$$\overline{m} = \frac{\sum_{i=1}^{N} \frac{m_i}{\sigma^2_{\mathrm{total,i}}}}{\sum_{i=1}^{N} \frac{1}{\sigma^2_{\mathrm{total,i}}}} \text{ and } \sigma^2_{\mathrm{total},\overline{\mathrm{m}}} = \frac{\sum_{i=1}^{N} \frac{\sigma^2_{\mathrm{indep,i}}}{\sigma^4_{\mathrm{total,i}}} + \left(\sum_{i=1}^{N} \frac{\sigma_{\mathrm{dep,i}}}{\sigma^2_{\mathrm{total,i}}}\right)^2}{\left(\sum_{i=1}^{N} \frac{1}{\sigma^2_{\mathrm{total,i}}}\right)^2} \tag{3.18}$$

Here, $\sigma_{\mathrm{dep,i}}$ and $\sigma_{\mathrm{indep,i}}$ mark the dependent and the independent uncertainty components of the individual measurements, the total mass uncertainty of which are given by $\sigma_{\mathrm{total,i}} = \sqrt{\sigma^2_{\mathrm{indep,i}} + \sigma^2_{\mathrm{dep,i}}}$.

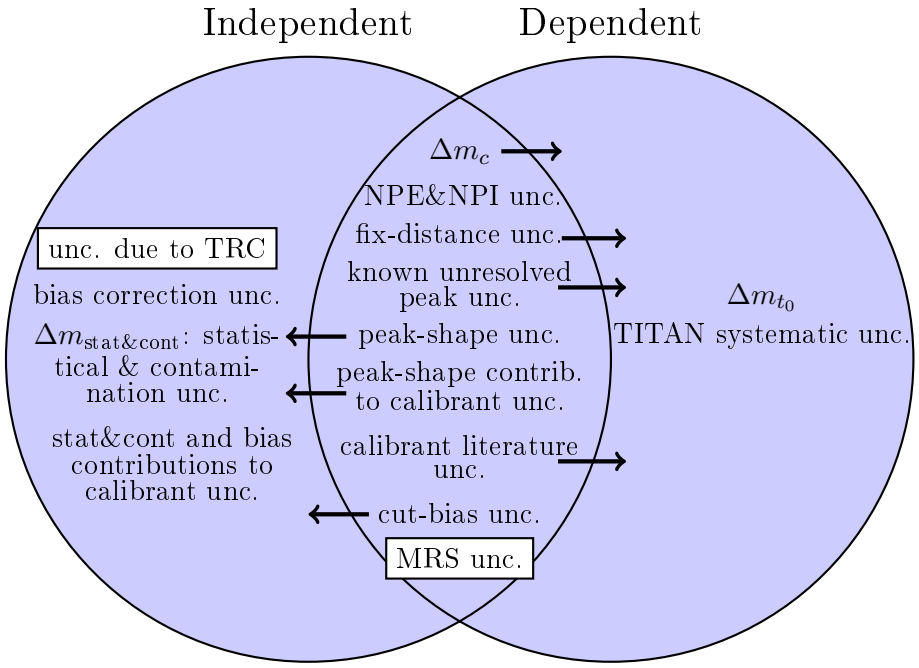

Figure 3.11: Venn-diagram illustrating the division of the different uncertainty contributions into dependent and independent contributions in case of the mass measurements reported here (see Chapters 4 and 5). The phrase "uncertainty" is abbreviated as "unc." in the figure. The uncertainty components that were mathematically zero in all measurements reported here are highlighted with a white background.

The Venn-diagram shown in Fig. 3.11 illustrates the division of the individual uncertainty components into dependent and independent uncertainties in case of the mass measurements reported here (see Chapters 4 and 5). There are certain uncertainty components, such as the statistical and contamination uncertainty of the calibrant ions and the ions of interest, which are

always treated as independent uncertainties, when averaging the results of multiple data sets. Similarly, there are also uncertainty components, such as the systematic uncertainty component in case of the mass measurements performed at TITAN, which are always treated as dependent uncertainties, when averaging the results of multiple data sets. And there are also uncertainty components, which are placed in the intersection of the Venn-diagram and, in principle, can be treated either as dependent or independent uncertainty components depending on whether their corresponding measurement conditions are the same or not. In this latter case, the arrows, shown in Fig. 3.11, indicate whether a given uncertainty component was treated as a dependent or independent uncertainty component during the analysis of the mass measurements reported here. For example, in case of the mass measurements reported in Chapter 5, the mass uncertainty contribution due to the uncertainty of the calibration parameter c, was used as a dependent uncertainty component for the weighted averaging of the three data sets (I, II and III). This is because, in these measurements, the multi-turn calibration was obtained from the data set III and it was applied to the other two data sets, where the ions of interests and calibrants underwent similar number of turns.

3.5 Special cases of overlapping peaks

The data analysis procedure has been proven to yield accurate mass values even in the case of overlapping mass lines [Ayet San Andrés et al., 2019, Hornung et al., 2020]. There can be, however, certain very challenging or special cases of overlapping peaks, which either cannot be treated by the previously-established methods discussed in [Ebert, 2016, Ayet San Andrés, 2018] or it is advantageous to treat them a bit differently (it leads to an increased accuracy for the deduced mass values).

For an easier naming convention, the previously-established methods of fitting overlapping peaks will be called as "free-distance" fits. Here, the distance between the two peaks is treated as a free parameter and is deduced as a result of the fit. This is, however, at the cost of the necessity to perform Monte Carlo simulations to correct the distance between the two peaks. This procedure is the so-called bias correction and it necessarily involves the inclusion of a corresponding uncertainty component, which decreases the overall mass accuracy. For treating the cases, where the distance between the two peaks is known with a high accuracy from literature, e.g. when fitting two long-lived states of the same nucleus, where the difference between the excitation energies of the two states has been determined through high-precision spectroscopy studies earlier, the so-called "fixed-distance" fits were developed. There is an additional consequence of the necessity to perform the bias correction, when performing free-distance fits: this correction can only be performed, if not more than two peaks are overlapping. In mass measurements with the FRS Ion Catcher it is relatively uncommon to have close-lying peaks, where more than two TOF peaks overlap with each other. At TITAN, however, multiple overlapping peaks are often present in the measurements due to the isobaric contamination typical for ISOL facilities. Additionally, multiple overlapping peaks can also be present in mass measurements with the MR-TOF-MS, where more than two long-lived ($T_{1/2} \gtrsim 1$ ms) states of the same nucleus are observed. In this work, attempts were made to enable fitting multiple overlapping peaks within the data analysis framework, although an ultimate solution is still a task for the future.

Fixed-distance fits

The first step of performing a fixed-distance fit is to determine the ratio of the areas of the two peaks and the mass-to-charge value of the first peak via a wMLE fit with a fixed peak shape determined from the model peak, while keeping also the distance between the two peaks fixed. Afterwards, the same fitting method is used to determine the peak-shape, statistical and contam-

ination uncertainty components of the mass-to-charge value of the first peak (see Section 3.3). This procedure results that the statistical and contamination uncertainty component of the determined mass-to-charge value is essentially defined by the total number of events inside the two peaks. Ultimately, through eliminating one degree of freedom from the fits of overlapping peaks, the distance between the two peaks, this leads to a more accurate mass-to-charge value determined for the first peak.

The final step of the fixed-distance fits is to estimate the uncertainty component of the mass-to-charge value of the first peak due to the uncertainty of the distance between the two peaks using the following equation:

$$\Delta m_{\text{peak1,fix-dist}} = \Delta E_x \cdot (R_{\text{peak2}} + \Delta R_{\text{peak2}}) \text{ , where } R_{\text{peak2}} = \frac{A_{\text{peak2}}}{A_{\text{peak1}} + A_{\text{peak2}}} \tag{3.19}$$

Here, $A_{\text{peak1/2}}$ marks the peak areas of the first and second peaks, respectively, and ΔE_x is the uncertainty of the distance between the two peaks. In a typical usage case of the fixed-distance fits, when fitting the ground and isomer state of the same nucleus, the ΔE_x is the uncertainty of the excitation energy of a given isomer state determined from previous spectroscopy studies.

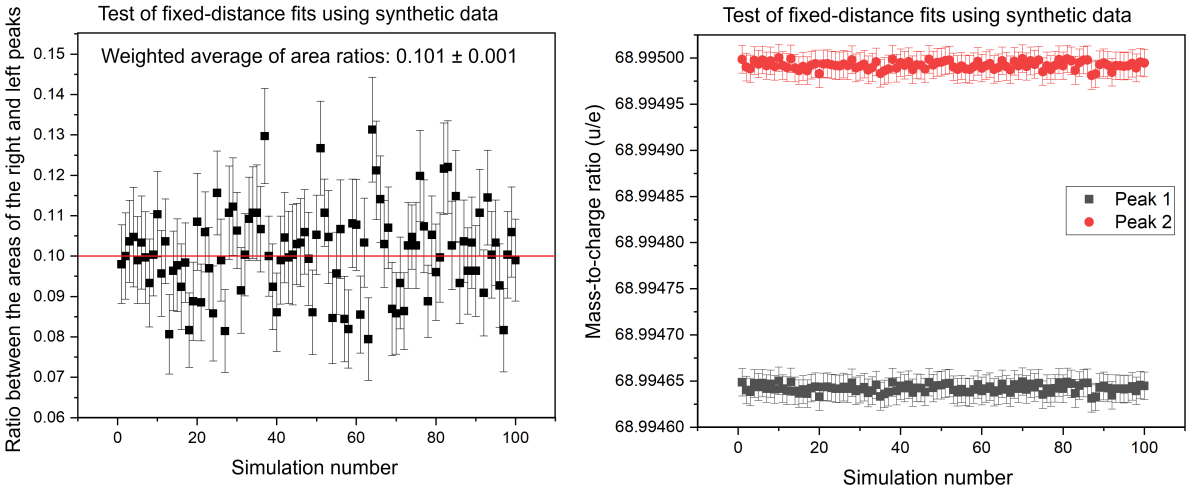

(a) (b)

Figure 3.12: Values of right-to-left peak areal ratios (a) and mass-to-charge ratios (b) obtained from the fixed-distance fits of 100 sets of synthetic data of overlapping peaks with 300 and 30 events for the peaks on the left and right side, respectively, and with a peak distance of 350 μu (the small right peak is situated in the right tail of the left peak). The data corresponding to both peaks was generated with the same Hyper-EMG peak shape incorporating one exponential tail on each sides and with a FWHM of 125 μu. The uncertainties of the determined mass-to-charge ratio values include only the uncertainties due to the overall statistics in the two peaks and the peak-shape uncertainties.

For checking the validity of the developed fixed-distance fits the same method was used as the one used in [Ayet San Andrés, 2018] for the tests of the free-distance fits. Fig. 3.12 shows the results of the fixed-distance fits performed on synthetic data of overlapping peaks with a right-to-left (or in other words second-to-first) peak area ratio of 10%. This test showed that both the expected mass-to-charge and areal ratio values can be reproduced by the fixed-distance method. Here, since the mass-to-charge value determined for the first peak essentially defines the mass-to-charge value of the second peak as well, both values have the same uncertainties even though the second peak has significantly less number of events than the first peak.

After completing the initial tests with synthetic data, the developed fixed-distance fits were used to fit the simultaneous mass measurements of different ground and isomer states with a well-known excitation energy measured via spectroscopy studies prior to the mass measurements, see e.g. [Mollaebrahimi et al., 2023b, Amanbayev, 2023, Fowler-Davis, 2025]. In case of fitting ^{97m,g}Rh reported in [Mollaebrahimi et al., 2023b], an additional advantage of the fixed-distance fits compared to the free-distance fits was demonstrated besides increasing the overall mass accuracy of the determined ground state mass value. Due to the extreme isomer-to-ground state ratio, the two states of ^{97m,g}Rh could only be resolved using the newly developed fixed-distance fits, while the free-distance fits failed to converge in this case.

Dealing with multiple (more than 2) overlapping peaks

The mass measurements of neutron-rich indium isotopes performed at TITAN (see Chapter 4) pose considerable challenges for the MR-TOF-MS data analysis procedure, since the measured ions of interest have several isomer states with various abundance ratios and excitation energies resulting in multiple overlapping peaks covering a large dynamic range.

In all cases of neutron-rich indium mass measurements, where more than 2 states of a given nucleus were observed, the low-lying isomer and the ground state had a similar abundance and they were strongly overlapping, often without a clear minimum between the two peaks. On the other hand, the high-lying isomer(s) were always measured with a significantly (typically by an order of magnitude) smaller number of events compared to the ground state and the low-lying isomer. Additionally, the high-lying isomer(s) were better separated from the first two peaks corresponding to the ground state and the low-lying isomer, i.e. there was a clear minimum between the first two peaks and the third (and sometimes fourth) peak (see e.g. Fig. 4.2). Since this minimum was in all cases below 5% of the peak height of the first two peaks, therefore the mass-to-charge range can be safely restricted to only fit these two peaks in the first step. Here, the fits of the ground and low-lying isomeric states were performed using the well-established fits to treat exactly two overlapping peaks. After determining mass-to-charge ratio and the isomer-to-ground state ratio corresponding to the ground and low-lying isomer states, the high-lying isomer state(s) were analyzed using so-called 2(fixed)+1(free) peak fitting method, which was developed in this work. Here, the mass-to-charge ratios and the isomer-to-ground state ratios of the ground and low-lying isomer states, obtained in the previous step, were used as fixed parameters and all observed states of indium isotopes were fitted together to obtain the mass-to-charge ratio and isomer-to-ground state ratio corresponding to the high-lying isomer state(s). For the results of this procedure, see Chapter 4.

The here developed 2(fixed)+1(free) peak fits, however, are tailored for the examples from the mass measurements of neutron-rich indium isotopes and might not be applicable in all cases, when multiple overlapping TOF peaks are measured with the MR-TOF-MS[16]. Therefore, a more general solution remains a task for the future.

3.6 Consistency checks

The measured ion species (molecules or atomic ions), which have a well-known mass in literature, can be used both for the multi-turn and precision calibration of the data and to check whether the overall experimental uncertainty is appropriately estimated and the mass measurements and data analysis yield accurate mass values. Since the mass measurement and data analysis procedures are relatively complex, there is a need to use or even develop standardized procedures to check the consistency of the deduced mass values and hence remove systematic errors from the procedure.

[16] Note that in case of the mass measurement of ^{211m,g}Po, where the isomeric state of ^{211m}Po was contaminated with ^{211m}Pb events, a differently tailored version of the triple peak fits was used, for details see [Hornung, 2018].

These consistency checks are done by a standalone R script developed within this work, which enables to analyze the final mass and uncertainty values stored in a standardized excel output file, the so-called compilation file, and to combine/compare the results of several different data sets or analysis.

In the first step, one can quantify the scatter of two parameters; the deviations between the measured and literature mass values (ΔME) and the same deviations normalized by their corresponding uncertainties (ΔME_σ). These two values are calculated with the following formulas:

$$\Delta\text{ME} = \text{ME}_{\text{TITAN/FRS-IC}} - \text{ME}_{\text{lit}} \text{ and } \Delta\text{ME}_\sigma = \frac{\Delta\text{ME}}{\sigma\left(\Delta\text{ME}\right)} \ , \tag{3.20}$$

where $\text{ME}_{\text{TITAN/FRS-IC}}$ and ME_{lit} mark the measured and literature mass excesses, respectively, $\sigma\left(\text{ME}_{\text{TITAN/FRS-IC}}\right)$ and $\sigma\left(\text{ME}_{\text{lit}}\right)$ denoting their corresponding uncertainties and $\sigma\left(\Delta\text{ME}\right) = \sqrt{\left(\sigma\left(\text{ME}_{\text{TITAN/FRS-IC}}\right)\right)^2 + \left(\sigma\left(\text{ME}_{\text{lit}}\right)\right)^2}$. There are various ways to quantify the scatter of ΔME, ΔME_σ values, a few of which are illustrated in Fig. 3.13. Firstly, one can calculate the standard deviation of ΔME_σ, which should be ideally around 1. A significantly smaller or larger $\text{sd}\left(\Delta\text{ME}_\sigma\right)$ value than 1 indicates that the experimental uncertainties are either over- or underestimated, respectively. Secondly, one can also prepare a histogram of the ΔME_σ values and fit it with a Gaussian, which should ideally have a mean value that is consistent with zero within uncertainties and a sigma of about 1. Thirdly, the compilation analysis script also enables to deduce the weighted average of the different ΔME values using the formulas given in Section 3.4, which should be consistent with zero within uncertainties. Finally, the Birge ratio [Birge, 1932, Kacker et al., 2010] of the ΔME values can be also determined, which should be ideally around 1. While the Birge test checks whether the ΔME_i values scatter around unknown, but equal expected values with known variances of $\left(\sigma\left(\Delta\text{ME}\right)_i\right)^2$, the weighted mean ensures that the measured masses are not systematically shifted from the literature masses. One can see from the example shown in Fig. 3.13, that the deduced Birge ratio is only about 0.5 for the different neutron-rich indium nuclides and other ion species at TITAN, which have a well-known literature mass. This is likely due to an overestimation of the TITAN systematic uncertainty for this data set (see Chapter 4 for more details).

Secondly, the compilation analysis script also enables to quickly compare the measured masses between several different data sets or analysis and deduce their weighted averages. In the example shown in Fig. 3.13, certain ions of interest are measured in two different data sets, which are illustrated with different colors on the figure. In case there is a need for a further quantitative comparison of two different data sets or analysis, one can determine the differences of the mass values of the given ions of interest determined from the two data sets or two analysis and define ΔME and ΔME_σ accordingly (as the differences or differences normalized by uncertainties between the two data sets or analysis). Afterwards the scatter of these differences or deviations can be checked the very same way as introduced in the previous paragraph. Here, in case of comparing two different analysis, it is expected that the standard deviation of ΔME_σ and the Birge ratio of ΔME is significantly smaller than 1, because the obtained mass and uncertainty values in the two different analysis are not independent. In this latter check, one can even include the more exotic nuclides, which have not been measured (directly) prior to our mass measurements. As a practical example, this check ensures that the newly measured mass values of a given exotic nuclide is the same even if the IOI undergo different turn numbers at the analyzer of the MR-TOF-MS ensuring their correct identification and mass determination.

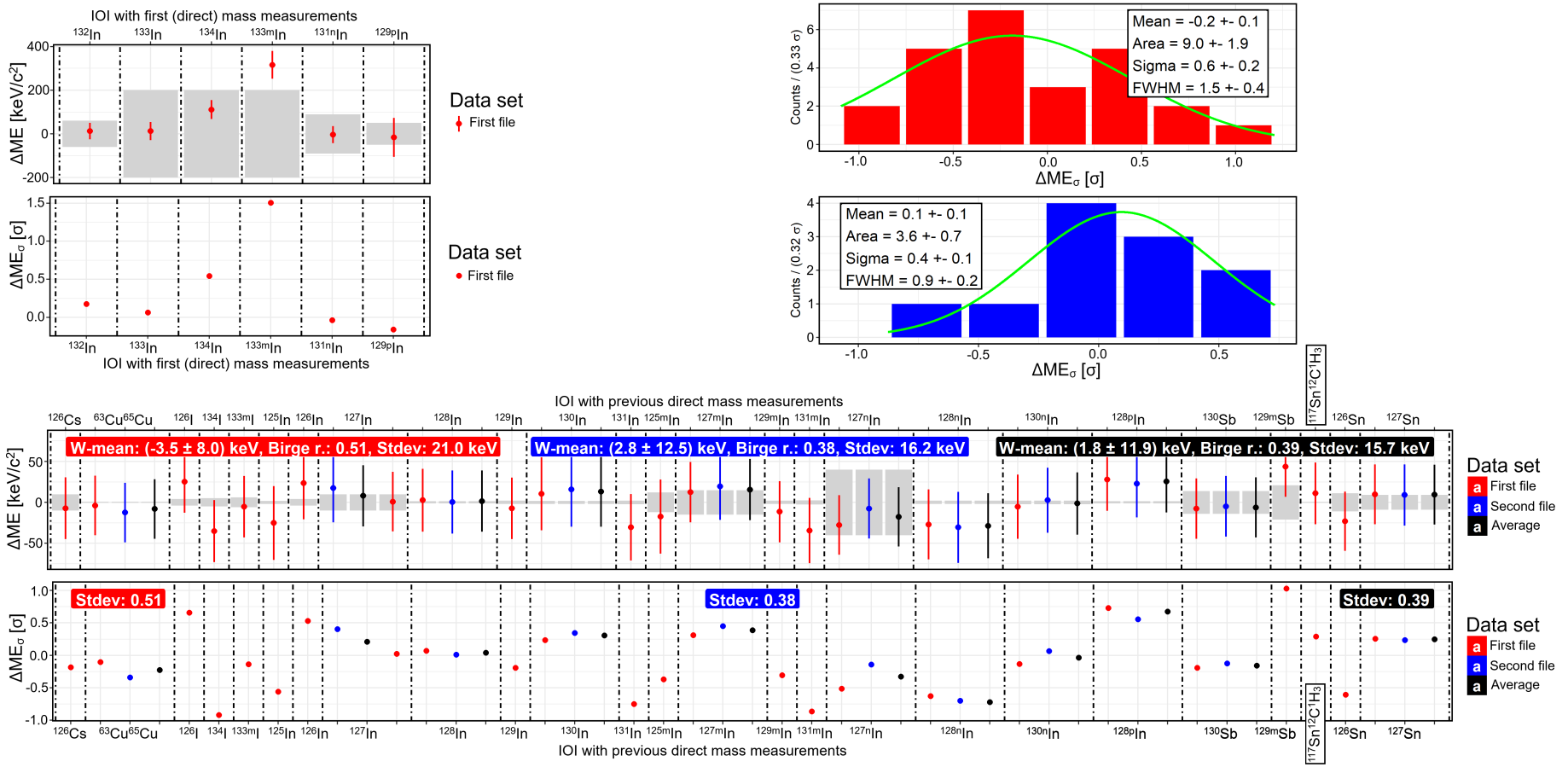

Figure 3.13: Example output plot of the compilation analysis R script to check the consistency of the determined mass values and their absolute and sigma deviations from the NUBASE2020 [Kondev et al., 2021] (ΔME and ΔME$_\sigma$). The gray band represents the uncertainties given in NUBASE2020 and the uncertainties of the points show the uncertainties determined in the mass measurements reported here. This example is based on the mass measurements of neutron-rich indium isotopes at TITAN, see more details in Chapter 4. The plot on the top left corner illustrates the deviations for the ions of interest, the mass of which was measured (directly) for the first time within the context of this work. The plot on the bottom and the histogram on the top right corner include the ions of interest, the mass of which has been already measured directly prior to this work. For the latter, different properties can be deduced to check the scatter of the deviations between the measured and literature mass values and their uncertainties, such as Birge-ratio, weighted mean or standard deviation (see text for more details).

In the MR-TOF-MS data acquired via broadband mass measurements covering a complete part of the nuclear chart, see e.g. [Amanbayev, 2023, Spătaru et al., 2025, Fowler-Davis, 2025], the ions of interest are spread across a wide range of turns, therefore an accurate multi-turn calibration is crucial. To deal with such data sets, dedicated consistency checks were developed. These consistency checks were originally developed for the broadband mass measurements obtained using the ^{252}Cf source at FRS-IC (for more details, see [Spătaru et al., 2025]). Here, however, the developed consistency checks are applied to the mass measurements performed during the S474 experiment at FRS-IC (Chapter 5). In particular, in Figs. 3.14 and 3.15, three dedicated consistency checks are highlighted, which are based on three data sets (I, II and III) obtained during the experiment. All three data sets correspond to mass measurements with a high mass resolving power of about 700,000 and are therefore ideal to accurately study small systematic effects. While data sets I and II cover only a relatively small mass-to-charge range of $m/q \sim (91-93)$ u/e, data set III corresponds to a broadband mass measurement, where peaks with $m/q \sim (80-101)$ u/e were identified spreading across a range of 706-to-794 isochronous turns (for more details, see Section 5.2). In order to validate the results of the multi-turn calibration and/or the precision calibration of the spectrum the following dedicated consistency tests can be performed:

- **Multi-turn calibrant-removal tests:** In order to achieve an accurate multi-turn calibration, the choice of the calibrant peaks has to be "optimized". Ideally, one should select as many calibrant peaks as possible covering the entire range of isochronous turns, because it will reduce the influence of the individual calibrant peaks on the final results of the calibration as explained earlier (see Fig. 3.6). This way, even if the measured TOF of a given calibrant peak is shifted due to some reason, e.g. due to an unresolved unknown contaminant hidden below the peak, the final results of the calibration will not be significantly affected. On the other hand, there may be also potential calibrant-peak candidates, the TOF of which are shifted so strongly that they should not be used as calibrants. This can be tested through the so-called calibrant-removal tests; i.e. through studying the influence of removing each calibrant ions separately on the results of the multi-turn calibration. As a result of this tests, the significantly shifted calibrant-peak candidates can be spotted and discarded from the calibration.

  This is illustrated in Fig. 3.14a for the example of data set III, where one can observe no significant change in the determined value of c, when removing the 10 selected calibrant ions separately from the calibration. This hints that there is no need to discard any peaks from this selection of calibrant-peak candidates and all 10 ions can be used to perform the multi-turn calibration of the spectrum. Since the ^{86}Kr and $^{12}C_2{}^{19}F_4$ ions have mass-to-charge ratios, which are on the two extremes of the mass-to-charge range covered by the selected calibrants, thus removing these two calibrant ions is expected to have a larger influence on the determined value and uncertainty of the calibration parameter c. This is in accordance with the results presented in Fig. 3.14a.

- **Linear fit of ΔME vs $N_{\mathbf{it,IoI}}/N_{\mathbf{it,cal}}$ ratio:** In the final step of the data analysis of the broadband mass measurements, the multi-turn calibration needs to be validated by checking the dependence of the ΔME of the ions of interest, where a direct mass measurement has been known before, on the $N_{\mathrm{it,IoI}}/N_{\mathrm{it,cal}}$ ratio. As illustrated in Fig. 3.14b, this dependence is fitted with a linear correlation according to Eq. (3.21), where the slope multiplied by a factor of (-1) is the same as the intercept.

$$\Delta\mathrm{ME}\left(\frac{N_{\mathrm{it,IoI}}}{N_{\mathrm{it,cal}}}\right) = B \cdot \left(\frac{N_{\mathrm{it,IoI}}}{N_{\mathrm{it,cal}}}\right) - B \tag{3.21}$$

  This is because, the mass-to-charge uncertainty, Δm_c, due to the uncertainty in c is math-

ematically zero, if $N_{\mathrm{it,IoI}}/N_{\mathrm{it,cal}} = 1$, i.e. the precision calibrant and the IOI undergo the same number of isochronous turns in the analyzer (see Eq. (3.9)). The higher the difference of the number of turns between the IOI and the precision calibrant ion, the higher the contribution of the Δm_c. Therefore, if the determined ΔME values of the ions with a well-known literature mass can be explained by Eq. (3.21), where the slope of the correlation (the parameter B) is consistent with zero within the experimental uncertainties, then this is indicative of a valid multi-turn calibration in the given broadband mass measurement. This is also the case for the multi-turn calibration of data set III, where a $B = -42(72)$ keV was deduced for the slope of the linear fit (see Fig. 3.14b).

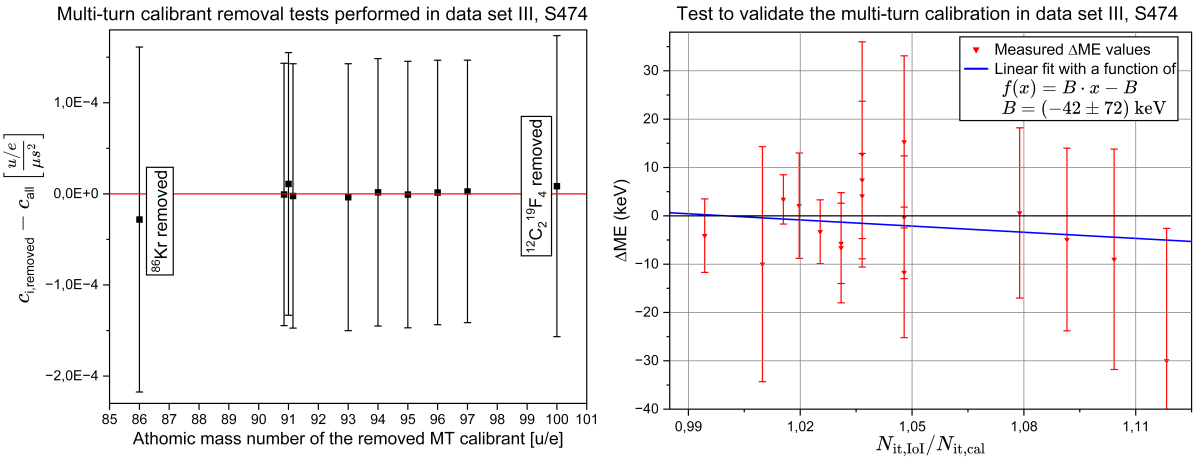

(a) (b)

Figure 3.14: Dedicated consistency checks used to check the results of the multi-turn calibration for broadband mass measurements. In particular, the here-presented examples are based on data set III obtained during the S474 experiment at FRS-IC (Chapter 5). (a) Investigation of the influence of individually removing the calibrant peaks used for the multi-turn calibration on the determined calibration parameter c and its uncertainty. Ideally, the difference between the c value determined using all, except the i$^{\mathrm{th}}$, calibrant ions ($c_{\mathrm{i,removed}}$) and the c value determined using all calibrant ions (c_{all}) is zero within experimental uncertainties, which is indicated by the red line on the figure. Note that the three calibrant ions with the same atomic mass number of 91 u/e are scattered on the figure for an easier separation of the data points. (b) Plot of the dependence of the deviations between the measured and literature mass for the IOI, which have previous direct mass measurements, on the $N_{\mathrm{it,IoI}}/N_{\mathrm{it,cal}(^{12}\mathrm{C}_2{}^{19}\mathrm{F}_4)}$ ratio. The blue line represents the linear fit of the data according to Eq. (3.21).

- **Testing whether the measured TOF of the precision calibrant is shifted:** In the step of the precision calibration, the mass-to-charge scale is re-established using a single calibrant ion (see Eq. (3.3)). In case there are reasons to think that the measured TOF of the given precision calibrant ion may be shifted, then the following consistency test can be performed: the same precision calibrant can be used to determine the mass of multiple ions in the spectrum, which have a well-known literature mass. Then the resulting ΔME values from this procedure can be checked with the "standard methods" explained earlier (see Fig. 3.13).

  For the example of data set I, the TOF of the high statistics (∼21,000 events) peak of $^{12}C_3{}^{19}F_3$ is shifted by about a tenth of the FWHM. As a consequence, if this peak is used for the precision calibration of the spectrum, the deduced ΔME of the 14 ions measured in data set I, which have direct mass measurements prior to this work, is shifted systematically.

The weighted mean of these ΔME values calculates to 13.5(34) keV. While the reason for the small TOF shift of the peak of $^{12}C_3{}^{19}F_3$ could, so far, not be understood, this consistency check clearly and self-consistently demonstrates that the peak of $^{12}C_3{}^{19}F_3$ can not be used for deducing accurate mass values in this data set and has to be discarded from the list of potential precision calibrant candidates.

- **Plot of ΔME vs the position of the ions in the TOF analyzer during ejection:** As discussed earlier, certain ions may feel different electric fields during their ejection from the TOF analyzer. This effect may be magnified and the TOF of the ions may be significantly shifted preventing an accurate mass measurement, if the ions are near the switched electrostatic mirrors during ejection. The goal of this consistency check is to investigate whether, in a given measurement, certain ions of interest or calibrant ions may be prone to systematic errors due to this effect.

  For this investigation, it is helpful to define a parameter called as ion position at ejection switching, or in short IP@ES. This IP@ES parameter can take values between -0.5 and $+0.5$ and reflects the fraction of the the ions' path in the TOF analyzer relative to the input mirror, where the ions are situated spatially during opening the output mirror for the extraction of the ions from the analyzer. The value of IP@ES is independent from the mass-to-charge ratio of the ions, where the IP@ES $= +0.5$ marks that the given ion is situated exactly in the output mirror moving towards the TOF detector, i.e. it has just started the leave the analyzer, when the mirror voltage gets switched. Similarly, the IP@ES $= -0.5$ marks that the given ion is also situated exactly in the output mirror, however in this case, the ion is moving towards the input mirror, i.e. it has just started its last turn in the analyzer, when the mirror voltage gets switched. The results of the offline measurement of the NPE uncertainty component, shown in Fig. 3.8, can be used to estimate that the two extremes of the analyzer transmission window correspond to the IP@ES $\approx \pm 0.39$ values, respectively, and the region of $+0.39 \lesssim$ IP@ES $\lesssim +0.24$ corresponds to the ringing region of analyzer during ejection. Last, but not least, the IP@ES $= 0$ marks that the ion is situated in the input mirror, when the output mirror voltage gets switched, i.e. in an ideal case, it is the furthest away from the switched electric fields. Prior to the measurements, when preparing the measurement settings of the MR-TOF-MS, it is attempted to optimize the conditions such that all IOI and calibrants are situated closer to the analyzer region with IP@ES $= 0$, when the output mirror voltage gets switched. During this optimization process, however, one needs to find a compromise between having all ions spatially at the same spot, when switching the mirror electrodes, and avoiding too many overlapping peaks in the resulting TOF spectrum (see more details in Section 2.1). As a consequence, it may happen that certain calibrant ions or IOI are situated closer to the output mirror, when its voltage is switched. The possible impact of this effect on the mass accuracy for different ions can be investigated, when checking the dependence of the deduced ΔME values for the ions, which were previously directly measured before, on the value of the above-defined parameter, IP@ES, calculated for the different ions.

  This is illustrated in Fig. 3.15 for the mass measurements performed in data sets I and III, which have two main take-home messages. Firstly, in general, one can notice that there is a constant behavior of the deduced ΔME values, independently from the ions' position in the analyzer, when the mirrors get switched. This hints that, in general, the experimental mass uncertainties and, in particular, the NPE uncertainty component are correctly estimated by the procedure explained in Section 3.3. On the other hand, in these two data sets there is not enough measured ions to have a final resolution on this question. Therefore, in the future, a comprehensive analysis of the results of all broadband mass measurements reported in [Spătaru et al., 2025, Fowler-Davis, 2025, Amanbayev, 2023] is

planned to investigate any systematic effects due to switched electric fields on the mass accuracy. These broadband measurements contain enough ions to accurately map the entire analyzer transmission window. Secondly, in the data set I, there is one ion, $^{12}C_3{}^{19}F_3$, the measured mass of which is deviated significantly from its literature mass (i.e. by more than 3 sigma), therefore it had to be removed from the list of potential precision calibrants (see also the results of the previous consistency check). The main question here is, whether the significant deviation between the measured and literature mass of $^{12}C_3{}^{19}F_3$, determined from data set I, could be resulted from an unexpected influence of the switched fields during the extraction of ions from the analyzer on its measured time-of-flight. Although Fig. 3.15 indicates a possible disagreement between the results of data sets I and III close to the negative extreme of the analyzer transmission window (around IP@ES ≈ -0.39), but there is not enough ions to clearly answer this question. Removing the data point of $^{12}C_3{}^{19}F_3$ from the figure, the possible disagreement between the results from the two data sets is not significant anymore, i.e. it is decreased to less than 1.5 sigma.

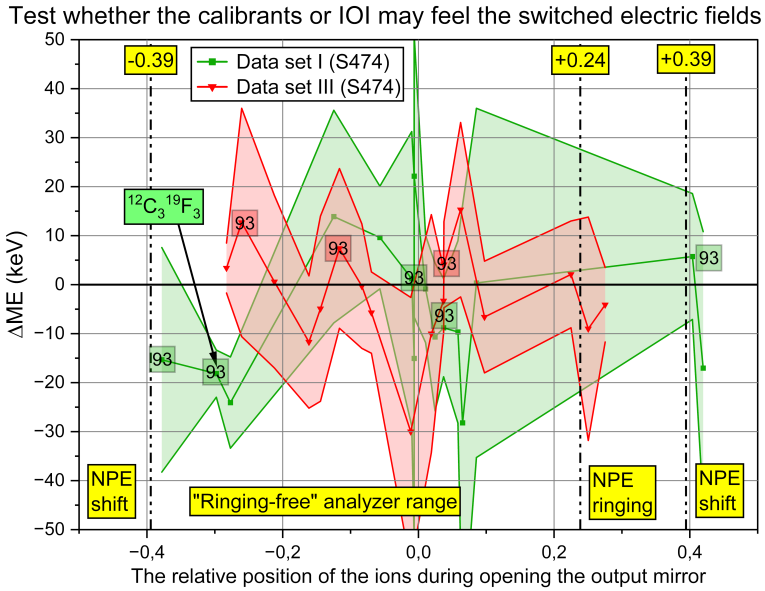

Figure 3.15: A dedicated consistency test used to check whether the different calibrants or IOI may feel unexpectedly strong switched electric fields during their extraction from the TOF analyzer. The determined ΔME values from two different data sets (I and III obtained during the S474 experiment at FRS-IC, see Chapter 5) are plotted against the values of the IP@ES parameter calculated for the different ions. The measured data points are connected with lines only to guide the eyes. The text fields highlighted in yellow indicate the different regions of the analyzer during ejection as defined from the offline measurement of the NPE uncertainty component (see text for more details). Certain data points are highlighted with a number "93", which indicates that they correspond to isobaric species with a mass-to-charge ratio of 93 u/e.

Overall, the above-discussed consistency checks in combination with broadband mass measurements, such as the ones from [Spătaru et al., 2025, Fowler-Davis, 2025, Amanbayev, 2023], help to avoid systematic errors from the measurement and data analysis procedure. Furthermore, some of the consistency tests are also applicable to measurements covering a smaller mass-to-charge range as demonstrated for the case of the mass measurements of neutron-rich indium isotopes at TITAN (Fig. 3.13) and for the data set I obtained during the S474 experiment at GSI (Fig. 3.15). Notably, with the newly commissioned laser ablation carbon cluster ion source for the FRS-IC, LACCI [Yu et al., 2024a], the systematic studies of the mass uncertainties will

be further continued in the future, where these consistency checks will also help.

Chapter 4

Mass measurements of neutron-rich indium isotopes at TITAN, TRIUMF

High-precision mass measurements of neutron-rich indium isotopes across the $N = 82$ shell closure were performed using TITAN's MR-TOF-MS at TRIUMF, which was developed by the IONAS group in Gießen, see Section 1.3 for more details.

In the experiment campaign the masses of two indium isotopes and one isomeric state was measured for the first time. Additionally, the ground-state mass of one indium isotope was measured directly for the first time and a measurement of two additional isomeric states are reported here, the excitation energies of which were deduced with significantly smaller uncertainties (by factors of 4-5) compared to the uncertainties given in the AME2020. The measured indium isotopes have multiple isomeric states with various half-lives ranging from a few milliseconds to a few seconds and excitation energies ranging from a few tens of keV to a few thousands of keV and covering a large dynamic range. Therefore, these measurements represent an ultimate test for the capabilities of TITAN's MR-TOF-MS and for the data analysis procedure introduced in the previous chapter.

The segment of the nuclear chart shown in Fig. 4.1 summarizes all nuclides identified in the performed mass measurements together with highlighting the neutron-rich indium isotopes, which are the key isotopes of this chapter. The results presented here have already been published in [Izzo et al., 2021], where the reported mass and excitation energy values are based on this work. Notably, a second and third independent analysis to confirm the identification of the ions and for an independent mass value determination have been also performed by C. Izzo and E. Dunling [Izzo et al., 2020] (priv. comm.), but the final mass values were obtained based on the data analysis procedure and its intricacies detailed here. For more details about the physics implications of the results, the reader is referred to [Izzo et al., 2021].

4.1 Description of the experiment

Neutron-rich indium isotopes were produced in spallation and fission reactions at the Isotope Separator and Accelerator (ISAC) facility [Ball et al., 2016] by impinging a 10-μA proton beam with an energy of 480 MeV, which was provided by TRIUMF's cyclotron, onto a uranium carbide target. The indium isotopes that effused out of the target were selectively ionized using the ion-guide laser ion source [Raeder et al., 2014], which was used to (i) suppress the surface ionized ions with an electrostatic potential barrier, i.e. to suppress the isobaric contamination, and (ii) to ionize the neutral indium atoms via resonant laser ionization behind the electrostatic barrier inside a radio-frequency quadrupole (RFQ), which was used to guide them toward the extraction. Then the extracted ions were separated according to their mass-to-charge ratio at a mass separation power of 2000 using ISAC's high-resolution mass separator

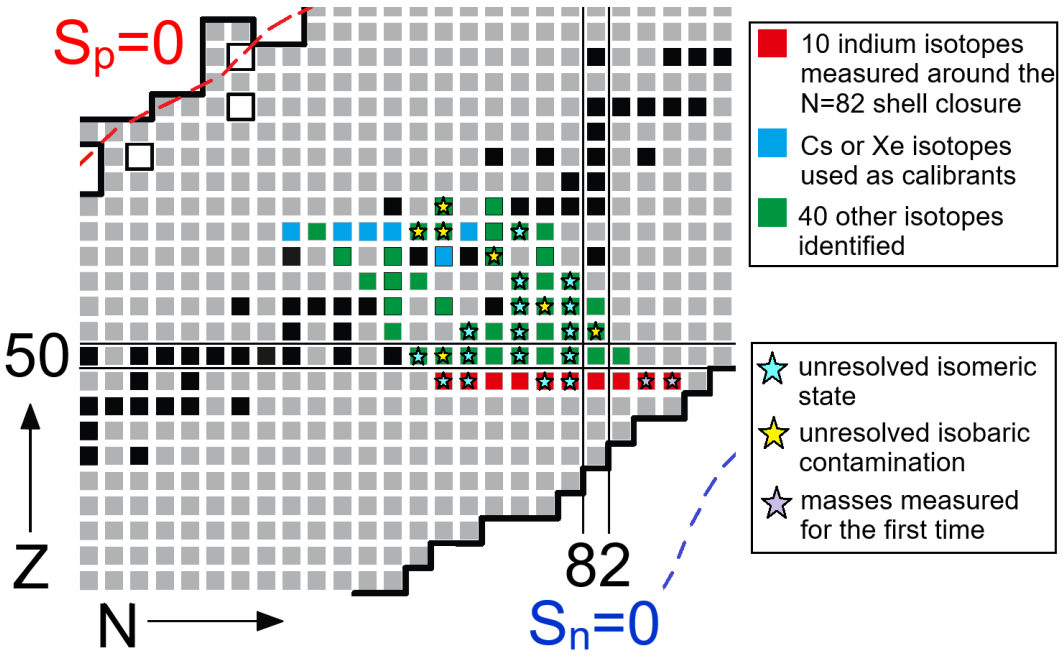

Figure 4.1: The segment of the nuclear chart illustrates the 56 nuclides identified during the experiment performed using TITAN's MR-TOF-MS, out of which the masses of the 10 measured neutron-rich indium isotopes and their corresponding isomers (highlighted in red) were determined in this work. The remaining identified nuclei are highlighted in blue, in case they were used as precision calibrants in the measured TOF spectra, and in green, otherwise. The stable nuclei are shown in black. The light blue and yellow stars indicate the nuclides with unresolved isomeric and/or isobaric contamination. The masses of ^{133}In, ^{133m}In and ^{134}In were measured for the first time as indicated by the purple stars. The dashed blue and red lines represent a schematic illustration of the boundaries between neutron and proton bound and unbound nuclei, i.e. the neutron and proton drip lines, respectively.

[Bricault et al., 2002]. The selected isobaric ion species, including mostly singly charged Cs, Xe, I, Te, Sb, Sn, In, Cu_2 and $SnCH_3$ ions, were then delivered to the TITAN facility [Dilling et al., 2006]. There, the radioactive beam was cooled and bunched in a linear RFQ [Brunner et al., 2012] filled with helium buffer gas. Ion bunches of about 1 μs in length were then sent to the MR-TOF-MS, which was operated at a repetition rate of 50 Hz corresponding to a measurement cycle length of 20 ms (for an introduction to TITAN's MR-TOF-MS, see Section 1.3). There, the ions were transported to the injection trap, cooled, and injected into the TOF analyzer, where after performing one time-focus shift turn [Dickel et al., 2017b] they were confined for about 300-to-375 isochronous turns between two elecrostatic mirrors, corresponding to a time-of-flight of about 7-to-8 ms. In the center of the TOF analyzer, the mass range selector (MRS) was used to limit the mass-to-charge range to one atomic mass unit, ensuring that all ions detected have undergone the same number of isochronous turns[1]. Afterwards, the ions were ejected from the TOF analyzer towards the TOF detector, where the time-of-flight of the different ion species with different mass-to-charge ratios was recorded. The resolving power achieved for the mass measurements varied between 200,000 and 300,000 depending on the performed number of isochronous turns and the measured count rate of the peak used for the time resolved calibration

[1]For the mass measurement of the indium isotopes at $A = 125 - 130$, a second data set was also acquired without using the MRS. There, the peak of ^{133}Cs, produced by the thermal ion source of the MR-TOF-MS, was also included in the TOF spectrum. This ^{133}Cs peak, in principle, could be used to obtain the peak shape from a fully isolated peak, which would avoid the necessity to restrict the peak tails, when obtaining the peak shape.

during data analysis.

After the mass measurements of each indium isotopes, an additional data set was acquired without the resonant laser ionization to verify the identification of the indium ions by comparing TOF spectra obtained with and without laser ionization. From this comparison, it could be seen that, when the laser was blocked, the indium ions created by the resonant laser ionization were nearly eliminated from the beam, while the count rate of other species remained unchanged. Additionally, this information could also be used to estimate an upper limit for the possible underlying contamination beneath the indium peaks for determining the contamination uncertainty component (see Section 3.3).

The overall rate of the radioactive beam sent to TITAN was limited to maintain the average rate of approximately one detected ion per cycle in the MR-TOF-MS in order to eliminate systematic uncertainties arising from ion-ion interactions inside the TOF analyzer. For the mass measurement of the indium isotopes at $A = 131 - 134$, the incoming rates of the IOI was several orders of magnitude lower than the rates of the isobaric contaminant species, especially of stable or near-stable cesium. Therefore, for these measurements, the mass-selective re-trapping technique [Dickel et al., 2017a, Beck, 2023] was required to suppress this background. There, the MR-TOF-MS was used as its own isobar separator, i.e. the ions of interest were separated from the isobaric contaminant ions prior to the mass measurement itself, thus improving the background handling capabilities of the MR-TOF-MS. In the first half of the 20-ms-long measurement cycle, the ions passed through the TOF analyzer for a certain number of isochronous turns (typically about 30-to-50 IT) to achieve a sufficient separation of the isobaric species and then were dynamically re-captured in the injection trap, with a re-capture timing chosen to transmit the ions of interest, while suppressing other isobaric species. The re-captured ions were then released again into the TOF analyzer for the mass measurement. This technique was first employed in an online experiment reported in Ref. [Beck et al., 2021]. In this experiment, in combination with offline studies beforehand, it has been shown that this technique can suppress the background by a factor of $\sim 10^4$ in a typical case, while transmitting the ions of interest with a high efficiency of $\sim$60% [Beck, 2023]. As a result, a much higher overall beam intensity (and thus a higher incoming yield of the neutron-rich indium ions) could be sent to TITAN, while still maintaining an approximately one ion per cycle in the TOF analyzer for the mass measurements.

As an example, the mass-to-charge spectrum of ^{131}In ions shown in Fig. 4.2 was obtained employing the mass-selective re-trapping technique; prior to re-trapping the peak of ^{131}Cs was about four orders of magnitude higher than any other peaks in the spectrum, while after employing re-trapping and increasing the beam intensity sent to TITAN, the peaks of the IOI became the largest peaks in the spectrum. As a consequence of this superior background handling capability, in combination with the fast, non-scanning and sensitive measurement characteristics of the MR-TOF-MS, mass measurements can be performed two-three neutrons further away from stability than one would expect achievable for TOF-ICR mass measurements with a Penning trap, compare e.g. [Babcock et al., 2018]. The most exotic isotope measured in this work, ^{134}In, was detected in the MR-TOF-MS with an average count rate of $\sim$0.45 events per minute. This was sufficient to achieve a smaller statistical uncertainty than the limiting systematic uncertainty component within the $\sim$6.1 hours of the mass measurement of ^{134}In.

4.2 Overview of measured masses and comparison to literature

To obtain the mass values of the neutron-rich indium ions, the acquired data have been analyzed following the procedure described in Chapter 3. Since the measured indium ions had a wide combination of isomers with different excitation energies and abundance ratios, these measurements represent ultimate tests for the data analysis procedure and, especially, for the treatment of overlapping TOF peaks.

Since all calibrant ions and IOI underwent the same number of isochronous turns, the TOF spectra were converted to mass-to-charge spectra according to Eq. (3.2), where the calibration parameter $t_0 = 164(2)$ ns was determined prior to the experiment, offline. The drift correction (time-resolved calibration) was performed using $^{125-126}$Sn and $^{127-134}$Cs ions for the mass measurements of $^{125-134}$In isotopes and their corresponding isomers, respectively. The peak shapes were determined using ^{125}Sn, $^{63}Cu_2$, $^{127-129}$Cs, ^{130}Sb, ^{131,132}Cs and $^{12}C_1{}^1H_3{}^{118,119}Sn_1$ ions for the mass measurements of $^{125-134}$In isotopes and their corresponding isomers, respectively. For the mass measurement of the indium isotopes at $A = 126 - 134$, the number of events in the model peaks were sufficiently large to achieve a relatively well-determined peak shape, which is essential for the treatment of overlapping TOF peaks. This was, however, not true in the data set containing the peaks of the ^{125}In ground state and its corresponding isomers, the consequences of which will be described later. Finally, the calibration parameter a from Eq. (3.2) was determined from an isobaric precision calibrant ion with a well-known mass that arrived with the radioactive beam and its corresponding peak was sufficiently isolated from other ions, i.e. no contamination due to unresolved isobaric or isomeric ions was expected. The precision calibrant ions corresponding to the different indium isotopes are listed in Table 4.1, the mass of which were taken from the atomic mass evaluation (AME2016) [Wang et al., 2017].

The uncertainties of the mass values were calculated by adding in quadrature the individual components as described in Section 3.3. The majority of the systematic uncertainty components were covered by a single uncertainty contribution (δm_{syst}), which represents an upper limit of the systematic uncertainties of TITAN's MR-TOF-MS. For experiments performed at TITAN before 2020, such as the mass measurements of neutron-rich indium isotopes reported here, the relative value of this uncertainty component was determined to be $\delta m_{\mathrm{syst}}/m = 3 \times 10^{-7}$ based on offline accuracy studies [Will, 2017], as well as, online measurements, see e.g. [Leistenschneider et al., 2018]. Here, the value of δm_{syst} is dominated by the non-perfect ejection uncertainty contribution, i.e., the effect that the different ion species (calibrants and ions of interests) may feel slightly different electric fields during their ejection from the TOF analyzer. In most cases, the determined total mass uncertainty of the neutron-rich indium isotopes was dominated by the above-described systematic uncertainty component. In case of the mass measurements of the ground states of ^{125}In, ^{126}In and ^{130}In and the middle-lying isomeric state, ^{129p}In, an additional uncertainty component was included to account for the unresolved isomeric state(s) with $T_{1/2} > 1$ ms and the determined mass value was corrected, accordingly, following the recommendations from the atomic mass evaluation:

- The low-lying isomer state, ^{125m}In, could not be resolved from the ground state and its excitation energy of 360.12(9) keV [ENSDF, 2024] was used to correct the mass value and uncertainty determined for the ground state.
- The excitation energies of 89.9(65) keV [Babcock et al., 2018] and 58.6(82) keV [Nesterenko et al., 2020] corresponding to the unresolved low-lying isomer states, ^{126m}In and ^{130m}In, respectively, were used to correct the mass values and uncertainties determined for the ground states of ^{126}In and ^{130}In.
- While the middle-lying isomeric state, ^{129p}In, could be resolved from the ground state of ^{129}In and the low-lying isomeric state, ^{129m}In, but could not be fit separately from the highest-lying isomeric state, ^{129q}In. In this case, the excitation energy difference of 281.0(2) keV [Gausemel et al., 2004] between the two high-lying isomer states was used to correct the mass value and uncertainty determined for the middle-lying isomer state, ^{129p}In.

In the cases, where the observed ground and isomeric states could be separated from each other during data analysis, the excitation energies of the isomeric states were determined from the mass difference between the ground and isomeric states. In these cases, the uncertainties of

Table 4.1: Measured mass excess (ME_{TITAN}) values of neutron-rich indium isotopes compared with the literature values, ME_{lit}, which are taken from the NUBASE2020 [Kondev et al., 2021]. The masses of ^{133}In, ^{133m}In and ^{134}In were measured for the first time. The used precision calibrants and the number of events detected for the IOI are also listed in the table. The $\Delta ME = ME_{TITAN} - ME_{lit}$ marks the deviation of the measured values from the literature. Listed spin/parity assignments are from ENSDF [ENSDF, 2024].

Nuclide	J^π	Precision calibrant	Events	ME_{TITAN} (keV)	ME_{lit} (keV)	ΔME (keV)
^{125}In	$9/2^+$	^{125}Cs	36034	-80511(110)[c]	-80412.3(18)	-99(110)
^{126}In	$3^{(+)}$	$^{63}Cu_2$	17481	-77785(44)[c]	-77809(4)	24(44)
^{127}In	$(9/2^+)$	^{127}Cs	27996	-76873(37)	-76880(10)[e]	7(39)
^{127m}In	$(1/2^-)$	^{127}Cs	23772	-76469(37)	-76486(15)[e]	17(40)
^{127n}In	$(21/2^-)$	^{127}Cs	8679	-75126(36)[d]	-75110(40)[e]	-16(54)
^{128}In	$(3)^+$	^{128}Cs	28121	-74183(38)	-74190.1(13)	7(38)
^{128n}In	(8^-)	^{128}Cs	18638	-73924(44)	-73905.0(20)	-19(44)
^{128p}In	(16^+)	^{128}Cs	1856	-72370(39)[d]	-72392.5(14)	22(39)
^{129}In	$(9/2^+)$	^{129}Cs	5630	-72846(37)	-72834.9(20)	-11(37)
^{129m}In	$(1/2^-)$	^{129}Cs	6283	-72399(37)	-72384.2(20)[e]	-15(37)
^{129p}In	$(23/2^-)$	^{129}Cs	1080	-71196(89)[c,d]	-71180(50)[b,e]	-16(102)
^{130}In	$1^{(-)}$	^{130}Xe	1254	-69893(43)[c]	-69906.5(18)	13(43)
^{130n}In	(5^+)	^{130}Xe	2133	-69523(38)	-69521.1(21)	-2(38)
^{131}In	$(9/2^+)$	$^{12}C_1{}^1H_3{}^{116}Sn_1$	4194	-68051(40)	-68024.4(22)	-26(40)
^{131m}In	$(1/2^-)$	$^{12}C_1{}^1H_3{}^{116}Sn_1$	5316	-67675(39)	-67648.4(25)	-27(40)
^{131n}In	$(21/2^+)$	$^{12}C_1{}^1H_3{}^{116}Sn_1$	1289	-64280(38)	-64280(90)[b]	0(98)
^{132}In	(7^-)	^{132}Cs	975	-62395(38)	-62410(60)[b]	15(71)
^{133}In	$(9/2^+)$	$^{12}C_1{}^1H_3{}^{118}Sn_1$	302	-57678(41)	-57690(200)[#]	12(204)
^{133m}In	$(1/2^-)$	$^{12}C_1{}^1H_3{}^{118}Sn_1$	76	-57036(69)	-57360(200)[#]	324(211)
^{134}In	$(6^-,7^-)$	$^{12}C_1{}^1H_3{}^{119}Sn_1$	165	-51855(44)	-51970(200)[#]	115(205)

[#] Literature mass and uncertainty is not derived from experimental data, but based on extrapolations.

[b] The mass values of ^{129p}In, ^{131n}In and ^{132}In reported in NUBASE2020 are based on Q_β measurements from Refs. [Gausemel et al., 2004, Fogelberg et al., 2004, Mezilev et al., 1995], respectively.

[c] The measured mass and uncertainty were adjusted to account for unresolved isomers (see text for details).

[d] The measured mass was obtained using the 2(fixed)+1(free) peak fitting method.

[e] Also measured at IGISOL recently [Jaries et al., 2024] with determined mass excesses of:
$ME(^{127}In,9/2^+) = -76891.2(13)$ keV, $ME(^{127m}In,1/2^-) = -76483.3(52)$ keV,
$ME(^{127n}In,21/2^-) = -75162.5(18)$ keV, $ME(^{129m}In,1/2^-) = -72385.8(63)$ keV,
$ME(^{129p}In,23/2^-) = -71188.3(39)$ keV

the excitation energies of isomeric states partially canceled and the only remaining uncertainties were as described in Section 3.3. As a result, the determined uncertainties of the excitation energies of isomeric states were dominated by the statistical uncertainty and, in a few cases, the peak-shape uncertainty and, if applicable, by the uncertainties due to the treatment of resolved overlapping peaks and due to unresolved isomeric states. In case of the high-lying isomeric states, ^{127n}In and ^{131n}In, the excitation energies were determined with smaller uncertainties compared

to the uncertainties given in the NUBASE2020 [Kondev et al., 2021]. For the indium isotopes, which were measured in two data sets, the results from the two data sets were weighted averaged according to the procedure described in Section 3.4. The final mass excess values, excitation energies and their corresponding uncertainties determined for the ground and isomeric states of the neutron-rich indium isotopes are summarized in Tables 4.1 and 4.3.

Table 4.3: Measured excitation energy ($E_{x,\mathrm{TITAN}}$) of neutron-rich indium isotopes compared with the literature values, $E_{x,\mathrm{lit}}$, which are taken from the NUBASE2020 [Kondev et al., 2021]. The excitation energy of ^{133m}In was measured for the first time. Listed half-lives and spin/parity assignments are from ENSDF [ENSDF, 2024].

Nuclide	J^π	$T_{1/2}$	$E_{x,\mathrm{TITAN}}$ (keV)	$E_{x,\mathrm{lit}}$ (keV)	$E_{x,\mathrm{TITAN}} - E_{x,\mathrm{lit}}$ (keV)
^{127m}In	$(1/2^-)$	3.618(32) s	406(12)	394(18)[e]	12(21)
^{127n}In	$(21/2^-)$	1.04(10) s	1743.7(92)[d]	1770(40)[e]	-26(41)
^{128n}In	(8^-)	720(100) ms	259(28)	285.1(22)	-26(28)
^{128p}In	(16^+)	>300 ms	1813(17)[d]	1797.6(16)	15(17)
^{129m}In	$(1/2^-)$	1.22(95) s	447(13)	450.7(2)[e]	-4(13)
^{129p}In	$(23/2^-)$	651.0(200) ms	1649(82)[c,d]	1650(50)[b,e]	-1(96)
^{130n}In	(5^+)	651.0(60) ms	370(25)	385.4(26)	-15(25)
^{131m}In	$(1/2^-)$	328.0(150 ms	375(18)	376(3)	-1(18)
^{131n}In	$(21/2^+)$	322.0(410) ms	3771(15)	3750(90)[b]	21(91)
^{133m}In	$(1/2^-)$	167.0(110) ms	642(60)	330(40)[#]	312(72)

[#] Literature excitation energy is not derived from experimental data, but based on extrapolations.

[b] The excitation energies of ^{129p}In and ^{131n}In reported in NUBASE2020 are based on Q_β measurements from Refs. [Gausemel et al., 2004, Fogelberg et al., 2004], respectively.

[c] The measured excitation energy and uncertainty were adjusted to account for unresolved isomers.

[d] The measured excitation energy was obtained using the 2(fixed)+1(free) peak fitting method.

[e] Also measured at IGISOL recently [Jaries et al., 2024] with determined excitation energies of:
$E_x\left(^{127m}\mathrm{In},1/2^-\right) = 407.9(50)$ keV, $E_x\left(^{127n}\mathrm{In},21/2^-\right) = 1728.7(12)$ keV,
$E_x\left(^{129m}\mathrm{In},1/2^-\right) = 449.1(59)$ keV, $E_x\left(^{129p}\mathrm{In},23/2^-\right) = 1646.6(33)$ keV

Treatment of overlapping peaks of indium ground and isomeric states

Fitting overlapping TOF peaks requires an accurate description of the peak shape and, in particular, an accurate description of the peak tails caused by ion-optical aberrations. The data analysis procedure, described in Chapter 3, takes into account the description of the peak tails through fitting the data with Hyper-EMG functions [Purushothaman et al., 2017] and has been shown to provide an accurate determination of the mass values even in case of overlapping peaks [Ayet San Andrés et al., 2019, Hornung et al., 2020]. As a result, in most cases, the mass values of close-lying peaks can be deduced from a slight broadening of the peak shape or a small shoulder peak present on a massive exponential tail of a bigger peak. The ability to detect and accurately fit such overlapping peaks heavily depends on case-specific factors, such as the total number of events, the mass differences and the relative areas between the overlapping peaks. Additionally, it also depends on how accurately the peak shape is described. This latter factor typically depends on the following three conditions: (i) whether the model peak used for the determination of the peak shape was measured under identical conditions as the IOI, (ii) whether the model

peak has higher statistics than the peaks of the IOI and (iii) whether the model peak is well isolated from all other peaks in the spectrum.

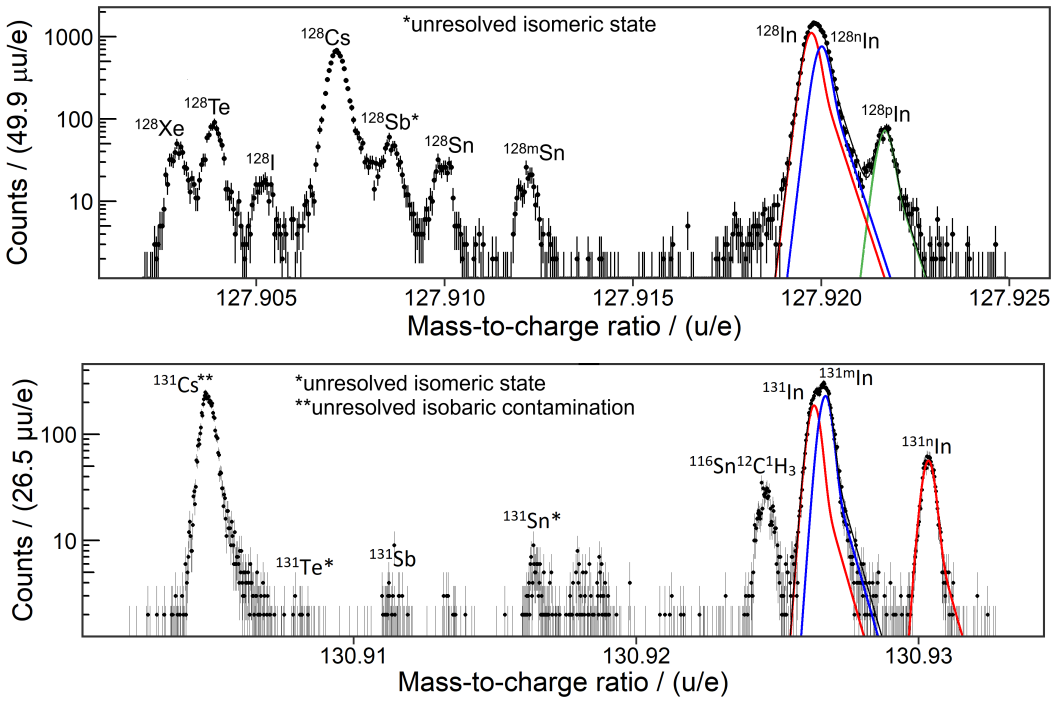

Figure 4.2: Mass-to-charge spectra of neutron-rich indium ions and their corresponding isobaric contaminant and calibrant ions with mass number (top) $A = 128$ and (bottom) $A = 131$. The curves represent the fits to the unbinned data with a fixed hyper-EMG peak shape (top: FWHM $\approx$ 426 keV, bottom: FWHM $\approx$ 497 keV), which was obtained from the peaks of ^{128,131}Cs for the top and bottom spectra, respectively. The precision calibration of the spectra was performed using the peaks of ^{128}Cs (top) and $^{12}C_1{}^1H_3{}^{116}Sn_1$ (bottom). The mass-to-charge spectrum of ^{128}In ions (top) illustrates a fit performed using the 2(fixed)+1(free) peak fitting method. The measurement of ^{131}In ions (bottom) was performed employing the mass-selective re-trapping technique suppressing the background dominated by ^{131}Cs ions. The identification of a new, high-lying isomer state reported in Ref. [Nesterenko et al., 2020], ^{128p}In, is confirmed by the here-presented measurements, which was verified by comparing the TOF spectra obtained with and without resonant laser ionization. The here-presented measurements significantly reduce the uncertainty of the excitation energy of the high-lying isomer, ^{131n}In, compared to the value reported in NUBASE2020, which is based on Q_β measurements [Fogelberg et al., 2004].

Concerning the mass measurements of neutron-rich indium ions reported here, the lowest-lying isomeric state, which could be resolved, ^{128n}In, was only about half of a FWHM $\approx$ 426 keV apart from the ground state of ^{128}In (see Fig. 4.2). The measured excitation energy of the ^{128n}In isomeric state is within experimental uncertainties the same as the literature excitation energy [Kondev et al., 2021]. The accurate determination of the excitation energy of this and other low-lying isomer states of the measured indium isotopes (see Table 4.3) further illustrates the robustness of the data analysis procedure for treating overlapping peaks.

Besides the challenge of treating very close-lying peaks, these mass measurements also required fitting multiple (more than two) overlapping peaks. For the analysis of the indium isotopes, where more than one isomeric states were observed and could be resolved from the ground state, the so-called 2(fixed)+1(free) peak fitting method was applied to fit the high-lying isomeric states (see more details in Section 3.5). As an example, this method was used to determine

the mass value of the high-lying isomeric state, ^{128p}In, the mass spectrum of which is shown in Fig. 4.2. As shown on the figure, this high-lying isomer state is situated on the peak tails from the ground and low-lying isomeric states, where the high-lying isomer has smaller number of events by more than an order of magnitude compared to the ground and low-lying isomeric states. Therefore, for fitting this high-lying isomer, an accurate description of the peak shape with special attention to the peak tails is essential. The mass values and excitation energies of the high-lying isomer states, ^{127n}In, ^{128p}In and ^{129p}In, are listed in Tables 4.1 and 4.3, all of which were determined using the 2(fixed)+1(free) peak fitting method[2]. As shown in the tables, the obtained mass and excitation energy values are in good agreement with the values listed in the NUBASE2020 [Kondev et al., 2021] and with the results of recent Penning-trap mass measurements employing the PI-ICR technique at IGISOL [Jaries et al., 2024].

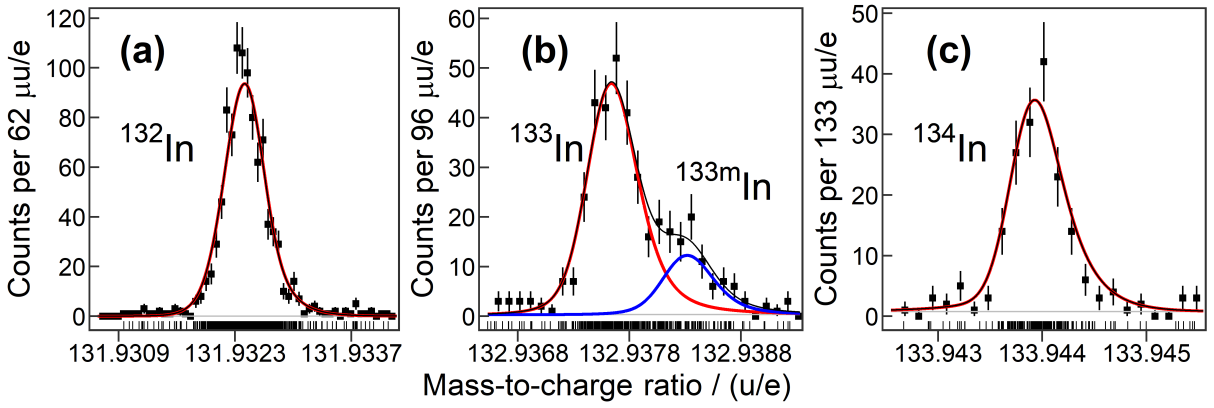

Figure 4.3: Mass-to-charge spectrum of (a) ^{132}In ions, (b) ^{133}In ions (including both ground and isomeric states) and (c) ^{134}In ions. The histogram of the measured spectrum (black data points) is only drawn to guide the eye. The curves represent the fits to the unbinned data ('rug' graph below the histogram) with a fixed hyper-EMG [Purushothaman et al., 2017] peak shape [(a): FWHM $\approx$ 470 keV, (b): FWHM $\approx$ 500 keV, (c): FWHM $\approx$ 565 keV], which was obtained from the peaks of (a) ^{132}Cs, (b) $^{12}C_1{}^1H_3{}^{118}Sn_1$ and (c) $^{12}C_1{}^1H_3{}^{119}Sn_1$ ions, which were also used to perform the precision calibration of the spectra. The measurements of $^{132-134}$In ions were performed employing the mass-selective re-trapping technique. The mass of ^{132}In was measured directly for the first time, reducing the uncertainty of the mass value compared to the previous value reported in the AME2020, which is based on Q_β measurements from [Mezilev et al., 1995]. The mass and excitation energy values of ^{133}In, ^{133m}In and ^{134}In were measured for the first time.

[2]Note that the results tabulated in Tables 4.1 and 4.3 were calculated without performing the cut-bias correction described in Section 3.3, which is used to correct the shift of the deduced mass-to-charge ratio, when restricting the peak tails. On the other hand, after developing the cut-bias correction and performing a new analysis of the data sets including the correction, the resulting mass values and excitation energies are in very good agreement with the previous results reported here and in [Izzo et al., 2021]. Performing the cut-bias correction only modifies the determined mass excess values by up to 5-10 keV and the determined excitation energies by up to 1-2 keV, both of which is well within the experimental uncertainties. The reason of this is that no stringent cuts had to be applied to the data for the analysis of these measurements, i.e., the peak tails of the calibrants and ions of interest were only cut at less than 5-10% of the peak height. For the analysis of the high-lying isomers, which were overlapping with the ground states and the low-lying isomer states, no cuts were applied to the data, instead, the 2(fixed)+1(free) peak fitting method was used. Since performing the cut-bias correction did not change the results significantly, here, the previously published results of Ref. [Izzo et al., 2021] are reported instead of the results of the new analysis. Nevertheless, with the development of the cut-bias correction, the robustness and flexibility of the data analysis procedure was further increased for treating overlapping peaks.

Technical highlight: observation of a short-lived (5 ms) isomer

The ^{125}In isotope has a low-lying isomeric state with spin and parity of $J^\pi = 1/2^{(-)}$, half-life of $T_{1/2} = 12.2(2)$ s and excitation energy of $E_{x,\mathrm{lit}} = 360.12(9)$ keV and a high-lying isomeric state with $J^\pi = (23/2^-)$, $T_{1/2} = 5.0(15)$ ms and $E_{x,\mathrm{lit}} = 2161.2(9)$ keV [ENSDF, 2024]. Both of these isomeric states together with the ground state of ^{125}In were observed in the here-presented measurement with TITAN's MR-TOF-MS. The measured mass-to-charge spectrum of ^{125}In ions is shown in Fig. 4.4.

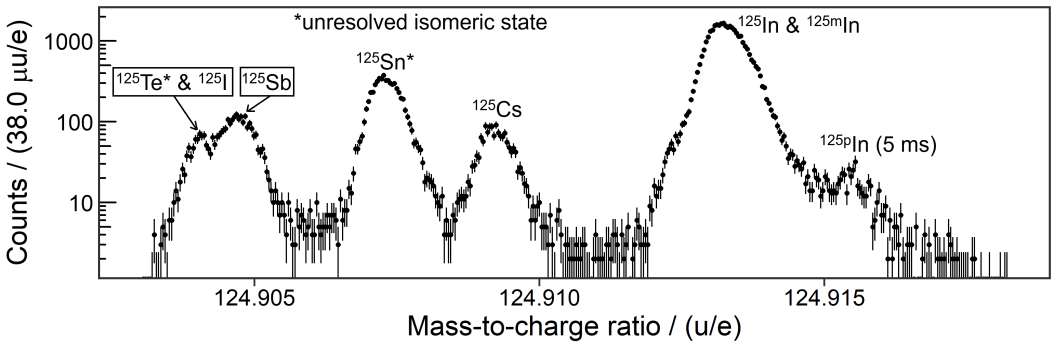

Figure 4.4: Mass-to-charge spectra of neutron-rich indium ions and their corresponding isobaric contaminant and calibrant ions with mass number $A = 125$. The mass resolving power in this measurement amounts to about 200,000 (FWHM $\approx$ 572 keV). During the analysis of this spectrum, the peak of ^{125}Sn ions, which has about an order of magnitude less events compared to the peak of ^{125}In ions, was used to perform the time-resolved calibration and obtain the peakshape. The precision calibration of the spectrum was performed using the peak of ^{125}Cs ions. The small shoulder peak lying in the massive tail from the ground and low-lying isomeric states of ^{125}In corresponds to its high-lying isomer with a half-life of 5 ms. The correct identification of this 5-ms isomer was confirmed by storing the ions longer ($\geq$61 ms) before injecting them into the MR-TOF-MS, see text for more details.

The high-lying isomer with a half-life of 5.0(15) ms was observed as a small shoulder peak lying in the massive tail from the ground and low-lying isomeric states. The count rates of these latter two states were larger by more than two orders of magnitude compared to the count rate of the high-lying isomer state. This high-lying, 5-ms isomer could be resolved with a clear minimum between its peak and the peak of the ground and low-lying isomer states (see Fig. 4.4). The identification of this 5-ms isomer was confirmed by increasing the storage time of the ions before injecting them into the MR-TOF-MS. This technique was first commissioned in Ref. [Mukul et al., 2020], where the half-life of the neutron-rich nuclide ^{100}Rb was measured employing this technique, and then applied for the mass measurements reported here. The ions were accumulated and cooled in two places; firstly, the ions were accumulated for an accumulation time of t_{acc} in the gas-filled linear RFQ [Brunner et al., 2012] used for cooling and bunching the radioactive beam and, secondly, they were stored for an additional storage time of t_{store} in the gas-filled transfer RFQ [Mukul et al., 2020] situated before the injection trap of the MR-TOF-MS. The original spectrum of ^{125}In ions shown in Fig. 4.4 was measured using an accumulation time of $t_{\mathrm{acc}} = 20$ ms corresponding to the 50 Hz repetition rate of the MR-TOF-MS and using an additional storage time of $t_{\mathrm{store}} = 1$ ms. In the next step, the accumulation and storage times were increased to $t_{\mathrm{acc}} = 40$ ms and $t_{\mathrm{store}} = 21$ ms. Finally, these times were increased to $t_{\mathrm{acc}} = 220$ ms and $t_{\mathrm{store}} = 181$ ms. While the count rate of the ground and low-lying isomeric states of ^{125}In stayed roughly the same, the small shoulder peak of the 5-ms isomer fully disappeared due to its short half-life, when the accumulation and storage times were increased.

Although the 5-ms isomer of ^{125}In could be clearly identified, accurately fitting the small

shoulder peak corresponding to this high-lying isomer state requires an accurate description of the peak shape of the ground and low-lying isomer states with special attention to the description of the peak tails. Achieving this in the measured mass-to-charge spectrum shown in Fig. 4.4, however, is very challenging, because the largest peak in the spectrum corresponds to the IOIs, which is broader due to the overlapping peaks of the ground and low-lying isomeric states. Any other peaks in the measured spectrum including the peak of ^{125}Sn ions, which was used to obtain the peak shape in this work, have less events by an order of magnitude or more compared to the peaks of the IOIs. This prevented an accurate peak-shape description and, therefore, in the first attempt to analyse this measurement, neither the low-lying nor the high-lying isomer could be fit independently from the ground state. An accurate mass determination of these isomer states requires further analysis and will be presented in a future paper.

Overall, the fact that the 5-ms isomer could be observed in these mass measurements, which is the shortest-lived state measured so far with TITAN's MR-TOF-MS, highlights the fast, non-scanning and sensitive measurement characteristics of the setup (see Fig. 1.3 for a comparison of the mass accuracies achieved using different direct mass measurement techniques and the half-lives of the measured isotopes).

Comparison between the measured and literature mass values

Many mass and excitation energy values corresponding to the ground and isomeric states of $^{125-132}$In isotopes were measured directly or indirectly prior to the mass measurements reported here. The mass and excitation energy values reported in the NUBASE2020 [Kondev et al., 2021] are based on, e.g., Penning-trap mass measurements performed at TITAN, IGISOL and CARIBU [Van Schelt et al., 2013, Hakala et al., 2012, Kankainen et al., 2013, Babcock et al., 2018, Nesterenko et al., 2020] or based on, e.g., Q_β measurements from Refs. [Gausemel et al., 2004, Fogelberg et al., 2004, Mezilev et al., 1995]. Additionally, recently, the mass and excitation energy of the ground and isomeric states of ^{127}In and ^{129}In were also measured at IGISOL using a Penning trap employing the PI-ICR technique [Jaries et al., 2024]. Some of the mass and excitation energy values reported in the primary literature as listed above disagree with each other depending on the used measurement technique, which motivates an independent direct mass measurement of these values. Furthermore, direct mass measurements of the neutron-rich indium isotopes of interest and other nuclides in that region of the nuclear chart frequently found significant systematic deviations from their masses determined indirectly via β end-point measurements (see, for example, the discussions in Refs. [Van Schelt et al., 2012, Van Schelt et al., 2013]). This further demonstrates the need for accurate, direct mass measurements of these neutron-rich isotopes of interest.

Tables 4.1 and 4.3 and Fig. 4.5 present a summary of the measured mass and excitation energy values of the ground and isomeric states of $^{125-134}$In isotopes observed in the measurements reported here and their comparison to the values reported in the NUBASE2020 [Kondev et al., 2021] and in Ref. [Jaries et al., 2024].

In order to check whether the mass values and uncertainties have been accurately determined in the mass measurements reported here, the ions of interest, where previous direct mass measurements were available, were used to check the scatter of the deviations between the measured and literature masses given in the NUBASE2020 [Kondev et al., 2021]. The consistency checks, highlighted in Fig. 3.13, indicate that the value of $\delta m_{\text{syst}}/m = 3 \times 10^{-7}$ [Will, 2017] used as an upper limit for the relative value of the systematic uncertainties of TITAN's MR-TOF-MS may have been slightly overestimated for the presently-reported measurements. Nevertheless, the results of these consistency checks are, in general, indicative of an accurate mass value determination in these measurements (see more details in Section 3.6).

A comprehensive comparison between the measured mass and excitation energy values and the corresponding literature values can be found in [Izzo et al., 2021] for all observed neutron-rich

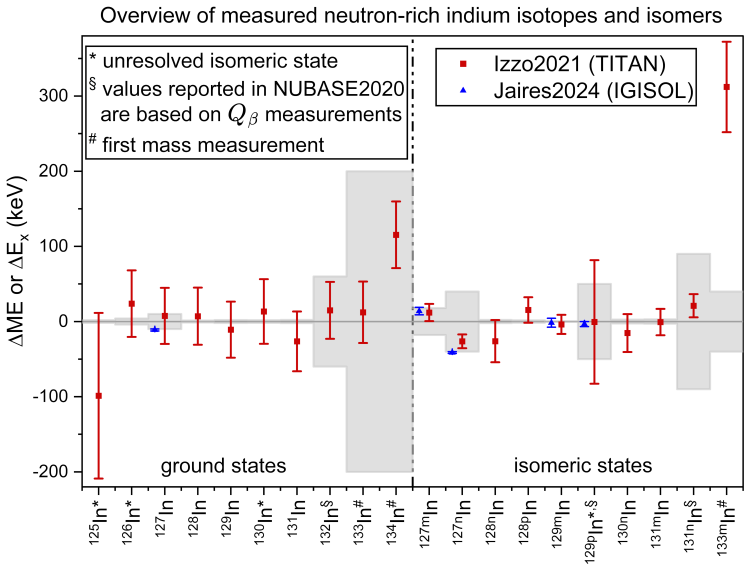

Figure 4.5: Deviation of the measured ground-state mass excesses (ΔME = ME$_{\text{TITAN}}$ − ME$_{\text{lit}}$ given in Table 4.1) and isomer excitation energies ($\Delta E_x = E_{x,\text{TITAN}} - E_{x,\text{lit}}$ given in Table 4.3) from the values given in the NUBASE2020 [Kondev et al., 2021] corresponding to the observed neutron-rich indium ions. The gray band represents the uncertainties given in the NUBASE2020 and the uncertainties of the red data points show the uncertainties determined in the mass measurements reported here (see also in Ref. [Izzo et al., 2021]). For comparison, the results of the recent mass measurements performed at IGISOL and reported in Ref. [Jaries et al., 2024] are shown as blue data points. The mass of the ground states of ^{133}In and ^{134}In and the excitation energy of the isomeric state of ^{133m}In given in the NUBASE2020 are not derived from experimental data, but based on extrapolations. These values were measured for the first time.

indium states. In the following, a few examples will be highlighted, where the measurements reported here provided new or substantial complementary information compared to the AME2020 [Huang et al., 2021, Wang et al., 2021] in case of the ground states and the NUBASE2020 [Kondev et al., 2021] or the ENSDF [ENSDF, 2024] in case of the isomeric states:

- **^{127n}In:** The excitation energy of the high-lying isomer state of ^{127n}In given in the NUBASE2020 [Kondev et al., 2021], 1770(40) keV, is based on two slightly contradictory measurements. Firstly, the Q_β measurements from Ref. [Gausemel et al., 2004] suggested an excitation energy value of 1863(58) keV. Secondly, the mass measurements performed using TITAN's Penning trap reported in Ref. [Babcock et al., 2018] resulted in an excitation energy of 1697(49) keV showing a deviation of about three standard deviations from the results of the Q_β measurement. In the here-presented mass measurements using TITAN's MR-TOF-MS a value of 1743.7(92) keV was determined, which is in agreement with the results using TITAN's Penning trap and reduces the uncertainty of the excitation energy by a factor of five. In comparison, the recent Penning-trap measurements performed at IGISOL [Jaries et al., 2024] resulted in a value of 1728.7(12) keV, which further reduces the uncertainty and only slightly deviates from the value reported here.

- **^{128p}In:** A new, high-lying isomeric state of ^{128}In, notated as ^{128p}In in NUBASE2020 [Kondev et al., 2021], was discovered by Penning-trap measurements performed at IGISOL and reported in Ref. [Nesterenko et al., 2020]. Independently from and in parallel to the studies performed at IGISOL, the identification of this high-lying isomeric state was confirmed with an excitation energy of 1813(17) keV in the mass measurements reported here, which

is in agreement with the excitation energy determined by the JYFLTRAP measurements (see Table 4.3 and Fig. 4.2). These results highlight the non-scanning measurement characteristics of the MR-TOF-MS making it an efficient tool for the discovery of new isomer states, see e.g. [Hornung et al., 2020].

- **^{129p}In:** The excitation energy of the high-lying isomer state of ^{129p}In given in the NUBASE2020 [Kondev et al., 2021], 1650(50) keV, is based on Q_β measurements from Ref. [Gausemel et al., 2004]. In that same work, another isomer state of ^{129q}In was also proposed based on an observed 281-keV γ transition with a 110-ms half-life, which was suggested to be an E3 transition from the isomeric state of ^{129q}In to the isomeric state of ^{129p}In. These two isomeric states could not be resolved by TITAN's MR-TOF-MS, therefore they were fitted together applying the 2(fixed)+1(free) peak fitting method, i.e. treating the ground and low-lying isomeric states of ^{129}In as fixed peaks and fitting the mass and areal ratio of the two high-lying states together. Afterwards, the reported mass of the high-lying isomer state of ^{129p}In was adjusted to take into consideration the possible isomeric contamination yielding an excitation energy of 1649(82) keV. Despite their limited accuracy, the mass measurements reported here provide complementary information on the excitation energy of ^{129p}In in addition to the previous Q_β measurements. In comparison, the recent Penning-trap measurements performed at IGISOL [Jaries et al., 2024] resulted in an excitation energy value of 1646.6(33) keV in agreement with the value reported here, but significantly decreasing the uncertainties.

- **^{131}In and ^{131m}In:** The ground-state mass excess of ^{131}In reported in the AME2020 [Huang et al., 2021, Wang et al., 2021] is based on two contradicting values, which were obtained from Penning-trap mass measurements performed at IGISOL and CARIBU [Hakala et al., 2012, Van Schelt et al., 2013]. Due to the presence of an unknown mixture of the ground and isomeric states in the CPT measurement, the deduced ground-state mass excess deviated by 149(35) keV from the value obtained by JYFLTRAP. In the mass measurements reported here, the ground and low-lying isomeric states of ^{131}In could be separated (see Table 4.1 and Fig. 4.2) and the determined ground-state mass excess agrees with the value obtained in the JYFLTRAP measurements, thus resolving the contradiction. Similarly, the excitation energy of the low-lying isomer state of ^{131m}In given in the NUBASE2020 [Kondev et al., 2021], 376(3) keV, is based on two slightly contradicting values deviating by 63(33) keV from each other, one of which was obtained from Q_β measurements from Ref. [Fogelberg et al., 2004] and the other one was obtained in Penning-trap mass measurements performed at IGISOL [Kankainen et al., 2013]. In the presently-reported mass measurements performed using TITAN's MR-TOF-MS, an excitation energy of 375(18) keV has been determined, which agrees with the value obtained in the JYFLTRAP measurements.

- **^{131n}In:** The excitation energy of the high-lying isomer state of ^{131n}In given in the NUBASE2020 [Kondev et al., 2021], 3750(90) keV, is based on Q_β measurements from Ref. [Fogelberg et al., 2004]. In the presently-reported mass measurements performed using TITAN's MR-TOF-MS, an excitation energy of 3771(15) keV has been determined (see Table 4.3 and Fig. 4.2), which is in excellent agreement with the value derived from Q_β measurements and reduces the uncertainty by more than a factor of five.

- **^{132}In:** The ground-state mass of ^{132}In was measured directly for the first time. The mass excess of ^{132}In reported in the AME2020 [Huang et al., 2021, Wang et al., 2021], $-62410(60)$ keV, is based on Q_β measurements from Ref. [Mezilev et al., 1995]. As discussed earlier, previous direct mass measurements in this region have found significant deviations from indirectly measured masses derived from β decay end-point energy measurements, emphasizing the importance of direct mass measurements. In the presently-

reported mass measurements performed using TITAN's MR-TOF-MS, a mass excess of $-62395(38)$ keV has been determined for ^{132}In, which agrees with the value derived from Q_β measurements and slightly reduces the uncertainty. Notably, the ^{132}In isotope has no experimentally known or predicted isomeric states so far, and none were observed in the mass measurements reported here either (see Fig. 4.3).

- **^{133}In and ^{133m}In:** The mass of the ground state of ^{133}In and the excitation energy of the isomeric state of ^{133m}In was measured for the first time, which would not have been possible without the usage of the mass-selective re-trapping technique (see Fig. 4.3). The first experimental proofs supporting the existence of the isomeric state of ^{133m}In with spin/parity of $(1/2^-)$ were presented in Refs. [Hoff et al., 1996, Piersa et al., 2019, Benito et al., 2020] based on the population of the ground and excited states of ^{133,132}Sn via ^{133}In β^- and ^{133,134}In $\beta^- n$ decays. On the other hand, its excitation energy given in the NUBASE2020 [Kondev et al., 2021], 330(40) keV, is not derived from experimental data, but based on the trend of the energy difference between the $(9/2^+)$ ground states and the $(1/2^-)$ isomeric states in odd-A indium isotopes in the vicinity. In comparison, the presently-reported mass measurements performed using TITAN's MR-TOF-MS resulted in an excitation energy of 642(60) keV for this isomeric state, which is significantly larger than the previous value based on systematic trends.

- **^{134}In:** The mass of the ground state of ^{134}In was measured for the first time, which would not have been possible without the usage of the mass-selective re-trapping technique. Notably, the ^{134}In isotope has no experimentally known or predicted isomeric states so far that are long-lived enough to be possible to be observed using TITAN's MR-TOF-MS ($T_{1/2} > 1$ ms), and none were observed in the mass measurements reported here either (see Fig. 4.3).

4.3 Desired improvements

In summary, this chapter presents details about the experimental setup and data analysis concerning the mass measurements of neutron-rich indium isotopes across the $N = 82$ shell closure performed using TITAN's MR-TOF-MS at TRIUMF, the results of which were published in [Izzo et al., 2021]. The multiplicity and variety of the long-lived ($T_{1/2} > 1$ ms) states of the ions of interest observed in these measurements pose considerable challenges both for the measurement and data analysis technique.

As an outlook, it is worth mentioning that the accuracy of the mass measurements reported here could, in principle, be further improved in the future with different developments to the mass measurement and data analysis techniques. A few examples of the desired improvements are listed below:

- Recently, the mass resolving power of TITAN's MR-TOF-MS has been improved significantly, routinely reaching mass resolving powers of $R_m > 600,000$, see e.g. [Porter et al., 2022]. With this improvement, the observed close-lying ground and isomeric states could be better separated from each other.
- The recent development of the technique called as "post re-trapping beam merging" enables to measure non-isobaric species, e.g., from the thermal ion source of TITAN's MR-TOF-MS, together with the beam-like isobaric ions of interest separated by the technique of the mass-selective re-trapping, see more details in Ref. [Jacobs, 2023]. Applying this technique would enable to include at least one fully isolated, high statistics peak in the measured spectra. These peak(s) could be used to accurately determine the peak shape in the given measurements, which is crucial for the treatment of overlapping peaks.

- With further studying the systematic uncertainty sources of TITAN's MR-TOF-MS, an overestimation of the systematic uncertainty component can be prevented in future measurements yielding more accurate estimates of the experimental uncertainties, see e.g. [Dunling, 2021, Jacobs, 2023, Lykiardopoulou et al., 2025] demonstrating that relative mass uncertainties of $\delta m/m \sim 1 \times 10^{-7}$ are reached routinely nowadays.
- Concerning the data analysis procedure, the development of a more generalized treatment of multiple overlapping TOF peaks still remains a task for the future.

Chapter 5

Mass measurements of neutron-deficient nuclides close to the $N = Z$ line below ^{100}Sn at FRS Ion Catcher, GSI

During the S474 experiment within FAIR Phase-0, neutron-deficient nuclides close to the $N = Z$ line below ^{100}Sn were measured at FRS-IC, GSI, see Section 1.2.3 for an introduction.

The exotic nuclei of interest were produced via projectile fragmentation at the FRS [Geissel et al., 1992] at GSI by impinging a 790 MeV/nucleon ^{124}Xe primary beam on a beryllium production target of 8045 mg/cm^2 areal density with primary beam intensities of approximately 1.2×10^9 ions per spill. While part of the results, including the first direct mass measurements of ^{98}Cd, were reported in Ref. [Mollaebrahimi et al., 2023b] and are omitted here, the first direct mass measurement of ^{93}Pd and its consequences are part of this work. In the first part of the measurements the typical spill length was 2 s with a spill period of approximately 3.5 s, while in the second part it was changed to a spill length of 1 s with a period of 2.5 s with the goal to maximize the integral of the count rate/yield. The produced fragments were separated in flight at the FRS, which was centered on ^{93}Pd, and they were delivered to the FRS-IC [Plaß et al., 2013a]. The monoenergetic Al-degrader at the central focal plane of the FRS had an areal density of 735 mg/cm^2. In addition to their accurate mass measurement at the FRS-IC, the ions were also identified by the FRS particle identification (PID) system. At the FRS-IC the ions were slowed down and thermalized in the gas-filled CSC, then they were extracted and transported via the RFQ beamline to the MR-TOF-MS for performing direct mass measurements. The pressure and the temperature of the helium gas inside the CSC was 100(5) mbar and 102(2) K, respectively, corresponding to an areal gas density of 4.7(3) mg/cm^2. In the RFQ beamline the isolation-dissociation-isolation method [Greiner et al., 2020] was used to suppress molecular background ions generated in the CSC. In the MR-TOF-MS the mass measurements were performed by injecting the ions into the TOF analyzer and confining them for about 750 isochronous turns between two electrostatic mirrors, corresponding to a time-of-flight of approximately 22 ms. In the center of the TOF analyzer the mass range selector was used to limit the mass-to-charge range to $m/q \sim (91 - 93)$ u/e and thus to suppress the ambiguity in the time-of-flight (TOF) spectra. Afterwards, the ions were ejected from the TOF analyzer towards the TOF detector, where the time-of-flight of the different ion species with different mass-to-charge ratios (m/q) was recorded. The mean ion extraction and measurement time from the CSC to the TOF detector of the MR-TOF-MS was about 130 ms.

The MR-TOF-MS was operated at 25 Hz repetition rate in order to enable longer flight

paths and larger resolving power. A few days before the measurements a quick and reliable change of repetition rate from the previous 50 Hz operation was performed, which was facilitated by the resistive divider commissioned before the S474 experiment (see Section 2.2). For the measurements reported here, a mass resolving power at full width at half maximum (FWHM) of 700,000 was achieved.

The production cross section of ^{93}Pd by projectile fragmentation of ^{124}Xe is only 8.6(10) nb [Suzuki et al., 2017], which is the smallest production cross-section of an ion of interest for which a mass measurement was achieved with the FRS-IC so far. Besides the fact that the FRS-IC has been proven to be a well-suited experimental setup for performing highly-accurate direct mass measurements with only a few detected ions per nuclide [Hornung et al., 2020, Mardor et al., 2021], in the S474 experiment two key techniques were applied in order to cope with the challenge of small production cross-sections and enable the successful measurement of ^{93}Pd and, within the same setting, ^{92}Rh. An overview of these two key approaches can be found in [Dickel et al., 2024]. Here, the most important aspects of these approaches are outlined:

1. Firstly, in order to achieve an efficient way of data taking, a novel technique was used to stop more than one nuclides in the CSC without significant efficiency losses. Because of the areal density of the CSC of a few mg/cm^2 only, it is usually difficult to stop and extract several exotic nuclides from the CSC at the same time, because the range of an ion depends on its mass and charge as well as its kinetic energy. In order to stop several nuclides of interest, usually several different degrader settings are needed. For the region of the nuclear chart addressed in this experiment, however, isotones can be manipulated to have the same range, if their kinetic energy after leaving the target amounts to about 300 MeV/nucleon. In this experiment, the primary beam energy was chosen accordingly, such that the three N=47 isotones ^{93}Pd, ^{92}Rh and ^{91}Ru were stopped simultaneously in the CSC, and, because of the broadband capabilities of the MR-TOF-MS, could be measured at the same time, directly yielding the corresponding one- and two-proton separation energies. During the measurements the FRS was operated in monochromatic mode, which enabled maintaining the maximum stopping efficiency for the three N=47 isotones of interest. This latter feature represents an important difference between this approach to simultaneously stop isotones and the technique of mean-range bunching, for which the FRS is operated in achromatic mode [Dickel et al., 2023]. This approach was developed specifically for this experiment, but is applicable broadly at synchrotron facilities for many proton-rich nuclides.

2. Secondly, in this experiment, the thickness of the production target (8045 mg/cm^2) was chosen large enough, such that secondary (multi-step) reactions started to play a significant role in the overall production of the fragments, thus increasing their production yields. On the other hand, generally, the increased thickness of the production target also results in an increased location straggling of the reactions inside the target, which can lead to significant efficiency losses in the further downstream parts of the measurement setup after the production target, including, e.g., a decreased transmission efficiency through the FRS and a decreased stopping efficiency in the cryogenic stopping cell. The location straggling in the target is minimized for the cases, when the primary beam and the fragment beam has the same energy loss inside the target, which ensures that the downstream efficiency losses are minimized in this special case. In this experiment, a ^{124}Xe primary beam was used, thus this latter condition applies for the measured fragments of interest, i.e. ^{98}Cd and ^{93}Pd have similar A/Z^2 ratio as ^{124}Xe. Ultimately, this enables that the usage of the thick production target can lead to an increased number of the ions of interest that are slowed down, thermalized and measured at the FRS Ion Catcher.

This chapter presents details of data analysis and discussion of the results of the S474 experiment with emphasis on the the first direct mass measurement of ^{93}Pd.

5.1 Verification of identification: yields observed in FRS vs. FRS Ion Catcher

The measurement of the neutron-deficient nuclides, including ^{93}Pd, ended earlier than expected due to a failure of the RF carpet of the CSC. As a result, only a few isotopes, the ones detected with high count rate, could be measured in a second MR-TOF-MS settings with a different turn number to confirm their correct identification. In addition, besides the goal isotones of ^{93}Pd, ^{92}Rh and ^{91}Ru at $N = 47$, which were planned to be stopped simultaneously by the cryogenic stopping cell, more unexpected, beam-correlated peaks appeared in the mass spectra corresponding to $N = 48 - 50$ isotones. As the first step of the data analysis, the correct identification of the measured isotopes had to be ensured and the mystery behind the detection of the unexpected nuclides had to be understood. This was achieved via comparing the yields of the isotopes measured by the FRS PID detectors to the yields measured by the MR-TOF-MS of the FRS Ion Catcher, which will be called as "efficiency analysis" in the following.

In order to ensure that the conclusions of the efficiency analysis are independent from the used experiment settings or the measured isotopes, the comparison of the synchronously-acquired FRS PID and FRS Ion Catcher data was extended to five different measurements. Table 5.1 shows a comparison of the different measurement settings and measured nuclides that were a subject of this analysis. While the settings used for the mass measurements reported in Ref. [Mollaebrahimi et al., 2023b] (in Table 5.1 named as settings2/3) were similar to the settings used for the measurement of ^{93}Pd (named as settings1), the measurement settings used for the validation of the experimental setup and the calibration of detectors using primary beam of ^{124}Xe and fragment beam with FRS center isotope of ^{115}Te (settings5 and settings4, respectively) was significantly different. This leads to increased uncertainties for the deduced relative efficiencies using the data obtained with settings4/5 as compared to the data obtained with settings1/2/3.

Analysis of FRS PID data and explanation of the changed stopping range of the unexpected isotopes

The FRS PID data were analyzed by C. Hornung [Hornung et al., 2022] (priv. comm.), here only the most important steps and corresponding conclusions of the FRS PID data analysis will be outlined. Firstly, the FRS PID plots were filtered by throwing away the nonphysical events with applying cuts based on different conditions, such as ensuring that the identified nuclides are not faster than the speed of light or filtering out the nuclides, whose trajectories that are outside of the used slits. One of the filtered FRS PID plots, which was prepared for the monoenergetic FRS settings with FRS center isotope of ^{93}Pd, is shown on Fig. 5.2b. In the next step, the count rate of the different beam-like isotopes hitting the cryogenic stopping cell was estimated. For the task, three correction factors were defined and calculated for the different measurement settings and corresponding isotopes, see Table 5.3 for their average values and definitions. Those correction factors were then applied to the number of counts belonging to the isotopes determined from the FRS PID plots resulting in the estimate of the number of counts of the beam-like isotopes hitting the cryogenic stopping cell. The FRS correction1 and correction2 factors are mostly influenced by the count rates at the central and the final focal planes of the FRS, which were smaller in case of the measurements with FRS center isotopes of ^{115}Te and ^{124}Xe, while larger in case of the measurements with FRS center isotopes of ^{93}Pd and ^{98}Cd. The FRS correction3 factor was determined by calculating the number of events in the FRS PID plots, which corresponded to a hit fired at the most downstream scintillator mounted close to the cryogenic stopping cell (named as Scintillator43 or SCI43 in the following) and dividing this number by the total number of events determined from the FRS PID plot. Note that the deduced 50-60% value of FRS correction3 factor (see Table 5.3) is smaller than

the 70(2)% measured in [Purushothaman et al., 2013], which was assigned to the losses due to nuclear reactions in the variable degrader. Although a one-to-one comparison is not possible due to the difference in fragment beam energies between the past and present measurements, this may indicate that there are more than one contributions to the FRS correction3 factor. Indeed, as a result of this efficiency analysis, it was found out that FRS correction3 factor has two main contributions: (i) it accounts for the losses due to fragmentation and fission inside the variable degrader in the final focal plane of FRS and (ii) it accounts for the losses due to the by-passing of Scintillator43.

The latter contribution (ii) is due to the fact that the height dimension of the Scintillator43, i.e. its dimension along the vertical axis perpendicular to the beam direction (further called as the y axis), was smaller as compared to the other FRS PID detectors, therefore some fraction of the beam may have a trajectory that flies next to ("by-passes") this scintillator, see Fig. 5.1 for a schematic illustration. Fig. 5.2a shows the angle between the trajectories of the ions and the beam direction and the y position of the ions measured by the time projection chamber (TPC) mounted at the final focal plane of the FRS is plotted. The TPC data is first gated on the hits in Scinillator42 resulting in the plot on the left side, while gating on the hits in the Scinillator43 results in the plot on the right side. Since Scinillator42 has a larger height (covering the full beam spot size) as compared to Scintillator43, the plot on the left side shows a broader beam spot distribution as compared to the plot on the right side, which looks more looks more restricted/cut, demonstrating that a portion of the ions may indeed fly by Scintillator43 without firing a hit there. Since Scintillator43 has a thickness of ∼100 mg/cm^2, the stopping range of the ions by-passing it becomes different compared to the ions that correspond to a hit inside Scinillator43. In order to estimate the stopping range difference due to by-passing Scintillator43 simulations with LISE++ [Tarasov & Bazin, 2008] were done using the settings1 with FRS center isotope of ^{93}Pd. The result of the simulations showed that the stopping range of ^{93}Ru, when by-passing the Scintillator43, becomes the same as the stopping range of ^{93}Pd without by-passing it. Since the experiment was set up in a way that the isotones have a similar stopping range, the LISE++ simulations suggest that the three $N = 47$ isotones without by-passing the Scintillator43 is expected to have a similar stopping range as the isotone lying closer to the valley of stability by 2 neutrons at $N = 49$, when by-passing this scintillator. The determined global FRS Ion Catcher efficiencies corresponding to settings1 as shown in Fig. 5.3 illustrate that this simulation results are consistent with the experimental observations, i.e. the measured global efficiencies are about an order of magnitude higher for the $N = 47$ and $N = 49$ isotones as compared to the $N = 48$ isotones. This suggests that the possibility that a certain portion of the beam by-passes the Scintillator43 would provide an explanation for the appearance of the unexpected beam-like isotopes in the mass spectra measured with the MR-TOF-MS. Unfortunately, a precise quantification of the portion of the beam by-passing Scintillator43 is not possible, because during the measurements MUSIC43 detector shown on Fig. 5.2a was switched off, thus the losses due to by-passing Scintillator43 could not be fully disentangled from the losses due to fragmentation and fission inside the variable degrader in the final focal plane of FRS.

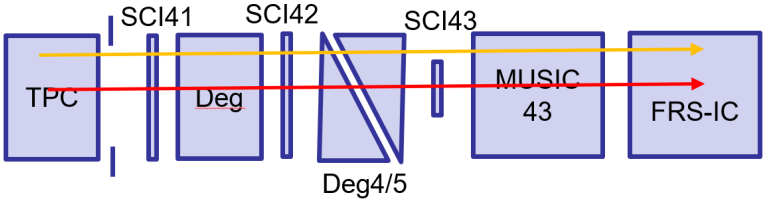

Figure 5.1: Schematic view of elements (PID detectors, degraders and slits) inserted in the final focal plane of the FRS during the S474 experiment. During the measurements the MUSIC43 was switched off. This figure also illustrate that a fraction of the beam may by-pass Scintillator43.

Table 5.1: Summary of the used measurement settings and the measured nuclides, whose yields observed in FRS and FRS Ion Catcher were determined and compared with each other to verify their correct identification.

	Settings1	**Settings2**	**Settings3**	**Settings4**	**Settings5**
FRS center isotope	^{93}Pd	^{98}Cd	^{98}Cd	^{115}Te	^{124}Xe (primary beam)
FRS settings description	monoenergetic			achromatic	"mixed" (no S2 degrader, no production target)
FRS-IC settings description	high resolving power			low resolving power	
Identified isotopes at FRS-IC	^{93}Pd, ^{92,93}Rh, $^{91-93}$Ru, $^{91-93}$Tc, ^{91}Mo[a]	^{98}Cd, ^{97}Ag, $^{96-98}$Pd, ^{96,97}Rh, ^{96}Ru[b]	^{100}Cd, ^{99,100}Ag[b]	^{115,116}Te	^{124}Xe
Expected (goal) isotopes at FRS-IC	^{93}Pd, ^{92}Rh, ^{91}Ru	^{98}Cd, ^{97}Ag, ^{96}Pd	^{100}Cd, ^{99}Ag	^{115,116}Te	^{124}Xe
Date and time of data acquisition	05:26-08:47[c] AM 07/03/2020	21:45-23:30 PM 06/03/2020	00:40-01:06 AM 07/03/2020	06:10-06:14 AM 02/03/2020	04:12-04:29 AM 02/03/2020
Primary beam information and FRS settings details	The ^{124}Xe primary beam energy, intensity, spill structure, the thickness of the production target, the position of the used slits, the angle of the wedge-shaped degrader at the central focal plane and the thickness of the degrader at the final focal plane of FRS were varied between the different settings.				
FWHM of measured stopping range distribution	22.6(20) mg/cm^2			92.3(75) mg/cm^2	32.5(1) mg/cm^2
CSC areal density	4.7(3) mg/cm^2			2.5(2) mg/cm^2	2.2(1) mg/cm^2
Total extraction time from CSC to TOF detector	∼130 ms			∼75 ms	∼70 ms
FRS-IC RFQ beam line settings	Similar settings of the FRS-IC RFQ beam line, i.e. same CID step, same pressures and similar low-mass cut-off of RFQs			Different settings of the RFQ beam line	
MR-TOF-MS settings	Similar settings of the MR-TOF-MS, i.e. 25 Hz repetition rate, same pressures and high turn number of 730-850 turns (high mass resolving power at FWHM up to almost 1 million)			Different settings of the MR-TOF-MS, i.e. 50 Hz repetition rate, different pressures and low turn number of about 64 turns	

[a] The measured mass spectrum also contained spontaneous fission products of the ^{252}Cf source (namely the nuclides $^{91-93}$Rb), which were used for calculating an independent estimate of the global efficiency of the FRS Ion Catcher setup.

[b] The results of the mass measurements were published in Ref. [Mollaebrahimi et al., 2023b].

[c] The same settings was also used to acquire more data on ^{93}Pd and its neighbouring isotopes at 14:01-14:29, 15:13-15:28 PM and 15:37-16:11 PM on 07/03/2020.

Table 5.3: The definitions and average values of the three FRS correction factors that were defined and calculated for the different measurement settings and isotopes.

	FRS center isotope	FRS correction1[a]	FRS correction2[b]	FRS correction3[c]
Settings1	^{93}Pd	4.68	2.93	0.52(2)
Settings2	^{98}Cd	5.21	3.07	0.52(2)
Settings3	^{98}Cd	5.15	3.06	0.52(4)
Settings4	^{115}Te	1.55	1.26	0.59(5)
Settings5	^{124}Xe	1.29	1.47	0.564(1)

[a] Accounts for the losses due to the efficiency and dead time of all the different detectors used in the FRS PID.

[b] The accepted-to-free trigger ratio (in the table named as FRS correction2 factor) was used to estimate the losses due to the dead time of the FRS data acquisition system.

[c] Accounts for the losses due to fragmentation and fission inside the variable degrader in the final focal plane of FRS and the losses due to by-passing Scintillator43.

Determination of the global efficiency of FRS Ion Catcher

The next steps of this efficiency analysis were based on data obtained by the FRS Ion Catcher. The main goal of this step was to correct the number of beam-like isotopes hitting the CSC, such that all settings-dependent and/or isotope-dependent efficiency components of the FRS Ion Catcher setup are removed from the number of ions hitting the CSC. For the task, three FRS Ion Catcher efficiency correction factors were defined, calculated and summarized in Table 5.5, the values of which are either settings-dependent and/or isotope-dependent. In the next step, the number of isotopes measured in the mass spectra obtained by the MR-TOF-MS were determined and divided by the number of ions hitting the CSC, which were multiplied by the above-defined correction factors. Ideally, when the three FRS-IC efficiency correction factors are correctly determined, this procedure should yield in the global extraction, transport and detection efficiency of the FRS-IC setup, which is independent from the measurement settings and/or the measured isotopes. On the other hand, in reality the determination of those three efficiency factors (especially in case of the stopping and chemical efficiencies) was hindered by multiple sources of inaccuracies due to the assumptions that were made during determining their "best guess" estimates. As shown in Table 5.1, the FRS-IC RFQ beam line and MR-TOF-MS settings were almost the same for the measurement settings1/2/3, therefore the related efficiency correction factor is only considered as a relative correction to account for the changed transmission of the experiment settings4/5 due to the different RFQ beam line and MR-TOF-MS settings. This relative efficiency correction factor was estimated based on various offline data measured before the beam time, which aimed at understanding the dependence of the transmission of the setup on different properties, such as buffer gas pressures or number of turns used in the MR-TOF-MS. On the contrary to this, the stopping and chemical efficiency corrections were considered as absolute corrections, the "best guess" estimation of which is explained in the following.

The stopping efficiency of the beam-like isotopes was estimated following the procedure explained in [Reiter, 2015, Purushothaman et al., 2013]. First the stopping range distribution was measured with the FRS Ion Catcher via varying the thickness of the FRS degrader at the final focus plane and monitoring the count rate of the ions stopped in the CSC and detected by the TOF detector of the MR-TOF-MS relative to the intensity of the primary beam. Then the measured stopping range distributions were analyzed individually for each measurement settings (see Table 5.1 for the determined FWHM of the range distributions). The stopping efficiency

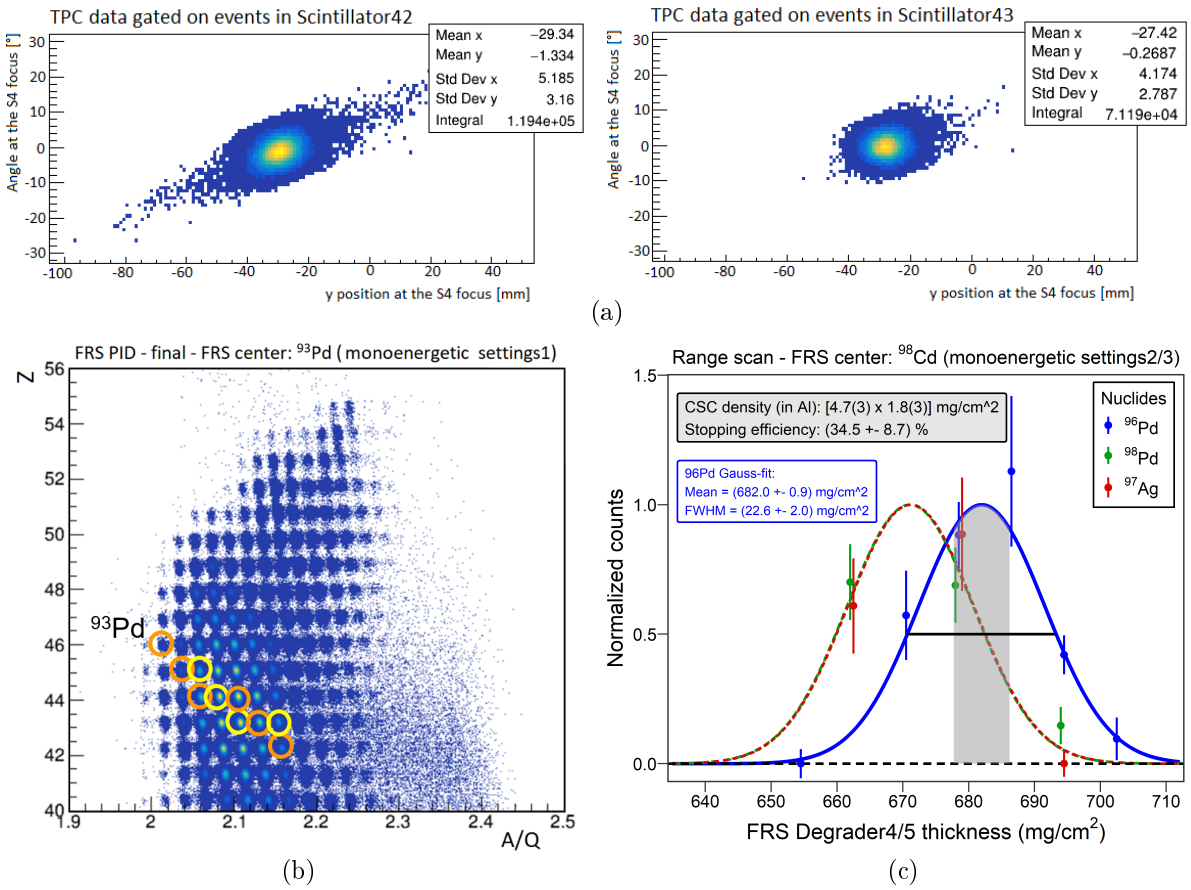

Figure 5.2: Example plots showing a few steps of the combined FRS PID & FRS Ion Catcher efficiency analysis. The example plots are based on results with the 3 different monoenergetic FRS settings (settings1/2/3). (a) The angle between the trajectories of the ions and the beam axis and the y position of the ions measured by time projection chamber (TPC) mounted at the final focal plane of the FRS is plotted for the settings1 with FRS center isotope of ^{93}Pd. The TPC data is first gated on the hits in Scinillator42 resulting in the plot on the left side, while gating on the hits in the Scinillator43 results in the plot on the right side. The pictures demonstrate that a certain portion of the beam may by-pass the Scinillator43, i.e. while the plot on the left side describes a broader beam spot distribution, the plot on the right side looks more restricted/cut at a certain y position and angle. (b) The final filtered FRS PID plot is shown for the settings1 with FRS center isotope of ^{93}Pd. (c) The stopping range distribution and the corresponding stopping efficiency estimate of the ^{97}Ag, ^{96}Pd and ^{98}Pd isotopes measured with the FRS Ion Catcher is shown. The measured abundances of the different isotopes were normalized by the maximum of the Gauss-fits, because the range scan of ^{98}Pd and ^{97}Ag (corresponding to the green and red data points, respectively) was carried out under a bit different measurement conditions as compared to the range scan of ^{96}Pd (corresponding to the black data points). However this differences in the measurement conditions don't affect the stopping range of the different isotopes, it only affects their abundance. When the uncertainty bands overlapped a jitter was introduced to the points to increase the readability of the plot. This jitter only affects the plot of the individual points it doesn't affect the Gaussian-fits. The blue curve shows a Gauss-fit of the range scan of ^{96}Pd, while the red and green dashed curves are Gauss-fits of the range scans of ^{97}Ag and ^{98}Pd, respectively, with a fixed FWHM from the blue fit of ^{96}Pd rage distribution. The gray region below the ^{96}Pd range distribution indicates the areal density covered by the cryogenic stopping cell.

Table 5.5: The definitions and values of the three FRS Ion Catcher correction factors that were defined and calculated for the different measurement settings and isotopes. The top part of the table contains the efficiency corrections, which were handled during the analysis as isotope-independent and only settings-dependent, while the bottom part, which is separated by two horizontal lines, contains the element-dependent chemical efficiency. For completeness the tables also include the efficiency correction factors that were used to achieve an independent estimate of the global extraction, transport and detection efficiency of the FRS-IC setup achieved via counting the spontaneous fission products of the ^{252}Cf source (namely the nuclides $^{91-93}$Rb) observed in the MR-TOF-MS mass spectra obtained using measurement settings1.

	Description of settings	Stopping efficiency correction[a]	Relative efficiency corr. (RFQs & MR-TOF-MS)[b]
Settings1/2/3	FRS center: ^{93}Pd/^{98}Cd	0.35(9)	1
Settings4	FRS center: ^{115}Te	0.05(1)	7.8(46)
Settings5	FRS center: ^{124}Xe	0.11(2)	7.0(44)
Settings1	observed fission products of the ^{252}Cf source ($^{91-93}$Rb)	0.15(3)[c]	1

Element	Measurement settings	Proton-number Z	Chemical efficiency corr.[d]
Cd, Ag, Pd, Rh, Ru, Tc	Settings1/2/3	43-48	∼1
Mo	Settings1	42	0.24(39)
Te	Settings4	52	0.60(34)
Xe	Settings5	54	0.08(14)
Rb	Settings1	37	∼1

[a] Estimates the losses due to the stopping efficiency of the different isotopes inside the cryogenic stopping cell. See text for more details.

[b] Relative efficiency correction due to difference in RFQ beam line and MR-TOF-MS settings. This relative correction factor only affects the yields measured with experiment settings4 and settings5, which have a different RFQ beam line and MR-TOF-MS settings, while keeping the yields measured with experiment settings1/2/3 unchanged.

[c] The stopping efficiency of the ^{252}Cf fission products was calculated following the procedure explained in [Waschitz et al., 2023] as the product of the emission efficiency from the Ti-covered source and the geometrical efficiency due to the dimensions of the CSC. Note that in the table the sum of the stopping efficiencies calculated for the three observed fission products of $^{91-93}$Rb is shown.

[d] Estimates the losses due to chemical reactions of the different elements inside the different parts of the FRS-IC setup following a phenomenological model of gas-phase chemistry [Amanbayev et al., 2022], which was built for this study. See text for more details.

was then calculated by the ratio of two integrals; the integral performed in a given window of the range distribution, which corresponds to the areal density covered by the CSC, was divided by the integral over the full range distribution between $\pm\infty$. For determining the first integral covered by the CSC areal density, it was assumed that each isotopes were measured at their optimum stopping range (at the mean of their range distribution). This assumption was necessary, because it was impossible to measure the stopping range distribution for the more exotic nuclides with much smaller production cross-sections within reasonable measurement duration. The devi-

ations from this assumption are expected to lead to significant differences between the stopping efficiencies of the different isotopes. Since the material of the variable degrader is aluminum, while the CSC is filled with helium buffer gas, a conversion factor was used in order to convert the areal density of the CSC in He into an effective areal density in Al and thus account for the ratio of the stopping power in Al to He. Simulations using the ATIMA software [Weick et al., 2018] were performed to estimate this conversion factor corresponding to the isotopes of interest of the present study and the experiment settings, which amounts to 1.8(3). The procedure of calculating the stopping efficiency and its inaccuracies due to the applied assumptions are illustrated in Fig. 5.2c for the monoenergetic FRS settings1/2/3. In the mass measurements reported in Ref. [Mollaebrahimi et al., 2023b] (settings2/3) a similar effect of also detecting certain, unexpected beam-like isotopes was observed. Instead of stopping only one isotone simultaneously (e.g. specifically in case of the monoenergetic settings2: the fragment beam energy and the variable degrader thickness were tuned such that the $N = 50$ isotone, including ^{97}Ag and ^{96}Pd, can be stopped simultaneously), more beam-like isotopes were identified in the mass spectra measured with the MR-TOF-MS of FRS Ion Catcher. In case of this settings2, one important evidence for the correct identification of the originally unexpected nuclide ^{98}Pd at $N = 52$ becomes obvious, when looking at it's range distribution measured with the FRS Ion Catcher (see Fig. 5.2c). Looking at the plot one can observe that ^{98}Pd follows the general behavior (with similar optimum degrader thickness) as the range distributions measured with the nuclides, which were expected to be stopped at the CSC simultaneously at $N = 50$, i.e. ^{97}Ag and ^{96}Pd. This observation provides a strong evidence supporting the correct identification of ^{98}Pd, which is 2 neutrons closer to the valley of stability as compared to the originally expected $N = 50$ isotone. In addition, this observation is also consistent with the earlier-mentioned LISE++ simulation results considering the possibility of by-passing Scintillator43, which suggests that the observed ^{98}Pd events shown on the range distribution measurement Fig. 5.2c may indeed originate from the portion of the beam by-passing this scintillator. The range scan performed with the cryogenic stopping cell also suggests that the assumption of hitting the optimum stopping range for all isotopes (or at least for all $N = 50$ isotones) simultaneously is clearly wrong. To illustrate this using the measured range distributions, the correct value of the stopping efficiency of ^{97}Ag was calculated assuming that the used degrader thickness is at the maximum of the range distribution of ^{96}Pd. In this hypothetical case, the stopping efficiency for ^{96}Pd would be maximal (35(9) %, see Fig. 5.2c), while the stopping efficiency for ^{97}Ag would be factor of 2-3 smaller; i.e. 21(10) %.

The nuclides, which are measured by the FRS Ion Catcher, undergo chemical reactions with the He buffer gas and impurities in the CSC and the residual gas in the rest of the FRS Ion Catcher setup, which leads to element-dependent (chemical) efficiencies. In the study of [Waschitz et al., 2023] a self-consistent method to extract the chemical efficiency correction factors for ^{252}Cf fission products was developed and reported. However, this self-consistent and brute-force method is only applicable for the chemical elements produced and measured using the spontaneous fission source. Moreover the losses due to chemical reactions also depend on the experiment conditions, therefore it is hard to extrapolate them from one measurement to another. In order to overcome this, efforts were made to further understand the underlying chemistry behind the element-dependent efficiencies, the chemical reactions inside the CSC, RFQ beam line and the MR-TOF-MS were studied empirically and a phenomenological gas-phase chemistry model was built [Amanbayev et al., 2022] (priv. comm.), the main assumptions and formalism of which are highlighted below. In the model it is assumed that simple bimolecular reactions [Pohjalainen, 2018] take place in different parts of the FRS-IC setup and the temperature-dependence of the reaction rates is predicted by the Arrhenius equation [Arrhenius, 1889a, Arrhenius, 1889b] and its modifications [Laidler, 1996, Burkholder et al., 2015]. The total time of the chemical reactions is estimated by the extraction time from the CSC to the TOF detector and the element-dependent chemical efficiency is calculated by the ratio of the initial and final concentration of the different

elements of interest after interacting with the impurities inside the FRS-IC setup, which are assumed to have a constant concentration. Although we expect multiple types of impurities in the CSC and the rest of the FRS Ion Catcher setup at a concentration level of ∼1 ppb, such as O_2, N_2, H_2O, CO [Mollaebrahimi et al., 2023a], the available data on the measured reaction rates is rather scarce for the ions of interest of the present study and, to this date, only their reaction rate with O_2 was measured [Anicich, 2003, Manion et al., 2024]. Therefore our simple chemistry model assumes that the ions of interest only undergo chemical reactions with O_2, where the concentration of the reactant was empirically fitted on the data obtained with the ^{252}Cf spontaneous fission source [Waschitz et al., 2023]. Despite the incorrect assumptions of our model, this empirical fit resulted in a considerably-good agreement with the chemical factors of the ^{252}Cf fission products determined by the self-consistent and brute-force method reported in [Waschitz et al., 2023]. After estimating the concentration of the reactant based on the ^{252}Cf data, this phenomenological model was applied to the chemical elements of interests of the present efficiency analysis, which enabled us to calculate an "educated guess estimate" of the element-dependent chemical factors. As shown in the Table 5.5, the resulting chemical factor was only significantly different from 1 in case of the Xe, Te and Mo elements, while the Cd, Ag, Pd, Rh, Ru, Tc and Rb elements experienced no significant chemical losses from reactions with O_2 on the time scales of the extraction times from the CSC. It is worth mentioning that all of the elements of interest of the present study are also produced by the ^{252}Cf source with good fission yields, therefore the validity of the model of gas-phase chemistry can be further tested in future measurements with the spontaneous fission source.

The measured mass spectrum obtained with settings1 also contained spontaneous fission products of the ^{252}Cf source with a known activity of 24(7) kBq mounted inside the cryogenic stopping cell (namely the nuclides $^{91-93}$Rb). Comparing the measured count rate of the fission products with the expected count rate emitted by the source and stopped in the CSC provided an independent estimate of the global extraction, transport and detection efficiency of the FRS Ion Catcher setup. Here, the expected count rate emitted by the ^{252}Cf source was calculated based on its known activity and using the isotopic fission yield and its uncertainty associated with the $^{91-93}$Rb fission products extracted from the ENDF/B-VII.0 database [Chadwick et al., 2006]. The measured fission products were extracted as singly-charged ions from the CSC, so the global FRS Ion Catcher efficiency estimate obtained from their measured count rate is representative of the measured beam-like isotopes in this experiment, which were all extracted as singly-charged ions from the CSC as well. The three FRS-IC efficiency correction factors corresponding to the spontaneous fission products of the ^{252}Cf source are included in Table 5.5.

Comparison of global efficiencies deduced for different settings and nuclides

Following the arguments presented above, ideally, the final value of the determined global FRS Ion Catcher efficiency should be constant for all measured isotopes and settings. Remaining variations from the constant behavior are expected due to three main reasons: (i) the precise portion of the beam by-passing the Scintillator43 is not known, (ii) the assumption of hitting the optimum stopping range for all isotopes is not correct and (iii) the model to estimate the chemical efficiencies of the different elements needs further improvements. Fig. 5.3 shows the normalized global efficiencies of the different isotopes plotted on the nuclear chart in case of two different monoenergetic settings (settings1/2). When looking at the plot, the first thing that one can notice is that the general pattern of the estimated global efficiency is similar to each other in case of the measurements with settings1 and settings2. In more details, all nuclides in the goal isotone of the measurements ($N = 47$ in case of settings1 and $N = 50$ in case of settings2) were measured with a global efficiency that is similar to the value determined using ^{252}Cf fission products (shown in red on the plot), the yield of the neighboring isotones $N = 48$ and $N = 51$ measured by the FRS Ion Catcher is significantly, by 2 orders of magnitudes,

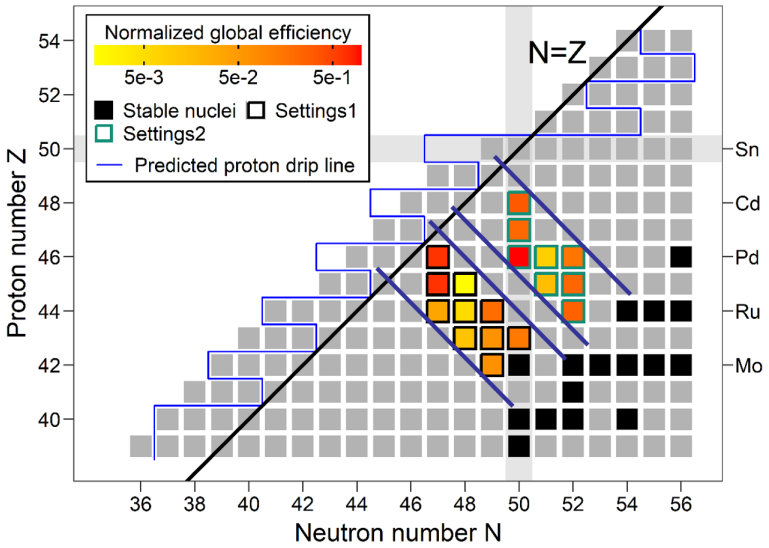

Figure 5.3: The segment of the nuclear chart shows a comparison of the estimated global FRS Ion Catcher efficiencies using two different monoenergetic FRS settings (settings1/2) normalized by the global efficiency of the ^{96}Pd ($N = 50$, $Z = 46$) isotope corresponding to the largest efficiency shown on the figure. Since the global efficiency of ^{96}Pd is close to the independent efficiency estimate determined using ^{252}Cf fission products, the color scheme of the plot can be interpreted the following way; while the red color corresponds to the isotopes that were measured with the "correct" global efficiency, the yellow color corresponds to isotopes, whose global efficiencies are smaller by 2 orders of magnitudes. For settings1 the MRS was used to limit the mass-to-charge range to $m/q \sim (91-93)$ u/e, and for settings2 an MRS range of $m/q \sim (96-98)$ u/e was used, which is illustrated by the dark blue lines on the figure. The boundary between proton bound and unbound nuclei (proton drip line) is drawn with the lighter blue line following predictions according to the global mass calculations reported in [Neufcourt et al., 2020], with exception of the few cases, where mass measurements were available, thus AME2020 [Huang et al., 2021, Wang et al., 2021] was used to calculate the position of the drip line.

reduced (shown in yellow on the plot) and finally the global efficiencies corresponding to the $N = 49$ and $N = 52$ isotones are again larger (shown in orange on the plot) in agreement with the LISE++ simulations considering the possibility of by-passing Scintillator43. The observed similarity in the pattern from settings1 and settings2 further increases our confidence in the correct identification of the different nuclides, including the ones different from the goal isotones that were originally unexpected to be measured. On the other hand, these unexpected isotopes are prone to too many unknowns, such as the points (i) and (ii) as mentioned above, therefore a further quantitative comparison of their calculated global efficiencies is meaningless.

Fig. 5.4 shows a comparison of the estimated global efficiencies of the "expected" beam-like isotopes. Considering how much the different efficiency components can vary throughout the different experimental settings and isotopes, all-in-all the Fig. 5.4 shows a very good agreement of the deduced global FRS-IC efficiency throughout various isotopes and experimental settings leaving only a few distinct sources of inaccuracies, which remain unconsidered by this analysis as discussed above. Taking into consideration the first possible source of this inaccuracies, i.e. the inaccuracy of the stopping efficiency estimate; as shown on Fig. 5.2c, the measured stopping range of ^{97}Ag and ^{96}Pd is different, which may lead up to a factor 2-3 difference in their apparent stopping efficiencies, which was neglected in this analysis. This may already be enough to explain most of the deviations from the constant behavior on Fig. 5.4.

To sum up, in this section the yields of the different isotopes observed in FRS and FRS Ion

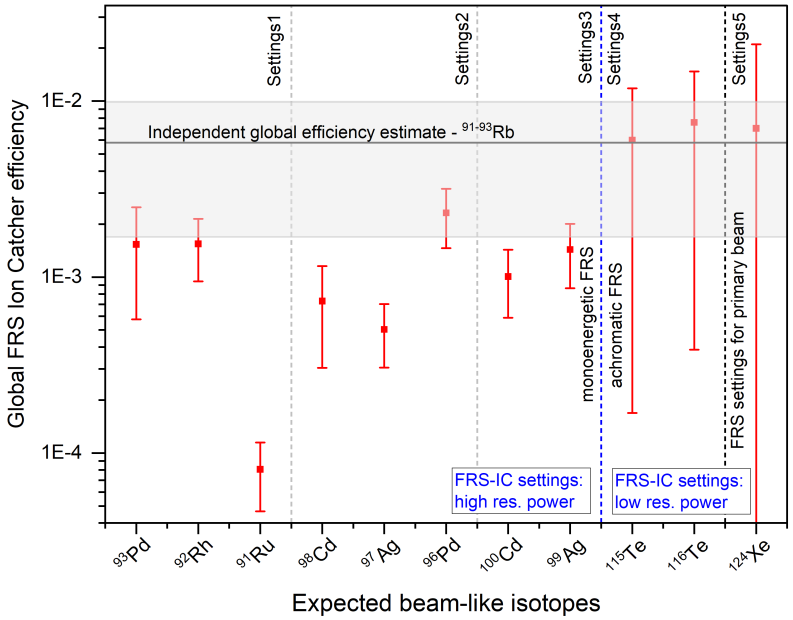

Figure 5.4: A comparison of the estimated global efficiencies corresponding to different beam-like isotopes and their corresponding measurement settings. The plot only includes the so-called "expected" ions, which were nearby the FRS center isotopes and which had a relatively well-understood stopping range and thus stopping efficiency for all 5 different experimental settings. The independent global efficiency estimate (determined using the measured count rates of the ^{252}Cf spontaneous fission products of $^{91-93}$Rb) is marked with the gray line and its corresponding uncertainty estimate is marked with the gray band, whose dominating uncertainty component was given by the uncertainties of the isotopic fission yields extracted from ENDF/B-VII.0 [Chadwick et al., 2006]

Catcher were compared in details and the sources for the necessary efficiency corrections were identified. The achieved good agreement of the determined global efficiencies for the expected beam-like isotopes and the similarities between the measurements using two different monoenergetic settings provide strong evidence supporting the correct identification of the neutron-deficient nuclides during the S474 experiment. Besides this, an explanation for the appearance of the unexpected beam-like isotopes in the mass spectra measured with the MR-TOF-MS was also provided via the possibility of a portion of the beam by-passing Scintillator43, which effect was seen for the first time in this very sensitive experiment. This investigation also marks the first study, where the measured yields were compared between so many different experimental settings and isotopes leading to a consistent picture between experiment and simulations. As a by-product, a model of chemical reactions inside the cryogenic stopping cell was also developed, which enables to provide an initial guess estimate of the element-dependent chemical efficiency factors, and can be used in the future to plan and execute measurements with the FRS Ion Catcher. Furthermore, an improved understanding of the different efficiency components and their uncertainties also provides good ground pillars for the planned reaction studies using the FRS Ion Catcher setup [Mardor et al., 2020, Dickel et al., 2020] in the future.

5.2 Overview of measured masses and comparison to literature

To obtain mass values of the neutron-deficient nuclides, two sets of data (I and II) have been analyzed following the procedure described in Chapter 3. To provide calibrant peaks with well-

known literature masses, the electron impact ion source of the MR-TOF-MS [Yu et al., 2024b] was used during all three measurements with $^{12}C_3{}^{19}F_8$ calibrant gas, which gives an abundant molecule at mass-to-charge of 93 u/e, namely $^{12}C_3{}^{19}F_3$. The partial pressure of the calibrant gas in the MR-TOF-MS Switchyard and the heating of the Tantalum band of the electron impact source were tuned such that the measured count rate of the $^{12}C_3{}^{19}F_3$ molecule was about 1 counts per seconds, therefore plenty of ions were available for the drift correction (time resolved calibration) of the TOF spectra and the determination of the peak shape. In the data set I, the $^{12}C_3{}^{19}F_3$ ions underwent 736, and in the data set II they underwent 750 isochronous turns in the MR-TOF-MS analyzer. For both data sets the mass range selector was used to limit the mass-to-charge range to $m/q \sim (91 - 93)$ u/e.

For both data sets, the TOF spectra were converted to mass-to-charge spectra according to Eq. (3.1), where the calibration parameter $t_0 = 274(2)$ ns was determined prior to the experiment, offline, and the calibration parameters b and c were obtained in the step of the multi-turn (MT) calibration from an offline measurement with similar MR-TOF-MS settings (data set III) from ten different calibrant ions from a broad mass-to-charge range of $m/q \sim (86 - 100)$ u/e, the mass of which is well-known. The time-resolved calibration and the peak shape were obtained from the molecule of $^{12}C_3{}^{19}F_3$, which corresponds to the peak with the highest count rate in the two data sets. Finally, the precision calibration was performed from the peak of ^{93}Ru in case of data set I, the mass of which was taken from the atomic mass evaluation (AME2020) [Huang et al., 2021, Wang et al., 2021]. While for data set II, the molecule of $^{12}C_3{}^{19}F_3$ was used for precision calibration. In case of data set I, the most abundant peak in the spectrum corresponding to the molecule of $^{12}C_3{}^{19}F_3$ failed to comply with the consistency checks and guidelines for calibrant selection presented in Section 3.6, therefore this molecule had to be removed from the list of potential precision calibrants and could only be used to deduce the peak shape. The results from two data sets were weighted averaged, when possible, according to the procedure described in Section 3.4. The final mass values and uncertainties determined for the neutron-deficient nuclides are summarized in Table 5.7.

Insights to peak identification, MT calibration and peak shape determination

Due to instabilities of the SIS18 synchrotron, the beam was switched on and off throughout the first measurement (data set I), which was used as an opportunity to also study the background spectrum within the same measurement settings. More precisely, while acquiring data set I, the beam was on between 05:26-08:47 AM, 14:01-14:29 PM and 15:13-15:28 PM on 07/03/2020, resulting in a total of about 4 hours measurement time for the neutron-deficient nuclides. Between the morning and the afternoon measurement slots of data set I, there was a larger break in the beam and the FRS dipole magnets were switched off. After this, the magnets were forgotten to be precycled, which resulted that the $B\rho$ of the FRS magnets changed a bit leading to a change of the number of different isotopes stopped in the CSC. An estimate from LISE++ simulations suggests that the change of the stopping range was about 15-50 mg/cm^2. This change, however, had no influence on the measured TOF values, which was verified during the mass analysis; i.e. determining the mass of the isotopes from the morning and afternoon parts of the data set I separately yields the same mass values within uncertainties. The measurement of data set II ended earlier due to a failure of the RF carpet, i.e. it was acquired only for less than half an hour (15:37-16:11 PM on 07/03/2020), which resulted that only the identification of ^{92,93}Tc and ^{93}Ru could be unambiguously confirmed in a second MR-TOF-MS setting with a different number of isochronous turns.

In view of the problems mentioned above, the peak identification needs to be validated. Firstly, in the previous section (Section 5.1) strong evidences were presented supporting the correct identification of the neutron-deficient nuclides. Further supports the correct peak identification, that the count rates of all neutron-deficient nuclides measured in data sets I and II

were correlated to the beam on-off changes, while no other peaks in data sets I and II showed beam correlation. Of the non-beam-correlated peaks in data sets I and II [$m/q \sim (91-93)$ u/e], three peaks were identified as the ^{252}Cf spontaneous fission products of $^{91-93}$Rb and eight other peaks were identified in at least two different MR-TOF-MS settings as molecules of $^{12}C_3{}^{19}F_3$, $^{12}C_4{}^{19}F_2{}^{1}H_5$, $^{12}C_3{}^{19}F_2{}^{16}O_1{}^{1}H_1$, $^{12}C_3{}^{19}F_2{}^{16}O_1{}^{1}H_3$, $^{34}S_1{}^{19}F_3$, $^{12}C_7{}^{1}H_7$, $^{12}C_7{}^{1}H_8$ and $^{12}C_7{}^{1}H_9$. A region of the TOF spectrum corresponding to data set I is shown on Fig. 5.5, which is zoomed in for the TOF range including the peaks corresponding to the neutron-deficient nuclides measured in the spectrum. In this TOF range there are only three unidentified or not clearly identified peaks. Note that the majority of the molecules identified in the data sets I and II and listed above are outside of the TOF range of the figure. For the example of the measurement of ^{93}Pd (data set I), there are in total six unidentified peaks in the entire TOF spectrum, most of which have <10 events. These unidentified peaks were used to deduce the contamination uncertainty component of the mass uncertainty (see Section 3.3).

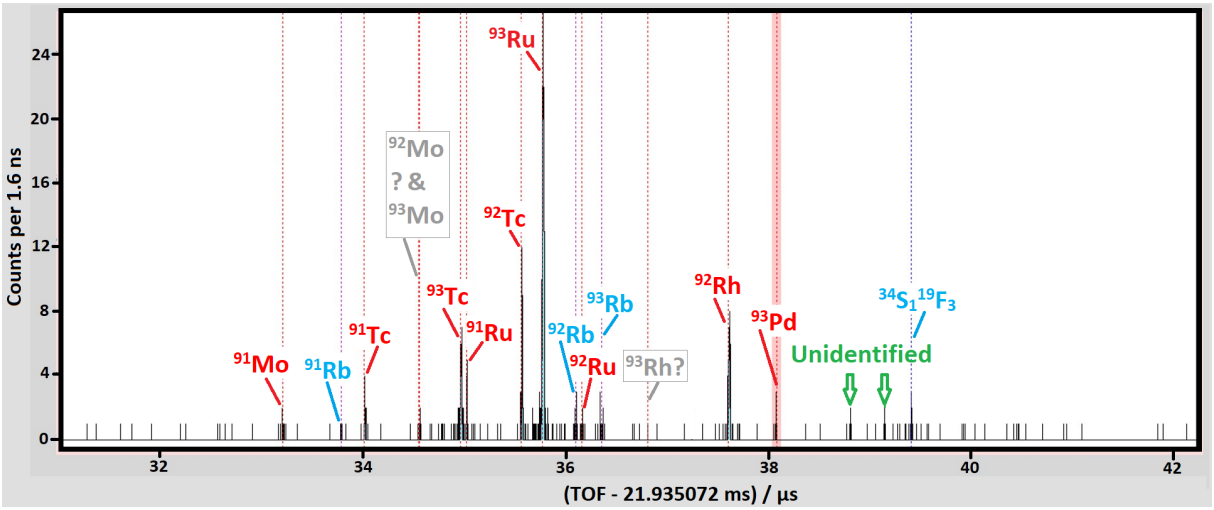

Figure 5.5: Time-of-flight spectrum corresponding to data set I, zoomed in for the TOF range including the peaks corresponding to the ions-of-interest. The neutron-deficient nuclides are marked with red, the peaks that did not show a beam correlation are marked with blue in case they could be identified and green otherwise. The ions of interest with unclear peak identification are marked with grey labels. Only one potential event was observed for ^{93}Rh, which could also correspond to a background event, thus resulting in an unclear peak identification. In this MR-TOF-MS settings the TOF corresponding to the peaks of ^{93}Mo and ^{92}Mo is expected to be nearly identical, therefore it was not possible to separate and clearly identify the two (or one) isotopes.

Although many different molecules were identified in data sets I and II, most of these molecules did not comply with the guidelines for calibrant selection (see Section 3.6) and could not be used for multi-turn calibration. Consequently, the MT calibration for data sets I and II had to be determined from a separate, offline measurement (data set III), which was acquired close to the data sets I and II in time and corresponds to very similar measurement settings. For this data set III, the $^{12}C_3{}^{19}F_3$ ions underwent 736 isochronous turns (IT) in the MR-TOF-MS analyzer, just like for data set I. As a minor difference, for the data set III the opening time of the second mirror was increased by 10 μs as compared to data set I. This was done to ensure that a second abundant molecule from the electron impact source, namely $^{12}C_2{}^{19}F_4$, is not dropped out by the TOF analyzer and can be also used for MT calibration. For data set III the mass range selector in the center of the TOF analyzer was switched off and the mass range was only limited by the mass-selective transport through the trap system of the MR-TOF-MS. As a consequence, many peaks undergoing a broad range of turn numbers from 706 to 794 IT could be

identified in the TOF spectrum (data set III) starting from the stable Kr peaks to the different carbon-fluoride molecules. For the MT calibration, ten different calibrant ions from a broad mass-to-charge range of $m/q \sim (86-100)$ u/e were selected and the deduced calibration parameters c and b in Eq. (3.1) were then applied both to data set I and II. Notably, this broadband multi-turn calibration resulted in decreasing the Δm_c uncertainty component associated with the multi-turn calibration by about an order of magnitude as compared to the results reported in [Mollaebrahimi et al., 2023b] corresponding to the same $N_{\mathrm{it}}/N_{\mathrm{cal}}$ ratios as here.

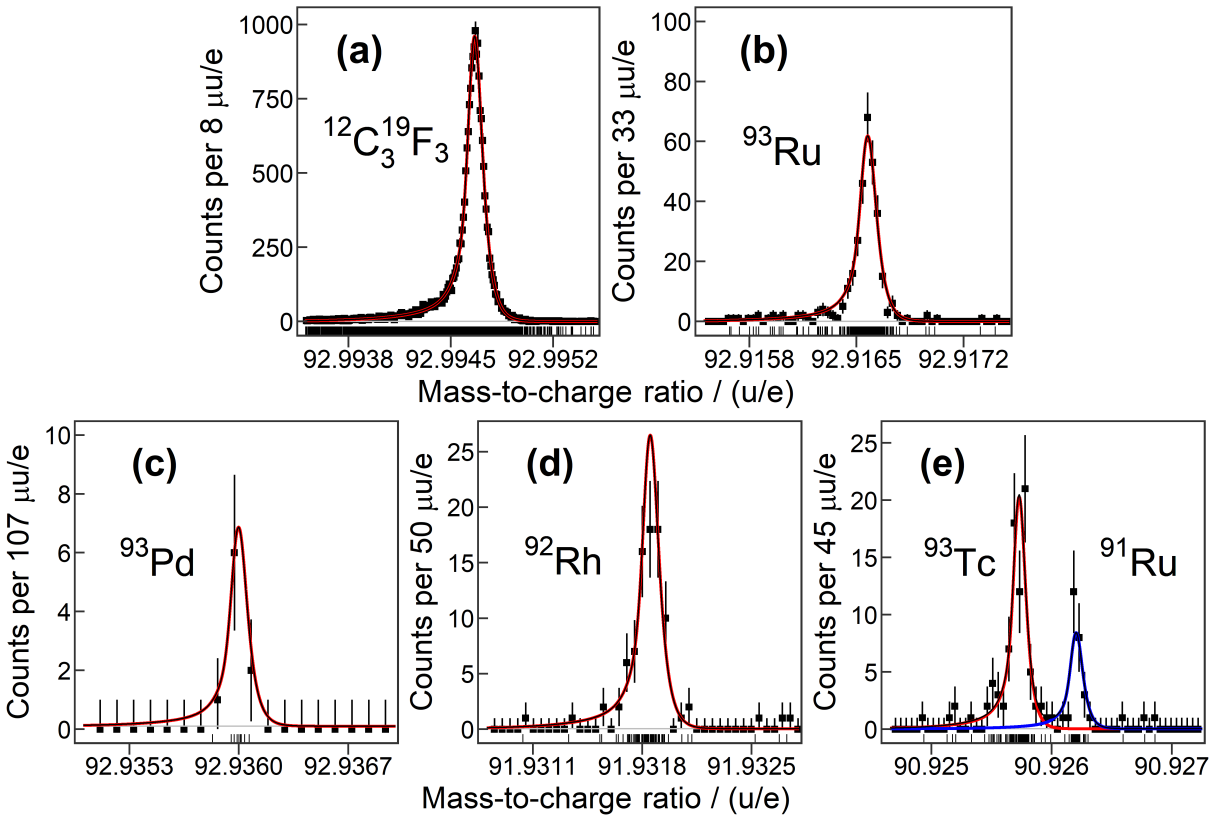

Figure 5.6: Mass-to-charge spectrum corresponding to data set I, zoomed in to the peaks of (a) $^{12}C_3{}^{19}F_3$ ions, (b) ^{93}Ru ions, (c) ^{93}Pd ions, (d) ^{92}Rh ions, (e) ^{93}Tc and ^{91}Ru ions. The histogram of the measured spectrum (black data points) is only drawn to guide the eye. The curves represent the fits to the unbinned data ('rug' graph below the histogram) with a fixed hyper-EMG [Purushothaman et al., 2017] peak shape (FWHM $\approx$ 120 keV), which was obtained from the peak of the molecule $^{12}C_3{}^{19}F_3$. The precision calibration of the spectrum was performed using the peak of ^{93}Ru.

For both data sets I and II, the most abundant peak in the spectra corresponding to the molecule of $^{12}C_3{}^{19}F_3$ was used to determine the peak shape. At variance, for the offline data set III, the most abundant peak in the spectrum corresponded to the molecule of $^{12}C_2{}^{19}F_4$ and has been used for the time-resolved calibration (TRC), peak shape determination and precision calibration. Since the count rate corresponding to the molecule of $^{12}C_2{}^{19}F_4$ was about an order of magnitude higher compared to that of $^{12}C_3{}^{19}F_3$, this enabled a smaller TRC block size and, ultimately, a slightly higher mass resolving power as compared to the other two data sets. For data sets I and II, a hyper-EMG function with two exponential tails on the left side and one exponential tail on the right side and, for data set III, a hyper-EMG function with two tails on each sides have been found to describe the peak shape best. For data sets I and II, a FWHM of about 120 keV was determined for the ions of interest corresponding to a mass resolving power

of about 700,000. For data set III, the determined mass resolving power corresponding to the molecule of $^{12}C_3{}^{19}F_3$ at 736 IT was about 750,000. For the case of data set I, Fig. 5.6 shows the fit of the molecule of $^{12}C_3{}^{19}F_3$ with ∼21,000 events. The deduced peak shape was then fixed and applied to the unbinned data of the precision calibrant, ^{93}Ru in case of data set I, and the ions of interest, see Fig. 5.6 for a few example fits.

Masses with previous direct measurements and consistency checks

The masses of the neutron-deficient nuclides ^{91}Mo, $^{91-93}$Tc, $^{91-93}$Ru, ^{92}Rh and ^{93}Pd were measured in the two data sets, the analysis of which is presented here. The deduced mass values (see Table 5.7) are assigned to the ground state of the nuclides, except for the case of ^{92}Rh, where it is assigned to the (6^+) state, which is most likely an isomer states, see more details in the upcoming paragraphs. For all isotopes reported in the table the statistical and contamination uncertainty was the dominating uncertainty contribution. Out of the mass values corresponding to the exotic nuclides reported in Table 5.7, ^{93}Tc has the smallest mass uncertainty, 8.4 keV, which corresponds to a relative mass uncertainty of 1×10^{-7}. With the exception of ^{93}Pd, the mass of all other neutron-deficient nuclides presented in Table 5.7 were measured directly prior to this work, in most cases, via Penning trap mass spectrometry, see e.g. [Weber et al., 2008, Fallis et al., 2011].

In addition to the 9 neutron-deficient nuclides, the mass of the 3 ^{252}Cf spontaneous fission products, $^{91-93}$Rb, the 4 stable Kr isotopes, ^{80,82,84,86}Kr, and the 18 molecules identified in data sets I, II and III were also determined. Considering the 34 deduced mass values in total, the smallest achieved mass uncertainty, 5.1 keV ($\delta m/m = 5.7 \times 10^{-8}$), corresponds to the molecule of $^{12}C_2{}^{19}F_3{}^{16}O_1$ with 783 events measured in data set III.

The deviations between the measured and literature [Huang et al., 2021, Wang et al., 2021] mass values (ΔME defined by Eq. (3.20)) corresponding to isotopes and molecules with previous direct mass measurements have been used to check the consistency of the data analysis using the methods explained in Section 3.6. Within the data sets I, II and III a single peak was used for the precision calibration of the entire spectrum, therefore the precision calibration uncertainty contribution was considered as a dependent uncertainty component for calculating the weighted average of the deviations from literature ($\overline{\Delta ME}$). As a result of this procedure, $\overline{\Delta ME}$ calculates to -5.5(62) keV for the 15 ions with well-known literature masses measured in data set I, -5.2(49) keV for the 7 ions with well-known literature masses measured in II and -0.9(31) keV for the 17 ions with well-known literature masses measured in data set III, respectively. Finally, after combining the mass values obtained from all three data sets, a Birge ratio [Birge, 1932] of 0.67 and a weighted mean of -2.5(24) keV is determined for the deviations between the measured and literature masses. The standard deviation of ΔME_σ defined by Eq. (3.20) calculates to 0.66. These results indicate that the overall experimental uncertainty is appropriately estimated and the data analysis procedure yield accurate mass values.

The $(1/2^-)$ isomeric states vs. $(9/2^+)$ ground states in the vicinity of ^{100}Sn

The presently reported mass measurements include six odd-even nuclides, which are expected to have a ground state with spin-parity of $(9/2^+)$ and a long-lived isomeric state with spin-parity of $(1/2^-)$, both of which could, in principle, be present in the mass measurements reported here due to their long half-lives. The excitation energy of the $(1/2^-)$ isomers of ^{91}Mo, ^{91,93}Tc, ^{91,93}Ru are all well-known experimentally [Kondev et al., 2021, Xing et al., 2023] and in most cases it is above 400 keV, which can be easily resolved by our mass measurements. The $(1/2^-)$ isomer of ^{91}Tc has the smallest excitation energy with 139.3(3) keV [Kondev et al., 2021] corresponding to a mass-to-charge ratio, which is a bit more than one FWHM away from the mass-to-charge ratio of its ground state and should be possible to resolve in our measurements. On the other hand,

Table 5.7: Measured mass excess (ME_{FRS-IC}) values close to the $N = Z$ line compared with the literature values ME_{lit}. Two sets of data (I and II) were analyzed and averaged with the weighted mean, when possible. The literature values are taken from AME2020 [Huang et al., 2021, Wang et al., 2021] except for the case of ^{92}Rh, see table notes for more details. The mass of ^{93}Pd was measured directly for the first time. The used precision calibrants and the total number of events (ions-of-interest + background counts) are also listed in the table. The $\Delta ME = ME_{FRS-IC} - ME_{lit}$ marks the deviation of the measured values from the literature.

Nuclide	Data set	Precision calibrant	Total events	ME_{FRS-IC} (keV)	ME_{lit} (keV)	ΔME (keV)
^{91}Ru	I	^{93}Ru	34	-68250(15)	-68239.8(22)	-11(15)
^{91}Tc	I	^{93}Ru	23	-75996(18)	-75986.7(24)	-10(19)
^{91}Mo	I	^{93}Ru	9	-82209(35)	-82209(6)	0(36)
^{92}Rh	I	^{93}Ru	85	-62989(10)[b]	-62999(15)[c] -63017(13)[d]	10(18) 28(17)
$J^\pi = (6^+)$[a]					-62999(4)[e]	10(11)
^{92}Ru	I	^{93}Ru	12	-74279(29)	-74301.2(27)	22(29)
^{92}Tc	I	^{93}Ru	74	-78927(11)		
	II	$^{12}C_3{}^{19}F_3$	5	-78865(48)		
	avg.			**-78924(10)**	**-78926(3)**	**2(11)**
^{93}Pd	I	^{93}Ru	9[f]	-59127(35)	-58980(370)	-147(372)
^{93}Ru	II	$^{12}C_3{}^{19}F_3$	14	-77201(23)	-77216.7(21)	15(23)
^{93}Tc	I	^{93}Ru	82	-83615(10)		
	II	$^{12}C_3{}^{19}F_3$	27	-83590(15)		
	avg.			**-83607.6(84)**	**-83606.1(10)**	**-1.5(84)**

[a] Another $J^\pi = (2^+)$ long-lived, β-decaying state was observed in Ref. [Dean et al., 2004, Park et al., 2019].

[b] The original 12 keV mass uncertainty was increased to 18 keV due to possible isomeric contamination.

[c] JYFLTRAP & SHIPTRAP [Weber et al., 2008]. The mass uncertainty was increased from 4.3 keV to 15 keV.

[d] CPT [Fallis et al., 2011]. No correction to the mass uncertainty was applied.

[e] AME2020 [Huang et al., 2021, Wang et al., 2021]. The mass uncertainty increase was not adopted from [Weber et al., 2008].

[f] The total number of detected ^{93}Pd events were determined by simple counting from Fig. 5.6 and not with the R data analysis framework.

no significant peak was seen in our measurements corresponding to the $(1/2^-)$ isomers of ^{91}Mo, ^{91,93}Tc, ^{91,93}Ru, which gives an upper limit for the isomer-to-ground state ratios corresponding to their population in projectile-fragmentation reactions of about 1% to 10% (see measured event numbers for the $(9/2^+)$ ground states of ^{91}Mo, ^{91,93}Tc, ^{91,93}Ru in Table 5.7). Indeed, other experiments employing projectile-fragmentation reactions in the vicinity of ^{100}Sn show only very small ($\leq 15\%$) isomer-to-ground state ratios for the $(1/2^-)$ isomers in this region [Mollaebrahimi et al., 2023b, Amanbayev, 2023, Xing et al., 2023]. The nuclide ^{93}Pd is also expected to have

a $(9/2^+)$ ground state and a $(1/2^-)$ isomer state with an extrapolated excitation energy of $E_x \approx 450$ keV [Xing et al., 2023]. In the presently reported mass measurements only one state was observed for the ^{93}Pd (Fig. 5.6) and it was assigned to the $(9/2^+)$ ground state based on the above argumentation. Assuming $E_x = 450$ keV, an upper limit of about 10% can be deduced for the ^{93}Pd isomer-to-ground state ratio from the present measurements employing projectile fragmentation reactions.

The unresolved isomer of ^{92}Rh

The nuclide ^{92}Rh has two low-lying, long-lived, β-decaying states with tentatively assigned spin-parities of $J^\pi = (2^+)$, $J^\pi = (6^+)$ and measured half-lives of $T_{1/2}(2^+) = 3.18(22)$ s, $T_{1/2}(6^+) = 5.61(8)$ s [Dean et al., 2004, Park et al., 2019], respectively, each of which could in principle be the ground state. Additionally, ^{92}Rh has also a low-lying, γ-decaying isomer state with $J^\pi = (4^+)$ and $T_{1/2}(4^+) = 232(15)$ ns, which was populated with an 8.3(12)% isomeric ratio in a fragmentation reaction of ^{124}Xe [Park et al., 2017, Häfner et al., 2019]. The experimental level scheme of low-energy states in ^{92}Rh is illustrated in Fig. 5.7. There are, in principle, two possible level orderings for the (2^+), (4^+), (6^+) states, which are compatible with the requirement of the long half-life of the (2^+) and (6^+) states:

(A) 2^+ ($E_x = 0$ keV), 6^+ (0 keV $\leq E_x \leq$ 55 keV), 4^+ ($E_x = 55.6(1)$ keV) and

(B) 6^+ ($E_x = 0$ keV), 2^+ ($E_x = X$ keV), 4^+ ($E_x = X + 55.6(1)$ keV).

Due to historical reasons, the ground state of ^{92}Rh has been assigned to (6^+) spin and parity [Kondev et al., 2021, Baglin, 2012], which corresponds to the (B) level ordering. On the other hand, according to shell model calculations, a 2^+ state is predicted either 35 keV [Park et al., 2017, Park et al., 2019] or ∼50 keV [Kast et al., 1996, Dean et al., 2004] or 211 keV [Herndl & Brown, 1997] below the 6^+ state. Therefore, the shell-model calculations suggest the (A) level ordering as the most likely scenario. Furthermore, the observed 55-keV γ-transition was assigned as $(4^+) \rightarrow (2^+)$ and no other γ ray from the 232(15)-ns isomeric state was observed in [Park et al., 2017, Häfner et al., 2019]. Given the large statistics measured for the 55-keV γ-transition, it is reasonable to ask, why the E2 transition of $(4^+) \rightarrow (6^+)$ was not observed in the same experiments. The most likely explanation for this is that the $(4^+) \rightarrow (6^+)$ γ-ray energy was below the detection threshold of about 30 keV in [Park et al., 2017, Häfner et al., 2019], which also suggests the (A) level ordering as the most likely scenario. Furthermore, the investigations reported in Ref. [Vilén et al., 2019, Garnsworthy et al., 2009, Park et al., 2019] suggest a similar low-spin level structure in ^{88}Tc, which is an odd-odd, $T_Z = \frac{1}{2}(N - Z) = 1$ nucleus just like ^{92}Rh. Altogether these observations hint that the ground state of ^{92}Rh has a spin and parity of (2^+) and the excitation energy of the long-lived (6^+) isomer is below 55 keV.

Although Fig. 5.6 shows no clear signature of an overlapping peak, but the mass-to-charge distribution of ^{92}Rh ions measured at FRS-IC could, in principle, include contributions from both long-lived, (2^+) and (6^+) states. On the other hand, the evidence shown in previous measurements of ^{92}Rh employing projectile fragmentation reactions [Lorusso et al., 2012, Park et al., 2019, Park et al., 2017, Häfner et al., 2019] indicate that the (6^+) state is expected to be produced much more abundantly than the (2^+) state and the (2^+)-to-(6^+) state ratio should be somewhere between 5% to 25%. In particular, in Ref. [Park et al., 2019] the half-life of the (2^+) state was deduced without contributions from the (6^+) state and it was then applied in the multi-component fit of the total β-decay time analysis to determine the half-life of the (6^+) state, see inset of Fig. 5.7. The figure clearly shows that the (6^+) state is produced much more abundantly than the (2^+) state employing projectile fragmentation reactions.

Consequently, in the presently reported mass measurements, the 85 detected ^{92}Rh events correspond mostly to its presumed (6^+) isomer state. In order to estimate the mass uncertainty

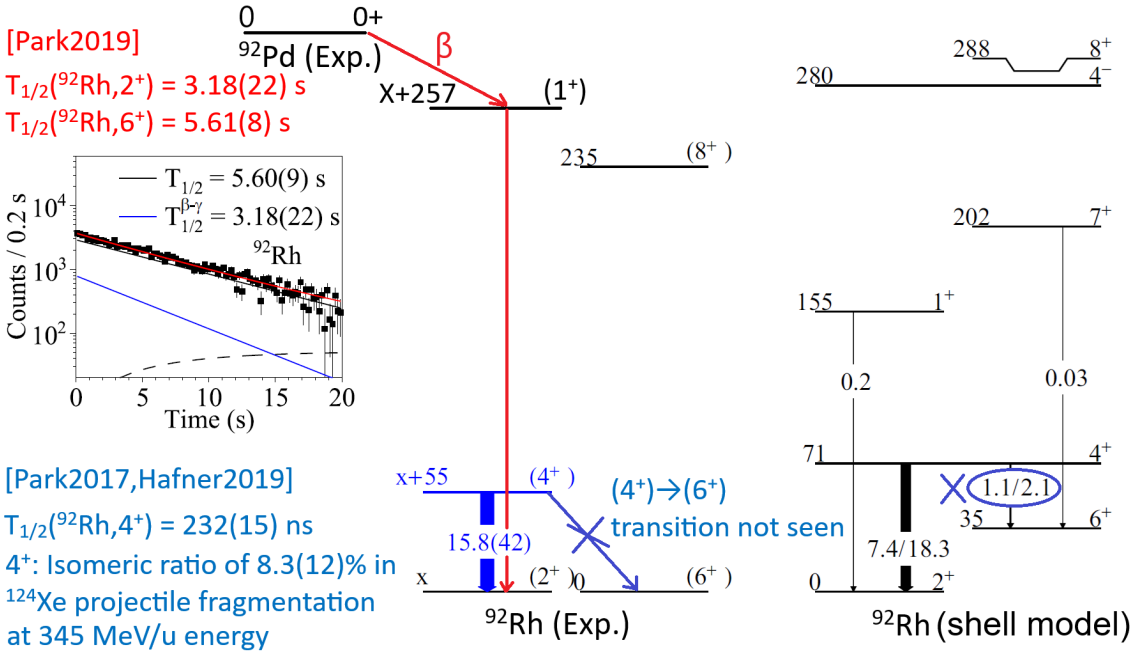

Figure 5.7: Schematic drawing of the experimental level scheme of low-energy states in ^{92}Rh illustrating the γ-ray transitions observed in [Park et al., 2017, Häfner et al., 2019, Park et al., 2019] (left side). In comparison, the results of shell-model calculations are shown from [Park et al., 2017] (right side). The inset on the left side shows the multi-component half-life fit adopted from [Park et al., 2019], where the blue and black solid lines correspond to the β-decay components of the (2^+) and (6^+) states of ^{92}Rh, respectively, and red solid line represents the sum of all the decay components. The level schemes were adopted and modified from [Park et al., 2017].

component resulting from the few events corresponding to the unresolved, presumed (2^+) ground state, Monte Carlo simulations were done. The general concept of the simulations is the same as the concept for the contamination uncertainty simulations (see Section 3.3), i.e. the unresolved, presumed (2^+) ground state is treated as a contaminant with a contaminant-to-main peak ratio of 5-to-25% and a contaminant mass smaller by up to 55 keV than the mass of the main peak. The Monte Carlo simulations resulted in a standard deviation of 8.2 keV, which is practically the same as the standard deviation of the Monte Carlo simulations for the statistical uncertainty calculation. The simulations also show that the unresolved presumed (2^+) ground state shifts the mass value on average only by 3.7 keV. This average shift, which is well below the standard deviation of the simulations, gives the uncertainty component corresponding to the unresolved (2^+) state and is quadratically added to the original mass uncertainty of ^{92}Rh of 9.7 keV. As a result, a mass excess value of $-62989(10)$ keV was determined for the presumed (6^+) isomer state of ^{92}Rh (Table 5.7).

Prior to this work, the mass of ^{92}Rh was measured by three Penning trap groups employing heavy-ion fusion-evaporation reactions [Weber et al., 2008, Fallis et al., 2011] and by CSRe employing projectile-fragmentation reactions [Xing et al., 2018]. The latter experiment at CSRe corresponds to a large mass uncertainty for ^{92}Rh and the deduced ^{92}Rh mass value is not reported in [Xing et al., 2018], except for the fact that it is in agreement with the results of the previous Penning-trap measurements [Weber et al., 2008, Fallis et al., 2011]. The presently reported experiment employed projectile-fragmentation reactions and used a different measurement device, an MR-TOF-MS, providing complementary information on ^{92}Rh. As shown in Table 5.7, the measured mass of ^{92}Rh is in perfect agreement with the Penning-trap measurements of

[Weber et al., 2008], and shows a small deviation of $\sim$1.5σ from the Penning-trap measurements of [Fallis et al., 2011]. This results indicate either a similar magnitude of isomeric contamination in the two complementary production mechanisms and/or a smaller energy difference between the long-lived (2^+) and (6^+) states of ^{92}Rh compared to the uncertainty of the presently reported MR-TOF-MS and previous Penning-trap measurements. Indeed, the similar relative intensities of β-delayed γ rays corresponding to the β decay of ^{92}Rh observed in two complementary studies employing projectile fragmentation [Lorusso et al., 2012] and fusion-evaporation [Dean et al., 2004] reactions indicate a similar production ratio of the two long-lived ^{92}Rh states in the complementary production mechanisms. Altogether this indicates that also in previous Penning-trap measurements [Weber et al., 2008, Fallis et al., 2011], the presumed (6^+) isomer state of ^{92}Rh was populated more abundantly than the presumed (2^+) ground state. On the other hand, this is contradictory to the observations of Ref. [Vilén et al., 2019], where the presumed (2^+) ground state of ^{88}Tc, which has a similar low-spin level structure as ^{92}Rh, was populated more abundantly than the presumed (6^+) isomer state employing fusion-evaporation reactions. For a final resolution concerning the order of the long-lived ^{92}Rh states a precise measurement of the energy difference of the (2^+) and (6^+) states of ^{92}Rh is necessary.

The first direct mass measurement of ^{93}Pd

The mass value of the ^{93}Pd ground state reported in the AME2020 [Huang et al., 2021, Wang et al., 2021] is from a β-decay end-point energy measurement with $Q_{\mathrm{EC}} = 10030(370)$ keV [Park et al., 2019]. It is worth mentioning that out of the 8 nuclei, for which the Q_{EC} values were deduced in Ref. [Park et al., 2019], the indirectly-measured mass values determined for 4 nuclei were listed as irregular in the AME2020 due to breaking the smoothness of the mass surface in this region, and the usage of the extrapolated mass values was recommended instead. Furthermore, it is not unusual that direct mass measurements reveal large deviations from the results of indirect measurements, see e.g. Ref. [Haettner et al., 2011, Xing et al., 2018]. Altogether, this calls for a direct mass measurement of ^{93}Pd.

In the present work, the mass of the ^{93}Pd ground state was measured directly for the first time. A mass excess value of $-59127(35)$ keV was obtained from the 9 detected ^{93}Pd events (Fig. 5.6). The new mass value agrees with the AME2020, but reduces the uncertainty by an order of magnitude.

5.3 Implications to the 1p/2p decay branches of the (21^+) spin-trap isomer of ^{94}Ag

The heavy $N = Z$ nuclei and the nuclei in their vicinity are highly interesting to study, they possess symmetries that are unique to these nuclei and have a high impact in modelling nuclear astrophysics processes (rp-process, νp-process). For an overview of experimental and theoretical efforts in the vicinity of ^{100}Sn, see e.g. Ref. [Faestermann et al., 2013].

In particular, the palladium isotopes were observed to undergo a structural change as their neutron number decreases from 50 to 46 [Cederwall et al., 2011, Nara Singh et al., 2012, Das et al., 2022]. Since ^{93}Pd corresponds to neutron number of 47, it is situated at the transitional region and therefore the mass of its ($9/2^+$) ground state and the excitation energy of its predicted ($1/2^-$) isomer state may provide interesting information about the observed nuclear structure change of palladium isotopes. Furthermore, a high-precision mass measurement of ^{93}Pd, the 1p decay daughter of ^{94}Ag, and measuring the mass of ^{92}Rh, the 2p decay daughter of ^{94}Ag, may have important consequences on the exotic decay modes of the (21^+) isomer of ^{94}Ag, which will be addressed in the present work.

Status of investigations prior to our mass measurements

The silver isotope ^{94}Ag, containing 47 protons and 47 neutrons and located next to the proton dripline [Čeliković et al., 2016], has been reported to have a spin-trap isomer with the highest spin observed so far for β-decaying nuclei, (21^+), and with a very high excitation energy of more than 6 MeV [Plettner et al., 2004]. Even more intriguingly, this isomer in ^{94}Ag has been reported to exhibit a unique competition of multiple decay modes, such as β decay [La Commara et al., 2002, Plettner et al., 2004], β-delayed proton emission [Mukha et al., 2004], direct one-proton (1p) decay [Mukha et al., 2005, Cerny et al., 2009] and, surprisingly, even direct two-proton (2p) decay [Mukha et al., 2006].

The β-decay half-life of this (21^+) isomer is 400(40) ms, which is the weighted average of the measured half-lives in the works of [La Commara et al., 2002, Plettner et al., 2004, Mukha et al., 2004], and it decays to the (20^+) state in ^{94}Pd with an experimentally not known β decay energy, Q_β. Additionally, it has been reported that there are two 1p branches from this isomer with $E_{1p,I} = 790(20)$ keV, $R_{1p,I} = 1.9(5)\%$ and $E_{1p,II} = 1010(30)$ keV, $R_{1p,II} = 2.2(4)\%$ decay energies and branching ratios, respectively, and one 2p-decay branch with $E_{2p} = 1900(100)$ keV, $R_{2p} = 0.5(3)\%$ decay energy and branching ratio [Mukha et al., 2005, Mukha et al., 2006, Cerny et al., 2009]. The 1p branch with the lower decay energy, denoted here as 1p(I) branch, was observed to decay to the previously experimentally-known $(33/2^+)$ state in ^{93}Pd. The 1p branch with the higher decay energy, denoted here as 1p(II) branch, has been assigned to a daughter state with a tentative spin-parity assignment of $(33/2^-, 35/2^-)$ and a tentative placement in the level scheme of ^{93}Pd, which was not observed by other in-beam γ-spectroscopy experiments of ^{93}Pd yet [Baglin, 2011, Lorusso et al., 2012, Park et al., 2019]. The 2p decay branch has been reported to decay to the previously experimentally-known (11^+) state in ^{92}Rh.

The 1p and 2p decay branches of the (21^+) isomer have been surrounded by two main puzzles starting from its observation:

(A) **The puzzle of simultaneous 2p emission:** Correlations between the two emitted protons indicate that the 2p decay occurs via simultaneous 2p emission (so-called "true 2p decay"), rather than via sequential 2p emission, in spite of the following two main counter-arguments:

- sequential 2p emission should be energetically possible and would be expected to have a much larger branching ratio than the simultaneous 2p emission [Mukha et al., 2006].
- ^{94}Ag is the only known nucleus that has been reported to decay by both 1p and simultaneous 2p emission, and the only known nucleus with an odd number of protons to decay by simultaneous 2p emission [Pfützner et al., 2023, Xing et al., 2021].

(B) **The puzzle of large deformation required for 2p emission:** A simple model has been employed to explain the observation of simultaneous 2p emission, according to which the two protons are emitted from different points of a strongly-deformed prolate state [Mukha et al., 2006]. On the other hand, the suggested deformation of the presumed 2p-emitting (21^+) isomer has been under intense debate [Mukha et al., 2006, Kaneko et al., 2008, Pechenaya et al., 2007].

A series of intensive studies followed the observations of 1p and 2p decay from the (21^+) isomer, many of which questioned the observation of the simultaneous 2p emission [Pechenaya et al., 2007, Kankainen et al., 2008, Jenkins, 2009, Cerny et al., 2009], giving rise to extended debate [Mukha et al., 2008, Pechenaya et al., 2008, Mukha et al., 2010]. An overview of these studies can be found in [Kankainen et al., 2012, Roeckl & Mukha, 2013]. With these studies, the list of the previous 2 puzzles have been extended by two additional puzzles:

(C) **The non-observation of 2p emission in Ref. [Cerny et al., 2009]:** An experiment at Berkeley has been performed to verify the observation of 2p decay, but could reproduce only the first of the two reported 1p decay branches and did not see the 2p decay [Cerny et al., 2009]. Note, however, that there are a few differences of this latter experiment performed at Berkeley as compared to the first experiment performed at GSI [Mukha et al., 2005, Mukha et al., 2006]:

- The experiment at GSI was done with a relatively short production and measurement time (about 30 ms determined for silver isotopes) thanks to the fast release time of the used FEBIAD-type ion source [Kirchner, 1992]. On the other hand, the experiment at Berkeley used a helium-jet system (with no mass separation) to transport the produced ions from the target area to the detection area, which took longer (about 200 to 300 ms) [Blönnigen et al., 1987].
- Due to the fact that no mass separation was used in the Berkeley experiment, there was a strong beta-delayed proton background, which affected the ability to observe low-energy, weak 1p branches. On the other hand, this did not affect the ability to see proton-proton coincidences at these low energies and thus to see the presumed simultaneous 2p emission from ^{94}Ag.
- Even though the decay energy and branching ratio of the 1p(I) branch was confirmed in the experiment at Berkeley, this experiment provides no information about the daughter state of the 1p branch in ^{93}Pd.

(D) **A possible mother-state energy mismatch:** Another important piece of evidence, reported in Ref. [Kankainen et al., 2008], suggested a possible disagreement in the excitation energy of the (21^+) isomer when calculating it from the observed one- and two-proton decay data, respectively, in combination with the ground state mass of ^{92}Rh and ^{93}Pd. However, at that time, the ground state mass of the 1p decay daughter, ^{93}Pd, could be obtained only by extrapolation, thus preventing a final conclusion.

To date, further intensive studies have been and are still being performed, experimental as well as theoretical in nature, in order to help further unraveling the puzzles surrounding the 1p/2p decay branches, see e.g. [Nara Singh et al., 2012, Xing et al., 2021, Aggarwal, 2010, Park, 2017, Lubos, 2016, Reponen et al., 2015, Zhu et al., 2022]. However, all attempts have failed so far to either consistently reconcile the observations with our understanding of nuclear structure or to disprove them beyond doubt.

On the other hand, studying the observed phenomena provides stringent tests for various theoretical models, either engaging to explain the existence of the (21^+) isomer [Plettner et al., 2004, Kaneko et al., 2008] or attempting to reproduce its proposed exotic decay modes [Mukha et al., 2006, Xing et al., 2021, Zhu et al., 2022], and hence it may reveal insights essential to the deeper understanding of the underlying quantum background driving these phenomena.

Consequence of our mass measurements on the 1p/2p decay branches of ^{94}Ag

With the newly-measured mass of the 1p decay daughter, ^{93}Pd, and the presently-reported mass of the 2p decay daughter, ^{92}Rh, the following two puzzles are further unraveled as a direct consequence of our mass measurements:

(D) **The possible mother-state energy mismatch confirmed as a 10σ disagreement:** Combining the newly measured mass excess of the 1p decay daughter, ^{93}Pd, the mass excess of hydrogen, ME$\left(^1\mathrm{H}\right)$ [Huang et al., 2021, Wang et al., 2021], the decay energy corresponding to the 1p(I) branch, $E_{\mathrm{1p,I}} = 790(20)$ keV [Mukha et al., 2005, Cerny et al., 2009], and the excitation energy of the populated $(33/2^+)$ state in ^{93}Pd, $E_{\mathrm{x}}\left(^{93}\mathrm{Pd}, 33/2^+\right) =$

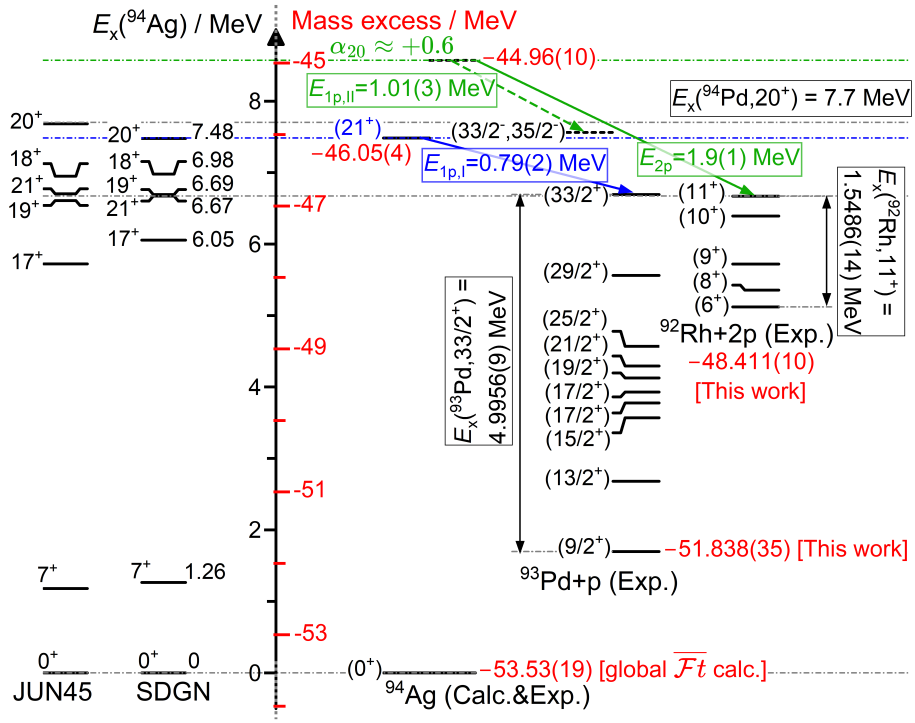

Figure 5.8: Decay scheme according to the new data and analysis of this work, showing the 10σ discrepancy in the mass excess value of the ^{94}Ag (21^+) isomer when calculating it using the 1p- [Mukha et al., 2005, Cerny et al., 2009] and 2p-decay data [Mukha et al., 2006], respectively. The black scale (left side) shows the ^{94}Ag level energies relative to its (0^+) ground state obtained by shell-model calculations, employing SDGN [Nowacki, 2002] and JUN45 [Honma et al., 2009] interactions, while the red scale (right side) shows the corresponding mass excess values resulting from our measurements. The mass of the ^{94}Ag ground state has been determined using the global $\overline{\mathcal{F}t}$ value and its measured half-life (see Section 5.3.1). The dashed green arrow marks a possible alternative placement of the 1p(II) decay branch as suggested in this work, see text for more details.

4995.6(9) keV [Baglin, 2011], gives a mass excess of the high-lying ^{94}Ag isomer of ME $\left(^{94}\text{Ag},\ 21^+\right)_{1p,I} = -46050(40)$ keV. On the other hand, summing up the mass excess of the 2p decay daughter, ^{92}Rh, with $2 \times$ ME $\left(^1\text{H}\right)$, the 2p decay energy, $E_{2p} = 1900(100)$ keV [Mukha et al., 2006], and $E_x\left(^{92}\text{Rh},\ 11^+\right) = 1548.6(14)$ keV [Baglin, 2012], the mass excess of the (21^+) isomer is determined to be ME$\left(^{94}\text{Ag},\ 21^+\right)_{2p} = -44960(100)$ keV. These two alternative mass excess values of the (21^+) isomer differ by 1090(110) keV, i.e. by 10 standard deviations, which is illustrated in Fig. 5.8. This disagreement calls into question the experimental observations [Mukha et al., 2005, Mukha et al., 2006]. Since the 1p(I) branch was confirmed [Cerny et al., 2009], the 2p decay becomes the most debatable observation.[1]

(A) **Implications on the puzzle of simultaneous 2p emission:** Using the new mass value of ^{93}Pd, the mass excess values of the presumed populated states in the 1p and 2p decay daughters, ME$\left(^{93}\text{Pd}+\text{p},\ 33/2^+\right)$ and ME$\left(^{92}\text{Rh}+2\text{p},\ 11^+\right)$, are the same within 21(37) keV, see Fig. 5.8. Assuming that all decay branches originally reported in [Mukha et al., 2005, Mukha et al., 2006] are correct, a sequential 2p emission involving the $(33/2^+)$

[1] It is worth mentioning that the extrapolated mass value of ^{93}Pd used in the previous examination of the energies of the 1p and 2p decay branches [Kankainen et al., 2008] differs by almost two standard deviations from the present result, which nicely demonstrates the importance of direct mass measurements over extrapolations.

state of ^{93}Pd and the (11^+) state of ^{92}Rh is energetically highly improbable. This would give an explanation for the observation in Ref. [Mukha et al., 2006], where the reported correlations between the two emitted protons indicate a simultaneous 2p emission. Note, however, that this is potentially contradictory with the placement of the 1p and 2p decay branches suggested in this work, see more details later.

To obtain the excitation energy from the mass excess of the (21^+) isomer, an accurate estimate of the ^{94}Ag ground-state mass is needed, see next subchapter (Section 5.3.1).

5.3.1 Estimating the ground-state mass of ^{94}Ag

In this subchapter the already existing methods for estimating the ^{94}Ag ground state mass will be reviewed, an independent method will be proposed and their results will be compared. The ground state of ^{94}Ag is presumed to be a $T = 1$, $J^\pi = 0^+$ isobaric analog state [Jänecke & O'Donnell, 2005], therefore the Q_{EC} value of the superallowed $0^+ \longrightarrow 0^+$ β decay of ^{94}Ag can be estimated quite accurately using two independent approaches, the latter of which is proposed here and is similar to the calculations performed in Ref. [Faestermann et al., 2002]. Since 2002 the direct mass measurements at SHIPTRAP and at CSRe have revealed large deviations from AME2003 up to 1.6 MeV at $N \approx Z$ and $Z = 39 - 43$ isotopes [Haettner et al., 2011, Xing et al., 2018], which ultimately resulted in a significant change of the adopted masses in AME reaching its maximum for Mo/Tc isotopes (for details see differences between AME2003 [Wapstra et al., 2003, Audi et al., 2003] and AME2020 [Huang et al., 2021, Wang et al., 2021] evaluations). In addition, since 2002, new, more precise half-life measurements became available for $N = Z$ nuclides in the vicinity of ^{100}Sn [Park et al., 2019]. Therefore it makes sense to update the initial mass estimates reported in [Faestermann et al., 2002] with putting emphasis on estimating the ^{94}Ag ground-state mass, and compare the new mass estimates to previously available values from literature. This work was performed under the continuous help and guidance of J. Äystö and X. Mougeot, who also performed the final computation of the new ^{94}Ag ground-state mass estimate [Mougeot et al., 2024] (priv. comm.).

Introduction to the concept of isobaric analog states

Firstly, the concept of isobaric analog states (IAS) is shortly reviewed and their characteristic properties are discussed. The nucleon-nucleon interaction exhibits an approximate charge symmetry and charge independence [Machleidt & Slaus, 2001], which is very helpful for interpreting the behavior of the otherwise exceptionally complex nuclear systems. These isospin-related symmetries can be described by the conceptual and mathematical formalism proposed in Ref. [Wigner, 1937] introducing Wigner's SU(4) spin-isospin symmetry, which enables the treatment of protons and neutrons in the same system, i.e. it treats neutrons and protons as up and down projections of an isospin $t = \frac{1}{2}$ nucleon, and defines the tools to model various symmetry-breaking phenomena. In this formalism the ground and excited states of a nucleus are assigned an isospin (T) quantum number with an isospin projection T_Z with allowed values of

$$\left|\frac{N-Z}{2}\right| \leq T \leq \frac{N+Z}{2} \text{ and } T_Z = \sum_{i=1}^{A} t_Z\left(i\right) = \frac{N-Z}{2} \tag{5.1}$$

where N, Z and $A = N+Z$ are the neutron, proton and mass numbers, respectively, and $t_Z(i) = \pm\frac{1}{2}$ denotes the individual isospin projection of the i^{th} neutron or proton, respectively. With the concept of isospin established, the members of a given isobaric multiplet with isospin T can be characterized by the projections T_Z running from $-T$ to $+T$. The isobaric analog states (IAS) are defined as the ground or excited states of the given isobaric multiplet, which have the same isospin

T and the same J^π spin-parity. In case of a perfectly-conserved isospin symmetry and in the absence of electromagnetic effects, the excitation energies of these IAS states would be identical. In reality the Coulomb interactions and any other isospin-non-conserving interactions, such as charge-dependent nuclear forces, lift this degeneracy. The status of the ongoing investigations connected to the excitation energy differences defined for mirror nuclei ($T_Z = \pm T$) and for isobaric triplets ($T = 1$ and $T_Z = 0, \pm 1$) was reviewed recently in Ref. [Bentley, 2022]. Besides the expected similarities in their excitation energies, the total binding energies of the IAS states are also expected to follow certain relations and trends. The works of [Antony et al., 1997, Britz et al., 1998, Lam et al., 2013, MacCormick & Audi, 2014] present the most recent, comprehensive evaluations of these characteristic mass relations of the observed IAS states, i.e their Coulomb-displacement energy (CDE) systematics and the isobaric multiplet mass equations (IMME), the latter of which enables mass predictions of IAS states in light and medium-heavy nuclei ($A \leq 71$, $T = \frac{1}{2}$, 1, $\frac{3}{2}$, 2, $\frac{5}{2}$, 3 multiplets) with tens of keV precision. Additionally, the excitation energies and masses of IAS states can be also used to reflect on various nuclear properties, e.g. they enable further refinement of isospin-symmetry-breaking effects within different nuclear structure models [Towner & Hardy, 2008, Bączyk et al., 2018, Kaneko et al., 2012, Bentley, 2022], they are used to access both the systematics of pairing energy and of symmetry energy [Jänecke, 1965, Danielewicz & Lee, 2014], to study the limits of existence in proton-rich nuclei up to $A = 100$ [Klochko & Smirnova, 2021, Kaneko et al., 2013] or to provide constrains for the equation of state of dense symmetrical nuclear matter, which is one of the essential components of realistic astrophysical modeling [Tsang et al., 2012]. Furthermore, the masses of IAS states with $J^\pi = 0^+$, $T = 1$ are also being used to test the conserved vector current (CVC) hypothesis of the weak interaction, which is part of a yet unresolved quest spanning more than 50 years [Hardy & Towner, 2020].

Secondly, the fact that the ground state of the odd-odd $N = Z$ nucleus ^{94}Ag is presumably a $T = 1$, $J^\pi = 0^+$ isobaric analog state [Jänecke & O'Donnell, 2005] needs to be understood. Normally, the lowest-energy set of states in any nucleus have the lowest allowed value of isospin, which is $T = 0$ in case of $N = Z$ nuclei. This is however not true in the case of odd-odd $N = Z$ nuclei with $A > 40$, where the $T = 1$, $J^\pi = 0^+$ state becomes the ground state in most cases except, possibly, near closed shells [Zeldes & Liran, 1976, Macchiavelli et al., 2000]. In nuclei close to the $N = Z$ line the protons and neutrons near the Fermi surface occupy identical orbitals, which allows for the neutron-proton (np) pairing correlations to start playing a significant role besides the nn and pp pairing. As demonstrated in Ref. [Macchiavelli et al., 2000, Frauendorf & Macchiavelli, 2014] the presence of the isovector ($T = 1$) np pairing correlations are at the same time necessary and also sufficient to provide the additional binding pushing down the $J^\pi = 0^+$, $T = 1$ IAS state to the ground state in medium-heavy, odd-odd $N = Z$ nuclei, such as ^{94}Ag.

Previous methods to estimate the ^{94}Ag ground-state mass

As a third step, the status of available literature on the ground-state mass of ^{94}Ag is reviewed. Since the mass of the β-decay daughter of ^{94}Ag, ^{94}Pd, is well known [Huang et al., 2021, Wang et al., 2021], it is sufficient to compare the Q_{EC} values of ^{94}Ag, which has three different sources in the literature. Out of this three sources there is only one, which is based on a measurement, the other two are both based on extrapolations, however, the latter "extrapolation" also incorporates physics considerations. Firstly, via measuring the total transition energy of the superallowed $0^+ \longrightarrow 0^+$ β decay of ^{94}Ag a $Q_{\mathrm{EC}}\left(^{94}\mathrm{Ag},0^+\right) = 13350^{+690}_{-610}$ keV was obtained [Park et al., 2019]. Secondly, this measured Q_{EC} value was listed as irregular in AME2020 [Huang et al., 2021, Wang et al., 2021] and the usage of the extrapolated ^{94}Ag mass value was recommended instead, which results in $Q_{\mathrm{EC}}\left(^{94}\mathrm{Ag},0^+\right) = 13700(400)\#$ keV. On the other hand, in the paper by Kankainen *et al.* [Kankainen et al., 2008] a $Q_{\mathrm{EC}}\left(^{94}\mathrm{Ag},0^+\right) = 12760(360)$ keV was determined through a linear fit to the Coulomb displacement energies for $T = 1$ isobaric analog states of odd-odd $N = Z$

nuclei, which would even more strongly break the smoothness of the mass surface in this region as given in AME2020. Although these two "extrapolations" reported in [Kankainen et al., 2008] and AME2020 [Huang et al., 2021, Wang et al., 2021] deviate by $\sim 2\sigma$ from each other, both of them agree with the measured $Q_{\mathrm{EC}}\left(^{94}\mathrm{Ag},0^{+}\right)$ reported in [Park et al., 2019]. Since the large uncertainties of the measured $Q_{\mathrm{EC}}\left(^{94}\mathrm{Ag},0^{+}\right)$ reported in [Park et al., 2019] prevents to favor the one or the other extrapolation and it also prevents to further study the riddle surrounding the exotic decay modes of the (21^{+}) spin-trap isomer in ^{94}Ag, it becomes inevitable to dig deeper in the topic of the ^{94}Ag ground state mass estimates.

At this point it is helpful to summarize the most important physics considerations and assumptions behind the $Q_{\mathrm{EC}}\left(^{94}\mathrm{Ag},0^{+}\right)$ estimate reported in [Kankainen et al., 2008]. A comprehensive review of the physics considerations can be found in Ref. [Nolen & Schiffer, 1969]. The Coulomb-displacement energy (CDE) between a pair of isobaric analog states is given by the equation

$$\Delta E_{\mathrm{C}} = \mathrm{ME}_{Z>} - \mathrm{ME}_{Z<} + \Delta_{\mathrm{nH}}, \tag{5.2}$$

where $\mathrm{ME}_{Z>}$ and $\mathrm{ME}_{Z<}$ are the mass excesses of a higher and a lower Z member of an IAS pair with given isospin T and its projection $T_Z(Z>) = T_Z(Z>) - 1$, respectively, and $\Delta_{\mathrm{nH}} = 782.34700(44)$ keV is the neutron–hydrogen mass difference [Huang et al., 2021, Wang et al., 2021]. In case of a perfectly-conserved isospin symmetry, i.e. if the nuclear wavefunctions of the IAS pair are identical and if the nucleon-nucleon force is charge independent and charge symmetric, ΔE_{C} represents only the Coulomb-energy difference between the two IAS pairs. In mirror nuclei with $T = \frac{1}{2}$ only charge symmetry is necessary. Using the model applied in Ref. [Nolen & Schiffer, 1969], which is historically based on the liquid-drop model of nuclei and also incorporates semi-classical considerations, the Coulomb-energy difference between two IAS pairs takes the form:

$$\Delta E_{\mathrm{C}} = a \cdot \frac{\frac{1}{2}\left(Z> + Z<\right)}{A^{1/3}} + b, \tag{5.3}$$

where the proportionality factor a is related to the nuclear charge radii via $a = \frac{6}{5} \cdot \frac{e^2}{4\pi\epsilon_0} \cdot \frac{1}{r_0}$ and the constant offset b is the so-called exchange term. Therefore one can fit a linear function using Eq. (5.3) to the ΔE_{C} of the measured IAS pairs with $T = 1$ and deduce the fit coefficients a and b and extrapolate a ΔE_{C} value for ^{94}Ag. After this, the Q_{EC} value of ^{94}Ag is calculated by $Q_{\mathrm{EC}}\left(^{94}\mathrm{Ag},0^{+}\right) = \Delta E_{\mathrm{C}}\left(^{94}\mathrm{Ag},0^{+}\right) - \Delta_{\mathrm{nH}}$. As pointed out in Ref. [Nolen & Schiffer, 1969], the coefficient b in Eq. (5.3) should be treated as a global constant describing all IAS pairs of a given isospin T instead of varying the coefficient in the fitting data in an arbitrary manner for even-even, odd-odd and odd-A nuclei as originally suggested in Ref. [Peaslee, 1954]. The most "up-to-date", comprehensive evaluation of Coulomb-displacement energy systematics of all IAS states with isospin of $T = \frac{1}{2}, 1, \frac{3}{2}, 2$ is from Ref. [Antony et al., 1997], where the derived proportionality factors a correspond to radius parameters of $r_0 = 1.22 - 1.28$ fm. The CDE linear fit coefficients from [Antony et al., 1997] based on $T = 1$ IAS pairs give a prediction of $Q_{\mathrm{EC}}\left(^{94}\mathrm{Ag},0^{+}\right) = 12770(3)$ keV, which is in good agreement with the estimate proposed by [Kankainen et al., 2008]. Thus it seems adequate to say that any disadvantages, which may result from the somewhat arbitrary choice of including only odd-odd $N = Z$ nuclei in the linear fit reported in Ref. [Kankainen et al., 2008], are not significant. Besides the assumption of the perfectly-conserved isospin symmetry, Eq. (5.3) also assumes that the radius of both IAS is the same with equivalent radius of a uniformly charged sphere given by $R_{\mathrm{eq}} = r_0 \cdot A^{1/3} = \sqrt{\frac{5}{3}\langle r^2\rangle}$. In Ref. [Reponen et al., 2021] a sudden increase in the nuclear size of proton-rich ^{96}Ag was observed and an increasing trend in the magnitude of the "kink" at $N = 50$ in nuclear charge radii as a function of increasing proton number towards ^{100}Sn was illustrated. In addition to its possible sensitivity to nuclear shape, as demonstrated in Ref. [Damgaard & Winter, 1966], the

Coulomb-displacement energy can be very sensitive to nuclear structure. Thus it is interesting to speculate how precisely the $Q_{\mathrm{EC}}\left(^{94}\mathrm{Ag},0^{+}\right)$ can be estimated by this method, when in reality the radius of ^{94}Ag and ^{94}Pd may be different from each other and/or the nuclear wavefunctions of the IAS pair may be different from each other due to various isospin-symmetry-breaking effects. In order to overcome this disadvantages, an independent method for estimating the mass of the ^{94}Ag presumably (0^{+}), $T = 1$ ground state [Jänecke & O'Donnell, 2005] based on the global $\overline{\mathcal{F}t}$ value is proposed here.

The global $\overline{\mathcal{F}t}$-based mass estimate of ^{94}Ag

The general concept of the calculations of this work is similar to [Faestermann et al., 2002] including a few improvements since then; the $Q_{\mathrm{EC}}\left(^{94}\mathrm{Ag},0^{+}\right)$ is deduced applying the global $\overline{\mathcal{F}t}$ value of the superallowed $0^{+} \longrightarrow 0^{+}$ β decays [Hardy & Towner, 2020] to the β decay between ^{94}Ag and ^{94}Pd ground states and using its measured half-life of 27(2) ms (weighted average of the half-life measurements published in [Park et al., 2019, Kienle et al., 2001, Moschner et al., 2015]). For deducing the $Q_{\mathrm{EC}}\left(^{94}\mathrm{Ag},0^{+}\right)$ value the general formalism is adopted from [Hardy & Towner, 2020]; i.e. a capital $\mathcal{F}t$ value, which is expected to be constant for all superallowed $0^{+} \longrightarrow 0^{+}$ β decays as a consequence of the CVC hypothesis, is defined by

$$\mathcal{F}t \equiv ft\left(1+\delta_{\mathrm{NS}}-\delta_{C}\right)\left(1+\delta_{R}^{\prime}\right), \tag{5.4}$$

where the δ_C gives the isospin-symmetry-breaking correction, the δ_{NS} and the $\delta_R^{\prime}$ corrections together represent the part of the radiative correction, which is dependent on the particular β transition involved, and the ft value characterizes any β transition depending on three quantities: the total transition energy Q_{EC}, the half-life $T_{1/2}$ of the parent state, and the branching ratio R for the particular transition of interest. While the statistical rate function f depends on the Q_{EC} value, the partial half-life t for each transition is obtained from the half-life $T_{1/2}$ and branching ratio R following the relationship of

$$t = \frac{T_{1/2}}{R}\left(1+P_{\mathrm{EC}}\right), \tag{5.5}$$

where P_{EC} is the electron-capture fraction calculated for each transitions. With the formalism of the superallowed $0^{+} \longrightarrow 0^{+}$ β decays established, the $Q_{\mathrm{EC}}\left(^{94}\mathrm{Ag},0^{+}\right)$ can be "reverse-engineered" using its measured half-life and the global $\overline{\mathcal{F}t}$ value and following the steps as explained below. Starting from the global $\overline{\mathcal{F}t} = 3072.24(185)$ s value and using $T_{1/2} = 27(2)$ ms, considering a $R = 100\%$ branching ratio for the superallowed $0^{+} \longrightarrow 0^{+}$ transition supported by Ref. [Hardy & Towner, 2020] and the $\delta_C - \delta_{\mathrm{NS}} = 1.5(10)\%$ correction factor, which is an estimate based on Ref. [Hardy & Towner, 2020, Satuła et al., 2012, Xayavong & Smirnova, 2024], the following relation is deduced for the ^{94}Ag superallowed $0^{+} \longrightarrow 0^{+}$ β decay:

$$\frac{ft\left(1+\delta_{R}^{\prime}\right)}{T_{1/2}/R} = f\left(1+P_{\mathrm{EC}}\right)\left(1+\delta_{R}^{\prime}\right) = 115519(8637) \tag{5.6}$$

In the above relation the 2 ms uncertainty of the measured half-life provides the dominating uncertainty contribution, thus it is essential to have trustworthy the half-life measurements of the given superallowed $0^{+} \longrightarrow 0^{+}$ transitions for this calculations. As the next step the BetaShape code [Mougeot, 2015, Mougeot, 2017, Mougeot, 2019], which provides an accurate calculation of the statistical rate function f, the $\delta_R^{\prime}$ correction and the electron-capture fraction P_{EC}, is used to minimize the following quantity iteratively for different values of $Q_{\mathrm{EC}}\left(^{94}\mathrm{Ag},0^{+}\right)$:

$$\chi^{2} = \frac{\left(\dfrac{ft\left(1+\delta_{R}^{\prime}\right)}{T_{1/2}/R} - 115519\right)^{2}}{(8637)^{2}} \tag{5.7}$$

The quadratic χ^2 distribution then allows to deduce the uncertainty of the $Q_{\mathrm{EC}}\left(^{94}\mathrm{Ag},0^+\right)$ via the Q_{EC} range at $\chi^2 = \chi^2_{\mathrm{min}} + 1$. This results in a $Q_{\mathrm{EC}}\left(^{94}\mathrm{Ag},0^+\right) = -12570(190)$ keV. Since the relative uncertainty of the measured ^{94}Ag ground-state half-life is as large as $\frac{\Delta T_{1/2}}{T_{1/2}} = 7.4\%$, at the first glance it may seem surprising that the global $\overline{\mathcal{F}t}$ calculations yield only $\frac{\Delta Q_{\mathrm{EC}}}{Q_{\mathrm{EC}}} = 1.5\%$ relative uncertainty for the deduced $Q_{\mathrm{EC}}\left(^{94}\mathrm{Ag},0^+\right)$. This can be empirically understood as a consequence of Sargent's law [Sargent, 1933]; i.e. the statistical rate function, f, for each transition depends primarily on the charge of the daughter nucleus, Z, and on the Q_{EC} value to the fifth power. Consequently, the following approximate relationship between the relative uncertainties of Q_{EC} and f is valid [Hardy & Towner, 2005]:

$$\frac{\Delta Q_{\mathrm{EC}}}{Q_{\mathrm{EC}}} \approx \frac{1}{5} \cdot \frac{\Delta f}{f} \text{ and, in addition, due to Eq. (5.6): } \frac{\Delta f}{f} \approx \frac{\Delta T_{1/2}}{T_{1/2}}. \tag{5.8}$$

This approximate relationship gives "the beauty of these calculations" leading to a small relative uncertainty for the resulting $Q_{\mathrm{EC}}\left(^{94}\mathrm{Ag},0^+\right)$ estimate.

After the formalism of the global $\mathcal{F}t$ calculations is clear, the assumptions and choices applied during the calculations need to be discussed:

(i) Although the choice of the $\delta_C - \delta_{\mathrm{NS}} = 1.5(10)\%$ correction factor estimate for ^{94}Ag is somewhat arbitrary, in the following an argumentation supporting this choice will be discussed. Firstly, the uncertainty of this correction factor covers all accepted $\delta_C - \delta_{\mathrm{NS}}$ values for the $T_Z = 0$ nuclei reported in [Hardy & Towner, 2020] (see Table XVI. of the paper) except the very light mass nucleus of ^{26}Al. It also covers all available δ_C values calculated by different theoretical approaches [Xayavong & Smirnova, 2018] at $Z = 37$, which is the highest Z value for which the $\mathcal{F}t$-value is known so far. In particular, this uncertainty also covers the $\delta_C = 0.96(18)\%$ value determined for the ^{94}Ag superallowed β decay from density functional theory calculations [Satuła et al., 2012], which is expected to give the dominating component in the $\delta_C - \delta_{\mathrm{NS}}$ correction. Those latter calculations are based on first principles in contrast to the semiphenomenological approaches adopted in the latest evaluation of superallowed $0^+ \longrightarrow 0^+$ β decays [Hardy & Towner, 2020]. Finally and most importantly, in order to check the influence of the $\delta_C - \delta_{\mathrm{NS}}$ correction, the global $\overline{\mathcal{F}t}$-based calculations were repeated with different $\delta_C - \delta_{\mathrm{NS}}$ choices, e.g. increasing this correction factor from 0.5% to 1.65%. In this test case the resulting $Q_{\mathrm{EC}}\left(^{94}\mathrm{Ag},0^+\right)$ increased only by 30 keV, which is well within the total uncertainties of the global $\overline{\mathcal{F}t}$-based $Q_{\mathrm{EC}}\left(^{94}\mathrm{Ag},0^+\right)$ estimate.

(ii) Secondly, an argumentation behind the assumption of the $R = 100\%$ branching ratio will be discussed. In case of the superallowed β decays from the $T_Z = 0$ parent nuclei the branching ratio $R \geq 99.5\%$ is in general a good assumption, because their even-even daughter nuclei typically do not have many low-lying 1^+ states [Hardy & Towner, 2020]. However, with the larger Q_{EC} value of the higher-Z $T_Z = 0$ parent nuclei also relatively high-lying 1^+ or non-analog 0^+ states of their daughter nuclei become accessible to β decay [Hardy & Towner, 2002, Piechaczek et al., 2003]. On the other hand, the level scheme of the ^{94}Ag β-decay daughter, ^{94}Pd, is quite well-known experimentally and theoretically [Plettner et al., 2004, Garnsworthy et al., 2009, Brock et al., 2010, Park et al., 2017, Häfner et al., 2019], but so far no experimental evidence was found on the possible existence of a high-lying 1^+ or a non-analog 0^+ state in ^{94}Pd up to 7.7 MeV. The theoretical calculations reported in [Mare & Petrovici, 2022] predicted an only 1.23% depletion of the ground-state to ground-state transition of ^{94}Ag. Considering all these evidence, the $R = 100\%$ branching ratio assumption seems quite reasonable.

(iii) Last but not least, ^{94}Ag is situated next to the proton-dripline [Čeliković et al., 2016]. Therefore it makes sense to wonder if and how the proximity of the proton dripline may influence the ^{94}Ag mass value estimate. Firstly, one can argue that ^{74}Rb is also situated next to the proton-unbound nucleus ^{73}Rb [Hoff et al., 2020], but this did not prevent including its superallowed β transition into the determination of the global $\overline{\mathcal{F}t}$ value [Hardy & Towner, 2020]. On the other hand, as demonstrated by the recent isospin-breaking calculations of [Xayavong & Smirnova, 2024], the closeness of the proton dripline at ^{70}Br, ^{74}Rb results in enhanced higher-order contributions of the calculated δ_C corrections. Nevertheless, all these variations of the δ_C corrections are well within uncertainties of the chosen $\delta_C - \delta_{\rm NS} = 1.5(10)\%$.

In summary, as long as the estimate of $Q_{\rm EC}\left(^{94}\text{Ag},0^+\right)$ has uncertainties that are dominated by the uncertainties from the half-life measurement of ^{94}Ag, any other sources of inaccuracies can be neglected, such as the ones arising from (i) an incorrect choice of the $\delta_C - \delta_{\rm NS}$ correction or (ii) the unaccounted uncertainties due to the unknown branching ratio R or (iii) the proximity of the proton dripline.

Comparison to previous mass estimates of ^{94}Ag

The results of the global $\overline{\mathcal{F}t}$ calculations of the present work are summarized and compared with previous estimates for $Q_{\rm EC}\left(^{94}\text{Ag},0^+\right)$ in Table 5.9. The uncertainty of the global $\overline{\mathcal{F}t}$-based $Q_{\rm EC}\left(^{94}\text{Ag},0^+\right)$ estimate is factor 2-3 smaller compared to the uncertainty of the previous estimates. Although the result of the global $\overline{\mathcal{F}t}$ calculations show a $\sim 3\sigma$ deviation from the value derived from systematic trends in AME2020 [Huang et al., 2021, Wang et al., 2021], it is in good agreement with the independent study by Kankainen *et al.* [Kankainen et al., 2008] based on Coulomb-displacement energy (CDE) systematics and within $\sim 1\sigma$ agreement with the indirect, β-decay end-point energy measurement [Park et al., 2019]. To further demonstrate the mismatch between the measured half-life of ^{94}Ag and the AME2020 extrapolations, the following thought experiment is considered: accepting the extrapolated $Q_{\rm EC}\left(^{94}\text{Ag},0^+\right) = 13700(400)\#$ keV value recommended in AME2020 [Huang et al., 2021, Wang et al., 2021] and applying the global $\overline{\mathcal{F}t}$ value for the superallowed $0^+ \longrightarrow 0^+$ β decay of ^{94}Ag, the deduced half-life for the ^{94}Ag ground state would be around 19 ms. This deduced half-life contradicts the three existing measurements [Park et al., 2019, Kienle et al., 2001, Moschner et al., 2015], which resulted in measured half-life values of 27(2) ms, 34.5(17.5) ms and 29(6) ms, respectively, with their weighted average 27.3(19) ms being $\sim 4\sigma$ off from 19 ms. This shows the clear contradiction between the extrapolated $Q_{\rm EC}\left(^{94}\text{Ag},0^+\right)$ value recommended in AME2020 and its measured half-life. In addition, Table 5.9 also shows a large scatter of the one- and two-proton separation energies of ^{94}Ag depending on which method is used for estimating the ^{94}Ag ground-state mass. The proton separation energy of the proton-unbound nucleus ^{93}Ag was measured to be $S_p\left(^{93}\text{Ag}\right) = -1060(30)$ keV in RIKEN [Čeliković et al., 2016], which was used in Table 5.9 to also deduce the empirical proton-neutron interaction strength (δV_{pn}) of ^{94}Ag, which also strongly scatters depending on which method is used for estimating the ^{94}Ag ground-state mass. This motivates an extension of the different mass estimates to all odd-odd $N = Z$ nuclei, and an examination of the evolution of the higher-order binding energy derivatives.

Extension of the methods to all, odd-odd $N = Z$ nuclei

The heaviest odd-odd $N = Z$ nucleus, whose ground-state mass was directly measured to this date is ^{74}Rb [Huang et al., 2021, Wang et al., 2021], while the ground-state masses of ^{90}Rh, ^{94}Ag and ^{98}In can be deduced from their indirect β-end-point energy measurements [Park et al., 2019], but all these indirect masses have large uncertainties and all of them were listed as irregular in

Table 5.9: Ground-state properties (mass excess, Q_{EC} value, one-/two-proton separation energies S_p/S_{2p} and empirical proton-neutron interaction strength δV_{pn}) of ^{94}Ag deduced in the present work based on the global $\overline{\mathcal{F}t}$ calculations compared with results from earlier works, such as the independent study by Kankainen *et al.* [Kankainen et al., 2008] based on Coulomb-displacement energy (CDE) systematics or the $Q_{\mathrm{EC}}\left(^{94}\mathrm{Ag},0^+\right)$ extracted from the β-decay end-point energy measurement by Park *et al.* [Park et al., 2019]. The deduced ^{94}Ag properties are also compared with the extrapolations reported in AME2020 [Huang et al., 2021, Wang et al., 2021] (#).

^{94}Ag properties	$\overline{\mathcal{F}t}$ calc. (this work) (keV/c^2)	CDE systematics[c] (keV/c^2)	Indirect meas.[d] (keV/c^2)	AME2020[e] (keV/c^2)
$Q_{\mathrm{EC}}\left(^{94}\mathrm{Ag},0^+\right)$	12570(190)	12760(360)	13350^{+690}_{-610}	13700(400)#
$\mathrm{ME}\left(^{94}\mathrm{Ag},0^+\right)$	-53530(190)	-53340(360)	-52750^{+690}_{-610}	-52400(400)#
$S_p\left(^{94}\mathrm{Ag},0^+\right)$[a]	1690(190)	1500(360)	910^{+610}_{-690}	560(400)#
$S_{2p}\left(^{94}\mathrm{Ag},0^+\right)$[b]	5120(190)	4930(360)	4340^{+610}_{-690}	3990(400)#
$\delta V_{pn}\left(^{94}\mathrm{Ag},0^+\right)$[a,f]	2750(200)	2560(360)	1970^{+610}_{-690}	1620(400)#

[a] Based on the presently-reported mass measurement of ^{93}Pd.
[b] Based on the presently-reported mass measurement of ^{92}Rh.
[c] [Kankainen et al., 2008].
[d] [Park et al., 2019].
[e] [Huang et al., 2021, Wang et al., 2021].
[f] Uses $S_p\left(^{93}\mathrm{Ag}\right) = -1060(30)$ keV measurement from [Čeliković et al., 2016].

AME2020 [Huang et al., 2021, Wang et al., 2021]. In order to be able check the evolution of the one-/two-proton separation energies S_p/S_{2p} at the $N = Z$ line towards ^{100}Sn, the masses of all unmeasured/only indirectly measured odd-odd $N = Z$ nuclides have to be estimated following the same procedure as used for ^{94}Ag. For these calculations the ground states of all odd-odd $N = Z$, $A \geq 62$ nuclides are assumed to be $T = 1$, $J^\pi = 0^+$ isobaric analog states, which is supported by Ref. [Jänecke & O'Donnell, 2005]. As a first step, a linear fit following Eq. (5.3) is performed to the Coulomb displacement energies for $T = 1$ isobaric analog states using the measured masses adopted by AME2020 [Huang et al., 2021, Wang et al., 2021]. This linear fit is performed in the same manner to [Kankainen et al., 2008], only including odd-odd $N = Z$ nuclei, because the goal here is to check if anything changed since [Kankainen et al., 2008] and not to repeat the comprehensive evaluation from [Antony et al., 1997]. In addition, due to the controversy around the ^{70}Br mass value pointed out in Ref. [Hardy & Towner, 2015, Huang et al., 2023], this mass is omitted from the CDE linear fit. The result of this linear fit is shown in Fig. 5.9; the fit parameters are determined to be $a = 1395(18)$ keV and $b = -853(89)$ keV, and a $Q_{\mathrm{EC}}\left(^{94}\mathrm{Ag},0^+\right) = 12630(400)$ keV is deduced from the fit. The deduced $Q_{\mathrm{EC}}\left(^{94}\mathrm{Ag},0^+\right)$ is still in agreement with both previous studies [Kankainen et al., 2008, Antony et al., 1997], therefore, in the following, this linear fit is used as the source of CDE-based mass estimates for all unmeasured odd-odd $N = Z$ nuclei. In comparison to this linear fit the Fig. 5.9 also shows the deduced ΔE_{C} values from different mass predictions/extrapolations or β-decay end-point energy measurements, such as [Park et al., 2019, Zong et al., 2022, Wang et al., 2021]. As the figure clearly demonstrates, there is an up to ∼1 MeV disagreement between the AME2020 extrapolations [Huang et al., 2021, Wang et al., 2021] and the linear fit of ΔE_{C}, which is true for several odd-odd $N = Z$ nuclei with $A \geq 86$. While the β-decay end-point energy measurement from [Park et al., 2019] is closer to the AME2020 extrapolation [Huang et al., 2021, Wang et al., 2021] in case of ^{90}Rh, ^{94}Ag, the situation is different at ^{98}In. The measured $Q_{\mathrm{EC}}\left(^{98}\mathrm{In},0^+\right)$

value from [Park et al., 2019] gives a Coulomb-displacement energy, which is closer to the linear fit of ΔE_{C} as compared to the AME2020 extrapolation. Besides depicting odd-odd $N = Z$ nuclei, the Fig. 5.9 also shows ΔE_{C} values of $T_Z = \pm 1/2$ mirror nuclei pairs with $A = 73 - 99$ with open purple triangles, which are deduced based on the assumption that the ground state of those mirror pairs is always a $T = 1/2$ IAS state with the same J^π spin-parity. In lack of experimental proofs for the ground-state J^π at $T_Z = -1/2$ and $A \geq 77$ [Kondev et al., 2021], the assumption of the same J^π for all $T_Z = \pm 1/2$ mirror pairs seems reasonable based on [Antony et al., 1997, Lam et al., 2013], where it is shown to be the case for all $T_Z = \pm 1/2$ pairs with $A \leq 71$. For calculating the ΔE_{C} ($T_Z = \pm 1/2$, $73 \leq A \leq 99$) values a combination of the measured masses from AME2020 [Huang et al., 2021, Wang et al., 2021] and the mass predictions from Ref. [Zong et al., 2022] is used. In case of ^{93}Pd the AME2020 is superseded by the presently-reported direct mass measurement, while the ground-state masses of ^{75}Sr, ^{95}Ag, ^{99}In are taken from [Wang et al., 2023, Ge et al., 2024, Nies et al., 2023], respectively. On the other hand for the $T_Z = -1/2$ and $A \geq 77$ nuclei no mass measurements are available to this date, therefore their masses are taken from Ref. [Zong et al., 2022], where mass predictions of proton-rich systems close to the proton dripline were proposed based on mass relations of mirror nuclei. The accuracy of the mass predictions proposed in Ref. [Zong et al., 2022] is demonstrated by the fact that the directly measured masses of the twelve $T_Z = -1$ and $T_Z = -1/2$ nuclei between $A = 58 - 75$ reported in Ref. [Wang et al., 2023] are in generally good agreement with their predicted masses, i.e. nine of the measured masses are matching with their mass predictions within uncertainties, while the other three are only $\leq 1.5\sigma$ deviated from their mass predictions. The ΔE_{C} ($T_Z = \pm 1/2$, $73 \leq A \leq 99$) values, which were deduced via the procedure explained above, are in good agreement with the linear fit of ΔE_{C} of $T = 1$ IAS pairs, while they are more deviated from the AME2020 extrapolations for the odd-odd $N = Z$ nuclei (see Fig. 5.9).

In addition to the above-mentioned mass estimates from [Park et al., 2019, Zong et al., 2022, Wang et al., 2021], there is also one more set of data points for odd-odd $N = Z$ nuclei shown as green rectangles on Fig. 5.9. These are deduced from the measured half-lives of their individual superallowed $0^+ \longrightarrow 0^+$ transitions and the global $\overline{\mathcal{F}t}$ value. These estimates for the remaining odd-odd $N = Z$ nuclei were calculated by a simpler, but less accurate procedure as compared to the above-described, more accurate global $\overline{\mathcal{F}t}$ calculations aiming at deducing Q_{EC} (^{94}Ag,0^+). The ft value of ^{74}Rb (ft (^{74}Rb) = 3082.8(65) s) was fixed from [Hardy & Towner, 2020] and the NNDC log(ft) calculator website (https://www.nndc.bnl.gov/logft/index.html) was used to deduce the Q_{EC} value of the individual transitions based on their measured half-lives and assuming an $R = 100\%$ branching ratio. This procedure neglects all small, transition-dependent radiative and nuclear-structure related corrections (see definition in Eq. (5.4)) and results in a Q_{EC} value for ^{94}Ag, which is ∼70 keV larger as compared to the more accurate, global $\overline{\mathcal{F}t}$-based value. This ∼70 keV absolute deviation and the corresponding ∼0.6% relative deviation is then used to estimate a systematic uncertainty component for the Q_{EC} values deduced from this less accurate procedure, which is linearly added to the dominating uncertainty component deduced from the experimental half-life uncertainties of the individual transitions. The resulting Q_{EC} estimates of odd-odd $N = Z$ nuclei are tabulated in Table 5.11 and also plotted in Fig. 5.9. Looking at Fig. 5.9 one can notice in general a good agreement between the global $\overline{\mathcal{F}t}$-based Q_{EC} estimates and the smooth trend of ΔE_{C} represented by the linear fit on the figure, except maybe the larger deviations at ^{86}Tc and ^{98}In. In order to better judge the source of these larger differences at ^{86}Tc and ^{98}In, Fig. 5.9 shows the Q_{EC} values deduced from their different, individual half-life measurements, while for the remaining of the odd-odd $N = Z$ nuclides the Q_{EC} values deduced from the weighted average of their individual half-life measurements are depicted. The $T_{1/2}$ (^{86}Tc,0^+) was measured by two different groups, at GSI and at GANIL (see Ref. [Kienle et al., 2001, Garcés Narro et al., 2001]), resulting in 59^{+8}_{-7} ms and 44(12) ms, respectively. While the GSI measurement with the smaller uncertainties from

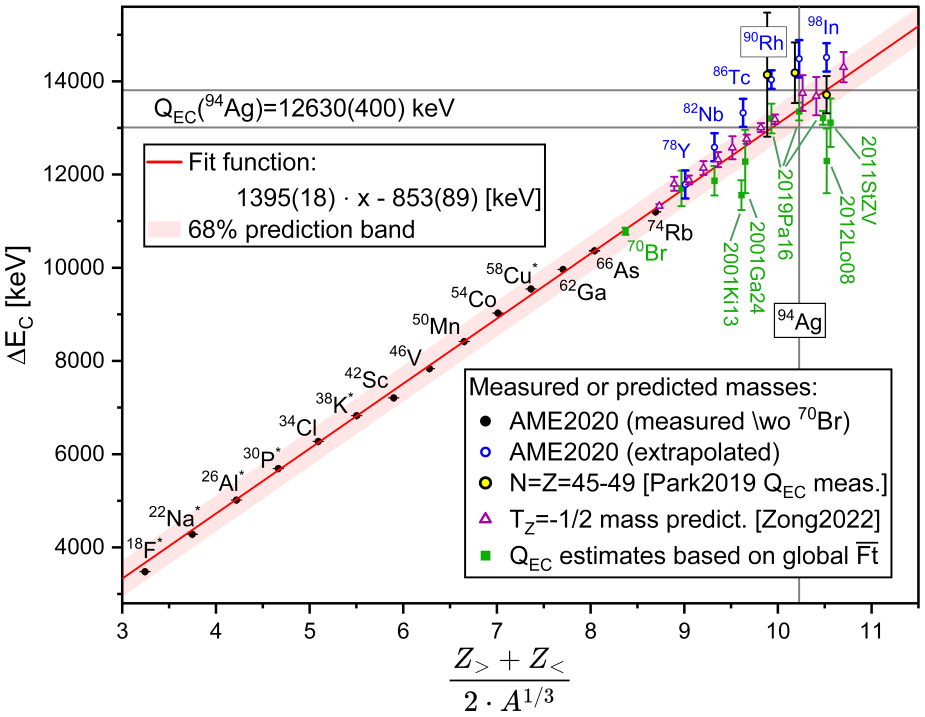

Figure 5.9: Experimental and predicted Coulomb-displacement energies (ΔE_C) for odd-odd $N = Z$ nuclei. The linear fit over the measured CDE values, which are drawn with black filled symbols, and the corresponding 68% prediction band is shown with red color. In comparison to the linear fit different mass estimates are shown; the open blue symbols represent AME2020 extrapolations [Huang et al., 2021, Wang et al., 2021] and the filled green symbols represent the global $\overline{\mathcal{F}t}$-based mass estimates for odd-odd $N = Z$ nuclei. In case of ^{86}Tc and ^{98}In, the global $\overline{\mathcal{F}t}$-based mass estimates based on the individual half-life measurements [Kienle et al., 2001, Garcés Narro et al., 2001, Park et al., 2019, Lorusso et al., 2012, Straub, 2011] are shown. In addition, the linear fit is also compared with the Coulomb-displacement energies for $T_Z = -1/2$ nuclei (open purple symbols) estimated based on the mass predictions from [Zong et al., 2022] and with the β-decay end-point energy measurements for ^{90}Rh, ^{94}Ag, ^{98}In isotopes from [Park et al., 2019] (filled yellow symbols).

[Kienle et al., 2001] results in a Q_{EC} (^{86}Tc,0^+), which disagrees with the smooth trend of ΔE_C, the GANIL half-life value from [Garcés Narro et al., 2001] results in a Q_{EC} (^{86}Tc,0^+) estimate, which agrees with the smooth trend within uncertainties. This discrepancy may demonstrate that the global $\overline{\mathcal{F}t}$-based Q_{EC} estimates are prone to uncertainties due to possible inaccuracies in the individual half-life measurements. Alternatively, as pointed out in [Faestermann et al., 2002] the reason may also be related to unconsidered nuclear structure or shape changes around ^{86}Tc. On the other hand, the $T_{1/2}$ (^{98}In,0^+) was measured four times (see Ref. [Park et al., 2019, Kienle et al., 2001, Straub, 2011, Lorusso et al., 2012]) with values of 30(1) ms, 32^{+32}_{-11} ms, 32(6) ms and 47(13) ms, respectively. The results of these four $T_{1/2}$ (^{98}In,0^+) measurements are all consistent with each other and they all give a little inconsistency between the global $\overline{\mathcal{F}t}$-based Q_{EC} estimates and the linear fit of ΔE_C. Consequently, the discrepancy at ^{98}In may indeed arise from unconsidered nuclear structure or shape changes in the vicinity of the doubly-magic nucleus ^{100}Sn. A future mass measurement of these odd-odd $N = Z$ nuclei will resolve these questions.

Table 5.11: Summary of measured half-lives (here only the weighted average of individual half-life measurements is shown) and Q_{EC} estimates of the presumed $T = 1$, 0^+ ground states of odd-odd $N = Z$ nuclides with $A \geq 78$. The Q_{EC} estimates deduced from four different methods are compared, see details in text.

Nuclide	$T_{1/2}$ (ms)	Q_{EC} global $\overline{\mathcal{F}t}$ calc. (keV/c^2)	Q_{EC} CDE systematics (keV/c^2)	Q_{EC} Indirect meas.[a] (keV/c^2)	Q_{EC} AME2020[b] (keV/c^2)
^{98}In	30(1)	12435(150)	13035(400)	12930(400)	13730(300)#
^{94}Ag	27(2)	12570(190)	12625(400)	13350^{+690}_{-610}	13700(400)#
^{90}Rh	29(3)	12420(320)	12215(400)	13190^{+1500}_{-1160}	13250(200)#
^{86}Tc	55(7)	10920(330)	11790(400)		12540(300)#
^{82}Nb	50(6)	11085(320)	11365(400)		11800(300)#
^{78}Y	53(8)	10920(380)	10930(400)		11000(300)#

[a] [Park et al., 2019].
[b] [Huang et al., 2021, Wang et al., 2021].

Influence to the systematic trends of binding energy derivatives

As the next step the different Q_{EC} estimates of the heavy, odd-odd $N = Z$ nuclides from Table 5.11 will be used to determine the systematic trends of certain binding energy (BE) derivatives, also called as BE filters. For an introduction to the BE derivatives, see Section 1.1. The selected BE derivatives of this study are the one-/two-proton separation energies S_p/S_{2p} and empirical proton-neutron interaction strength δV_{pn}, which are plotted on Fig. 5.10. The first thing that one can notice when looking at the plots is that moving towards ^{100}Sn the evolution of the different BE filters of the odd-odd $N = Z$ nuclides deduced from the CDE-based and global $\overline{\mathcal{F}t}$-based mass estimates deviate by about ∼1 MeV from the extrapolated masses recommended in AME2020 [Huang et al., 2021, Wang et al., 2021], while the CDE-based and global $\overline{\mathcal{F}t}$-based mass estimates in general agree with each other with the exception of the two cases at ^{86}Tc and ^{98}In as discussed above. In comparison, theoretical predictions of the BE filters for $N = Z$ isotopes are plotted based on the masses predicted by five popular mass models; HFB21 [Goriely et al., 2010], FRDM2012 [Möller et al., 2016], WS4+RBF [Wang et al., 2014], DZ31 [Duflo & Zuker, 1995] and KTUY05 [Koura et al., 2005]. While the CDE-based and global $\overline{\mathcal{F}t}$-based mass estimates can be applied only locally for the odd-odd $N = Z$ isotopes, the above-listed mass models give a global description of nuclides, therefore it is interesting to compare the mass model predictions to the local mass estimates. More details about the selected models are not relevant for the present discussion, therefore they are skipped from here[2].

Firstly, the evolution of two-proton separation energies S_{2p} plotted on the top right figure in Fig. 5.10 is examined. The CDE-based and global $\overline{\mathcal{F}t}$-based mass estimates suggest that there is a change in the local trends for the S_{2p} values of $N = Z$ nuclides in the vicinity of the

[2]While the HFB21 model is classified as a purely microscopic (self-consistent) model, where the binding energy is deduced from single-particle effective interactions, the models based on the WS mass formula, just like WS4+RBF, and FRDM2012 are classified as macroscopic-microscopic models and KTUY05, DZ31 models are classified as models of "another kind" in Ref. [Sobiczewski & Litvinov, 2014]. The macroscopic-microscopic models usually treat the nucleus as a liquid drop in the macroscopic part and incorporate microscopic corrections to account for residual contributions such as shell and pairing effects. The WS4+RBF model shows the smallest root-mean-square (rms) deviation from experimental masses among the macroscopic-microscopic models [Wang et al., 2014].

$N = Z = 50$ doubly-magic nucleus ^{100}Sn and the S_{2p} values of the heavy $N = Z$ and $N = Z + 1$ nuclides are suggested to be similar to each other. It is worth mentioning that at the sub-shell closure $N = Z = 40$ the recent mass measurement of ^{80}Zr reported in [Hamaker et al., 2021] also gives a similar crossing of the S_{2p} values at $N = Z = 40$ and $N = Z + 1 = 41$ as depicted on the top right plot on Fig. 5.10. The S_{2p} values based on the indirect mass measurements reported in [Park et al., 2019] are in general closer to the AME2020 extrapolations [Huang et al., 2021, Wang et al., 2021], however at $N = Z = 49$ the indirect measurements agree better with the CDE-based and global $\overline{\mathcal{F}t}$-based mass estimates. Below the $N = Z = 28$ shell closure the S_{2p} values predicted by the different theoretical mass models scatter by ∼1 MeV around the measured masses, however for heavier $N = Z$ isotopes the models seem to underpredict the S_{2p} values, i.e. the predicted S_{2p} values at $N = Z = 31 \ldots 37$ isotopes are systematically lower as compared to the S_{2p} values based on mass measurements.

In the next step, the evolution of proton separation energies S_p and empirical proton-neutron interaction strengths δV_{pn} plotted on the left-side figures in Fig. 5.10 are discussed. The measurements reported in Ref. [Ge et al., 2024, Čeliković et al., 2016] result in proton separation energies for the neutron-deficient Ag isotopes of $S_p\left(^{95}\mathrm{Ag}\right) = 930(5)$ keV, $S_p\left(^{96}\mathrm{Ag}\right) = 1980(3)$ keV, $S_p\left(^{93}\mathrm{Ag}\right) = -1060(30)$ keV. It is then interesting to see how the S_p value of ^{94}Ag from the CDE-based and global $\overline{\mathcal{F}t}$-based mass estimates summarized in Table 5.9 fits into this trend, i.e. the global $\overline{\mathcal{F}t}$-based mass estimate results in proton separation energy of ^{94}Ag, where the following relation is true: $S_p\left(^{93}\mathrm{Ag}\right) \ll S_p\left(^{94}\mathrm{Ag}\right) > S_p\left(^{95}\mathrm{Ag}\right)$. As shown in Fig. 5.10, a similar swapping of S_p values at the $N = Z$ and $N = Z + 1$ lines happens in other cases as well; e.g. in case of the Rb ($Z = 37$) isotopes the $N = Z$ nucleus ^{74}Rb is also directly next to the proton dripline [Hoff et al., 2020], just like ^{94}Ag, and the evolution of proton separation energies at Rb isotopes is similar to the case of Ag ($Z = 47$) isotopes. Another feature of the plot of the proton separation energy is that there is always a larger difference between the $N = Z$ and $N = Z - 1$ lines, which is related to the dramatic increase of the empirical proton-neutron interaction strength δV_{pn} for $N = Z$ isotopes as compared to $N \neq Z$ isotopes [Van Isacker et al., 1995]. In addition, as explained in Section 1.1, δV_{pn} has been related to the spatial overlap between the valence proton and neutron wave functions, therefore it is expected that for $N = Z$ nuclei (and in general), δV_{pn} will decrease with increasing proton number (Z) [Brenner et al., 1990]. As shown on Fig. 5.10, the CDE-based and global $\overline{\mathcal{F}t}$-based mass estimates for the heavy odd-odd $N = Z$ nuclei result in δV_{pn} values that are larger as compared to the ones solely based on AME2020 extrapolations. It is also noteworthy that for $N = Z = 29 \ldots 37$ isotopes the decreasing trend of δV_{pn} breaks, which may be to the partial restoration of a symmetry that is unique to these nuclei [Mardor et al., 2021]. In the next step, it is examined whether the CDE-based and global $\overline{\mathcal{F}t}$-based mass estimates are still consistent with a decreasing trend of δV_{pn} with increasing proton number (Z). Unfortunately, above $Z = 37$, the S_p values of $N = Z - 1$ isotopes are yet unmeasured, therefore this question cannot be answered quantitatively for all heavy $N = Z$ nuclides. On the other hand, the $S_p\left(^{93}\mathrm{Ag}\right)$ measurement from Ref. [Čeliković et al., 2016] solves this problem in case of the δV_{pn} value of ^{94}Ag, which can be thus checked quantitatively (see Table 5.9). While the heaviest measured δV_{pn} value at ^{74}Rb is 3293(42) keV, the global $\overline{\mathcal{F}t}$-based ^{94}Ag mass estimate results in $\delta V_{pn}\left(^{94}\mathrm{Ag}\right) = 2750(200)$ keV. Consequently, the newly calculated mass estimate for ^{94}Ag is still consistent with a decreasing trend of δV_{pn} above $Z = 37$, but it would suggest a decrease that is less steep as compared to the trend solely based on AME2020 extrapolations. In comparison, the theoretical mass models do not reproduce the measured δV_{pn} restrengthening for $N = Z = 29 \ldots 37$ isotopes [Mardor et al., 2021] and suggest a weaker interaction strength between the last (highest orbitals) proton and neutron for the heavy odd-odd $N = Z$ nuclides.

In summary, as long as high-precision, direct mass measurements of the heavy, odd-odd $N = Z$ nuclides are not available, reliable mass estimates of these nuclides are needed. In this subchapter, a new global $\overline{\mathcal{F}t}$-based ground-state mass estimate of ^{94}Ag was proposed and

extended to all heavy, odd-odd $N = Z$ nuclides. This results were compared with other existing methods for estimating the mass of the heavy, odd-odd $N = Z$ nuclides. While the global $\overline{\mathcal{F}t}$-based Q_{EC} estimates, in general, follow a smooth trend for all odd-odd N=Z nuclides up to Z=49, the AME2020 [Huang et al., 2021, Wang et al., 2021] extrapolations suggest a sudden change in the trend of Q_{EC} values by up to 1 MeV for odd-odd N=Z nuclides with $Z \geq 41$. This validates the choice to adopt the global $\overline{\mathcal{F}t}$-based ground-state mass estimate of ^{94}Ag for the further discussion. Notably, the systematic studies presented in this subchapter may also have important consequences on our understanding of the nuclear structure of these nuclides and for the path of the astrophysical rapid proton-capture process (*rp*-process).

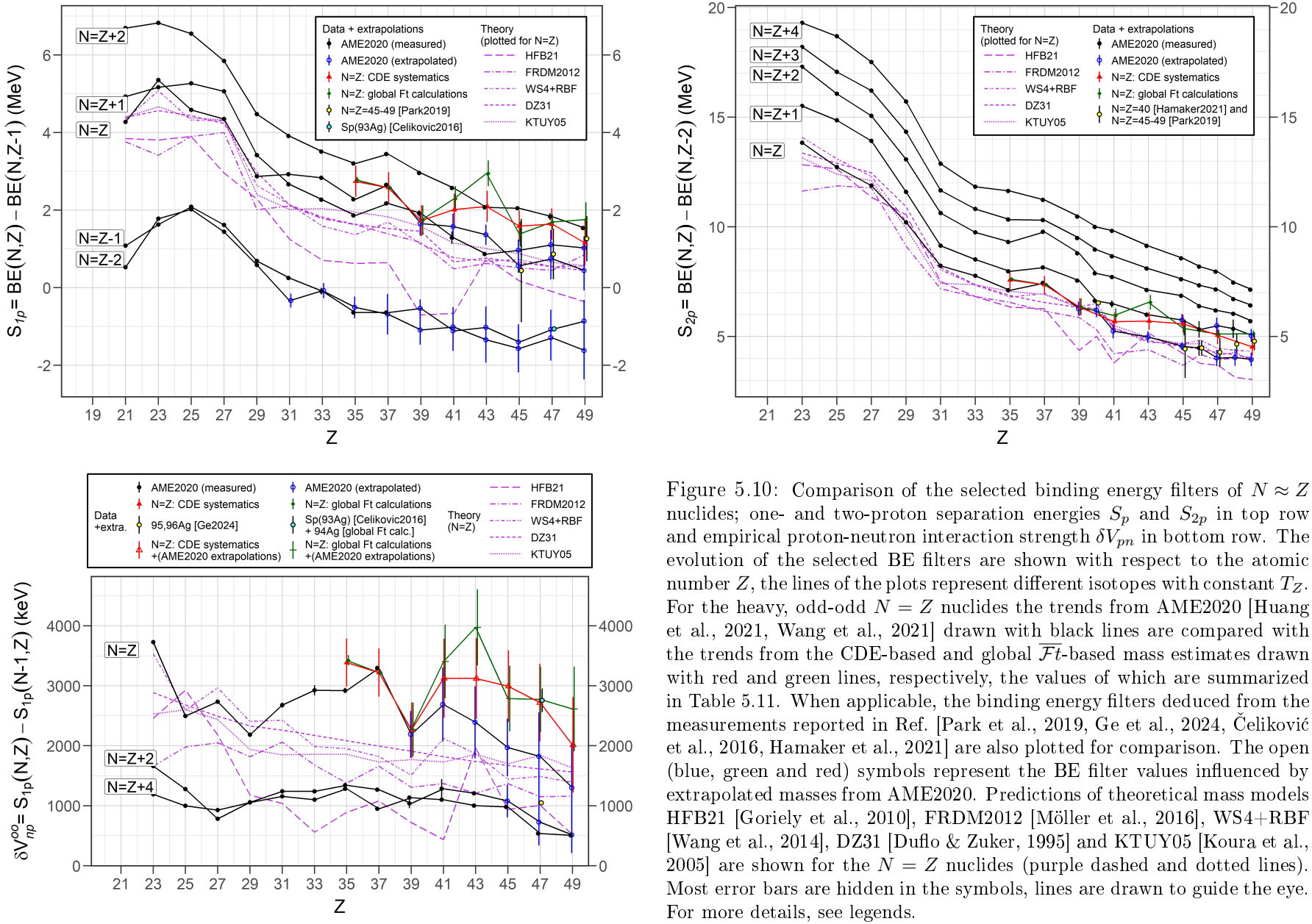

Figure 5.10: Comparison of the selected binding energy filters of $N \approx Z$ nuclides; one- and two-proton separation energies S_p and S_{2p} in top row and empirical proton-neutron interaction strength δV_{pn} in bottom row. The evolution of the selected BE filters are shown with respect to the atomic number Z, the lines of the plots represent different isotopes with constant T_Z. For the heavy, odd-odd $N = Z$ nuclides the trends from AME2020 [Huang et al., 2021, Wang et al., 2021] drawn with black lines are compared with the trends from the CDE-based and global $\overline{\mathcal{F}t}$-based mass estimates drawn with red and green lines, respectively, the values of which are summarized in Table 5.11. When applicable, the binding energy filters deduced from the measurements reported in Ref. [Park et al., 2019, Ge et al., 2024, Čeliković et al., 2016, Hamaker et al., 2021] are also plotted for comparison. The open (blue, green and red) symbols represent the BE filter values influenced by extrapolated masses from AME2020. Predictions of theoretical mass models HFB21 [Goriely et al., 2010], FRDM2012 [Möller et al., 2016], WS4+RBF [Wang et al., 2014], DZ31 [Duflo & Zuker, 1995] and KTUY05 [Koura et al., 2005] are shown for the $N = Z$ nuclides (purple dashed and dotted lines). Most error bars are hidden in the symbols, lines are drawn to guide the eye. For more details, see legends.

5.3.2 Scenarios to resolve the discrepancy between the 1p/2p decay branches

Table 5.13 summarizes the different ground-state mass estimates of ^{94}Ag and the corresponding excitation energy values of the ^{94}Ag (21^+) isomer, which were deduced based on either combining the measured mass of ^{93}Pd and the 1p decay data [Mukha et al., 2005, Cerny et al., 2009] or combining the measured mass of ^{92}Rh and the 2p decay data [Mukha et al., 2006], respectively.

Table 5.13: Q_{EC} value and mass excess (ME) of the ^{94}Ag (0^+) ground state and excitation energy (E_x) of the (21^+) isomer(s) deduced in the present work via combining the measured masses of ^{93}Pd and ^{92}Rh, the 1p decay data [Mukha et al., 2005, Cerny et al., 2009], the 2p decay data [Mukha et al., 2006] and either of the ^{94}Ag ground-state mass estimates. For the latter, the results from the global $\overline{\mathcal{F}t}$ calculations of this work, the extrapolation based on Coulomb-displacement energy (CDE) systematics [Kankainen et al., 2008], the indirect, β-decay end-point energy measurement [Park et al., 2019] and the AME2020 extrapolation [Huang et al., 2021, Wang et al., 2021] (#) are given.

^{94}Ag properties	global $\overline{\mathcal{F}t}$ calc. (keV/c^2)	CDE systematics[a] (keV/c^2)	Indirect meas.[b] (keV/c^2)	AME2020[c] (keV/c^2)
Q_{EC} (^{94}Ag, 0^+)	12570(190)	12760(360)	13350^{+690}_{-610}	13700(400)#
ME(^{94}Ag, 0^+)	−53530(190)	−53340(360)	-52750^{+690}_{-610}	−52400(400)#
Independent from ^{94}Ag ground-state mass: ME(^{94}Ag, 21^+)$_{1p}$ = −46050(40) keV and ME(^{94}Ag, 21^+)$_{2p}$ = −44960(100) keV				
E_x (^{94}Ag, 21^+)$_{1p,I}$	7480(190)	7290(360)	6700^{+610}_{-690}	6350(400)#
E_x (^{94}Ag, 21^+)$_{2p}$	8570(220)	8380(370)	7790^{+620}_{-700}	7440(410)#

[a] [Kankainen et al., 2008].
[b] [Park et al., 2019].
[c] [Huang et al., 2021, Wang et al., 2021].

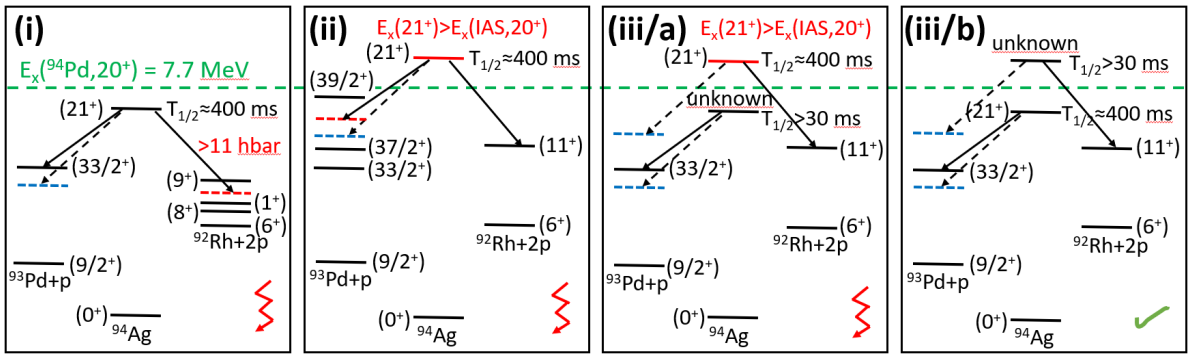

Figure 5.11: Schematic illustration of the three scenarios that could reconcile the observation of both 1p and 2p decays of ^{94}Ag with the mass measurements reported here. The drawing only includes the excited states of ^{93}Pd and ^{92}Rh that are relevant for the discussion of a given scenario, while other states are omitted. The dashed arrows and the corresponding dashed blue states mark different possibilities for the tentative placement of the 1p(II) decay branch with a presumed negative parity daughter state. The red color indicates the problem with a given scenario making that scenario rather unlikely, see text for details.

There are, in principle, three scenarios that could reconcile the observation of both 1p and 2p decays of ^{94}Ag as reported in Refs. [Mukha et al., 2005, Mukha et al., 2006] with the mass measurements reported here (see Fig. 5.11 for a schematic illustration)[3]

(i) The mass excess of the (21^+) isomer amounts to $\mathrm{ME}(^{94}\mathrm{Ag}, 21^+)_{1p,I} = -46050(40)$ keV, according to the 1p(I) decay branch [Mukha et al., 2005, Cerny et al., 2009] and the measured mass of ^{93}Pd. This suggests the 2p decay of the (21^+) isomer to feed a state in ^{92}Rh with the lower excitation energy of 450(110) keV, as constrained by the the newly measured ^{93}Pd mass, instead of the previously-reported (11^+) state [Mukha et al., 2006]. However, no such state has been observed experimentally so far [Baglin, 2012, Park et al., 2017, Häfner et al., 2019, Park et al., 2019]. This makes scenario (i) rather unlikely. There are three experimentally-known ^{92}Rh states within about 1.5σ-2σ distance from the excitation energy of 450(110) keV, namely the (9^+), (8^+) and (1^+) states from Figs. 5.7 and 5.8. All these alternative 2p-emission daughter state candidates, however, require an angular momentum transfer of $>11\hbar$ carried by the two protons, which would be difficult to explain, see e.g. the argumentation from Ref. [Pechenaya et al., 2007]. Furthermore, the mean-field theory results reported in this work (see Section 5.3.3) suggest that the possibility of such a large angular momentum transfer, i.e. the possibility of scenario (i), can be excluded following simple quantum mechanical considerations.

(ii) The mass excess of the (21^+) isomer amounts to $\mathrm{ME}(^{94}\mathrm{Ag}, 21^+)_{2p} = -44960(100)$ keV, according to the 2p decay data [Mukha et al., 2006] and the measured mass of ^{92}Rh. This is only possible if the 1p(I) decay branch feeds a state in ^{93}Pd with a higher excitation energy, 6080(110) keV, compared to the previously-reported $(33/2^+)$ state [Mukha et al., 2005]. The present experimental level scheme of ^{93}Pd [Baglin, 2011, Lorusso et al., 2012, Park et al., 2019] does not include a level at this energy. The closest-lying experimentally-known ^{93}Pd states, the $(37/2^+)$ and $(39/2^+)$ states, are both $\geq 4\sigma$ apart from the excitation energy of 6080(110) keV. This makes also scenario (ii) rather improbable. Nevertheless, it may be possible that some transitions were missed or misplaced in earlier experiments. One connected issue could be uncertainties in the spin-parity assignment of the ^{93}Pd states, e.g., recently an alternative assignment of $J^\pi=(7/2^+)$ was suggested for its ground state based on the experimentally-observed β-decay feeding of different states in its β-decay daughter, ^{93}Rh [Park et al., 2019]. On the other hand, with the discovery of the presumed (19^-) gamma-decaying isomer of ^{94}Pd [Brock et al., 2010], the confidence in the earlier-measured 7.7 MeV excitation energy of the (20^+) state in ^{94}Pd [Plettner et al., 2004] was further increased. The isobaric analog states of a given isobaric multiplet are expected to have the same excitation energies within $\sim$100 keV [Bentley, 2022, Lenzi et al., 2018]. Therefore, the T=1, (20^+) IAS in ^{94}Ag is expected to lie at the same excitation energy as in ^{94}Pd, 7.7 MeV [Plettner et al., 2004]. This is thought to give an upper limit for the excitation energy of the (21^+) spin-trap isomer to be able to explain the hindrance of the internal decay [Plettner et al., 2004]. Using the global $\overline{\mathcal{F}t}$-based or the CDE-based ^{94}Ag ground-state mass estimate, the (21^+) isomer in scenario (ii), however, lies above this level (Fig. 5.8, Table 5.13). Thus, scenario (ii) becomes even more unlikely.

(iii) The 1p(I)- and the 2p-decay branches are fed from two separate isomeric states of ^{94}Ag with an excitation energy difference of 1090(110) keV as determined in this work (Fig. 5.8). The possibility of this scenario has been proposed in Ref. [Roeckl & Mukha, 2013], but its scientific basis has, so far, not been examined. It is reasonable to assume that one of the

[3]Note that the placement of the 1p(II)-decay branch with the presumed negative-parity daughter state in the level scheme of ^{93}Pd has been so far only tentative, therefore multiple possibilities exist for its placement as depicted in Fig. 5.11.

two high-lying ^{94}Ag isomers corresponds to the β-decaying and β-delayed-proton-decaying, presumably spin-trap, (21^+) isomer with β half-life of 400(40) ms, while the spin and parity of the second isomer is not known experimentally. The lifetime of this second isomer is also not known experimentally except for the requirement to survive the production and measurement (>30 ms) [Mukha et al., 2006, Kirchner, 1992]. In principle there are two different possibilities for the order of this two high-lying isomers (see Fig. 5.11):

(iii/a) It could be hypothesized that the experimentally unknown isomer corresponds to the ∼1 MeV lower-lying state feeding the 1p(I) branch, while the (21^+) isomer with β half-life of 400(40) ms is responsible for 2p emission.

(iii/b) As a much more likely option, it is possible that the the (21^+) isomer with β half-life of 400(40) ms corresponds to the ∼1 MeV lower-lying state feeding the 1p(I) branch, while the experimentally unknown isomer is responsible for 2p emission.

There are multiple arguments against option (iii/a) making this option rather unlikely. Firstly, in this case the presumed spin-trap (21^+) isomer would have an excitation energy of more than 7.7 MeV using the global $\overline{\mathcal{F}t}$-based or the CDE-based ^{94}Ag ground-state mass estimate and the hindrance of the internal decay could not be explained following the same argumentation as for scenario (ii). Additionally, two independent measurements with significantly different transport and measurement times measured the same branching ratio for the 1p(I) branch [Mukha et al., 2005, Cerny et al., 2009], which likely indicates that the 1p(I) branch corresponds to the same spin-trap, (21^+) isomer that gives the majority of the β decay and β-delayed proton decay events. As argued above, the option (iii/b) is the most likely option and in the further discussion, this will be referred to as scenario (iii). In this scenario, the complete experimental decay information for the 1p and 2p decay branches is consistent with the mass measurements reported here.

5.3.3 Theoretical interpretation and possible explanations to the puzzles

To further elucidate the three scenarios discussed in Section 5.3.2, shell-model and mean-field calculations have been performed. The shell-model calculations were performed by F. Nowacki, D. D. Dao and co-workers [Dao et al., 2024] (priv. comm.), while the mean field calculations were performed by J. Dudek, I. Dedes and co-workers [Dedes et al., 2024] (priv. comm.).

Shell-model calculations

The shell-model calculations were performed using the m-scheme code ANTOINE [Caurier & Nowacki, 1999, Caurier et al., 2005, Nowacki et al., 2021] and employing the two most advanced interactions, SDGN and JUN45, in the full diagonalization of the nuclear Hamiltonian. Both interactions are well-benchmarked in the vicinity of ^{100}Sn and have been frequently used to study the effect of proton-neutron interactions and/or the formation of high-spin spin-trap isomers in this nuclear chart region, see e.g. [Mollaebrahimi et al., 2023b, Yaneva et al., 2024, Nara Singh et al., 2011, Das et al., 2022]. The key properties of the two interactions and their corresponding results are outlined below.

Large-scale shell model (LSSM) calculations were done in the $\pi\nu(gds)$ model space, comprising the $1g_{9/2}$, $1g_{7/2}$, $3s_{1/2}$, $2d_{5/2}$ and $2d_{3/2}$ orbitals for protons and neutrons, employing the SDGN effective interaction [Plettner et al., 2004, Nowacki, 2002, Yaneva et al., 2024], assuming a hypothetical ^{80}Zr core and allowing $14p14h$ excitations across the N=Z=50 shell gap. This is within the largest Slater determinants diagonalisations performed so far. The excitation energies of the relevant states with isospin T=1 and T=0 predicted by the LSSM calculations are shown on Fig. 5.8. Concerning the T=0 states, a 21^+ state is predicted at 6672 keV with

a configuration involving $1g_{9/2}$ orbitals, $(\pi g^{-1}_{9/2,9/2} g^{-1}_{9/2,7/2} g^{-1}_{9/2,5/2} \nu g^{-1}_{9/2,9/2} g^{-1}_{9/2,7/2} g^{-1}_{9/2,5/2})_{21}$, preceded by a 17^+ state, thus successfully reproducing the spin-trap isomerism of the 21^+ state. The calculations also predict a 20^+ state at 7478 keV, which is the IAS with isospin T=1 of the experimentally observed (20^+) state in ^{94}Pd [Plettner et al., 2004]. No second high-spin isomer candidate is predicted within the $\pi\nu(gds)$ valence space, therefore no information on the plausibility of scenario (iii) can be given in this theoretical framework.

For comparison, shell-model calculations using the JUN45 interaction [Honma et al., 2009] in the $\pi\nu(f_5pg_9)$ model space, comprising the $2p_{3/2}$, $1f_{5/2}$, $2p_{1/2}$ and $1g_{9/2}$ orbitals for protons and neutrons, were performed. The relevant states predicted by employing this latter interaction are also shown on Fig. 5.8. As shown on the figure, the JUN45 results are in excellent agreement with the predicted level energies deduced using the SDGN interaction, which complements the predicted excitation energy of the 21^+ state around 6.7 MeV rather firmly. On the other hand, in this case the order of 21^+-19^+ states is swapped, which yields that the 21^+ state is not predicted as a spin-trap isomer in this second shell model approach. This clearly shows the advantage of the $\pi\nu(gds)$ model space, which enables an incorporation of core excitations across N=Z=50.

Notably, the excitation energy of the 21^+ isomer predicted by the shell-model calculations is $\sim$ 0.8 MeV smaller than the value deduced using the global $\overline{\mathcal{F}t}$-based E_x $\left(^{94}\text{Ag},\ 21^+\right)_{1p,I}$ estimate (Fig. 5.8). This mismatch is, however, not far beyond the expected uncertainties. Additionally, since the excitation energy of the 21^+ state reflects an energy difference between a T=1 and T=0 state, the mismatch could also be explained by the lack of an accurate measurement of a T=0 − T=1 energy difference in heavy N=Z nuclides, which could be used for the parametrization of the LSSM calculations.

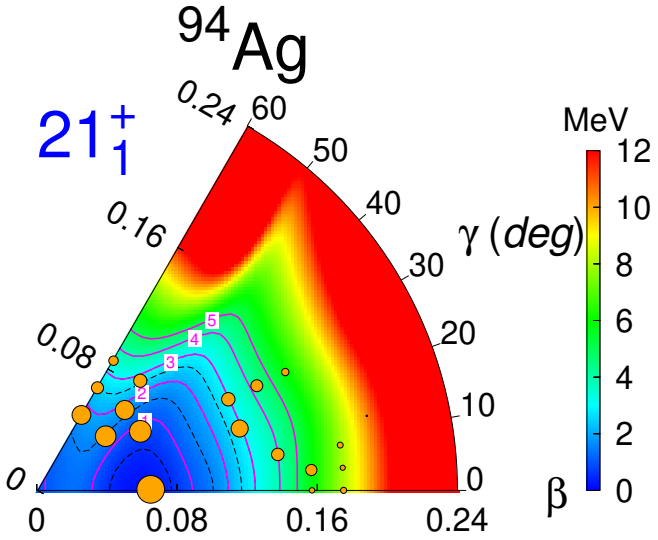

Figure 5.12: Potential energy surface (PES) of the ^{94}Ag 21^+ state as a function of quadrupole deformation parameters (β_2,γ) calculated by the DNO-SM approach. The radii of the yellow circles are proportional to the normalized probability to find the ^{94}Ag 21^+ state in a given deformation (β_2,γ). The red numbers inside the white squares indicate the potential energy in MeV corresponding to the different contour lines on the surface.

Furthermore, the performed shell-model calculations also provide additional insights for the intense historical debate around the topic of the deformation of the (21^+) spin-trap isomer [Mukha et al., 2006, Kaneko et al., 2008, Pechenaya et al., 2007]. To access the structure of the predicted 21^+ isomer and its associated nuclear deformation within the $\pi\nu(gds)$ valence space, the potential energy surface of ^{94}Ag 21^+ state was obtained using the discrete nonorthogonal shell model (DNO-SM) approach [Dao & Nowacki, 2022, Rocchini et al., 2023, Yaneva et al., 2024].

The deduced potential energy surface as a function of quadrupole deformation parameters (β_2,γ) is shown in Fig. 5.12. The plot follows the so-called Lund convention, where the parameter β_2 provides a measure of the extent of deformation, while γ provides a measure of the departure from axial symmetry. Here, the quadrupole deformation parameters are defined with the following relations $\alpha_{20} = \beta_2 \cdot \cos\gamma$ and $\alpha_{22} = \alpha_{2,-2} = \frac{1}{\sqrt{2}} \cdot \beta_2 \cdot \sin\gamma$, where $\alpha_{\lambda\mu}$ correspond to the coefficients of the spherical harmonics $Y_{\lambda\mu}(\theta, \phi)$ in the description of deformed nuclei, for more details see e.g. [Sensharma, 2021]. In Fig. 5.12, prolate shapes correspond to $\gamma = 0^o$ and oblate shapes correspond to $\gamma = 60^o$. As shown on the figure, the calculations predict a nearly spherical (slightly prolate) shape for the ^{94}Ag 21^+ state with $\beta_2 < 0.1$ for the 21^+ state.

Mean-field calculations

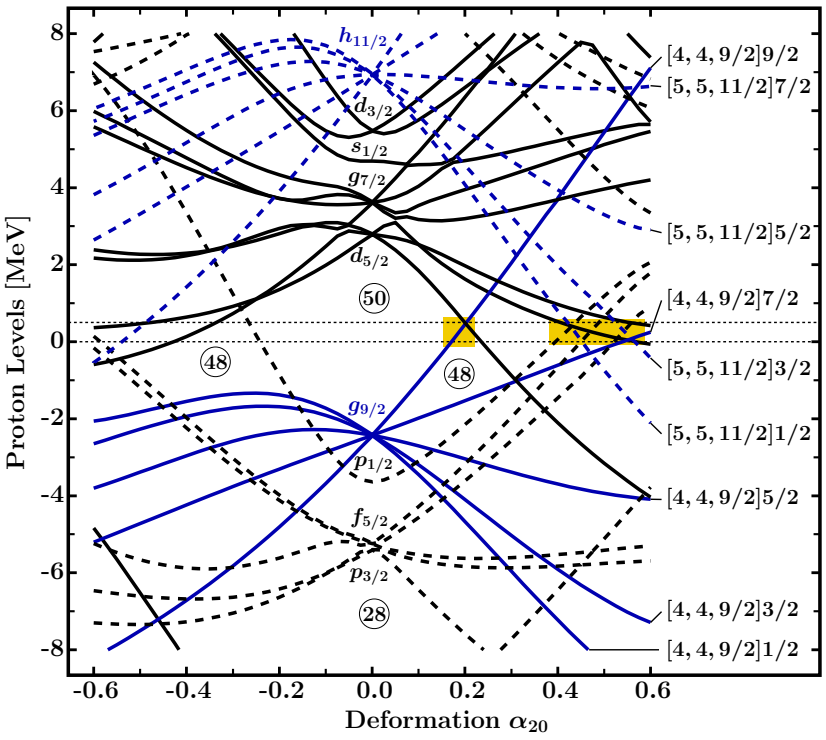

Figure 5.13: Proton single-particle 'universal' Woods-Saxon mean field energies for ^{94}Ag as a function of the quadrupole deformation parameter α_{20}. The two orbitals playing decisive roles in the discussion of the proton emission, $1g_{9/2}$ (full lines) and $1h_{11/2}$ (dashed lines), are shown in blue color. The yellow areas mark the corresponding regions of interest with energies between 0 and 500 keV. The labels give the Nilsson labelling $|[N, \ell, j]\Omega\rangle$ for the dominating single-particle content.

The mean-field calculations were performed employing the phenomenological, deformed Woods-Saxon Hamiltonian in its so-called universal parametrisation, which have been developed in a series of articles [Dudek & Werner, 1978, Dudek et al., 1979, Dudek et al., 1980, Dudek et al., 1981, Cwiok et al., 1987]. The term "universal" indicates that the parameters are applicable to all nuclides in the Table of the Nuclides. Notably, this mean-field theory framework is frequently used for studying both the formation of high-spin spin-trap isomers and the process of charged-particle emission, see e.g. [Cerkaski et al., 1979, Delion & Liotta, 2013, Delion et al., 2013, Maglione et al., 1998], therefore it is an ideal tool for studying the 1p/2p-decay branches of

the ^{94}Ag high-spin isomer(s). Within the same theoretical framework, proton-emission lifetimes were deduced using the semiclassical Wentzel-Kramers-Brillouin (WKB) approximation [Landau & Lifsitz, 1977], i.e. through deducing the penetration probability for the emitted proton penetrating the "nuclear plus Coulomb" effective potential barrier obtained with the Woods-Saxon Hamiltonian corresponding to different deformations.

Fig. 5.13 shows the calculated proton single-particle energy spectrum for ^{94}Ag as a function of the quadrupole deformation parameter α_{20}. In the spectrum one can find orbitals with strong deformation dependence, see the curves with remarkably big slopes on Fig. 5.13. Occupying such orbitals will result in strong deformation driving tendencies induced by the single nucleon particle-hole excitations; i.e. strong shape variation from one spin state to another should be expected. To enable proton emission, the emitting orbitals must have positive energies, and to fulfil the requirement to survive the production and measurement (>30 ms) [Mukha et al., 2006, Kirchner, 1992], the WKB estimates suggest that their energy should be below 500 keV. Within this energy range, the most likely explanation for the angular momentum transfer of $9/2\,\hbar$ in the 1p(I) decay branch from the (21^+) isomer in ^{94}Ag to the $(33/2^+)$ state in ^{93}Pd, while conserving the parity, necessarily involves the $1g_{9/2}$ orbital at $\alpha_{20} \approx +0.2$ (left yellow region in Fig. 5.13). However, at this deformation, there is no second orbital available to explain the total angular momentum transfer of $10\,\hbar$ required for the 2p emission to the (11^+) state in ^{92}Rh, should it indeed originate from the same (21^+) isomer as the 1p(I) branch. Therefore, a second state is required as a parent for the 2p emission, in agreement with scenario (iii). The spin and parity of this state are experimentally not known. Nevertheless, for the angular momentum transfer required for the 2p emission from a high-spin state in ^{94}Ag to the (11^+) state in ^{92}Rh, in Fig. 5.13 one can identify two orbitals with dominating $1h_{11/2}$ content or, alternatively, one orbital with dominating $1g_{9/2}$ content and one orbital with dominating $1h_{11/2}$ content as likely candidates. Both cases are found only at strongly-elongated shapes with $\alpha_{20} \approx +0.4 \ldots +0.6$ (right yellow region in Fig. 5.13). While the prior configuration conserves parity under 2p emission, the latter configuration alters the parity.

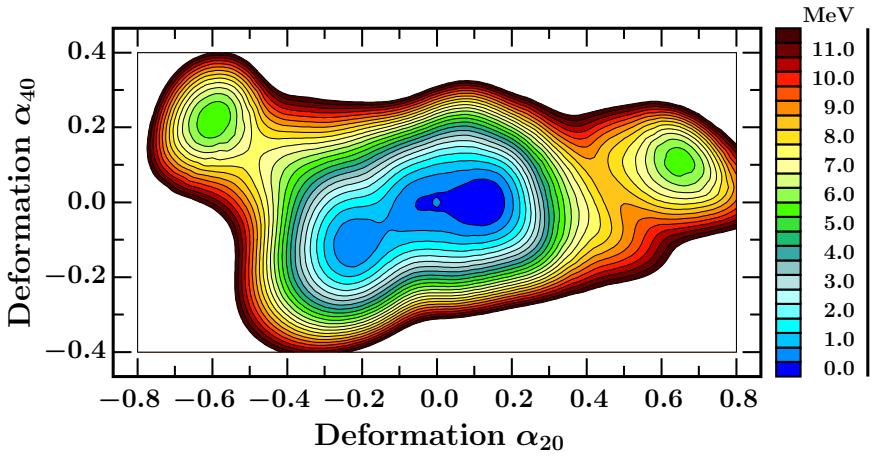

Figure 5.14: Potential energy surface as a function of axially symmetric (appropriate for the spin isomer description) multipole deformation parameters (α_{20}, α_{40}) for ^{92}Pd, the even-even neighbour of ^{94}Ag, deduced by the 'universal' Woods-Saxon mean-field approach. Note that in mean-field theory it has become a practical solution to investigate a nucleus with the help of the (lighter) even-even neighbor plus the respective single-particle orbitals, often giving close-lying results.

The mean-field potential energy surface in Fig. 5.14 shows four possible axially symmetric configurations (four local minima).[4] The deformation of possible isomeric states can be obtained by a minimization of the sum of this potential energy and the particle-hole excitations that define the isomeric structures. There are two high-lying minima, both above 6 MeV excitation energies; super-deformed oblate at $\alpha_{20} \approx -0.6$ and super-deformed prolate at $\alpha_{20} \approx +0.6$. Additionally, there are two low-lying minima; normal deformed oblate at $\alpha_{20} \approx -0.2$ and normal deformed prolate at $\alpha_{20} \approx +0.2$. The 1p(I)-emission candidate discussed above corresponds to the minimum at $\alpha_{20} \approx +0.2$, while the 2p-emission candidate can be associated with the minimum at $\alpha_{20} \approx +0.6$. This strong prolate deformation is in agreement with the conclusions of Ref. [Mukha et al., 2006], but in the present work it is predicted as the result of a rigorous nuclear model and does not have to be postulated.

Tilted Fermi surface calculations, similar to those in Ref. [Liu et al., 2025, Hornung et al., 2020, Cerkaski et al., 1977, Cerkaski et al., 1979, de Voigt et al., 1983], predict a normal deformed prolate 21^+ state at an excitation energy of 7.77 MeV, the parent-state candidate for the 1p(I) branch, as a spin-trap isomer with $(\pi g^{-1}_{9/2,9/2} g^{-1}_{9/2,7/2} g^{-1}_{9/2,5/2} \nu g^{-1}_{9/2,9/2} g^{-1}_{9/2,7/2} g^{-1}_{9/2,5/2})_{21}$ configuration, in agreement with the results of the large-scale shell model calculations performed in this work. Additionally, the tilted Fermi surface calculations also predict that the deformation of the ground state of ^{92}Pd can be found at a small elongation of $\alpha_{20} \approx +0.12$, in agreement with the experimental, complemented by theoretical, findings of Ref. [Yaneva et al., 2024]. Furthermore, a 7^+ state is also predicted as a spin-trap isomer with $(\pi g^{-1}_{9/2,7/2} \nu g^{-1}_{9/2,7/2})_7$ configuration in agreement with experimental observations, which reported β decay and β-delayed proton emission from a low-spin (7^+) isomer in ^{94}Ag, see e.g. [Plettner et al., 2004, Mukha et al., 2004, Park et al., 2019]. Note that this latter finding is at variance to the shell-model predictions of Ref. [Kaneko et al., 2008], which suggest the 7^+ state as an oblate-deformed shape isomer, not as a spin-trap isomer. For the 2p-emission candidate no further quantitative results could be obtained. Its electromagnetic decay hindrance is very likely due to the fact that there are no (or very few) lower-energy super-deformed state candidates for such a decay, whereas the normal deformed states differ dramatically in terms of both the geometry and the particle-hole structures. Note, however, that the precise prediction of electromagnetic decay probabilities and, thus, β-decay lifetimes is not available in the mean-field theory framework at present.

In Ref. [Mukha et al., 2005] another 1p decay branch was observed with $E_{1p,II} = 1010(30)$ keV decay energy, denoted here as 1p(II) branch, and assigned to a daughter state with a tentative spin-parity assignment of $(33/2^-, 35/2^-)$ and a tentative placement in the level scheme of ^{93}Pd [Baglin, 2011, Lorusso et al., 2012, Park et al., 2019]. There is no orbital available in Fig. 5.13 to explain the presumed parity change of the 1p(II) branch, should it indeed originate from the same (21^+) isomer as the 1p(I) branch. Consequently, the two 1p branches should not stem from the same isomer. It is conceivable that the 1p(II) branch originates from the same super-deformed prolate isomer as the 2p emission (Fig. 5.8). Here, a negative-parity daughter state in ^{93}Pd can be realized in both possible 2p-emission configurations from a $1h_{11/2}$ or a $1g_{9/2}$ orbital for a positive- or negative-parity parent state, respectively.

The normal deformed (21^+) isomer feeding the 1p(I) branch can be expected to be produced much more abundantly than the super-deformed 2p-emitting state, since the former is located at the yrast line. Thus, the measured β half-life of 400(40) ms [La Commara et al., 2002, Plettner et al., 2004, Mukha et al., 2004] should correspond mostly to the parent-state candidate for the 1p(I) branch, and the candidate for the 2p emission and the 1p(II) branch could have a much shorter lifetime, with the lower limit of about 30 ms [Mukha et al., 2006, Kirchner, 1992]. This would explain the fact that only the 1p(I) decay branch could be experimentally confirmed in the Berkeley experiment [Cerny et al., 2009], but not the 2p and 1p(II) decay branches, since in

[4] For an axially symmetric case, where $\gamma = 0^o$, a negative $\beta_2 \equiv \alpha_{20}$ indicates an oblate nucleus and a positive $\beta_2 \equiv \alpha_{20}$ indicates a prolate nucleus [Sensharma, 2021].

this latter experiment the time required to transport the produced ions from the target area to the detection area was longer (200-300 ms) [Blönnigen et al., 1987].

Possible explanations to the puzzles surrounding the 1p/2p branches of ^{94}Ag

Overall, the results of the investigation of the structure of ^{94}Ag and neighboring nuclei through state-of-the-art shell-model and mean-field calculations are revealing. A slightly prolate deformed 21^+ state, the mother-state candidate of the 1p(I) branch, is successfully predicted as a spin-trap isomer by both calculations. Furthermore, the mean-field calculations also show that assuming the correctness of the complete experimental decay information, the 2p-decay branch cannot stem from the same, slightly prolate deformed 21^+ state, in agreement with scenario (iii). Including the $1h_{11/2}$ intruder orbitals, these latter calculations are the first ones to support the existence of a strongly-deformed prolate high-spin isomer in ^{94}Ag feeding the 2p and likely also the 1p(II) decay branches.

This scenario, (iii), can, in principle, reconcile both the 1p and 2p decay data with the mass measurements reported here and it provides possible explanations to almost all puzzles surrounding the 1p/2p-decay branches in ^{94}Ag:

(A) **The puzzle of simultaneous 2p emission:** Using the new mass value of ^{93}Pd, it has been shown that a sequential 2p emission involving the $(33/2^+)$ state of ^{93}Pd and the (11^+) state of ^{92}Rh is energetically highly improbable. Note, however, that the present results cannot rule out the involvement of a different ^{93}Pd state in a sequential 2p emission process, therefore they don't provide a fully conclusive explanation for this puzzle.

(D) **The puzzle of the excitation energy mismatch:** The possible mother-state energy mismatch is confirmed as a 10σ disagreement using the first direct mass measurement of ^{93}Pd and a possible explanation is provided to resolve the discrepancy via proposing two separate mother states feeding the 1p(I) and 2p decay branches.

(B) **The puzzle of large deformation required for 2p emission:** The suggestion of two separate mother states feeding the 1p(I) and 2p decay branches, one normal deformed prolate (21^+) state and one super-deformed prolate high-spin state, also resolves the historical debate about the deformation of the presumed 2p-emitting isomer.

(C) **The non-observation of 2p emission in Ref. [Cerny et al., 2009]:** It is conceivable that the super-deformed prolate high-spin state is significantly shorter lived than 200-300 ms, which would explain the non-observation of the 2p and 1p(II) decay branches in the Berkeley experiment.

For a final resolution of these puzzles, more experimental as well as theoretical evidence is needed and are being pursued [Reponen et al., 2015, Reponen et al., 2021, Ge et al., 2024]. Nevertheless, the results presented in this work help to avoid jumping to the wrong conclusions by incorrectly assuming that the observed 1p- and 2p-decay branches must occur from the same isomer in ^{94}Ag and, thus, they provide substantial information for these upcoming studies.

A publication of most of the results reported in this chapter have been submitted recently [Kripkó-Koncz et al., 2025].

Chapter 6

Summary and outlook

In this work, advances were made to two instances of MR-TOF-MS setups, one of them belonging to the TITAN experiment at TRIUMF and another one belonging to the FRS-IC experiment at GSI, and these measurement setups were used to study different ground and isomeric states in medium-heavy exotic nuclei, including the particularly striking example of the proton-emitting isomer(s) in ^{94}Ag.

The improvements implemented in this work are mainly related to the data acquisition and analysis techniques specialized to collect and accurately treat data sets obtained with an MR-TOF-MS. For example, with the newly-commissioned continuous and accurate readout of the TOF analyzer voltages, changing its repetition frequency can now be achieved within a few minutes. This ensures a quick and reproducible change of its operation mode from longer flight times, enabling higher mass resolving powers and accuracies [Beck, 2023, Mardor et al., 2021], to shorter cycle lengths, allowing access to nuclei with small half-lives of a few milliseconds [Rink, 2017, Tortorelli, 2024]. Additionally, the class of MR-TOF-MSs used in this work were designed to enable broadband mass measurements, and the developments presented here allow to fully exploit these capabilities; standardized procedures to perform and analyze mass measurements covering a broad relative mass-to-charge range of more than 10% have been established. These procedures are already applied routinely, allowing the simultaneous and accurate mass measurement of more than 50 nuclides within a single settings of the MR-TOF-MS, see e.g. [Spătaru et al., 2025, Fowler-Davis, 2025]. Overall, the data analysis procedure developed in this and previous works allows an accurate treatment of data sets containing only 3-10 detected events per ion species and overlapping mass lines, see e.g. [Ayet San Andrés et al., 2019, Hornung et al., 2020, Mardor et al., 2021, Mollaebrahimi et al., 2023b].

TITAN's MR-TOF-MS at TRIUMF was used to measure the mass of neutron-rich indium isotopes across the $N = 82$ shell closure. In these measurements, multiple low- and high-lying isomeric states of the measured indium isotopes were observed in addition to their ground states, posing considerable challenges for the employed mass measurement and data analysis techniques. The data analysis procedure was tailored to accurately treat the specific data sets, where indium isotopes with multiple isomeric states were observed. The observation of the high-lying isomer of ^{125}In with a half-life of 5.0(15) ms shows that TITAN's MR-TOF-MS is an efficient tool to measure the mass of short-lived ions with half-lives of only a few milliseconds.

The mass measurements reported here mark the first mass measurement of ^{133,134}In isotopes and the first direct mass measurement of ^{132}In. Furthermore, the excitation energy of the $(1/2^-)$ isomeric state of ^{133}In was also measured for the first time. Additionally, the uncertainties of the excitation energies of two high-lying isomeric states, $^{127\mathrm{n}}$In and $^{131\mathrm{n}}$In, have been significantly improved compared to previous literature values.

These measurements enable, e.g., to benchmark the results of different nuclear mass models in the vicinity of the $N = 82$, $Z = 50$ double shell closure, to study the formation of the

second abundance peak of the astrophysical rapid neutron-capture process (r-process) and to investigate the microscopic interactions driving the evolution of the energy difference between the $(9/2^+)$ ground states and the $(1/2^-)$ isomeric states in odd-A indium isotopes [Izzo et al., 2021]. Additionally, determining the isomer-to-ground state ratios of the isomeric states observed in this work might yield important information on the employed production mechanism, see e.g. the studies reported in Ref. [Gao et al., 2023] employing proton-induced fission of ^{238}U.

FRS-IC's MR-TOF-MS at GSI was used to measure the mass of neutron-deficient nuclei in the vicinity of ^{100}Sn. Due to the small production yields of these nuclei, the measurements were only possible employing two key approaches: (a) using a very thick production target to enable multi-step reactions and (b) using a novel technique of tuning the primary beam energy such that more than one nuclides can be stopped in the CSC without significant efficiency losses, the mass of which can then measured simultaneously due to the broadband measurement characteristics of the MR-TOF-MS. After verifying the particle identification, the masses of the observed nuclides were determined, including the masses of ^{93}Pd and ^{92}Rh, the 1p/2p-decay daughters of ^{94}Ag. This marks the first direct mass measurement of ^{93}Pd, resulting in a mass excess value of $-59127(35)$ keV, the mass uncertainty of which is reduced by an order of magnitude compared to the literature mass uncertainty.

The measured masses of ^{93}Pd and ^{92}Rh were then used to study the historical riddles surrounding the 1p and 2p decay branches of a high-spin isomer in ^{94}Ag, which is known to possess properties that are unique in the entire Chart of Nuclei. In this work, it is shown for the first time beyond doubt that the energies of the presumed parent states of the 1p(I) and 2p decay branches in ^{94}Ag disagree, which calls into question the present interpretation of the 2p decay.

To further support this study, a new estimate for the ground-state mass of ^{94}Ag was derived using the global $\overline{\mathcal{F}t}$ value and compared with previous estimates available in the literature. In order to allow for a systematic comparison of the values, in this work the available mass estimates were extended to all odd-odd $N = Z$ nuclei. This study showed systematic deviations up to 1 MeV between the different estimates for the heavy odd-odd $N = Z$ nuclei with $Z \geq 41$, which may have important consequences on our understanding of the nuclear structure of these nuclei and for the path of the astrophysical rapid proton-capture process (rp-process).

Three different scenarios (i, ii and iii), which could reconcile the 2p decay data with the present measurement, are discussed and were investigated by performing state-of-the-art shell-model and mean-field calculations. These latter calculations include $1h_{11/2}$ intruder orbitals and show that, based on the reported decay information, the 2p emission cannot be fed from the same (21^+) isomer as the 1p(I) branch, but could stem from a strongly deformed high-spin isomer in ^{94}Ag, in favor of scenario (iii). This specific scenario can resolve almost all puzzles surrounding the 1p/2p emissions from ^{94}Ag. For example, it can explain the origin of the suggested strong prolate deformation of the 2p-emission candidate [Mukha et al., 2006] and provide a possible explanation for the non-observation of the 1p(II) and the 2p branches in a later experiment [Cerny et al., 2009].

More experimental as well as theoretical evidence is needed for a final resolution on the puzzles surrounding the 1p/2p decay branches in ^{94}Ag. Concerning theory, for example, including the $1h_{11/2}$ orbitals in the shell-model valence space is desired to examine if the existence of a second high-spin isomer is supported in this framework. Concerning experiments, mass measurements, decay and laser spectroscopy studies of the proton-emitting isomer(s) in ^{94}Ag and their 1p/2p-decay daughters are needed and being pursued [Reponen et al., 2015, Reponen et al., 2021, Ge et al., 2024]. Guided by the results presented here, in these upcoming studies, the possibly incorrect assumption that the observed 1p- and 2p-decay branches must occur from the same isomer in ^{94}Ag can be avoided, which prevents jumping to the wrong conclusions.

Furthermore, it is worth mentioning that our results may also have important consequences on the question if and when the emergence of prolate deformation and shape coexistence starts to be-

come relevant with removing nucleons from the doubly-magic system, ^{100}Sn, see e.g. [Yaneva et al., 2024]. The results of this work indicate the importance of the $1h_{11/2}$ intruder orbitals for driving the deformation of high-lying states in this nuclear chart region, which may also play decisive roles in this question.

Finally, it is noteworthy that some of the improvements developed and/or tested in the context of this work are not restricted to the measurement setups of TITAN, TRIUMF and FRS-IC, GSI. For instance, the novel technique employed in this work allowing to stop more than one nuclides in the CSC without significant efficiency losses can be applied broadly at synchrotron facilities combined with experiments with trapped radioactive ions. As another example, the usage of thick production targets will be further exploited in the future with the higher beam energies available at the Super-FRS at FAIR, Darmstadt, Germany.

Acknowledgements

Throughout my PhD journey, my path has been greatly supported by many individuals, whose main contributions are attempted to be acknowledged in this section.

First and foremost, I want to thank my academic advisor, Christoph Scheidenberger, for providing me with this invaluable research opportunity in the IONAS group, within the Helmholtz Graduate School for Hadron and Ion Research "HGS-HIRe for FAIR", and for being an inspiration to us all to try and understand all observations no matter how strange they may be.

Additionally, my special thanks go to Timo Dickel, who always found time in his long and dense days to guide me through every ups and downs of my PhD journey and to show me to always look at the big picture first. Our in-depth and sometimes heated discussions with Timo about the data analysis procedure has laid down one of the foundation stones of this work. Further, I am also very grateful to Wolfgang Plaß for supporting my PhD journey in many ways, ranging from improving my scientific writing skills to our in-depth discussions about possible explanations for the multitude of riddles discussed in this work. On a personal note, with his presence in our group's life in many ways, always full of new ideas, Hans Geissel has also been a great inspiration to me throughout my PhD journey, for which I want to thank him.

I would like to extend my gratitudes to Samuel Ayet, Sönke Beck, Julian Bergmann and Makar Simonov for our collaborative code development, which ultimately lead to the improvements of the data acquisition and analysis procedures presented in this work. Concerning the developments allowing to analyze broadband mass measurements established in this work, the systematic studies performed by Anamaria Spataru with the mass measurements of ^{252}Cf spontaneous fission products are gratefully acknowledged here.

Having started my PhD journey with a limited set of laboratory skills, all support from my fellow FRS-IC team members including, e.g., Samuel Ayet, Christine Hornung, Sönke Beck, Ali Mollaebrahimi and Daler Amanbayev, has been very much welcome and are graciously acknowledged here. In one way or another, together, we always managed to crawl through any obstacles that the experimental work has put in front of us. Additionally, I am also thankful to Meetika Narang, Jiajun Yu, Zhuang Ge, Jianwei Zhao, Nazarena Tortorelli and Kriti Mahajan, who have seamlessly overtook my laboratory duties and have contributed in performing systematic offline measurements with the MR-TOF-MS of FRS Ion Catcher, the results of which are included in this thesis. The means to allow a continuous and accurate readout of the voltages of the TOF analyzer have been developed mainly by Matjaž Vencelj, our discussions with whom during the commissioning of the device are graciously acknowledged here.

The results of this work have been or will be published in Refs. [Izzo et al., 2021, Kripkó-Koncz et al., 2025], all authors of which are gratefully acknowledged here for the data collection, support with the data analysis and theoretical interpretation of the results.

In particular, concerning the mass measurements of neutron-rich indium isotopes across $N = 82$ performed at TITAN, I want to thank Pascal Reiter, Andrew Jacobs and, later joining to the MR-TOF-MS team, Tobias Murböck, for their hospitality and thorough explanations about the measurement setup at TITAN. I am also thankful to Chris Izzo for our in-depth discussions on the data analysis of these measurements.

Further, I am deeply indebted to Juha Aystö and Xavier Mougeot for their continuous support throughout our investigations of different ground-state mass estimates of odd-odd $N = Z$ nuclei and for the computation of the global $\overline{\mathcal{F}t}$-based mass estimate of ^{94}Ag. Additionally, I am also thankful to Jerzy Dudek, Irene Dedes, Andzrej Baran, Duy Duc Dao, Frederic Nowacki, Andrey Blazhev, Magdalena Górska-Ott and co-workers for our insightful discussions and for developing a physics interpretation of our experimental results in two different state-of-the-art theoretical frameworks. Further, our fruitful discussions with Ivan Mukha about the experimental observations of 1p/2p-emission of ^{94}Ag are also gratefully acknowledged here.

I am also profoundly grateful to Israel Mardor for the opportunity to spend 6 months at the Tel Aviv University within the 'Sandwich' PhD scholarship from the Planning and Budgeting Committee of the Israel Council for Higher Education. This research stay have immensely motivated me to dig deeper into nuclear structure studies, including the studies of the evolution of shell closures and related effects of binding energy derivatives. Our friendship, formed in Israel, and scientific discussions with Heinrich Wilsenach is something that I'll always remember.

I want to thank Evelin Prinz, Rita Krause, Daniela Press and Luise Dörsching-Steitz for their support with all matters of bureaucracy and beyond. Additionally, I am also grateful to Michael Will, Bogdan Szczepanczyk, Philipp Schwarz, Simeon Glöckner and all members of the technical staff of the FRS/Super-FRS for their help with all mechanical and electronics-related issues that we faced in the laboratory.

Further, I want to thank Profs. Meng Wang and Xu Xing for providing me with an up-to-date plot of relative mass accuracy with respect to half-life, which is shown in Fig. 1.3.

Last, but not least, I want to thank my family and friends for their endless support throughout my PhD journey. This includes my husband, Áron, who was always waiting for me with warm meal even when I arrived home near Gießen at late hours after a long day trip to the laboratory at GSI, Darmstadt. The support of my parents, Andrea and Csaba, my brother, Tamás, my parents-in-law, Mónika and Tamás, my grandparents, Julianna and Ilona, and my extended family(-in-law) is also gratefully acknowledged. My visits to Hungary to meet family and friends always allowed me to fully "re-charge my batteries" and, afterwards, continue my PhD journey with a renewed strength and motivation.

Notably, the list of individuals and their contributions to this work given above is in no ways comprehensive. I am thankful to anyone and everyone, who in any ways supported me throughout my PhD journey. All these support and the friendships formed on the way made my journey a joyful, exciting and very memorable experience.

List of Figures

1.1 Schematic figure of the experimental setup, including the FRS and the FRS-IC. . 10
1.2 Schematic drawings of (i) the TOF analyzer of the MR-TOF-MS setups used in this work and (ii) electrostatic potentials along the optical axis. 15
1.3 Plot of relative mass uncertainty using different direct mass measurement techniques with respect to the half-life of the measured isotopes. 17

2.1 Comparison between two TOF spectra of neutron-rich nuclei produced in spontaneous fission of ^{252}Cf measured at the FRS-IC in 2020 using the long DC Cage of the CSC (top) and in 2023 using the short DC Cage of the CSC (bottom). 21
2.2 Photograph of the newly-commissioned 8-fold resistive divider device (a) and two examples of its most frequent applications at the FRS Ion Catcher (b and c). . . 23
2.3 Measurement of the difference between timing delay set by the trigger system ($t_{\mathrm{delay,TTL}}$) and measured using the TDC (t_{TDC}) as a function of $t_{\mathrm{delay,TTL}}$ performed at FRS-IC and at TITAN. 25

3.1 Schematic overview of the main steps and software used during data analysis. . . 28
3.2 Figure to illustrate the enhanced speed of the data analysis framework due to parallel coding. 32
3.3 A schematic overview of the relationship of uncertainty contributions to the total mass uncertainty. 34
3.4 Calculation of the background density in the time-of-flight spectrum corresponding to the measurement of ^{93}Pd. 36
3.5 Results of simulations for the statistical and contamination uncertainty calculations of the ^{91}Tc peak measured during the S474 experiment at FRS-IC. 39
3.6 Individual $\Delta c_{i=1,2,\ldots,n}$ components determined in the MT calibration of a broadband mass measurement of ^{252}Cf fission products as a function of the turn number of the individual calibrant ions. 40
3.7 Measurement of peak broadening due to the statistics inside the TRC blocks. . . 44
3.8 Measurement of the non-perfect ejection uncertainty (Δt_{NPE}) relevant for the mass measurements performed in 2020 at the FRS-IC. 45
3.9 Measurement of the non-perfect injection uncertainty (Δt_{NPI}) relevant for the mass measurements performed in 2020 at the FRS-IC. 46
3.10 Results of simulations for the cut-bias correction tested with synthetic data of various number of events, but identical peak shapes with a FWHM of 116 keV. . 49
3.11 Venn-diagram illustrating the division of the different uncertainty contributions into dependent and independent contributions in case of the mass measurements reported here. 51
3.12 Results of the fixed-distance fits tested with 100 simulated spectra of overlapping peaks. 53

3.13 Example output plot of the compilation analysis R script to check the consistency of the determined mass values and plot their deviations from literature. 56
3.14 Dedicated consistency checks used to check the results of the multi-turn calibration for broadband mass measurements. 58
3.15 A dedicated consistency test used to check whether the different calibrants or IOI may feel switched electric fields during their extraction from the TOF analyzer. . 60

4.1 The segment of the nuclear chart illustrates the 56 nuclides identified during the experiment performed using TITAN's MR-TOF-MS, out of which the masses of the 10 measured neutron-rich indium isotopes and their corresponding isomers were determined in this work. 63
4.2 Mass-to-charge spectra of neutron-rich indium ions and their corresponding isobaric contaminant and calibrant ions with mass number (top) $A = 128$ and (bottom) $A = 131$. 68
4.3 Mass-to-charge spectrum of (a) ^{132}In ions, (b) ^{133}In ions (including both ground and isomeric states) and (c) ^{134}In ions. 69
4.4 Mass-to-charge spectra of neutron-rich indium ions and their corresponding isobaric contaminant and calibrant ions with mass number $A = 125$. 70
4.5 Deviation of the measured ground-state mass excesses and isomer excitation energies from the values given in the NUBASE2020 corresponding to the observed neutron-rich indium ions. 72

5.1 Figure to illustrate the by-passing of Scintillator43. 79
5.2 Example plots showing a few steps of the combined FRS PID & FRS Ion Catcher efficiency analysis. 82
5.3 The segment of the nuclear chart shows a comparison of the estimated global FRS Ion Catcher efficiencies using two different monoenergetic FRS settings (settings1/2) normalized by the global efficiency of the ^{96}Pd isotope corresponding to the largest efficiency shown on the figure. 86
5.4 A comparison of the estimated global efficiencies corresponding to the "expected" beam-like isotopes and their corresponding measurement settings. 87
5.5 Time-of-flight spectrum corresponding to the measurement of ^{93}Pd. 89
5.6 Mass-to-charge spectrum of (a) $^{12}C_3{}^{19}F_3$ ions, (b) ^{93}Ru ions, (c) ^{93}Pd ions, (d) ^{92}Rh ions, (e) ^{93}Tc and ^{91}Ru ions. 90
5.7 Schematic drawing of experimental and theoretical level schemes of low-energy states in ^{92}Rh. 94
5.8 Decay scheme according to the new data and analysis of this work, showing the 10σ discrepancy in the mass excess value of the ^{94}Ag (21^+) isomer when calculating it using the 1p- and 2p-decay data, respectively. 98
5.9 Experimental and predicted Coulomb-displacement energies for odd-odd $N = Z$ nuclei. 107
5.10 Comparison of different selected binding energy (BE) filters of $N \approx Z$ nuclides. . 111
5.11 Schematic illustration of the three scenarios that could reconcile the observation of both 1p and 2p decays of ^{94}Ag with the mass measurements reported here. . . 112
5.12 Potential energy surface of the ^{94}Ag 21^+ state as a function of quadrupole deformation parameters (β_2,γ) calculated by the DNO-SM approach. 115
5.13 Proton single-particle 'universal' Woods-Saxon mean field energies for ^{94}Ag as a function of the quadrupole deformation parameter α_{20}. 116
5.14 Potential energy surface as a function of multipole deformation parameters (α_{20}, α_{40}) for ^{92}Pd deduced by the 'universal' Woods-Saxon mean-field approach. . . . 117

List of Tables

4.1 Measured mass excess values of neutron-rich indium isotopes compared with the literature values. 66
4.3 Measured excitation energy of neutron-rich indium isotopes compared with the literature values. 67

5.1 Summary of the used measurement settings and the measured nuclides, whose yields observed in FRS and FRS Ion Catcher were determined and compared with each other to verify their correct identification. 80
5.3 The definitions and average values of the three FRS correction factors that were defined and calculated for the different measurement settings and isotopes. 81
5.5 The definitions and values of the three FRS Ion Catcher correction factors that were defined and calculated for the different measurement settings and isotopes. . 83
5.7 Measured mass excess values close to the $N = Z$ line compared with the literature values. 92
5.9 Ground-state properties of ^{94}Ag deduced in the present work and compared with results from earlier works. 105
5.11 Ground-state properties of odd-odd $N = Z$ nuclides deduced in the present work and compared with results from earlier works. 108
5.13 Mass excess values and excitation energies of the ^{94}Ag (21^+) isomer state(s) deduced in the present work and compared with results from earlier works. 112

References

[Aggarwal, 2010] Aggarwal, M. (2010). Proton radioactivity at non-collective prolate shape in high spin state of ^{94}Ag. *Phys. Lett. B*, 693(4), 489–493. https://doi.org/10.1016/j.physletb.2010.08.077

[Amanbayev, 2023] Amanbayev, D. (2023). *Mass measurements at the N=Z and N=126 limits at the FRS Ion Catcher and development of the Cryogenic Stopping Cell for the Super-FRS*. Universität Gießen. http://geb.uni-giessen.de

[Amanbayev et al., 2022] Amanbayev, D., Plaß, W., & Kripkó-Koncz, G. (2022). *A phenomenological model of gas-phase chemistry in the FRS Ion Catcher*. (private communication, internal report).

[Andreyev et al., 2013] Andreyev, A. N., Huyse, M., & Van Duppen, P. (2013). Colloquium: Beta-delayed fission of atomic nuclei. *Rev. Mod. Phys.*, 85, 1541–1559. https://doi.org/10.1103/RevModPhys.85.1541

[Angert & Schmelzer, 1969] Angert, N. & Schmelzer, C. (1969). The UNILAC, a variable energy linear accelerator for atomic ions of any mass. *Kerntech.*, 11, 690–695. https://www.osti.gov/biblio/4184513

[Anicich, 2003] Anicich, V. G. (2003). An index of the literature for bimolecular gas phase cation-molecule reaction kinetics. https://ntrs.nasa.gov/citations/20060029368

[Anne et al., 1990] Anne, R., Arnell, S., Bimbot, R., Emling, H., Guillemaud-Mueller, D., Hansen, P., Johannsen, L., Jonson, B., Lewitowicz, M., Mattsson, S., Mueller, A., Neugart, R., Nyman, G., Pougheon, F., Richter, A., et al. (1990). Observation of forward neutrons from the break-up of the ^{11}Li neutron halo. *Phys. Lett. B*, 250(1), 19–23. https://doi.org/10.1016/0370-2693(90)91147-4

[Antony et al., 1997] Antony, M., Pape, A., & Britz, J. (1997). Coulomb displacement energies between analog levels for $3 \leq A \leq 239$. *At. Data Nucl. Data Tables*, 66(1), 1–63. https://doi.org/10.1006/adnd.1997.0740

[Arrhenius, 1889a] Arrhenius, S. (1889a). Über die Dissociationswärme und den Einfluss der Temperatur auf den Dissociationsgrad der Elektrolyte. *Z. Phys. Chem.*, 4U(1), 96–116. https://doi.org/10.1515/zpch-1889-0408

[Arrhenius, 1889b] Arrhenius, S. (1889b). Über die Reaktionsgeschwindigkeit bei der Inversion von Rohrzucker durch Säuren. *Z. Phys. Chem.*, 4U(1), 226–248. https://doi.org/10.1515/zpch-1889-0416

[Audi et al., 2003] Audi, G., Wapstra, A., & Thibault, C. (2003). The AME2003 atomic mass evaluation: (II). Tables, graphs and references. *Nuclear Physics A*, 729(1), 337–676. The 2003 NUBASE and Atomic Mass Evaluations. https://doi.org/10.1016/j.nuclphysa.2003.11.003

[Ayet San Andrés, 2018] Ayet San Andrés, S. (2018). *Developments for Multiple-Reflection Time-of-Flight Mass Spectrometers and their Application to High Resolution Mass Measurements of Exotic Nuclei.* Universität Gießen. http://geb.uni-giessen.de

[Ayet San Andres et al., 2021] Ayet San Andres, S., Dickel, T., Beck, S., Glöckner, S., Mollaebrahimi, A., & Kripkó-Koncz, G. (2020-2021). *Investigation, quantification and reduction of the correction to the time base given by the trigger systems of the FRS Ion Catcher and TITAN setups.* (private communication, internal report).

[Ayet San Andrés et al., 2019] Ayet San Andrés, S., Hornung, C., Ebert, J., Plaß, W. R., Dickel, T., Geissel, H., Scheidenberger, C., Bergmann, J., Greiner, F., Haettner, E., Jesch, C., Lippert, W., Mardor, I., Miskun, I., Patyk, Z., et al. (2019). High-resolution, accurate multiple-reflection time-of-flight mass spectrometry for short-lived, exotic nuclei of a few events in their ground and low-lying isomeric states. *Phys. Rev. C*, 99, 064313. https://doi.org/10.1103/PhysRevC.99.064313

[Ayet San Andrés et al., 2024] Ayet San Andrés, S., Kripkó-Koncz, G., Dickel, T., Beck, S., Das, D., Hornung, C., Plaß, W., & the FRS-IC team (2019-2024). *Developments of the data analysis framework specialized to treat MR-TOF-MS data.* (private communication).

[Ayet San Andrés et al., 2020] Ayet San Andrés, S., Mollaebrahimi, A., Dickel, T., Bergmann, J., Ebert, J., Geissel, H., Greiner, F., Haettner, E., Hornung, C., Kalantar-Nayestanaki, N., Miskun, I., Plaß, W. R., Purushothaman, S., Rink, A.-K., Scheidenberger, C., et al. (2020). Mass and half-life measurements of neutron-deficient iodine isotopes. *Eur. Phys. J. A*, 56(5), 143. https://doi.org/10.1140/epja/s10050-020-00153-5

[Babcock et al., 2018] Babcock, C., Klawitter, R., Leistenschneider, E., Lascar, D., Barquest, B. R., Finlay, A., Foster, M., Gallant, A. T., Hunt, P., Kootte, B., Lan, Y., Paul, S. F., Phan, M. L., Reiter, M. P., Schultz, B., et al. (2018). Mass measurements of neutron-rich indium isotopes toward the $n = 82$ shell closure. *Phys. Rev. C*, 97, 024312. https://doi.org/10.1103/PhysRevC.97.024312

[Baglin, 2011] Baglin, C. M. (2011). Nuclear Data Sheets for A = 93. *Nucl. Data Sheets*, 112(5), 1163–1389. https://doi.org/https://doi.org/10.1016/j.nds.2011.04.001

[Baglin, 2012] Baglin, C. M. (2012). Nuclear Data Sheets for A = 92. *Nucl. Data Sheets*, 113(10), 2187–2389. https://doi.org/https://doi.org/10.1016/j.nds.2012.10.001

[Ball et al., 2016] Ball, G. C., Hackman, G., & Krücken, R. (2016). The TRIUMF-ISAC facility: two decades of discovery with rare isotope beams. *Phys. Scr.*, 91(9), 093002. https://doi.org/10.1088/0031-8949/91/9/093002

[Beck, 2023] Beck, S. (2023). *Direct Mass Measurements of Neutron-Deficient Lanthanides for Nuclear Structure Studies at the Proton Dripline.* Universität Gießen. http://geb.uni-giessen.de

[Beck et al., 2021] Beck, S., Kootte, B., Dedes, I., Dickel, T., Kwiatkowski, A. A., Lykiardopoulou, E. M., Plaß, W. R., Reiter, M. P., Andreoiu, C., Bergmann, J., Brunner, T., Curien, D., Dilling, J., Dudek, J., Dunling, E., et al. (2021). Mass Measurements of Neutron-Deficient Yb Isotopes and Nuclear Structure at the Extreme Proton-Rich Side of the $N = 82$ Shell. *Phys. Rev. Lett.*, 127, 112501. https://doi.org/10.1103/PhysRevLett.127.112501

[Bender & Heenen, 2011] Bender, M. & Heenen, P.-H. (2011). What can be learned from binding energy differences about nuclear structure: The example of δV_{pn}. *Phys. Rev. C*, 83, 064319. https://doi.org/10.1103/PhysRevC.83.064319

[Benito et al., 2020] Benito, J., Fraile, L. M., Korgul, A., Piersa, M., Adamska, E., Andreyev, A. N., Álvarez-Rodríguez, R., Barzakh, A. E., Benzoni, G., Berry, T., Borge, M. J. G., Carmona, M., Chrysalidis, K., Costache, C., Cubiss, J. G., et al. (2020). Detailed spectroscopy of doubly magic ^{132}Sn. *Phys. Rev. C*, 102, 014328. https://doi.org/10.1103/PhysRevC.102.014328

[Bentley, 2022] Bentley, M. A. (2022). Excited States in Isobaric Multiplets — Experimental Advances and the Shell-Model Approach. *Physics*, 4(3), 995–1011. https://doi.org/10.3390/physics4030066

[Bergmann, 2024] Bergmann, J. (2024). *High-Resolution Tandem Mass Spectrometry of Complex Mixtures with a Multiple-Reflection Time-of-Flight Mass-Spectrometer*. Universität Gießen. http://geb.uni-giessen.de

[Bergmann et al., 2020] Bergmann, J., Beck, S., Kripkó-Koncz, G., & the FRS-IC crew (2018-2020). *Development of a refined operation mode of the trigger system at the FRS Ion Catcher including the development and validation of the software package used for the preparation of the measurement settings.* (private communication, internal report).

[Bethe & Bacher, 1936] Bethe, H. A. & Bacher, R. F. (1936). Nuclear Physics A. Stationary States of Nuclei. *Rev. Mod. Phys.*, 8, 82–229. https://doi.org/10.1103/RevModPhys.8.82

[Birge, 1932] Birge, R. T. (1932). The calculation of errors by the method of least squares. *Phys. Rev.*, 40, 207–227. https://doi.org/10.1103/PhysRev.40.207

[Bączyk et al., 2018] Bączyk, P., Dobaczewski, J., Konieczka, M., Satuła, W., Nakatsukasa, T., & Sato, K. (2018). Isospin-symmetry breaking in masses of $N \simeq Z$ nuclei. *Phys. Lett. B*, 778, 178–183. https://doi.org/10.1016/j.physletb.2017.12.068

[Blasche et al., 1993] Blasche, K., Franczak, B., Langenbeck, B., Moritz, G., & Riedel, C. (1993). The heavy ion synchrotron SIS-a progress report. *Proceedings of International Conference on Particle Accelerators*, volume 5, 3736–3738. https://doi.org/10.1109/PAC.1993.309772

[Blaum, 2006] Blaum, K. (2006). High-accuracy mass spectrometry with stored ions. *Physics Reports*, 425(1), 1–78. https://doi.org/10.1016/j.physrep.2005.10.011

[Blönnigen et al., 1987] Blönnigen, F., Moltz, D., Lang, T., Knoll, W., Xu, X., Hotchkis, M., Reiff, J., & Cerny, J. (1987). Improvements to the helium-jet coupled on-line mass separator RAMA. *Nucl. Instrum. Methods B*, 26(1), 328–332. https://doi.org/10.1016/0168-583X(87)90772-5

[Blumenfeld et al., 2013] Blumenfeld, Y., Nilsson, T., & Van Duppen, P. (2013). Facilities and methods for radioactive ion beam production. *Phys. Scr.*, 2013(T152), 014023. https://doi.org/10.1088/0031-8949/2013/T152/014023

[Borer et al., 1975] Borer, J., Bramham, P., Hereward, H. G., Hübner, K., Schnell, W., & Thorndahl, L. (1975). Non-destructive diagnostics of coasting beams with schottky noise. Proceedings, Springfield, Nat. Tech. Inf. Serv., 1974, CONF 740522, p. 53-56. https://cds.cern.ch/record/310532

[Brenner et al., 1990] Brenner, D., Wesselborg, C., Casten, R., Warner, D., & Zhang, J.-Y. (1990). Empirical p-n interactions: global trends, configuration sensitivity and $N = Z$ enhancements. *Phys. Lett. B*, 243(1), 1–6. https://doi.org/10.1016/0370-2693(90)90945-3

[Brenner et al., 2006] Brenner, D. S., Cakirli, R. B., & Casten, R. F. (2006). Valence proton-neutron interactions throughout the mass surface. *Phys. Rev. C*, 73, 034315. https://doi.org/10.1103/PhysRevC.73.034315

[Bricault et al., 2002] Bricault, P., Baartman, R., Dombsky, M., Hurst, A., Mark, C., Stanford, G., & Schmor, P. (2002). TRIUMF-ISAC target station and mass separator commissioning. *Nucl. Phys. A*, 701(1), 49–53. https://doi.org/https://doi.org/10.1016/S0375-9474(01)01546-9

[Britz et al., 1998] Britz, J., Pape, A., & Antony, M. (1998). Coefficients of the isobaric mass equation and their correlations with various nuclear parameters. *At. Data Nucl. Data Tables*, 69(1), 125–159. https://doi.org/10.1006/adnd.1998.0773

[Brock et al., 2010] Brock, T. S., Nara Singh, B. S., Boutachkov, P., Braun, N., Blazhev, A., Liu, Z., Wadsworth, R., Górska, M., Grawe, H., Pietri, S., Domingo-Pardo, C., Rudolph, D., Steer, S. J., Ataç, A., Bettermann, L., et al. (2010). Observation of a new high-spin isomer in ^{94}Pd. *Phys. Rev. C*, 82, 061309. https://doi.org/10.1103/PhysRevC.82.061309

[Brunner et al., 2012] Brunner, T., Smith, M., Brodeur, M., Ettenauer, S., Gallant, A., Simon, V., Chaudhuri, A., Lapierre, A., Mané, E., Ringle, R., Simon, M., Vaz, J., Delheij, P., Good, M., Pearson, M., & Dilling, J. (2012). TITAN's digital RFQ ion beam cooler and buncher, operation and performance. *Nucl. Instrum. Methods A*, 676, 32–43. https://doi.org/https://doi.org/10.1016/j.nima.2012.02.004

[Burbidge et al., 1957] Burbidge, E. M., Burbidge, G. R., Fowler, W. A., & Hoyle, F. (1957). Synthesis of the elements in stars. *Rev. Mod. Phys.*, 29, 547–650. https://doi.org/10.1103/RevModPhys.29.547

[Burkholder et al., 2015] Burkholder, J., Sander, S., Abbatt, J., Barker, J., Huie, R., Kolb, C., Kurylo, M., Orkin, V., Wilmouth, D., & Wine, P. (2015). *Chemical Kinetics and Photochemical Data for Use in Atmospheric Studies, Evaluation Number 18*. https://doi.org/10.13140/RG.2.1.2504.2806

[Cakirli et al., 2005] Cakirli, R. B., Brenner, D. S., Casten, R. F., & Millman, E. A. (2005). Proton-Neutron Interactions and the New Atomic Masses. *Phys. Rev. Lett.*, 94, 092501. https://doi.org/10.1103/PhysRevLett.94.092501

[Caurier et al., 2005] Caurier, E., Martínez-Pinedo, G., Nowacki, F., Poves, A., & Zuker, A. P. (2005). The shell model as a unified view of nuclear structure. *Rev. Mod. Phys.*, 77, 427–488. https://doi.org/10.1103/RevModPhys.77.427

[Caurier & Nowacki, 1999] Caurier, E. & Nowacki, F. (1999). Present status of shell model techniques. *Acta Phys. Pol. B*, 30(3), 705. https://www.actaphys.uj.edu.pl/R/30/3/749/pdf

[Cederwall et al., 2011] Cederwall, B., Ghazi Moradi, F., Bäck, T., Johnson, A., Blomqvist, J., Clément, E., de France, G., Wadsworth, R., Andgren, K., Lagergren, K., Dijon, A., Jaworski, G., Liotta, R., Qi, C., Nyakó, B. M., et al. (2011). Evidence for a spin-aligned neutron–proton paired phase from the level structure of ^{92}Pd. *Nature*, 469, 68–71. https://doi.org/10.1038/nature09644

[Cerkaski et al., 1979] Cerkaski, M., Dudek, J., Rozmej, P., Szymański, Z., & Nilsson, S. G. (1979). Particle-hole structure of nuclear isomers at high angular momenta. *Nucl. Phys. A*, 315(3), 269–290. https://doi.org/10.1016/0375-9474(79)90611-0

[Cerkaski et al., 1977] Cerkaski, M., Dudek, J., Szymański, Z., Andersson, C. G., Leander, G., Aberg, S., Nilsson, S. G., & Ragnarsson, I. (1977). Nucleon binding in nuclei at high angular momentum. *Phys. Lett. B*, 72(2), 149–151. https://doi.org/10.1016/0370-2693(77)90687-6

[Cerny et al., 2009] Cerny, J., Moltz, D. M., Lee, D. W., Peräjärvi, K., Barquest, B. R., Grossman, L. E., Jeong, W., & Jewett, C. C. (2009). Reinvestigation of the direct two-proton decay of the long-lived isomer $^{94}Ag^{m}$ [0.4 s, 6.7 MeV, (21+)]. *Phys. Rev. Lett.*, 103, 152502. https://doi.org/10.1103/PhysRevLett.103.152502

[Chadwick et al., 2006] Chadwick, M., Oblozinský, P., Herman, M., Greene, N., McKnight, R., Smith, D., Young, P., MacFarlane, R., Hale, G., Frankle, S., Kahler, A., Kawano, T., Little, R., Madland, D., Moller, P., et al. (2006). ENDF/B-VII.0: Next Generation Evaluated Nuclear Data Library for Nuclear Science and Technology. *Nuclear Data Sheets*, 107(12), 2931–3060. Evaluated Nuclear Data File ENDF/B-VII.0. https://doi.org/10.1016/j.nds.2006.11.001

[Changizi et al., 2015] Changizi, S., Qi, C., & Wyss, R. (2015). Empirical pairing gaps, shell effects, and di-neutron spatial correlation in neutron-rich nuclei. *Nucl. Phys. A*, 940, 210–226. https://doi.org/10.1016/j.nuclphysa.2015.04.010

[Chen et al., 2009] Chen, L., Litvinov, Y. A., Plaß, W. R., Beckert, K., Beller, P., Bosch, F., Boutin, D., Caceres, L., Cakirli, R. B., Carroll, J. J., Casten, R. F., Chakrawarthy, R. S., Cullen, D. M., Cullen, I. J., Franzke, B., et al. (2009). Schottky Mass Measurement of the ^{208}Hg Isotope: Implication for the Proton-Neutron Interaction Strength around Doubly Magic ^{208}Pb. *Phys. Rev. Lett.*, 102, 122503. https://doi.org/10.1103/PhysRevLett.102.122503

[Cwiok et al., 1987] Cwiok, S., Dudek, J., Nazarewicz, W., Skalski, J., & Werner, T. (1987). Single-particle energies, wave functions, quadrupole moments and g-factors in an axially deformed woods-saxon potential with applications to the two-centre-type nuclear problems. *Comput. Phys. Commun.*, 46(3), 379–399. https://doi.org/10.1016/0010-4655(87)90093-2

[Cyburt et al., 2016] Cyburt, R. H., Amthor, A. M., Heger, A., Johnson, E., Keek, L., Meisel, Z., Schatz, H., & Smith, K. (2016). Dependence of x-ray burst models on nuclear reaction rates. *The Astrophysical Journal*, 830(2), 55. https://doi.org/10.3847/0004-637X/830/2/55

[Damgaard & Winter, 1966] Damgaard, J. & Winter, A. (1966). Use of conserved vector current theory in first forbidden β-decay. *Physics Letters*, 23(6), 345–346. https://doi.org/10.1016/0031-9163(66)90461-6

[Danielewicz & Lee, 2014] Danielewicz, P. & Lee, J. (2014). Symmetry energy II: Isobaric analog states. *Nucl. Phys. A*, 922, 1–70. https://doi.org/10.1016/j.nuclphysa.2013.11.005

[Dao et al., 2024] Dao, D., Nowacki, F., Blazhev, A., Górska, M., Plaß, W., & Kripkó-Koncz, G. (2023-2024). *Shell-model calculations for investigating the high-lying* (21^{+}) *isomer in* ^{94}Ag. (private communication).

[Dao & Nowacki, 2022] Dao, D. D. & Nowacki, F. (2022). Nuclear structure within a discrete nonorthogonal shell model approach: New frontiers. *Phys. Rev. C*, 105, 054314. https://doi.org/10.1103/PhysRevC.105.054314

[Das et al., 2022] Das, B., Cederwall, B., Qi, C., Górska, M., Regan, P. H., Aktas, O., Albers, H. M., Banerjee, A., Chishti, M. M. R., Gerl, J., Hubbard, N., Jazrawi, S., Jolie, J., Mistry, A. K., Polettini, M., et al. (2022). Nature of seniority symmetry breaking in the semimagic nucleus ^{94}Ru. *Phys. Rev. C*, 105, L031304. https://doi.org/10.1103/PhysRevC.105.L031304

[de Voigt et al., 1983] de Voigt, M. J. A., Dudek, J., & Szymański, Z. (1983). High-spin phenomena in atomic nuclei. *Rev. Mod. Phys.*, 55, 949–1046. https://doi.org/10.1103/RevModPhys.55.949

[Dean et al., 2004] Dean, S., Górska, M., Aksouh, F., de Witte, H., Facina, M., Huyse, M., Ivanov, O., Krouglov, K., Kudryavtsev, Y., Mukha, I., Smirnov, D., Thomas, J.-C., Van de Vel, K., Van de Walle, J., Van Duppen, P., et al. (2004). The beta decay of neutron-deficient rhodium and ruthenium isotopes. *Eur. Phys. J. A*, 21, 243–255. https://doi.org/10.1140/epja/i2003-10204-2

[Dedes et al., 2024] Dedes, I., Dudek, J., Gaamouci, A., Baran, A., Yang, J., Plaß, W., & Kripkó-Koncz, G. (2023-2024). *Nuclear mean-field calculations for investigating the 1p/2p-decay branches of the high-lying isomer(s) in* ^{94}*Ag.* (private communication).

[Delion & Liotta, 2013] Delion, D. S. & Liotta, R. J. (2013). Shell-model representation to describe α emission. *Phys. Rev. C*, 87, 041302. https://doi.org/10.1103/PhysRevC.87.041302

[Delion et al., 2013] Delion, D. S., Liotta, R. J., & Wyss, R. (2013). Simple approach to two-proton emission. *Phys. Rev. C*, 87, 034328. https://doi.org/10.1103/PhysRevC.87.034328

[Détraz et al., 1979] Détraz, C., Guillemaud, D., Huber, G., Klapisch, R., Langevin, M., Naulin, F., Thibault, C., Carraz, L. C., & Touchard, F. (1979). Beta decay of $^{27-32}$Na and their descendants. *Phys. Rev. C*, 19, 164–176. https://doi.org/10.1103/PhysRevC.19.164

[Dickel, 2010] Dickel, T. (2010). *Design and Commissioning of an Ultra-High-Resolution Time-of-Flight Based Isobar Separator and Mass Spectrometer.* Universität Gießen. https://repository.gsi.de/record/200291

[Dickel et al., 2023] Dickel, T., Hornung, C., Amanbayev, D., Ayet San Andrés, S., Beck, S., Bergmann, J., Geissel, H., Gerl, J., Górska, M., Gröf, L., Haettner, E., Hucka, J.-P., Kostyleva, D. A., Kripko-Koncz, G., Mollaebrahimi, A., et al. (2023). Mean range bunching of exotic nuclei produced by in-flight fragmentation and fission — Stopped-beam experiments with increased efficiency. *Nucl. Instrum. Methods B*, 541, 275–278. https://doi.org/https://doi.org/10.1016/j.nimb.2023.05.018

[Dickel et al., 2020] Dickel, T., Kankainen, A., Spătaru, A., Amanbayev, D., Beliuskina, O., Beck, S., Constantin, P., Benyamin, D., Geissel, H., Gröf, L., Hornung, C., Karpov, A. V., Mardor, I., Münzenberg, G., Nichita, D., et al. (2020). Multi-nucleon transfer reactions at ion catcher facilities - a new way to produce and study heavy neutron-rich nuclei. *J. Phys.: Conf. Ser.*, 1668(1), 012012. https://doi.org/10.1088/1742-6596/1668/1/012012

[Dickel & Mollaebrahimi, 2024] Dickel, T. & Mollaebrahimi, A. (2024). Unveiling nuclear isomers through multiple-reflection time-of-flight mass spectrometry. *Eur. Phys. J.: Spec. Top.*, 233, 1181–1190. https://doi.org/10.1140/epjs/s11734-024-01156-9

[Dickel et al., 2015a] Dickel, T., Plaß, W. R., Ayet San Andrés, S., Ebert, J., Geissel, H., Haettner, E., Hornung, C., Miskun, I., Pietri, S., Purushothaman, S., Reiter, M. P., Rink, A. K., Scheidenberger, C., Weick, H., Dendooven, P., Diwisch, M., Greiner, F., Heisse, F., Knöbel, R., Lippert, W., Moore, I. D., Pohjalainen, I., Prochazka, A., Ranjan, M., Takechi, M., Winfield, J. S., & Xu, X. (2015a). First spatial separation of a heavy ion isomeric beam with a multiple-reflection time-of-flight mass spectrometer. *Phys. Lett. B*, 744, 137–141.

[Dickel et al., 2015b] Dickel, T., Plaß, W. R., Becker, A., Czok, U., Geissel, H., Haettner, E., Jesch, C., Kinsel, W., Petrick, M., Scheidenberger, C., Simon, A., & Yavor, M. I. (2015b). A

high-performance multiple-reflection time-of-flight mass spectrometer and isobar separator for the research with exotic nuclei. *Nucl. Instrum. Methods A*, 777, 172–188. https://doi.org/10.1016/j.nima.2014.12.094

[Dickel et al., 2017a] Dickel, T., Plaß, W. R., Lippert, W., Lang, J., Yavor, M. I., Geissel, H., & Scheidenberger, C. (2017a). Isobar Separation in a Multiple-Reflection Time-of-Flight Mass Spectrometer by Mass-Selective Re-Trapping. *J. Am. Soc. Mass Spectr.*, 28(6), 1079–1090. https://doi.org/10.1007/s13361-017-1617-z

[Dickel et al., 2024] Dickel, T., Plaß, W. R., Haettner, E., Hornung, C., Purushothaman, S., Scheidenberger, C., & Weick, H. (2024). High-Precision Experiments with Trapped Radioactive Ions Produced at Relativistic Energies. *Atoms*, 12(10). https://doi.org/10.3390/atoms12100051

[Dickel et al., 2017b] Dickel, T., Yavor, M. I., Lang, J., Plaß, W. R., Lippert, W., Geissel, H., & Scheidenberger, C. (2017b). Dynamical time focus shift in multiple-reflection time-of-flight mass spectrometers. *Int. J. Mass Spectrom.*, 412, 1–7.

[Dilling et al., 2006] Dilling, J., Baartman, R., Bricault, P., Brodeur, M., Blomeley, L., Buchinger, F., Crawford, J., Crespo López-Urrutia, J., Delheij, P., Froese, M., Gwinner, G., Ke, Z., Lee, J., Moore, R., Ryjkov, V., Sikler, G., Smith, M., Ullrich, J., & Vaz, J. (2006). Mass measurements on highly charged radioactive ions, a new approach to high precision with TITAN. *Int. J. Mass Spectrom.*, 251(2), 198–203. https://doi.org/https://doi.org/10.1016/j.ijms.2006.01.044

[Dilling et al., 2018] Dilling, J., Blaum, K., Brodeur, M., & Eliseev, S. (2018). Penning-trap mass measurements in atomic and nuclear physics. *Annu. Rev. Nucl. Part. Sci.*, 68(1), 45–74. https://doi.org/10.1146/annurev-nucl-102711-094939

[Dudek et al., 1979] Dudek, J., Majhofer, A., Skalski, J., Werner, T., Cwiok, S., & Nazarewicz, W. (1979). Parameters of the deformed Woods-Saxon potential outside A=110-210 nuclei. *J. of Phys. G: Nucl. Phys.*, 5(10), 1359. https://doi.org/10.1088/0305-4616/5/10/014

[Dudek et al., 1980] Dudek, J., Nazarewicz, W., & Werner, T. (1980). Discussion of the improved parametrisation of the Woods-Saxon potential for deformed nuclei. *Nucl. Phys. A*, 341(2), 253–268. https://doi.org/10.1016/0375-9474(80)90312-7

[Dudek et al., 1981] Dudek, J., Szymański, Z., & Werner, T. (1981). Woods-saxon potential parameters optimized to the high spin spectra in the lead region. *Phys. Rev. C*, 23, 920–925. https://doi.org/10.1103/PhysRevC.23.920

[Dudek & Werner, 1978] Dudek, J. & Werner, T. (1978). New parameters of the deformed Woods-Saxon potential for A=110-210 nuclei. *J. Phys. G: Nucl. Phys.*, 4(10), 1543. https://doi.org/10.1088/0305-4616/4/10/006

[Duflo & Zuker, 1995] Duflo, J. & Zuker, A. (1995). Microscopic mass formulas. *Phys. Rev. C*, 52, R23–R27. https://doi.org/10.1103/PhysRevC.52.R23

[Dunling, 2021] Dunling, E. (2021). *Exploring magicity around $N = 32$ & 34 in $Z >= 20$ isotopes via precision mass measurements and developments with the TITAN MR-TOF mass spectrometer*. University of York. https://etheses.whiterose.ac.uk/29383/

[Ebert, 2016] Ebert, J. (2016). *Mass Measurements of 238-U-Projectile Fragments for the First Time with a Multiple-Reflection Time-Of-Flight Mass Spectrometer*. Universität Gießen. http://geb.uni-giessen.de

[Eliseev et al., 2014] Eliseev, S., Blaum, K., Block, M., Dörr, A., Droese, C., Eronen, T., Goncharov, M., Höcker, M., Schweikhard, L., Ketter, J., Ramirez, E. M., Nesterenko, D. A., Novikov, Y. N., & Schweikhard, L. (2014). A phase-imaging technique for cyclotron-frequency measurements. *Appl. Phys. B*, 114, 107–128. https://doi.org/10.1007/s00340-013-5621-0

[Eliseev et al., 2013] Eliseev, S., Blaum, K., Block, M., Droese, C., Goncharov, M., Minaya Ramirez, E., Nesterenko, D. A., Novikov, Y. N., & Schweikhard, L. (2013). Phase-Imaging Ion-Cyclotron-Resonance Measurements for Short-Lived Nuclides. *Phys. Rev. Lett.*, 110, 082501. https://doi.org/10.1103/PhysRevLett.110.082501

[ENSDF, 2024] ENSDF (2024). From ENSDF database as of December 16th, 2024. Version available at http://www.nndc.bnl.gov/ensarchivals/.

[Eronen et al., 2016] Eronen, T., Kankainen, A., & Äystö, J. (2016). Ion traps in nuclear physics — Recent results and achievements. *Prog. Part. Nucl. Phys.*, 91, 259–293. https://doi.org/10.1016/j.ppnp.2016.08.001

[Faestermann et al., 2013] Faestermann, T., Górska, M., & Grawe, H. (2013). The structure of ^{100}Sn and neighbouring nuclei. *Prog. Part. Nucl. Phys.*, 69, 85–130. https://doi.org/10.1016/j.ppnp.2012.10.002

[Faestermann et al., 2002] Faestermann, T., Schneider, R., Stolz, A., Sümmerer, K., Wefers, E., Friese, J., Geissel, H., Hellström, M., Kienle, P., Körner, H.-J., Mineva, M., Münch, M., Münzenberg, G., Schlegel, C., Schmidt, K., et al. (2002). Decay studies of $N \approx Z$ nuclei from ^{75}Sr to ^{102}Sn. *Eur. Phys. J. A*, 15, 185–188. https://doi.org/10.1140/epja/i2001-10251-7

[Fallis et al., 2011] Fallis, J., Clark, J. A., Sharma, K. S., Savard, G., Buchinger, F., Caldwell, S., Chaudhuri, A., Crawford, J. E., Deibel, C. M., Gulick, S., Hecht, A. A., Lascar, D., Lee, J. K. P., Levand, A. F., Li, G., et al. (2011). Mass measurements of isotopes of Nb, Mo, Tc, Ru, and Rh along the νp- and rp-process paths using the Canadian Penning trap mass spectrometer. *Phys. Rev. C*, 84, 045807. https://doi.org/10.1103/PhysRevC.84.045807

[Fogelberg et al., 2004] Fogelberg, B., Gausemel, H., Mezilev, K. A., Hoff, P., Mach, H., Sanchez-Vega, M., Lindroth, A., Ramström, E., Genevey, J., Pinston, J. A., & Rejmund, M. (2004). Decays of ^{131}In, ^{131}Sn, and the position of the $h_{11/2}$ neutron hole state. *Phys. Rev. C*, 70, 034312. https://doi.org/10.1103/PhysRevC.70.034312

[Fowler-Davis, 2025] Fowler-Davis, T. (2025). *Pushing the Limits: Mass Measurements of Neutron-Deficient Lanthanides at the Proton Drip Line & Ion Trapping Advancements using Printed Circuit Boards*. The University of Edinburgh. https://era.ed.ac.uk/

[Franzke, 1987] Franzke, B. (1987). The heavy ion storage and cooler ring project ESR at GSI. *Nucl. Instrum. Methods B*, 24-25, 18–25. https://doi.org/10.1016/0168-583X(87)90583-0

[Franzke et al., 2008] Franzke, B., Geissel, H., & Münzenberg, G. (2008). Mass and lifetime measurements of exotic nuclei in storage rings. *Mass Spectrometry Reviews*, 27(5), 428–469. https://doi.org/https://doi.org/10.1002/mas.20173

[Frauendorf & Macchiavelli, 2014] Frauendorf, S. & Macchiavelli, A. (2014). Overview of neutron–proton pairing. *Prog. Part. Nucl.*, 78, 24–90. https://doi.org/10.1016/j.ppnp.2014.07.001

[Freedman & Diaconis, 1981] Freedman, D. & Diaconis, P. (1981). On the histogram as a density estimator:L2 theory. *Z. Wahrscheinlichkeit.*, 57(4), 453–476.

[Fröhlich et al., 2006] Fröhlich, C., Martínez-Pinedo, G., Liebendörfer, M., Thielemann, F.-K., Bravo, E., Hix, W. R., Langanke, K., & Zinner, N. T. (2006). Neutrino-Induced Nucleosynthesis of $A > 64$ Nuclei: The νp Process. *Phys. Rev. Lett.*, 96, 142502. https://doi.org/10.1103/PhysRevLett.96.142502

[Gabrielse, 2009] Gabrielse, G. (2009). Why Is Sideband Mass Spectrometry Possible with Ions in a Penning Trap? *Phys. Rev. Lett.*, 102, 172501. https://doi.org/10.1103/PhysRevLett.102.172501

[Gallant et al., 2017] Gallant, A. T., Alanssari, M., Bale, J. C., Andreoiu, C., Barquest, B. R., Chowdhury, U., Even, J., Finlay, A., Frekers, D., Gwinner, G., Klawitter, R., Kootte, B., Kwiatkowski, A. A., Lascar, D., Leach, K. G., et al. (2017). Mass determination near $N = 20$ for Al and Na isotopes. *Phys. Rev. C*, 96, 024325. https://doi.org/10.1103/PhysRevC.96.024325

[Gao et al., 2023] Gao, Z., Solders, A., Al-Adili, A., Cannarozzo, S., Lantz, M., Pomp, S., Beliuskina, O., Eronen, T., Geldhof, S., Kankainen, A., Moore, I. D., Nesterenko, D., & Penttilä, H. (2023). Isomeric yield ratios in proton-induced fission of ^{238}U. *Phys. Rev. C*, 108, 054613. https://doi.org/10.1103/PhysRevC.108.054613

[Garcés Narro et al., 2001] Garcés Narro, J., Longour, C., Regan, P. H., Blank, B., Pearson, C. J., Lewitowicz, M., Miehé, C., Gelletly, W., Appelbe, D., Axelsson, L., Bruce, A. M., Catford, W. N., Chandler, C., Clark, R. M., Cullen, D. M., et al. (2001). Fermi superallowed β^+ decays and $T = 1$ ground states of heavy odd-odd $N = Z$ nuclei. *Phys. Rev. C*, 63, 044307. https://doi.org/10.1103/PhysRevC.63.044307

[Garnsworthy et al., 2009] Garnsworthy, A. B., Regan, P. H., Pietri, S., Sun, Y., Xu, F. R., Rudolph, D., Górska, M., Cáceres, L., Podolyák, Z., Steer, S. J., Hoischen, R., Heinz, A., Becker, F., Bednarczyk, P., Doornenbal, P., et al. (2009). Isomeric states in neutron-deficient A $\sim$ 80–90 nuclei populated in the fragmentation of ^{107}Ag. *Phys. Rev. C*, 80, 064303. https://doi.org/10.1103/PhysRevC.80.064303

[Gausemel et al., 2004] Gausemel, H., Fogelberg, B., Engeland, T., Hjorth-Jensen, M., Hoff, P., Mach, H., Mezilev, K. A., & Omtvedt, J. P. (2004). Decay of ^{127}In and ^{129}In. *Phys. Rev. C*, 69, 054307. https://doi.org/10.1103/PhysRevC.69.054307

[Ge et al., 2024] Ge, Z., Reponen, M., Eronen, T., Hu, B., Kortelainen, M., Kankainen, A., Moore, I., Nesterenko, D., Yuan, C., Beliuskina, O., Cañete, L., de Groote, R., Delafosse, C., Dickel, T., et al. (2024). High-Precision Mass Measurements of Neutron Deficient Silver Isotopes Probe the Robustness of the $N = 50$ Shell Closure. *Phys. Rev. Lett.*, 133, 132503. https://doi.org/10.1103/PhysRevLett.133.132503

[Geissel et al., 1992] Geissel, H., Armbruster, P., Behr, K., Brünle, A., Burkard, K., Chen, M., Folger, H., Franczak, B., Keller, H., Klepper, O., Langenbeck, B., Nickel, F., Pfeng, E., Pfützner, M., Roeckl, E., et al. (1992). The GSI projectile fragment separator (FRS): a versatile magnetic system for relativistic heavy ions. *Nucl. Instrum. Methods B*, 70(1), 286–297. https://doi.org/10.1016/0168-583X(92)95944-M

[Geissel et al., 2006] Geissel, H., Knöbel, R., Litvinov, Y. A., Sun, B., Beckert, K., Beller, P., Bosch, F., Boutin, D., Brandau, C., Chen, L., Fabian, B., Hausmann, M., Kozhuharov, C., Kurcewicz, J., Litvinov, S. A., et al. (2006). A new experimental approach for isochronous mass measurement of short-lived exotic nuclei with the FRS-ERS facility. *Hyperfine Interact.*, 173, 49–54. https://doi.org/10.1007/s10751-007-9541-4

[Geissel & Morrissey, 2023] Geissel, H. & Morrissey, D. J. (2023). *Exotic Nuclei and Their Separation, Electromagnetic Devices*, 3–61. Springer Nature Singapore. https://doi.org/10.1007/978-981-19-6345-2_100

[Geissel et al., 1995] Geissel, H., Münzenberg, G., & Riisager, K. (1995). Secondary exotic nuclear beams. *Annu. Rev. Nucl. Part. Sci.*, 45(1), 163–203.

[Geissel & Scheidenberger, 1998] Geissel, H. & Scheidenberger, C. (1998). Slowing down of relativistic heavy ions and new applications. *Nucl. Instrum. Methods B*, 136-138, 114–124. Ion Beam Analysis. https://doi.org/10.1016/S0168-583X(97)00660-5

[Goriely et al., 2010] Goriely, S., Chamel, N., & Pearson, J. M. (2010). Further explorations of Skyrme-Hartree-Fock-Bogoliubov mass formulas. XII. Stiffness and stability of neutron-star matter. *Phys. Rev. C*, 82, 035804. https://doi.org/10.1103/PhysRevC.82.035804

[Greiner et al., 2020] Greiner, F., Dickel, T., Ayet San Andrés, S., Bergmann, J., Constantin, P., Ebert, J., Geissel, H., Haettner, E., Hornung, C., Miskun, I., Lippert, W., Mardor, I., Moore, I., Plaß, W., Purushothaman, S., et al. (2020). Removal of molecular contamination in low-energy RIBs by the isolation–dissociation–isolation method. *Nucl. Instrum. Methods B*, 463, 324–326. https://doi.org/10.1016/j.nimb.2019.04.072

[Groeppert Mayer, 1948] Groeppert Mayer, M. (1948). On Closed Shells in Nuclei. *Phys. Rev.*, 74, 235–239. https://doi.org/10.1103/PhysRev.74.235

[Groeppert Mayer, 1949] Groeppert Mayer, M. (1949). On Closed Shells in Nuclei. II. *Phys. Rev.*, 75, 1969–1970. https://doi.org/10.1103/PhysRev.75.1969

[Haettner et al., 2011] Haettner, E., Ackermann, D., Audi, G., Blaum, K., Block, M., Eliseev, S., Fleckenstein, T., Herfurth, F., Heßberger, F. P., Hofmann, S., Ketelaer, J., Ketter, J., Kluge, H.-J., Marx, G., Mazzocco, M., et al. (2011). Mass measurements of very neutron-deficient Mo and Tc isotopes and their impact on *rp* process nucleosynthesis. *Phys. Rev. Lett.*, 106, 122501. https://doi.org/10.1103/PhysRevLett.106.122501

[Haettner et al., 2018] Haettner, E., Plaß, W. R., Czok, U., Dickel, T., Geissel, H., Kinsel, W., Petrick, M., Schäfer, T., & Scheidenberger, C. (2018). A versatile triple radiofrequency quadrupole system for cooling, mass separation and bunching of exotic nuclei. *Nucl. Instrum. Methods A*, 880, 138–151. https://doi.org/10.1016/j.nima.2017.10.003

[Häfner et al., 2019] Häfner, G., Moschner, K., Blazhev, A., Boutachkov, P., Davies, P. J., Wadsworth, R., Ameil, F., Baba, H., Bäck, T., Dewald, M., Doornenbal, P., Faestermann, T., Gengelbach, A., Gerl, J., Gernhäuser, R., et al. (2019). Properties of γ-decaying isomers in the ^{100}Sn region populated in fragmentation of a ^{124}Xe beam. *Phys. Rev. C*, 100, 024302. https://doi.org/10.1103/PhysRevC.100.024302

[Hakala et al., 2012] Hakala, J., Dobaczewski, J., Gorelov, D., Eronen, T., Jokinen, A., Kankainen, A., Kolhinen, V. S., Kortelainen, M., Moore, I. D., Penttilä, H., Rinta-Antila, S., Rissanen, J., Saastamoinen, A., Sonnenschein, V., & Äystö, J. (2012). Precision Mass Measurements beyond ^{132}Sn: Anomalous Behavior of Odd-Even Staggering of Binding Energies. *Phys. Rev. Lett.*, 109, 032501. https://doi.org/10.1103/PhysRevLett.109.032501

[Hamaker et al., 2021] Hamaker, A., Leistenschneider, E., Jain, R., Bollen, G., Giuliani, S. A., Lund, K., Nazarewicz, W., Neufcourt, L., Nicoloff, C. R., Puentes, D., Ringle, R., Sumithrarachchi, C. S., & Yandow, I. T. (2021). Precision mass measurement of lightweight self-conjugate nucleus ^{80}Zr. *Nature Physics*, 17, 1408–1412. https://doi.org/10.1038/s41567-021-01395-w

[Hardy et al., 1977] Hardy, J., Carraz, L., Jonson, B., & Hansen, P. (1977). The essential decay of pandemonium: A demonstration of errors in complex beta-decay schemes. *Phys. Lett. B*, 71(2), 307–310. https://doi.org/10.1016/0370-2693(77)90223-4

[Hardy & Towner, 2002] Hardy, J. C. & Towner, I. S. (2002). Superallowed Beta Decay of Nuclei with $A \geq 62$: The Limiting Effect of Weak Gamow-Teller Branches. *Phys. Rev. Lett.*, 88, 252501. https://doi.org/10.1103/PhysRevLett.88.252501

[Hardy & Towner, 2005] Hardy, J. C. & Towner, I. S. (2005). Superallowed $0^+ \rightarrow 0^+$ nuclear β decays: A critical survey with tests of the conserved vector current hypothesis and the standard model. *Phys. Rev. C*, 71, 055501. https://doi.org/10.1103/PhysRevC.71.055501

[Hardy & Towner, 2015] Hardy, J. C. & Towner, I. S. (2015). Superallowed $0^+ \rightarrow 0^+$ nuclear β decays: 2014 critical survey, with precise results for V_{ud} and CKM unitarity. *Phys. Rev. C*, 91, 025501. https://doi.org/10.1103/PhysRevC.91.025501

[Hardy & Towner, 2020] Hardy, J. C. & Towner, I. S. (2020). Superallowed $0^+ \rightarrow 0^+$ nuclear β decays: 2020 critical survey, with implications for V_{ud} and CKM unitarity. *Phys. Rev. C*, 102, 045501. https://doi.org/10.1103/PhysRevC.102.045501

[Hausmann et al., 2013] Hausmann, M., Aaron, A., Amthor, A., Avilov, M., Bandura, L., Bennett, R., Bollen, G., Borden, T., Burgess, T., Chouhan, S., Graves, V., Mittig, W., Morrissey, D., Pellemoine, F., Portillo, M., et al. (2013). Design of the Advanced Rare Isotope Separator ARIS at FRIB. *Nucl. Instrum. Methods B*, 317, 349–353. https://doi.org/10.1016/j.nimb.2013.06.042

[Hausmann et al., 2000] Hausmann, M., Attallah, F., Beckert, K., Bosch, F., Dolinskiy, A., Eickhoff, H., Falch, M., Franczak, B., Franzke, B., Geissel, H., Kerscher, T., Klepper, O., Kluge, H.-J., Kozhuharov, C., Löbner, K., et al. (2000). First isochronous mass spectrometry at the experimental storage ring ESR. *Nucl. Instrum. Methods A*, 446(3), 569–580. https://doi.org/10.1016/S0168-9002(99)01192-4

[Herndl & Brown, 1997] Herndl, H. & Brown, B. A. (1997). Shell-model calculations for the properties of nuclei with A = 86–100 near the proton drip line. *Nucl. Phys. A*, 627(1), 35–52. https://doi.org/10.1016/S0375-9474(97)00407-7

[Hirsh et al., 2016] Hirsh, T. Y., Paul, N., Burkey, M., Aprahamian, A., Buchinger, F., Caldwell, S., Clark, J. A., Levand, A. F., Ying, L. L., Marley, S. T., Morgan, G. E., Nystrom, A., Orford, R., Galván, A. P., Rohrer, J., et al. (2016). First operation and mass separation with the CARIBU MR-TOF. *Nucl. Instrum. Methods B*, 376, 229–232. https://doi.org/10.1016/j.nimb.2015.12.037

[Hoff et al., 2020] Hoff, D. E. M., Rogers, A. M., Meisel, Z., Bender, P. C., Brandenburg, K., Childers, K., Clark, J. A., Dombos, A. C., Doucet, E. R., Jin, S., Lewis, R., Liddick, S. N., Lister, C. J., Morse, C., Schatz, H., et al. (2020). Influence of ^{73}Rb on the ashes of accreting neutron stars. *Phys. Rev. C*, 102, 045810. https://doi.org/10.1103/PhysRevC.102.045810

[Hoff et al., 1996] Hoff, P., Baumann, P., Huck, A., Knipper, A., Walter, G., Marguier, G., Fogelberg, B., Lindroth, A., Mach, H., Sanchez-Vega, M., Taylor, R. B. E., Van Duppen, P., Jokinen, A., Lindroos, M., Ramdhane, M., et al. (1996). Single-Neutron States in ^{133}Sn. *Phys. Rev. Lett.*, 77, 1020–1023. https://doi.org/10.1103/PhysRevLett.77.1020

[Honma et al., 2009] Honma, M., Otsuka, T., Mizusaki, T., & Hjorth-Jensen, M. (2009). New effective interaction for f_5pg_9-shell nuclei. *Phys. Rev. C*, 80, 064323. https://doi.org/10.1103/PhysRevC.80.064323

[Hornung, 2018] Hornung, C. (2018). *High-Resolution Experiments with the Multiple-Reflection Time-Of-Flight Mass Spectrometer at the Fragment Separator FRS.* Universität Gießen. http://geb.uni-giessen.de

[Hornung et al., 2020] Hornung, C., Amanbayev, D., Dedes, I., Kripko-Koncz, G., Miskun, I., Shimizu, N., Ayet San Andrés, S., Bergmann, J., Dickel, T., Dudek, J., Ebert, J., Geissel, H., Górska, M., Grawe, H., Greiner, F., et al. (2020). Isomer studies in the vicinity of the doubly-magic nucleus ^{100}Sn: Observation of a new low-lying isomeric state in ^{97}Ag. *Phys. Lett. B*, 802, 135200. https://doi.org/10.1016/j.physletb.2020.135200

[Hornung et al., 2023] Hornung, C., Dickel, T., Amanbayev, D., Ayet San Andrés, S., Balabanski, D. L., Beck, S., Bergmann, J., Constantin, P., Ebert, J., Geissel, H., Greiner, F., Gröf, L., Haettner, E., Harakeh, M. N., Hucka, J.-P., et al. (2023). Mass tagging: Verification and calibration of particle identification by high-resolution mass measurements. *Nucl. Instrum. Methods B*, 541, 257–259. https://doi.org/10.1016/j.nimb.2023.04.045

[Hornung et al., 2022] Hornung, C., Plaß, W., Dickel, T., Mollaebrahimi, A., & Kripkó-Koncz, G. (2022). *FRS PID data analysis and interpretation of the results for the S474 experiment.* (private communication, internal report).

[Huang et al., 2021] Huang, W. J., Wang, M., Kondev, F. G., Audi, G., & Naimi, S. (2021). The AME 2020 atomic mass evaluation (I). Evaluation of input data, and adjustment procedures. *Chin. Phys. C*, 45(3), 030002. https://doi.org/10.1088/1674-1137/abddb0

[Huang et al., 2023] Huang, W. J., Zhou, X., Zhang, Y. H., Wang, M., Litvinov, Y. A., & Blaum, K. (2023). Ground-state mass of the odd-odd $n = z$ nuclide ^{70}Br. *Phys. Rev. C*, 108, 034301. https://doi.org/10.1103/PhysRevC.108.034301

[Izzo et al., 2021] Izzo, C., Bergmann, J., Dietrich, K. A., Dunling, E., Fusco, D., Jacobs, A., Kootte, B., Kripkó-Koncz, G., Lan, Y., Leistenschneider, E., Lykiardopoulou, E. M., Mukul, I., Paul, S. F., Reiter, M. P., Tracy, J. L., et al. (2021). Mass measurements of neutron-rich indium isotopes for r-process studies. *Phys. Rev. C*, 103, 025811. https://doi.org/10.1103/PhysRevC.103.025811

[Izzo et al., 2020] Izzo, C., Kripkó-Koncz, G., Dickel, T., & Dunling, E. (2019-2020). *Discussions and sanity checks concerning the data analysis of the mass measurements of neutron-rich indium isotopes performed at TITAN.* (private communication).

[Jacobs, 2023] Jacobs, A. (2023). *Refinement of the first r-process abundance peak via high-precision mass measurements.* University of British Columbia. https://doi.org/http://dx.doi.org/10.14288/1.0437099

[Jain et al., 2021] Jain, A. K., Maheshwari, B., & Goel, A. (2021). *Nuclear Isomers.* Springer Cham, Switzerland, (First Edition ed.). https://doi.org/https://doi.org/10.1007/978-3-030-78675-5

[Jajčišinová et al., 2024] Jajčišinová, E., Dockx, K., Au, M., Bara, S., Cocolios, T. E., Chrysalidis, K., Farooq-Smith, G. J., Fedorov, D. V., Fedosseev, V. N., Flanagan, K. T., Heines, M., Houngbo, D., Johnson, J. D., Kellerbauer, A., Kraemer, S., et al. (2024). Production study of Fr, Ra and Ac radioactive ion beams at ISOLDE, CERN. *Sci. Rep.*, 14, 11033. https://doi.org/10.1038/s41598-024-60331-z

[Jänecke, 1965] Jänecke, J. (1965). On isobaric analogue states. *Nucl. Phys.*, 73(1), 97–112. https://doi.org/10.1016/0029-5582(65)90157-4

[Jänecke & O'Donnell, 2005] Jänecke, J. & O'Donnell, T. (2005). Isospin inversion and n–p pairing in self-conjugate nuclei A=58–98. *Phys. Lett. B*, 605(1), 87–94. https://doi.org/10.1016/j.physletb.2004.11.037

[Jaries et al., 2024] Jaries, A., Stryjczyk, M., Kankainen, A., Al Ayoubi, L., Beliuskina, O., Canete, L., de Groote, R. P., Delafosse, C., Delahaye, P., Eronen, T., Flayol, M., Ge, Z., Geldhof, S., Gins, W., Hukkanen, M., et al. (2024). Isomeric states of fission fragments explored via penning trap mass spectrometry at igisol. *Phys. Rev. C*, 110, 034326. https://doi.org/10.1103/PhysRevC.110.034326

[Jenkins, 2009] Jenkins, D. G. (2009). Reviewing the evidence for two-proton emission from the high-spin isomer in ^{94}Ag. *Phys. Rev. C*, 80, 054303. https://doi.org/10.1103/PhysRevC.80.054303

[Jesch, 2016] Jesch, C. (2016). *The multiple-reflection time-of-flight isobar separator for TITAN and direct mass measurements at the FRS Ion Catcher*. Universität Gießen. http://geb.uni-giessen.de/geb/volltexte/2016/12096

[Juodagalvis & Dean, 2005] Juodagalvis, A. & Dean, D. J. (2005). Gamow-Teller GT_+ distributions in nuclei with mass $A = 90-97$. *Phys. Rev. C*, 72, 024306. https://doi.org/10.1103/PhysRevC.72.024306

[Jurado et al., 2007] Jurado, B., Savajols, H., Mittig, W., Orr, N., Roussel-Chomaz, P., Baiborodin, D., Catford, W., Chartier, M., Demonchy, C., Dlouhy, Z., Gillibert, A., Giot, L., Khouaja, A., Lépine-Szily, A., et al. (2007). Mass measurements of neutron-rich nuclei near the N=20 and 28 shell closures. *Phys. Lett. B*, 649(1), 43–48. https://doi.org/10.1016/j.physletb.2007.04.006

[Kacker et al., 2010] Kacker, R. N., Kessel, R., & Sommer, K.-D. (2010). Assessing differences between results determined according to the Guide to the Expression of Uncertainty in Measurement. *J. Res. Natl. Inst. Stand. Technol.*, 115, 453–459. https://doi.org/10.6028/jres.115.031

[Kajino et al., 2019] Kajino, T., Aoki, W., Balantekin, A., Diehl, R., Famiano, M., & Mathews, G. (2019). Current status of r-process nucleosynthesis. *Prog. Part. Nucl. Phys.*, 107, 109–166. https://doi.org/10.1016/j.ppnp.2019.02.008

[Kaneko et al., 2012] Kaneko, K., Mizusaki, T., Sun, Y., Tazaki, S., & de Angelis, G. (2012). Coulomb Energy Difference as a Probe of Isospin-Symmetry Breaking in the Upper fp-Shell Nuclei. *Phys. Rev. Lett.*, 109, 092504. https://doi.org/10.1103/PhysRevLett.109.092504

[Kaneko et al., 2008] Kaneko, K., Sun, Y., Hasegawa, M., & Mizusaki, T. (2008). Structure of upper-$g_{9/2}$-shell nuclei and shape effect in the ^{94}Ag isomeric states. *Phys. Rev. C*, 77, 064304. https://doi.org/10.1103/PhysRevC.77.064304

[Kaneko et al., 2013] Kaneko, K., Sun, Y., Mizusaki, T., & Tazaki, S. (2013). Variation in Displacement Energies Due to Isospin-Nonconserving Forces. *Phys. Rev. Lett.*, 110, 172505. https://doi.org/10.1103/PhysRevLett.110.172505

[Kankainen et al., 2008] Kankainen, A., Elomaa, V.-V., Batist, L., Eliseev, S., Eronen, T., Hager, U., Hakala, J., Jokinen, A., Moore, I. D., Novikov, Y. N., Penttilä, H., Popov, A., Rahaman, S., Rinta-Antila, S., Rissanen, J., et al. (2008). Mass measurements and implications for the energy of the high-spin isomer in ^{94}Ag. *Phys. Rev. Lett.*, 101, 142503. https://doi.org/10.1103/PhysRevLett.101.142503

[Kankainen et al., 2013] Kankainen, A., Hakala, J., Eronen, T., Gorelov, D., Jokinen, A., Kolhinen, V. S., Moore, I. D., Penttilä, H., Rinta-Antila, S., Rissanen, J., Saastamoinen, A., Sonnenschein, V., & Äystö, J. (2013). Isomeric states close to doubly magic ^{132}Sn studied with the double Penning trap JYFLTRAP. *Phys. Rev. C*, 87, 024307. https://doi.org/10.1103/PhysRevC.87.024307

[Kankainen et al., 2012] Kankainen, A., Novikov, Y. N., Oinonen, M., Batist, L., Elomaa, V.-V., Eronen, T., Hakala, J., Jokinen, A., Karvonen, P., Reponen, M., Rissanen, J., Saastamoinen, A., Vorobjev, G., Weber, C., & Äystö, J. (2012). Isomer and decay studies for the *rp* process at IGISOL. *Eur. Phys. J. A*, 48(4), 49. https://doi.org/10.1140/epja/i2012-12049-x

[Kast et al., 1996] Kast, D., Jungclaus, A., Harder, A., Lieb, K., Rudolph, D., Schubart, R., Grawe, H., Foltescu, D., Roth, H., Skeppstedt, Ö., Bearden, I., & Shizuma, T. (1996). First identification and shell model structure of ^{92}Rh. *Z. Phys. A*, 356, 363–365. https://doi.org/10.1007/BF02769240

[Kellerbauer et al., 2003] Kellerbauer, A., Blaum, K., Bollen, G., Herfurth, F., Kluge, H.-J., Kuckein, M., Sauvan, E., Scheidenberger, C., & Schweikhard, L. (2003). From direct to absolute mass measurements: A study of the accuracy of ISOLTRAP. *Eur. Phys. J. D*, 22, 53–64. https://doi.org/10.1140/epjd/e2002-00222-0

[Kienle et al., 2001] Kienle, P., Faestermann, T., Friese, J., Körner, H.-J., Münch, M., Schneider, R., Stolz, A., Wefers, E., Geissel, H., Münzenberg, G., Schlegel, C., Sümmerer, K., Weick, H., Hellström, M., & Thirolf, P. (2001). Synthesis and halflives of heavy nuclei relevant for the rp-process. *Prog. Part. Nucl. Phys.*, 46(1), 73–78. https://doi.org/10.1016/S0146-6410(01)00109-0

[Kirchner, 1992] Kirchner, R. (1992). On the release and ionization efficiency of catcher-ion-source systems in isotope separation on-line. *Nucl. Instrum. Methods B*, 70(1), 186–199. https://doi.org/https://doi.org/10.1016/0168-583X(92)95930-P

[Klochko & Smirnova, 2021] Klochko, O. & Smirnova, N. A. (2021). Isobaric-multiplet mass equation in a macroscopic-microscopic approach. *Phys. Rev. C*, 103, 024316. https://doi.org/10.1103/PhysRevC.103.024316

[Kondev et al., 2021] Kondev, F. G., Wang, M., Huang, W. J., Naimi, S., & Audi, G. (2021). The NUBASE2020 evaluation of nuclear physics properties. *Chin. Phys. C*, 45(3), 030001. https://doi.org/10.1088/1674-1137/abddae

[Koura et al., 2005] Koura, H., Tachibana, T., Uno, M., & Yamada, M. (2005). Nuclidic Mass Formula on a Spherical Basis with an Improved Even-Odd Term. *Prog. Theor. Phys.*, 113(2), 305–325. https://doi.org/10.1143/PTP.113.305

[Kripkó-Koncz et al., 2025] Kripkó-Koncz, G., Plaß, W., Dedes, I., Dao, D., Dickel, T., Hornung, C., Amanbayev, D., Ayet San Andrés, S., Beck, S., Bergmann, J., Blazhev, A., Dudek, J., Geissel, H., Haettner, E., Kalantar-Nayestanaki, N., et al. (2025). *Direct Mass Measurement of ^{93}Pd and Implications for the Isomer Structures in ^{94}Ag: Tracing the Two-proton Decay Branch.* (submitted).

[Kubo, 2003] Kubo, T. (2003). In-flight RI beam separator BigRIPS at RIKEN and elsewhere in Japan. *Nucl. Instrum. Methods B*, 204, 97–113. https://doi.org/10.1016/S0168-583X(02)01896-7

[Kugler, 2000] Kugler, E. (2000). The ISOLDE facility. *Hyperfine Interact.*, 129, 23–42. https://doi.org/10.1023/A:1012603025802

[La Commara et al., 2002] La Commara, M., Schmidt, K., Grawe, H., Döring, J., Borcea, R., Galanopoulos, S., Górska, M., Harissopulos, S., Hellström, M., Janas, Z., Kirchner, R., Mazzocchi, C., Ostrowski, A. N., Plettner, C., Rainovski, G., et al. (2002). Beta decay of medium and high spin isomers in ^{94}Ag. *Nucl. Phys. A*, 708(3), 167–180. https://doi.org/10.1016/S0375-9474(02)01024-2

[Laidler, 1996] Laidler, K. J. (1996). A glossary of terms used in chemical kinetics, including reaction dynamics (IUPAC Recommendations 1996). *Pure and Applied Chemistry*, 68(1), 149–192. https://doi.org/10.1351/pac199668010149

[Lam et al., 2013] Lam, Y. H., Blank, B., Smirnova, N. A., Bueb, J. B., & Antony, M. S. (2013). The isobaric multiplet mass equation for $A \leq 71$ revisited. *At. Data Nucl. Data Tables*, 99(6), 680–703. https://doi.org/10.1016/j.adt.2012.11.002

[Landau & Lifsitz, 1977] Landau, L. D. & Lifsitz, E. M. (1977). Chapter VII - The Quasi-Classical Case. *Quantum Mechanics (Non-Relativistic Theory)*, 171. Pergamon Press, Oxford, (Third Edition ed.). https://doi.org/https://doi.org/10.1016/C2013-0-02793-4

[Leistenschneider et al., 2018] Leistenschneider, E., Reiter, M. P., Ayet San Andrés, S., Kootte, B., Holt, J. D., Navrátil, P., Babcock, C., Barbieri, C., Barquest, B. R., Bergmann, J., Bollig, J., Brunner, T., Dunling, E., Finlay, A., Geissel, H., et al. (2018). Dawning of the $n = 32$ shell closure seen through precision mass measurements of neutron-rich titanium isotopes. *Phys. Rev. Lett.*, 120, 062503. https://doi.org/10.1103/PhysRevLett.120.062503

[Lenzi et al., 2018] Lenzi, S. M., Bentley, M. A., Lau, R., & Diget, C. A. (2018). Isospin-symmetry breaking corrections for the description of triplet energy differences. *Phys. Rev. C*, 98, 054322. https://doi.org/10.1103/PhysRevC.98.054322

[Litvinov et al., 2005] Litvinov, Y., Geissel, H., Radon, T., Attallah, F., Audi, G., Beckert, K., Bosch, F., Falch, M., Franzke, B., Hausmann, M., Hellström, M., Kerscher, T., Klepper, O., Kluge, H.-J., Kozhuharov, C., et al. (2005). Mass measurement of cooled neutron-deficient bismuth projectile fragments with time-resolved Schottky mass spectrometry at the FRS-ESR facility. *Nucl. Phys. A*, 756(1), 3–38. https://doi.org/https://doi.org/10.1016/j.nuclphysa.2005.03.015

[Liu et al., 2025] Liu, B., Brodeur, M., Clark, J. A., Dedes, I., Dudek, J., Kondev, F. G., Ray, D., Savard, G., Valverde, A. A., Baran, A., Burdette, D. P., Houff, A. M., Orford, R., Porter, W. S., Rivero, F., et al. (2025). Precise mass measurement of the longest odd-odd chain of nuclei with 1^+ ground states. *Phys. Rev. C*, 111, 034308. https://doi.org/10.1103/PhysRevC.111.034308

[Lorusso et al., 2012] Lorusso, G., Becerril, A., Amthor, A., Baumann, T., Bazin, D., Berryman, J. S., Brown, B. A., Cyburt, R. H., Crawford, H. L., Estrade, A., Gade, A., Ginter, T., Guess, C. J., Hausmann, M., Hitt, G. W., et al. (2012). β-delayed proton emission in the ^{100}Sn region. *Phys. Rev. C*, 86, 014313. https://doi.org/10.1103/PhysRevC.86.014313

[Lubos, 2016] Lubos, D. (2016). *Decay Spectroscopy of* ^{100}Sn *and Neighboring Nuclei*. Technische Universität München. https://mediatum.ub.tum.de/1327650

[Lunney, 2008] Lunney, D. (2008). *The legacy of A.H. Wapstra and the future of the Atomic Mass Evaluation*. arXiv:2211.10496v1 [nucl-ex] (2008).

[Lunney, 2015] Lunney, D. (2015). Advances in radioactive-isotope science from mass measurements. *JPS Conf. Proc.*, 6, 010018. Proceedings of the Conference on Advances in Radioactive Isotope Science (ARIS2014). https://doi.org/10.7566/JPSCP.6.010018

[Lunney, 2019] Lunney, D. (2019). New mass measurements with trapped (radioactive) ions and related fundamental physics. *Hyperfine Interact.*, 240, 48. https://doi.org/10.1007/s10751-019-1581-z

[Lykiardopoulou et al., 2023] Lykiardopoulou, E. M., Audi, G., Dickel, T., Huang, W. J., Lunney, D., Plaß, W. R., Reiter, M. P., Dilling, J., & Kwiatkowski, A. A. (2023). Exploring the limits of existence of proton-rich nuclei in the $Z = 70 - 82$ region. *Phys. Rev. C*, 107, 024311. https://doi.org/10.1103/PhysRevC.107.024311

[Lykiardopoulou et al., 2025] Lykiardopoulou, E. M., Walls, C., Bergmann, J., Brodeur, M., Brown, C., Cardona, J., Czihaly, A., Dickel, T., Duguet, T., Ebran, J.-P., Frosini, M., Hockenbery, Z., Holt, J. D., Jacobs, A., Kakkar, S., et al. (2025). Refined Topology of the $N = 20$ Island of Inversion with High Precision Mass Measurements of $^{31-33}$Na and $^{31-35}$Mg. *Phys. Rev. Lett.*, 134, 052503. https://doi.org/10.1103/PhysRevLett.134.052503

[Macchiavelli et al., 2000] Macchiavelli, A. O., Fallon, P., Clark, R. M., Cromaz, M., Deleplanque, M. A., Diamond, R. M., Lane, G. J., Lee, I. Y., Stephens, F. S., Svensson, C. E., Vetter, K., & Ward, D. (2000). Is there np pairing in $N = Z$ nuclei? *Phys. Rev. C*, 61, 041303. https://doi.org/10.1103/PhysRevC.61.041303

[MacCormick & Audi, 2014] MacCormick, M. & Audi, G. (2014). Evaluated experimental isobaric analogue states from T=1/2 to T=3 and associated IMME coefficients. *Nucl. Phys. A*, 925, 61–95. https://doi.org/10.1016/j.nuclphysa.2014.01.007

[Machleidt & Slaus, 2001] Machleidt, R. & Slaus, I. (2001). The nucleon-nucleon interaction. *J. Phys. G Nucl. Part. Phys.*, 27(5), R69. https://doi.org/10.1088/0954-3899/27/5/201

[Maglione et al., 1998] Maglione, E., Ferreira, L. S., & Liotta, R. J. (1998). Nucleon decay from deformed nuclei. *Phys. Rev. Lett.*, 81, 538–541. https://doi.org/10.1103/PhysRevLett.81.538

[Manea et al., 2023] Manea, V., Mougeot, M., & Lunney, D. (2023). The empirical shell gap revisited in light of recent high precision mass spectrometry data. *Eur. Phys. J. A*, 59, 22. https://doi.org/10.1140/epja/s10050-023-00929-5

[Manion et al., 2024] Manion, J. A., Huie, R. E., Levin, R. D., Burgess Jr., D. R., Orkin, V. L., Tsang, W., McGivern, W. S., Hudgens, J. W., Knyazev, V. D., Atkinson, D. B., Chai, E., Tereza, A. M., Lin, C.-Y., Allison, T. C., Mallard, W. G., et al. (2024). *NIST Chemical Kinetics Database, NIST Standard Reference Database 17, Version 7.0 (Web Version), Release 1.6.8, Data version 2024*. Web address: https://kinetics.nist.gov/kinetics/.

[Manufacturers & Products, 2025] Manufacturers & Products (2025). *List of products, manufacturers and corresponding websites relevant for this thesis.*
HVD5-A50M-050-05 Ultra-Precision Voltage Divider [CADDOCK, Roseburg, USA]
https://www.caddock.com/online-catalog/voltage-dividers-networks/voltage-dividers-networks.html
LabJack T7-Pro analog-to-digital converter [LabJack Corporation, Lakewood, USA]
https://labjack.com/collections/daq-devices
MCS6A time-to-digital converter [FAST ComTec GmbH, Oberhaching, Germany]
https://www.fastcomtec.com/ftp/manuals/mcs6adoc.pdf
TF930 frequency counter [TME Germany GmbH, Leipzig, Germany]
https://www.tme.eu/de/details/tf930/generatoren-und-frequenzmesser/aim-tti/
OCXO AOCJY1A-10.000MHZ and AOC2012VAJC-10.0000C [ABRACON, Bee Cave, USA]
https://abracon.com/product-lineup/frequency-control-timing-devices/oscillators/ocxo

Intel Core i7-13700K CPU [Intel Corporation, Santa Calra, USA] (website link)
Intel Xeon W-2123 CPU [Intel Corporation, Santa Calra, USA] (website link).

[Mardor et al., 2021] Mardor, I., Ayet San Andrés, S., Dickel, T., Amanbayev, D., Beck, S., Bergmann, J., Geissel, H., Gröf, L., Haettner, E., Hornung, C., Kalantar-Nayestanaki, N., Kripko-Koncz, G., Miskun, I., Mollaebrahimi, A., Plaß, W. R., et al. (2021). Mass measurements of As, Se, and Br nuclei, and their implication on the proton-neutron interaction strength toward the $N = Z$ line. *Phys. Rev. C*, 103, 034319. https://doi.org/10.1103/PhysRevC.103.034319

[Mardor et al., 2020] Mardor, I., Dickel, T., Amanbayev, D., Ayet San Andrés, S., Beck, S., Benyamin, D., Bergmann, J., Constantin, P., Cléroux Cuillerier, A., Geissel, H., Gröff, L., Hornung, C., Kripko-Koncz, G., Mollaebrahimi, A., Miskun, I., et al. (2020). Determining spontaneous fission properties by direct mass measurements with the FRS Ion Catcher. *EPJ Web Conf.*, 239, 02004. https://doi.org/10.1051/epjconf/202023902004

[Mare & Petrovici, 2022] Mare, A. S. & Petrovici, A. (2022). Shape coexistence and isomeric states in ^{94}Pd within a beyond-mean-field approach. *Phys. Rev. C*, 106, 054306. https://doi.org/10.1103/PhysRevC.106.054306

[Marsh, 2014] Marsh, B. A. (2014). Resonance ionization laser ion sources for on-line isotope separators. *Rev. Sci. Instrum.*, 85(2), 02B923. https://doi.org/10.1063/1.4858015

[Massey, 1951] Massey, F. J. (1951). The kolmogorov-smirnov test for goodness of fit. *J. Am. Stat. Assoc.*, 46(253), 68–78. https://doi.org/10.1080/01621459.1951.10500769

[Matos et al., 2012] Matos, M., Estradé, A., Schatz, H., Bazin, D., Famiano, M., Gade, A., George, S., Lynch, W., Meisel, Z., Portillo, M., Rogers, A., Shapira, D., Stolz, A., Wallace, M., & Yurkon, J. (2012). Time-of-flight mass measurements of exotic nuclei. *Nucl. Instrum. Methods A*, 696, 171–179. https://doi.org/10.1016/j.nima.2012.08.104

[Mezilev et al., 1995] Mezilev, K. A., Novikov, Y. N., Popov, A. V., Fogelberg, B., & Spanier, L. (1995). Experimental masses at doubly magic nuclide ^{132}Sn. *Phys. Scr.*, 1995(T56), 272. https://doi.org/10.1088/0031-8949/1995/T56/047

[Michimasa et al., 2018] Michimasa, S., Kobayashi, M., Kiyokawa, Y., Ota, S., Ahn, D. S., Baba, H., Berg, G. P. A., Dozono, M., Fukuda, N., Furuno, T., Ideguchi, E., Inabe, N., Kawabata, T., Kawase, S., Kisamori, K., et al. (2018). Magic Nature of Neutrons in ^{54}Ca: First Mass Measurements of $^{55-57}$Ca. *Phys. Rev. Lett.*, 121, 022506. https://doi.org/10.1103/PhysRevLett.121.022506

[Misch & Mumpower, 2024] Misch, G. W. & Mumpower, M. R. (2024). Astromers: status and prospects. *Eur. Phys. J. Spec. Top.*, 233, 1075–1099. https://doi.org/10.1140/epjs/s11734-024-01136-z

[Misch et al., 2021] Misch, G. W., Sprouse, T. M., & Mumpower, M. R. (2021). Astromers in the Radioactive Decay of r-process Nuclei. *Astrophys. J. Lett.*, 913(1), L2. https://doi.org/10.3847/2041-8213/abfb74

[Miskun, 2019] Miskun, I. (2019). *A novel method for the measurement of half-lives and decay branching ratios of exotic nuclei with the FRS Ion Catcher*. Universität Gießen. http://geb.uni-giessen.de

[Miskun et al., 2019] Miskun, I., Dickel, T., Mardor, I., Hornung, C., Amanbayev, D., Ayet San Andrés, S., Bergmann, J., Ebert, J., Geissel, H., Górska, M., Greiner, F., Haettner, E., Plaß, W. R., Purushothaman, S., Scheidenberger, C., et al. (2019). A novel method for the measurement of half-lives and decay branching ratios of exotic nuclei. *Eur. Phys. J. A*, 55(9), 148. https://doi.org/10.1140/epja/i2019-12837-8

[Mollaebrahimi et al., 2023a] Mollaebrahimi, A., Amanbayev, D., Andrés, S. A. S., Beck, S., Bergmann, J., Dickel, T., Geissel, H., Hornung, C., Kalantar-Nayestanaki, N., Kripko-Koncz, G., Miskun, I., Nichita, D., Plaß, W., Pohjalainen, I., Scheidenberger, C., et al. (2023a). Recent Upgrades of the Gas Handling System for the Cryogenic Stopping Cell of the FRS Ion Catcher. *Nucl. Instrum. Methods A*, 1055, 168554. https://doi.org/10.1016/j.nima.2023.168554

[Mollaebrahimi et al., 2025] Mollaebrahimi, A., Constantin, P., Dickel, T., Amanbayev, D., Glöckner, S., Haettner, E., Kar, D., Kripko-Koncz, G., Kumar, D., Mahajan, K., Mardor, I., Morrissey, D., Narang, M., Plaß, W. R., Shrayer, A., et al. (2025). First observation of MNT isotope beams at the FRS Ion Catcher. *Nucl. Phys. A*, 1057, 123041. https://doi.org/10.1016/j.nuclphysa.2025.123041

[Mollaebrahimi et al., 2023b] Mollaebrahimi, A., Hornung, C., Dickel, T., Amanbayev, D., Kripko-Koncz, G., Plaß, W. R., Ayet San Andrés, S., Beck, S., Blazhev, A., Bergmann, J., Geissel, H., Górska, M., Grawe, H., Greiner, F., Haettner, E., et al. (2023b). Studying Gamow-Teller transitions and the assignment of isomeric and ground states at $N = 50$. *Phys. Lett. B*, 839, 137833. https://doi.org/10.1016/j.physletb.2023.137833

[Möller et al., 2016] Möller, P., Sierk, A., Ichikawa, T., & Sagawa, H. (2016). Nuclear ground-state masses and deformations: FRDM(2012). *At. Data Nucl. Data Tables*, 109-110, 1–204. https://doi.org/10.1016/j.adt.2015.10.002

[Moschner et al., 2015] Moschner, K., Blazhev, A., Warr, N., Boutachkov, P., Davies, P., Wadsworth, R., Ameil, F., Baba, H., Bäck, T., Dewald, M., Doornenbal, P., Faestermann, T., Gengelbach, A., Gerl, J., Gernhäuser, R., et al. (2015). Study of ground and excited state decays in N≈Z Ag nuclei. *EPJ Web Conf.*, 93, 01024. https://doi.org/10.1051/epjconf/20159301024

[Mougeot, 2015] Mougeot, X. (2015). Reliability of usual assumptions in the calculation of β and ν spectra. *Phys. Rev. C*, 91, 055504. https://doi.org/10.1103/PhysRevC.91.055504

[Mougeot, 2017] Mougeot, X. (2017). BetaShape: A new code for improved analytical calculations of beta spectra. *EPJ Web Conf.*, 146, 12015. Software available online at http://www.lnhb.fr/rd-activities/spectrum-processing-software/. https://doi.org/10.1051/epjconf/201714612015

[Mougeot, 2019] Mougeot, X. (2019). Towards high-precision calculation of electron capture decays. *Appl. Radiat. Isot.*, 154, 108884. https://doi.org/10.1016/j.apradiso.2019.108884

[Mougeot et al., 2024] Mougeot, X., Äystö, J., Plaß, W., & Kripkó-Koncz, G. (2023-2024). *Different mass estimates of odd-odd $N = Z$ nuclei with emphasis on the ^{94}Ag ground state mass.* (private communication, internal report).

[Mukha et al., 2004] Mukha, I., Batist, L., Roeckl, E., Grawe, H., Döring, J., Blazhev, A., Hoffman, C. R., Janas, Z., Kirchner, R., La Commara, M., Dean, S., Mazzocchi, C., Plettner, C., Tabor, S. L., & Wiedeking, M. (2004). β-delayed proton decay of a high-spin isomer in ^{94}Ag. *Phys. Rev. C*, 70, 044311. https://doi.org/10.1103/PhysRevC.70.044311

[Mukha et al., 2008] Mukha, I., Grawe, H., Roeckl, E., & Tabor, S. (2008). Comment on "Level structure of ^{92}Rh: Implications for the two-proton decay of ^{94}Ag^{m}". *Phys. Rev. C*, 78, 039803. https://doi.org/10.1103/PhysRevC.78.039803

[Mukha et al., 2006] Mukha, I., Roeckl, E., Batist, L., Blazhev, A., Döring, J., Grawe, H., Grigorenko, L., Huyse, M., Janas, Z., Kirchner, R., La Commara, M., Mazzocchi, C., Tabor, S. L., & Van Duppen, P. (2006). Proton-proton correlations observed in two-proton radioactivity of ^{94}Ag. *Nature*, 439, 298–302. https://doi.org/10.1038/nature04453

[Mukha et al., 2005] Mukha, I., Roeckl, E., Döring, J., Batist, L., Blazhev, A., Grawe, H., Hoffman, C. R., Huyse, M., Janas, Z., Kirchner, R., La Commara, M., Mazzocchi, C., Plettner, C., Tabor, S. L., Van Duppen, P., et al. (2005). Observation of proton radioactivity of the (21^{+}) high-spin isomer in ^{94}Ag. *Phys. Rev. Lett.*, 95, 022501. https://doi.org/10.1103/PhysRevLett.95.022501

[Mukha et al., 2010] Mukha, I., Roeckl, E., Grawe, H., & Tabor, S. (2010). *Comment on "Reviewing the evidence for two-proton emission from the high-spin isomer in ^{94}Ag"*. arXiv:1008.5346v1 [nucl-ex] (2010).

[Mukul et al., 2020] Mukul, I., Andreoiu, C., Brodeur, M., Brunner, T., Dietrich, K., Dickel, T., Dillmann, I., Dunling, E., Fusco, D., Gwinner, G., Izzo, C., Jacobs, A., Kootte, B., Lan, Y., Leistenschneider, E., et al. (2020). Measuring the half-life of n-rich ^{100}Rb with the TITAN MR-TOF-MS. *Journal of Physics: Conference Series*, 1643(1), 012057. https://doi.org/10.1088/1742-6596/1643/1/012057

[Mumpower et al., 2016] Mumpower, M., Surman, R., McLaughlin, G., & Aprahamian, A. (2016). The impact of individual nuclear properties on r-process nucleosynthesis. *Prog. Part. Nucl. Phys.*, 86, 86–126. https://doi.org/10.1016/j.ppnp.2015.09.001

[Münzenberg et al., 1979] Münzenberg, G., Faust, W., Hofmann, S., Armbruster, P., Güttner, K., & Ewald, H. (1979). The velocity filter ship, a separator of unslowed heavy ion fusion products. *Nucl. Instrum. Methods*, 161(1), 65–82. https://doi.org/10.1016/0029-554X(79)90362-8

[Mutschler et al., 2017] Mutschler, A., Lemasson, A., Sorlin, O., Bazin, D., Borcea, C., Borcea, R., Dombrádi, Z., Ebran, J.-P., Gade, A., Iwasaki, H., Khan, E., Lepailleur, A., Recchia, F., Roger, T., Rotaru, F., et al. (2017). A proton density bubble in the doubly magic ^{34}Si nucleus. *Nature Physics*, 13, 152–156. https://doi.org/10.1038/nphys3916

[Myers, 2024] Myers, E. G. (2024). Progress in High-Precision Mass Measurements of Light Ions. *Atoms*, 12(2). https://doi.org/10.3390/atoms12020008

[Nara Singh et al., 2012] Nara Singh, B. S., Brock, T. S., Wadsworth, R., Grawe, H., Boutachkov, P., Braun, N., Blazhev, A., Liu, Z., Górska, M., Pietri, S., Rudolph, D., Domingo-Pardo, C., Steer, S. J., Ataç, A., Bettermann, L., et al. (2012). Influence of the *np* interaction on the β decay of ^{94}Pd. *Phys. Rev. C*, 86, 041301. https://doi.org/10.1103/PhysRevC.86.041301

[Nara Singh et al., 2011] Nara Singh, B. S., Liu, Z., Wadsworth, R., Grawe, H., Brock, T. S., Boutachkov, P., Braun, N., Blazhev, A., Górska, M., Pietri, S., Rudolph, D., Domingo-Pardo, C., Steer, S. J., Ataç, A., Bettermann, L., et al. (2011). 16^{+} Spin-Gap Isomer in ^{96}Cd. *Phys. Rev. Lett.*, 107, 172502. https://doi.org/10.1103/PhysRevLett.107.172502

[Narang, 2024] Narang, M. (2023-2024). *Analysis of broadband mass measurements of ^{252}Cf fission products performed in 2023 using the short DC Cage of the CSC at the FRS-IC.* (private communication).

[Nesterenko et al., 2020] Nesterenko, D., Kankainen, A., Kostensalo, J., Nobs, C., Bruce, A., Beliuskina, O., Canete, L., Eronen, T., Gamba, E., Geldhof, S., de Groote, R., Jokinen, A., Kurpeta, J., Moore, I., Morrison, L., et al. (2020). Three beta-decaying states in ^{128}In and ^{130}In resolved for the first time using Penning-trap techniques. *Phys. Lett. B*, 808, 135642. https://doi.org/https://doi.org/10.1016/j.physletb.2020.135642

[Neufcourt et al., 2020] Neufcourt, L., Cao, Y., Giuliani, S., Nazarewicz, W., Olsen, E., & Tarasov, O. B. (2020). Beyond the proton drip line: Bayesian analysis of proton-emitting nuclei. *Phys. Rev. C*, 101, 014319. https://doi.org/10.1103/PhysRevC.101.014319

[Nies et al., 2023] Nies, L., Atanasov, D., Athanasakis-Kaklamanakis, M., Au, M., Blaum, K., Dobaczewski, J., Hu, B. S., Holt, J. D., Karthein, J., Kulikov, I., Litvinov, Y. A., Lunney, D., Manea, V., Miyagi, T., Mougeot, M., et al. (2023). Isomeric Excitation Energy for $^{99}In^{m}$ from Mass Spectrometry Reveals Constant Trend Next to Doubly Magic ^{100}Sn. *Phys. Rev. Lett.*, 131, 022502. https://doi.org/10.1103/PhysRevLett.131.022502

[Nolden et al., 2004] Nolden, F., Beckert, K., Beller, P., Franzke, B., Peschke, C., & Steck, M. (2004). Experience and prospects of stochastic cooling of radioactive beams at GSI. *Nucl. Instrum. Methods A*, 532(1), 329–334. https://doi.org/10.1016/j.nima.2004.06.062

[Nolen & Schiffer, 1969] Nolen, J. & Schiffer, J. (1969). Coulomb Energies. *Annu. Rev. Nucl. Sci.*, 19(1), 471–526. https://doi.org/10.1146/annurev.ns.19.120169.002351

[Nowacki, 2002] Nowacki, F. (2002). Shell model description of correlations in ^{56}Ni and ^{100}Sn. *Nucl. Phys. A*, 704(1), 223–231. RIKEN Symposium Shell Model 2000. https://doi.org/https://doi.org/10.1016/S0375-9474(02)00782-0

[Nowacki et al., 2021] Nowacki, F., Obertelli, A., & Poves, A. (2021). The neutron-rich edge of the nuclear landscape: Experiment and theory. *Prog. Part. Nucl. Phys.*, 120, 103866. https://doi.org/10.1016/j.ppnp.2021.103866

[Park, 2017] Park, J. (2017). *Decay spectroscopy of* N $\sim$ Z *nuclei in the vicinity of* ^{100}Sn. University of British Columbia. https://doi.org/http://dx.doi.org/10.14288/1.0343436

[Park et al., 2017] Park, J., Krücken, R., Lubos, D., Gernhäuser, R., Lewitowicz, M., Nishimura, S., Ahn, D. S., Baba, H., Blank, B., Blazhev, A., Boutachkov, P., Browne, F., Čeliković, I., de France, G., Doornenbal, P., et al. (2017). Properties of γ-decaying isomers and isomeric ratios in the ^{100}Sn region. *Phys. Rev. C*, 96, 044311. https://doi.org/10.1103/PhysRevC.96.044311

[Park et al., 2019] Park, J., Krücken, R., Lubos, D., Gernhäuser, R., Lewitowicz, M., Nishimura, S., Ahn, D. S., Baba, H., Blank, B., Blazhev, A., Boutachkov, P., Browne, F., Čeliković, I., de France, G., Doornenbal, P., et al. (2019). New and comprehensive β- and βp-decay spectroscopy results in the vicinity of ^{100}Sn. *Phys. Rev. C*, 99, 034313. https://doi.org/10.1103/PhysRevC.99.034313

[Peaslee, 1954] Peaslee, D. C. (1954). Coulomb Energies of Light Nuclei. *Phys. Rev.*, 95, 717–723. https://doi.org/10.1103/PhysRev.95.717

[Pechenaya et al., 2007] Pechenaya, O. L., Chiara, C. J., Sarantites, D. G., Reviol, W., Charity, R. J., Carpenter, M. P., Janssens, R. V. F., Lauritsen, T., Lister, C. J., Seweryniak, D., Zhu, S., Andersson, L.-L., Johansson, E. K., & Rudolph, D. (2007). Level structure of ^{92}Rh: Implications for the two-proton decay of ^{94}Ag^{m}. *Phys. Rev. C*, 76, 011304. https://doi.org/10.1103/PhysRevC.76.011304

[Pechenaya et al., 2008] Pechenaya, O. L., Sarantites, D. G., Reviol, W., Chiara, C. J., Janssens, R. V. F., Lister, C. J., & Seweryniak, D. (2008). Reply to "Comment on 'Level structure of ^{92}Rh: Implications for the two-proton decay of ^{94}Ag^{m}' ". *Phys. Rev. C*, 78, 039804. https://doi.org/10.1103/PhysRevC.78.039804

[Pfützner et al., 2023] Pfützner, M., Mukha, I., & Wang, S. (2023). Two-proton emission and related phenomena. *Prog. Part. Nucl. Phys.*, 132, 104050. https://doi.org/https://doi.org/10.1016/j.ppnp.2023.104050

[Piechaczek et al., 2003] Piechaczek, A., Zganjar, E. F., Ball, G. C., Bricault, P., D'Auria, J. M., Hardy, J. C., Hodgson, D. F., Iacob, V., Klages, P., Kulp, W. D., Leslie, J. R., Lipoglavsek, M., Macdonald, J. A., Mak, H.-B., Moltz, D. M., et al. (2003). High precision branching ratio measurement for the superallowed β decay of ^{74}Rb : A prerequisite for exacting tests of the standard model. *Phys. Rev. C*, 67, 051305. https://doi.org/10.1103/PhysRevC.67.051305

[Piersa et al., 2019] Piersa, M., Korgul, A., Fraile, L. M., Benito, J., Adamska, E., Andreyev, A. N., Álvarez-Rodríguez, R., Barzakh, A. E., Benzoni, G., Berry, T., Borge, M. J. G., Carmona, M., Chrysalidis, K., Correia, J. G., Costache, C., et al. (2019). β decay of ^{133}In: γ emission from neutron-unbound states in ^{133}Sn. *Phys. Rev. C*, 99, 024304. https://doi.org/10.1103/PhysRevC.99.024304

[Plaß et al., 2019] Plaß, W., Dickel, T., Mardor, I., Pietri, S., Geissel, H., Scheidenberger, C., Amanbayev, D., Ayet San Andrés, S., Äystö, J., Balabanski, D., Beck, S., Bergmann, J., Charviakova, V., Constantin, P., Eronen, T., et al. (2019). The science case of the FRS Ion Catcher for FAIR Phase-0. *Hyperfine Interact.*, 240, 73. https://doi.org/10.1007/s10751-019-1597-4

[Plaß et al., 2008] Plaß, W. R., Dickel, T., Czok, U., Geissel, H., Petrick, M., Reinheimer, K., Scheidenberger, C., & Yavor, M. (2008). Isobar separation by time-of-flight mass spectrometry for low-energy radioactive ion beam facilities. *Nucl. Instrum. Methods B*, 266(19-20), 4560–4564. https://doi.org/10.1016/j.nimb.2008.05.079

[Plaß et al., 2013a] Plaß, W. R., Dickel, T., Purushothaman, S., Dendooven, P., Geissel, H., Ebert, J., Haettner, E., Jesch, C., Ranjan, M., Reiter, M., Weick, H., Amjad, F., Ayet, S., Diwisch, M., Estrade, A., et al. (2013a). The FRS Ion Catcher – A facility for high-precision experiments with stopped projectile and fission fragments. *Nucl. Instrum. Methods B*, 317, 457–462. https://doi.org/10.1016/j.nimb.2013.07.063

[Plaß et al., 2013b] Plaß, W. R., Dickel, T., & Scheidenberger, C. (2013b). Multiple-reflection time-of-flight mass spectrometry. *Int. J. Mass Spectrom.*, 349-350, 134–144. https://doi.org/10.1016/j.ijms.2013.06.005

[Plettner et al., 2004] Plettner, C., Grawe, H., Mukha, I., Döring, J., Nowacki, F., Batist, L., Blazhev, A., Hoffman, C. R., Janas, Z., Kirchner, R., La Commara, M., Mazzocchi, C., Roeckl, E., Schwengner, R., Tabor, S. L., et al. (2004). On the β-decaying (21^{+}) spin gap isomer in ^{94}Ag. *Nucl. Phys. A*, 733(1), 20–36. https://doi.org/10.1016/j.nuclphysa.2003.12.014

[Pohjalainen, 2018] Pohjalainen, I. (2018). *Gas-phase chemistry, recoil source characterization and in-gas-cell resonance laser ionization of actinides at IGISOL.* University of Jyväskylä. https://jyx.jyu.fi/handle/123456789/58547

[Porter et al., 2022] Porter, W. S., Ashrafkhani, B., Bergmann, J., Brown, C., Brunner, T., Cardona, J. D., Curien, D., Dedes, I., Dickel, T., Dudek, J., Dunling, E., Gwinner, G., Hockenbery, Z., Holt, J. D., Hornung, C., et al. (2022). Mapping the $N = 40$ island of inversion: Precision mass measurements of neutron-rich Fe isotopes. *Phys. Rev. C*, 105, L041301. https://doi.org/10.1103/PhysRevC.105.L041301

[Pruet et al., 2006] Pruet, J., Hoffman, R. D., Woosley, S. E., Janka, H.-T., & Buras, R. (2006). Nucleosynthesis in Early Supernova Winds. II. The Role of Neutrinos. *Astrophys. J.*, 644(2), 1028. https://doi.org/10.1086/503891

[Purushothaman et al., 2017] Purushothaman, S., Ayet San Andrés, S., Bergmann, J., Dickel, T., Ebert, J., Geissel, H., Hornung, C., Plaß, W. R., Rappold, C., Scheidenberger, C., Tanaka, Y. K., & Yavor, M. I. (2017). Hyper-EMG: A new probability distribution function composed of Exponentially Modified Gaussian distributions to analyze asymmetric peak shapes in high-resolution time-of-flight mass spectrometry. *Int. J. Mass Spectrom.*, 421, 245–254. https://doi.org/10.1016/j.ijms.2017.07.014

[Purushothaman et al., 2013] Purushothaman, S., Reiter, M. P., Haettner, E., Dendooven, P., Dickel, T., Geissel, H., Ebert, J., Jesch, C., Plaß, W. R., Ranjan, M., Weick, H., Amjad, F., Ayet, S., Diwisch, M., Estrade, A., et al. (2013). First experimental results of a cryogenic stopping cell with short-lived, heavy uranium fragments produced at 1000 MeV/u. *Europhys. Lett.*, 104(4), 42001. https://doi.org/10.1209/0295-5075/104/42001

[R Core Team, 2021] R Core Team (2021). *R: A Language and Environment for Statistical Computing.* R Foundation for Statistical Computing, Vienna, Austria. http://www.R-project.org/

[Raeder et al., 2014] Raeder, S., Heggen, H., Lassen, J., Ames, F., Bishop, D., Bricault, P., Kunz, P., Mjøs, A., & Teigelhöfer, A. (2014). An ion guide laser ion source for isobar-suppressed rare isotope beams. *Rev. Sci. Instrum.*, 85(3). https://doi.org/10.1063/1.4868496

[Ranjan et al., 2015] Ranjan, M., Dendooven, P., Purushothaman, S., Dickel, T., Reiter, M., Ayet San Andrés, S., Haettner, E., Moore, I., Kalantar-Nayestanaki, N., Geissel, H., Plaß, W., Schäfer, D., Scheidenberger, C., Schreuder, F., Timersma, H., et al. (2015). Design, construction and cooling system performance of a prototype cryogenic stopping cell for the Super-FRS at FAIR. *Nucl. Instrum. Methods A*, 770(Supplement C), 87–97. https://doi.org/10.1016/j.nima.2014.09.075

[Ranjan et al., 2011] Ranjan, M., Purushothaman, S., Dickel, T., Geissel, H., Plaß, W. R., Schäfer, D., Scheidenberger, C., de Walle, J. V., Weick, H., & Dendooven, P. (2011). New stopping cell capabilities: RF carpet performance at high gas density and cryogenic operation. *Europhys. Lett.*, 96(5), 52001. https://doi.org/10.1209/0295-5075/96/52001

[Reed et al., 2010] Reed, M. W., Cullen, I. J., Walker, P. M., Litvinov, Y. A., Blaum, K., Bosch, F., Brandau, C., Carroll, J. J., Cullen, D. M., Deo, A. Y., Detwiller, B., Dimopoulou, C., Dracoulis, G. D., Farinon, F., Geissel, H., et al. (2010). Discovery of Highly Excited Long-Lived Isomers in Neutron-Rich Hafnium and Tantalum Isotopes through Direct Mass Measurements. *Phys. Rev. Lett.*, 105, 172501. https://doi.org/10.1103/PhysRevLett.105.172501

[Reinhard et al., 2006] Reinhard, P.-G., Bender, M., Nazarewicz, W., & Vertse, T. (2006). From finite nuclei to the nuclear liquid drop: Leptodermous expansion based on self-consistent mean-field theory. *Phys. Rev. C*, 73, 014309. https://doi.org/10.1103/PhysRevC.73.014309

[Reiter et al., 2020] Reiter, M., Ames, F., Andreoiu, C., Ayet San Andrés, S., Babcock, C., Barquest, B., Bergmann, J., Bollig, J., Brunner, T., Dickel, T., Dilling, J., Dillmann, I., Dunling, E., Finlay, A., Gwinner, G., et al. (2020). Improved beam diagnostics and optimization at ISAC via TITAN's MR-TOF-MS. *Nucl. Instrum. Methods B*, 463, 431–436. https://doi.org/10.1016/j.nimb.2019.04.034

[Reiter et al., 2016] Reiter, M., Rink, A.-K., Dickel, T., Haettner, E., Heiße, F., Plaß, W., Purushothaman, S., Amjad, F., Ayet San Andrés, S., Bergmann, J., Blum, D., Dendooven, P., Diwisch, M., Ebert, J., Geissel, H., et al. (2016). Rate capability of a cryogenic stopping cell for uranium projectile fragments produced at 1000 MeV/u. *Nucl. Instrum. Methods B*, 376, 240–245. https://doi.org/10.1016/j.nimb.2015.12.016

[Reiter, 2015] Reiter, M. P. (2015). *Pilot experiments with relativistic uranium projectile and fission fragments thermalized in a cryogenic gas-filled stopping cell.* Universität Gießen. http://geb.uni-giessen.de/geb/volltexte/2015/11827

[Reponen et al., 2021] Reponen, M., de Groote, R. P., Al Ayoubi, L., Beliuskina, O., Bissell, M. L., Campbell, P., Cañete, L., Cheal, B., Chrysalidis, K., Delafosse, C., Roubin, A., Devlin, C. S., Eronen, T., Garcia Ruiz, R. F., Geldhof, S., et al. (2021). Evidence of a sudden increase in the nuclear size of proton-rich silver-96. *Nat. Commun.*, 12, 4596. https://doi.org/10.1038/s41467-021-24888-x

[Reponen et al., 2015] Reponen, M., Moore, I. D., Pohjalainen, I., Rothe, S., Savonen, M., Sonnenschein, V., & Voss, A. (2015). An inductively heated hot cavity catcher laser ion source. *Rev. Sci. Instrum.*, 86, 123501. https://doi.org/10.1063/1.4936569

[Riisager, 1994] Riisager, K. (1994). Nuclear halo states. *Rev. Mod. Phys.*, 66, 1105–1116. https://doi.org/10.1103/RevModPhys.66.1105

[Rink, 2017] Rink, A.-K. (2017). *Mass and Life-time Measurement of the 1.7 ms 215-Po Isotope - A Crucial Test of the Novel Concept of the Cryogenic Ion Catcher for the Super-FRS at GSI-FAIR.* Universität Gießen.

[Rocchini et al., 2023] Rocchini, M., Garrett, P. E., Zielińska, M., Lenzi, S. M., Dao, D. D., Nowacki, F., Bildstein, V., MacLean, A. D., Olaizola, B., Ahmed, Z. T., Andreoiu, C., Babu, A., Ball, G. C., Bhattacharjee, S. S., Bidaman, H., et al. (2023). First Evidence of Axial Shape Asymmetry and Configuration Coexistence in ^{74}Zn: Suggestion for a Northern Extension of the $N = 40$ Island of Inversion. *Phys. Rev. Lett.*, 130, 122502. https://doi.org/10.1103/PhysRevLett.130.122502

[Roeckl & Mukha, 2013] Roeckl, E. & Mukha, I. (2013). Q values of radioactive decay: Examples from nuclear physics and related fields. *Int. J. Mass Spectrom.*, 349-350, 47–56. https://doi.org/10.1016/j.ijms.2013.03.021

[Sargent, 1933] Sargent, B. W. (1933). The maximum energy of the β-Rays from uranium X and other bodies. *Proc. R. Soc. London A*, 139, 659—-673. https://doi.org/10.1098/rspa.1933.0045

[Satula et al., 1997] Satula, W., Dean, D., Gary, J., Mizutori, S., & Nazarewicz, W. (1997). On the origin of the Wigner energy. *Phys. Lett. B*, 407(2), 103–109. https://doi.org/10.1016/S0370-2693(97)00711-9

[Satuła et al., 2012] Satuła, W., Dobaczewski, J., Nazarewicz, W., & Werner, T. R. (2012). Isospin-breaking corrections to superallowed Fermi β decay in isospin- and angular-momentum-projected nuclear density functional theory. *Phys. Rev. C*, 86, 054316. https://doi.org/10.1103/PhysRevC.86.054316

[Savajols, 2001] Savajols, H. (2001). The SPEG Mass Measurement Program at GANIL. *Hyperfine Interact.*, 132, 243–252. https://doi.org/10.1023/A:1011964401634

[Schatz et al., 2001] Schatz, H., Aprahamian, A., Barnard, V., Bildsten, L., Cumming, A., Ouellette, M., Rauscher, T., Thielemann, F.-K., & Wiescher, M. (2001). End Point of the *rp* Process on Accreting Neutron Stars. *Phys. Rev. Lett.*, 86, 3471–3474. https://doi.org/10.1103/PhysRevLett.86.3471

[Scheidenberger et al., 2003] Scheidenberger, C., Geissel, H., Maier, M., Münzenberg, G., Portillo, M., Savard, G., Van Duppen, P., Weick, H., Winkler, M., Yavor, M., Attallah, F., Behr, K.-H., Chichkine, V., Eliseev, S., Hausmann, M., et al. (2003). Energy and range focusing of in-flight separated exotic nuclei - A study for the energy-buncher stage of the low-energy branch of the Super-FRS. *Nucl. Instrum. Methods B*, 204, 119–123. https://doi.org/10.1016/S0168-583X(02)01898-0

[Scheidenberger et al., 1998] Scheidenberger, C., Stöhlker, T., Meyerhof, W., Geissel, H., Mokler, P., & Blank, B. (1998). Charge states of relativistic heavy ions in matter. *Nucl. Instrum. Methods B*, 142(4), 441–462. https://doi.org/10.1016/S0168-583X(98)00244-4

[Schlitt et al., 1997] Schlitt, B., Beckert, K., Bosch, F., Eickhoff, H., Franzke, B., Fujita, Y., Geissel, H., Hausmann, M., Irnich, H., Klepper, O., Kluge, H.-J., Kozhuharov, C., Kraus, G., Münzenberg, G., Nickel, F., et al. (1997). Schottky mass spectrometry at the ESR: a novel tool for precise direct mass measurements of exotic nuclei. *Nucl. Phys. A*, 626(1), 315–325. https://doi.org/10.1016/S0375-9474(97)00552-6

[Semchenkov et al., 2008] Semchenkov, A., Brüchle, W., Jäger, E., Schimpf, E., Schädel, M., Mühle, C., Klos, F., Türler, A., Yakushev, A., Belov, A., Belyakova, T., Kaparkova, M., Kukhtin, V., Lamzin, E., & Sytchevsky, S. (2008). The TransActinide Separator and Chemistry Apparatus (TASCA) at GSI – Optimization of ion-optical structures and magnet designs. *Nucl. Instrum. Methods B*, 266(19), 4153–4161. https://doi.org/10.1016/j.nimb.2008.05.132

[Sensharma, 2021] Sensharma, N. (2021). *Wobbling Motion in Nuclei: Transverse, Longitudinal and Chiral*. University of Notre Dame. https://doi.org/10.7274/mg74qj7626t

[Sobiczewski & Litvinov, 2014] Sobiczewski, A. & Litvinov, Y. A. (2014). Accuracy of theoretical descriptions of nuclear masses. *Phys. Rev. C*, 89, 024311. https://doi.org/10.1103/PhysRevC.89.024311

[Sorlin & Porquet, 2008] Sorlin, O. & Porquet, M.-G. (2008). Nuclear magic numbers: New features far from stability. *Prog. Part. Nucl. Phys.*, 61(2), 602–673. https://doi.org/10.1016/j.ppnp.2008.05.001

[Spataru et al., 2024] Spataru, A., Kripkó-Koncz, G., Dickel, T., Bergmann, J., & Simonov, M. (2021-2024). *Sytematic investigation of the MT calibration of broadband mass measurements of ^{252}Cf fission products with the FRS-IC.* (private communication).

[Spătaru et al., 2025] Spătaru, A., Kripkó-Koncz, G., Dickel, T., Hornung, C., Plaß, W. R., Constantin, P., Amanbayev, D., Ayet San Andrés, S., Balabanski, D. L., Beck, S., Bergmann, J., Geissel, H., Kalantar-Nayestanaki, N., Kehat, J., Mardor, I., et al. (2025). Broadband mass

measurements with the FRS Ion Catcher facility at GSI and theory developments investigating the shape-phase transition near $N = 90$. *Phys. Rev. C*, 111, 054307. https://doi.org/10.1103/PhysRevC.111.054307

[Spyrou et al., 2012] Spyrou, A., Kohley, Z., Baumann, T., Bazin, D., Brown, B. A., Christian, G., DeYoung, P. A., Finck, J. E., Frank, N., Lunderberg, E., Mosby, S., Peters, W. A., Schiller, A., Smith, J. K., Snyder, J., et al. (2012). First Observation of Ground State Dineutron Decay: ^{16}Be. *Phys. Rev. Lett.*, 108, 102501. https://doi.org/10.1103/PhysRevLett.108.102501

[Steck et al., 2004] Steck, M., Beller, P., Beckert, K., Franzke, B., & Nolden, F. (2004). Electron cooling experiments at the ESR. *Nucl. Instrum. Methods A*, 532(1), 357–365. https://doi.org/10.1016/j.nima.2004.06.065

[Steck & Litvinov, 2020] Steck, M. & Litvinov, Y. (2020). Heavy-ion storage rings and their use in precision experiments with highly charged ions. *Prog. Part. Nucl. Phys.*, 115, 103811. https://doi.org/10.1016/j.ppnp.2020.103811

[Stoitsov et al., 2007] Stoitsov, M., Cakirli, R. B., Casten, R. F., Nazarewicz, W., & Satuła, W. (2007). Empirical Proton-Neutron Interactions and Nuclear Density Functional Theory: Global, Regional, and Local Comparisons. *Phys. Rev. Lett.*, 98, 132502. https://doi.org/10.1103/PhysRevLett.98.132502

[Straub, 2011] Straub, K. (2011). *Zerfallseigenschaften von Nukliden in der Umgebung von ^{100}Sn.* Technische Universität München. https://mediatum.ub.tum.de/node?id=1006184

[Stryjczyk et al., 2025] Stryjczyk, M., Jaries, A., Ryssens, W., Bender, M., Kankainen, A., Eronen, T., Ge, Z., Moore, I., Mougeot, M., Raggio, A., & Ruotsalainen, J. (2025). Discovery of a new long-lived isomer in 114Rh via Penning-trap mass spectrometry. *Phys. Lett. B*, 862, 139359. https://doi.org/10.1016/j.physletb.2025.139359

[Suzuki et al., 2017] Suzuki, H., Sinclair, L., Söderström, P.-A., Lorusso, G., Davies, P., Ferreira, L. S., Maglione, E., Wadsworth, R., Wu, J., Xu, Z. Y., Nishimura, S., Doornenbal, P., Ahn, D. S., Browne, F., Fukuda, N., et al. (2017). Discovery of ^{72}Rb: A nuclear sandbank beyond the proton drip line. *Phys. Rev. Lett.*, 119, 192503. See also its Supplemental Material and the BigRIPS website at https://www.nishina.riken.jp/ribf/BigRIPS/intensity.html for the numerical cross-section value. https://doi.org/10.1103/PhysRevLett.119.192503

[Tarasov & Bazin, 2008] Tarasov, O. B. & Bazin, D. (2008). Lise++: Radioactive beam production with in-flight separators. *Nucl. Instrum. Methods B*, 266(19-20), 4657–4664.

[Thibault et al., 1975] Thibault, C., Klapisch, R., Rigaud, C., Poskanzer, A. M., Prieels, R., Lessard, L., & Reisdorf, W. (1975). Direct measurement of the masses of ^{11}Li and $^{26-32}$Na with an on-line mass spectrometer. *Phys. Rev. C*, 12, 644–657. https://doi.org/10.1103/PhysRevC.12.644

[Tortorelli, 2024] Tortorelli, N. (2024). *Innovative approaches to Superdeformed Nuclear Shapes Studies in Heavy Actinides.* Technische Universität Münich. https://www.ub.tum.de/en/theses

[Towner & Hardy, 2008] Towner, I. S. & Hardy, J. C. (2008). Improved calculation of the isospin-symmetry-breaking corrections to superallowed Fermi β decay. *Phys. Rev. C*, 77, 025501. https://doi.org/10.1103/PhysRevC.77.025501

[Tsang et al., 2012] Tsang, M. B., Stone, J. R., Camera, F., Danielewicz, P., Gandolfi, S., Hebeler, K., Horowitz, C. J., Lee, J., Lynch, W. G., Kohley, Z., Lemmon, R., Möller, P., Murakami, T., Riordan, S., Roca-Maza, X., et al. (2012). Constraints on the symmetry energy and neutron skins from experiments and theory. *Phys. Rev. C*, 86, 015803. https://doi.org/10.1103/PhysRevC.86.015803

[U. Köster, 2002] U. Köster (2002). Intense radioactive-ion beams produced with the ISOL method. *Eur. Phys. J. A*, 15(1), 255–263. https://doi.org/10.1140/epja/i2001-10264-2

[Valentine & Rana, 1996] Valentine, J. & Rana, A. (1996). Centroid and full-width at half maximum uncertainties of histogrammed data with an underlying Gaussian distribution-the moments method. *IEEE Transactions on Nuclear Science*, 43(5), 2501–2508. https://doi.org/10.1109/23.539399

[Van Isacker et al., 1995] Van Isacker, P., Warner, D. D., & Brenner, D. S. (1995). Test of Wigner's Spin-Isospin Symmetry from Double Binding Energy Differences. *Phys. Rev. Lett.*, 74, 4607–4610. https://doi.org/10.1103/PhysRevLett.74.4607

[Van Schelt et al., 2013] Van Schelt, J., Lascar, D., Savard, G., Clark, J. A., Bertone, P. F., Caldwell, S., Chaudhuri, A., Levand, A. F., Li, G., Morgan, G. E., Orford, R., Segel, R. E., Sharma, K. S., & Sternberg, M. G. (2013). First Results from the CARIBU Facility: Mass Measurements on the r-Process Path. *Phys. Rev. Lett.*, 111, 061102. https://doi.org/10.1103/PhysRevLett.111.061102

[Van Schelt et al., 2012] Van Schelt, J., Lascar, D., Savard, G., Clark, J. A., Caldwell, S., Chaudhuri, A., Fallis, J., Greene, J. P., Levand, A. F., Li, G., Sharma, K. S., Sternberg, M. G., Sun, T., & Zabransky, B. J. (2012). Mass measurements near the r-process path using the Canadian Penning Trap mass spectrometer. *Phys. Rev. C*, 85, 045805. https://doi.org/10.1103/PhysRevC.85.045805

[Čeliković et al., 2016] Čeliković, I., Lewitowicz, M., Gernhäuser, R., Krücken, R., Nishimura, S., Sakurai, H., Ahn, D., Baba, H., Blank, B., Blazhev, A., Boutachkov, P., Browne, F., de France, G., Doornenbal, P., Faestermann, T., et al. (2016). New Isotopes and Proton Emitters–Crossing the Drip Line in the Vicinity of ^{100}Sn. *Phys. Rev. Lett.*, 116, 162501. https://doi.org/10.1103/PhysRevLett.116.162501

[Vencelj et al., 2020] Vencelj, M., Ayet San Andres, S., & Dickel, T. (2018-2020). *Development of a temperature-stabilized, 8-fold resistive divider for the readout the voltage of the electrodes of the TOF analyzer at the FRS-IC.* (private communication, internal report).

[Vilén et al., 2019] Vilén, M., Kankainen, A., Baczyk, P., Canete, L., Dobaczewski, J., Eronen, T., Geldhof, S., Jokinen, A., Konieczka, M., Kostensalo, J., Moore, I. D., Nesterenko, D. A., Penttilä, H., Pohjalainen, I., Reponen, M., et al. (2019). High-precision mass measurements and production of neutron-deficient isotopes using heavy-ion beams at IGISOL. *Phys. Rev. C*, 100, 054333. https://doi.org/10.1103/PhysRevC.100.054333

[Walker & Podolyák, 2020] Walker, P. & Podolyák, Z. (2020). 100 years of nuclear isomers - then and now. *Physica Scripta*, 95(4), 044004. https://doi.org/10.1088/1402-4896/ab635d

[Wang et al., 2017] Wang, M., Audi, G., Kondev, F. G., Huang, W. J., Naimi, S., & Xu, X. (2017). The AME2016 atomic mass evaluation (II). Tables, graphs and references. *Chinese Phys. C*, 41(3).

[Wang et al., 2021] Wang, M., Huang, W. J., Kondev, F. G., Audi, G., & Naimi, S. (2021). The AME 2020 atomic mass evaluation (II). Tables, graphs and references. *Chin. Phys. C*, 45(3), 030003. https://doi.org/10.1088/1674-1137/abddaf

[Wang et al., 2023] Wang, M., Zhang, Y. H., Zhou, X., Zhou, X. H., Xu, H. S., Liu, M. L., Li, J. G., Niu, Y. F., Huang, W. J., Yuan, Q., Zhang, S., Xu, F. R., Litvinov, Y. A., Blaum, K., Meisel, Z., et al. (2023). Mass Measurement of Upper fp-Shell $N = Z - 2$ and $N = Z - 1$ Nuclei and the Importance of Three-Nucleon Force along the $N = Z$ Line. *Phys. Rev. Lett.*, 130, 192501. https://doi.org/10.1103/PhysRevLett.130.192501

[Wang et al., 2014] Wang, N., Liu, M., Wu, X., & Meng, J. (2014). Surface diffuseness correction in global mass formula. *Phys. Lett. B*, 734, 215–219. https://doi.org/https://doi.org/10.1016/j.physletb.2014.05.049

[Wapstra et al., 2003] Wapstra, A., Audi, G., & Thibault, C. (2003). The AME2003 atomic mass evaluation: (I). Evaluation of input data, adjustment procedures. *Nuclear Physics A*, 729(1), 129–336. The 2003 NUBASE and Atomic Mass Evaluations. https://doi.org/10.1016/j.nuclphysa.2003.11.002

[Waschitz et al., 2023] Waschitz, Y., Amanbayev, D., Spătaru, A., Mardor, I., Dickel, T., Cohen, E. O., Aviv, O., Ayet San Andrés, S., Balabanski, D. L., Beck, S., Bergmann, J., Brencic, Z., Constantin, P., Dehghan, M., Geissel, H., et al. (2023). Independent isotopic fission yields of ^{252}Cf spontaneous fission via mass measurements at the FRS Ion Catcher. *EPJ Web Conf.*, 284, 04005. https://doi.org/10.1051/epjconf/202328404005

[Weber et al., 2008] Weber, C., Elomaa, V.-V., Ferrer, R., Fröhlich, C., Ackermann, D., Äystö, J., Audi, G., Batist, L., Blaum, K., Block, M., Chaudhuri, A., Dworschak, M., Eliseev, S., Eronen, T., Hager, U., et al. (2008). Mass measurements in the vicinity of the rp-process and the νp-process paths with the Penning trap facilities JYFLTRAP and SHIPTRAP. *Phys. Rev. C*, 78, 054310. https://doi.org/10.1103/PhysRevC.78.054310

[Weick et al., 2018] Weick, H., Geissel, H., Iwasa, N., Scheidenberger, C., Sanchez, J. L. R., Prochazka, A., S., P., & the Super-FRS experiment collaboration (2018). Improved accuracy of the code ATIMA for energy loss of heavy ions in matter. *GSI Sci. Rep. 2017*. Software available online at https://www.isotopea.com/webatima/. https://web-docs.gsi.de/~weick/atima/ATIMA_GSI_scientific_report_2017-5.pdf

[Weizsäcker, 1935] Weizsäcker, C. F. v. (1935). Zur Theorie der Kernmassen. *Z. Phys.*, 96, 431–458. https://doi.org/10.1007/BF01337700

[Wigner, 1937] Wigner, E. (1937). On the Consequences of the Symmetry of the Nuclear Hamiltonian on the Spectroscopy of Nuclei. *Phys. Rev.*, 51, 106–119. https://doi.org/10.1103/PhysRev.51.106

[Will, 2017] Will, C. (2017). *TITAN's Multiple-Reflection Time-of-Flight Mass Spectrometer and Isobar Separator Characterization and First Experiments*. geb.uni-giessen.de

[Wolf et al., 2013] Wolf, R., Wienholtz, F., Atanasov, D., Beck, D., Blaum, K., Borgmann, C., Herfurth, F., Kowalska, M., Kreim, S., Litvinov, Y. A., Lunney, D., Manea, V., Neidherr, D., Rosenbusch, M., Schweikhard, L., et al. (2013). ISOLTRAP's multi-reflection time-of-flight mass separator/spectrometer. *Int. J. Mass Spectrom.*, 349-350, 123–133. https://doi.org/10.1016/j.ijms.2013.03.020

[Wollnik, 1987] Wollnik, H. (1987). Laterally and longitudinally dispersive recoil mass separators. *Nucl. Instrum. Methods B*, 26(1), 267–272. https://doi.org/10.1016/0168-583X(87)90762-2

[Wollnik & Becker, 1985] Wollnik, H. & Becker, K. (1985). Ion optical design for an on-line mass separator with low cross contamination and the capability of good mass resolution. *Nucl. Instrum. Methods A*, 238(2), 206–214. https://doi.org/10.1016/0168-9002(85)90456-5

[Wollnik & Przewloka, 1990] Wollnik, H. & Przewloka, M. (1990). Time-of-flight mass spectrometers with multiply reflected ion trajectories. *Int. J. Mass Spectrom. Ion Processes*, 96(3), 267–274. https://doi.org/10.1016/0168-1176(90)85127-N

[Wu et al., 2016] Wu, Z., Changizi, S. A., & Qi, C. (2016). Empirical residual neutron-proton interaction in odd-odd nuclei. *Phys. Rev. C*, 93, 034334. https://doi.org/10.1103/PhysRevC.93.034334

[Xayavong & Smirnova, 2018] Xayavong, L. & Smirnova, N. A. (2018). Radial overlap correction to superallowed $0^+ \to 0^+$ β decay reexamined. *Phys. Rev. C*, 97, 024324. https://doi.org/10.1103/PhysRevC.97.024324

[Xayavong & Smirnova, 2024] Xayavong, L. & Smirnova, N. A. (2024). Higher-order isospin-symmetry-breaking corrections to nuclear matrix elements of fermi β decays. *Phys. Rev. C*, 109, 014317. https://doi.org/10.1103/PhysRevC.109.014317

[Xia et al., 2002] Xia, J., Zhan, W., Wei, B., Yuan, Y., Song, M., Zhang, W., Yang, X., Yuan, P., Gao, D., Zhao, H., Yang, X., Xiao, G., Man, K., Dang, J., Cai, X., et al. (2002). The heavy ion cooler-storage-ring project (HIRFL-CSR) at Lanzhou. *Nucl. Instrum. Methods A*, 488(1), 11–25. https://doi.org/10.1016/S0168-9002(02)00475-8

[Xing et al., 2021] Xing, F., Cui, J., Wang, Y., & Gu, J. (2021). Two-proton radioactivity of ground and excited states within a unified fission model. *Chin. Phys. C*, 45(12), 124105. https://doi.org/10.1088/1674-1137/ac2425

[Xing & Wang, 2023] Xing, X. & Wang, M. (2023). *Plot of relative mass uncertainty using different direct mass measurement techniques with respect to the half-life of the measured isotopes.* (private communication, plot presented by M. Wang on NUSTAR seminar at GSI (01.11.2023)).

[Xing et al., 2018] Xing, Y., Li, K., Zhang, Y., Zhou, X., Wang, M., Litvinov, Y., Blaum, K., Wanajo, S., Kubono, S., Martínez-Pinedo, G., Sieverding, A., Chen, R., Shuai, P., Fu, C., Yan, X., et al. (2018). Mass measurements of neutron-deficient Y, Zr, and Nb isotopes and their impact on rp and νp nucleosynthesis processes. *Phys. Lett. B*, 781, 358–363. https://doi.org/10.1016/j.physletb.2018.04.009

[Xing et al., 2023] Xing, Y. M., Yuan, C. X., Wang, M., Zhang, Y. H., Zhou, X. H., Litvinov, Y. A., Blaum, K., Xu, H. S., Bao, T., Chen, R. J., Fu, C. Y., Gao, B. S., Ge, W. W., He, J. J., Huang, W. J., et al. (2023). Isochronous mass measurements of neutron-deficient nuclei from ^{112}Sn projectile fragmentation. *Phys. Rev. C*, 107, 014304. https://doi.org/10.1103/PhysRevC.107.014304

[Yamaguchi et al., 2021] Yamaguchi, T., Koura, H., Litvinov, Y., & Wang, M. (2021). Masses of exotic nuclei. *Prog. Part. Nucl. Phys.*, 120, 103882. https://doi.org/10.1016/j.ppnp.2021.103882

[Yamaguchi et al., 2013] Yamaguchi, Y., Wakasugi, M., Uesaka, T., Ozawa, A., Abe, Y., Fujinawa, T., Kase, M., Komiyama, M., Kubo, T., Kumagai, K., Maie, T., Nagae, D., Ohnishi, J., Suzaki, F., Tokuchi, A., et al. (2013). Construction of rare-RI ring at RIKEN RI Beam Factory. *Nucl. Instrum. Methods B*, 317, 629–635. https://doi.org/10.1016/j.nimb.2013.06.004

[Yaneva et al., 2024] Yaneva, A., Jazrawi, S., Mikolajczuk, M., Górska, M., Regan, P., Das, B., Albers, H., Alhomaidhi, S., Arici, T., Banerjee, A., Benzoni, G., Cederwall, B., Chishti, M., Dao, D., Davinson, T., et al. (2024). The shape of the $T_Z = +1$ nucleus ^{94}Pd and the role of proton-neutron interactions on the structure of its excited states. *Phys. Lett. B*, 855, 138805. https://doi.org/10.1016/j.physletb.2024.138805

[Yavor et al., 2015] Yavor, M. I., Plaß, W. R., Dickel, T., Geissel, H., & Scheidenberger, C. (2015). Ion-optical design of a high-performance multiple-reflection time-of-flight mass spectrometer and isobar separator. *Int. J. Mass Spectrom.*, 381-382, 1–9. https://doi.org/10.1016/j.ijms.2015.01.002

[Yu et al., 2024a] Yu, J., Hornung, C., Dickel, T., Plaß, W. R., Amanbayev, D., Bergmann, J., Ge, Z., Greiner, F., Geissel, H., Gröf, L., Kripko-Koncz, G., Narang, M., Rink, A.-K., Scheidenberger, C., & Zhao, J. (2024a). A laser ablation carbon cluster ion source for the FRS Ion Catcher. *Nucl. Instrum. Methods A*, 1064, 169371. https://doi.org/10.1016/j.nima.2024.169371

[Yu et al., 2024b] Yu, J., Mollaebrahimi, A., San Andrés, S. A., Dickel, T., Plaß, W. R., Wilsenach, H., Beck, S., Ge, Z., Geissel, H., Hornung, C., Jacobs, A., Kripko-Koncz, G., Kwiatkowski, A. A., Narang, M., Scheidenberger, C., et al. (2024b). A compact ion source combining electron-impact and thermal ionization for multiple-reflection time-of-flight mass spectrometry. *Rev. Sci. Instrum.*, 95(8), 083309. https://doi.org/10.1063/5.0213443

[Zeldes & Liran, 1976] Zeldes, N. & Liran, S. (1976). Pairing-isopairing competition in odd-odd nuclei. *Phys. Lett. B*, 62(1), 12–14. https://doi.org/10.1016/0370-2693(76)90034-4

[Zhang et al., 1989] Zhang, J.-Y., Casten, R., & Brenner, D. (1989). Empirical proton-neutron interaction energies. Linearity and saturation phenomena. *Physics Letters B*, 227(1), 1–5. https://doi.org/10.1016/0370-2693(89)91273-2

[Zhang et al., 2023] Zhang, M., Zhou, X., Wang, M., Zhang, Y. H., Litvinov, Y. A., Xu, H. S., Chen, R. J., Deng, H. Y., Fu, C. Y., Ge, W. W., Li, H. F., Liao, T., Litvinov, S. A., Shuai, P., Shi, J. Y., et al. (2023). $B\rho$-defined isochronous mass spectrometry and mass measurements of ^{58}Ni fragments. *Eur. Phys. J. A*, 59, 27. https://doi.org/10.1140/epja/s10050-023-00928-6

[Zhu et al., 2022] Zhu, D.-X., Xu, Y.-Y., Liu, H.-M., Wu, X.-J., He, B., & Li, X.-H. (2022). Two-proton radioactivity of the excited state within the Gamow-like and modified Gamow-like models. *Nucl. Sci. Tech.*, 33, 122. https://doi.org/10.1007/s41365-022-01116-9

[Zong et al., 2022] Zong, Y. Y., Ma, C., Lin, M. Q., & Zhao, Y. M. (2022). Mass relations of mirror nuclei for both bound and unbound systems. *Phys. Rev. C*, 105, 034321. https://doi.org/10.1103/PhysRevC.105.034321

Selbstständigkeitserklärung

Ich erkläre: Ich habe die vorgelegte Dissertation selbständig und ohne unerlaubte fremde Hilfe und nur mit den Hilfen angefertigt, die ich in der Dissertation angegeben habe. Alle Textstellen, die wörtlich oder sinngemäß aus veröffentlichten Schriften entnommen sind, und alle Angaben, die auf mündlichen Auskünften beruhen, sind als solche kenntlich gemacht. Ich stimme einer evtl. Überprüfung meiner Dissertation durch eine Antiplagiat-Software zu. Bei den von mir durchgeführten und in der Dissertation erwähnten Untersuchungen habe ich die Grundsätze guter wissenschaftlicher Praxis, wie sie in der „Satzung der Justus-Liebig-Universität Gießen zur Sicherung guter wissenschaftlicher Praxis“ niedergelegt sind, eingehalten.

Datum

Gabriella Kripkó-Koncz

Erstgutachter: Prof. Dr. Christoph Scheidenberger
Zweitgutachter: Prof. Dr. Kai-Thomas Brinkmann